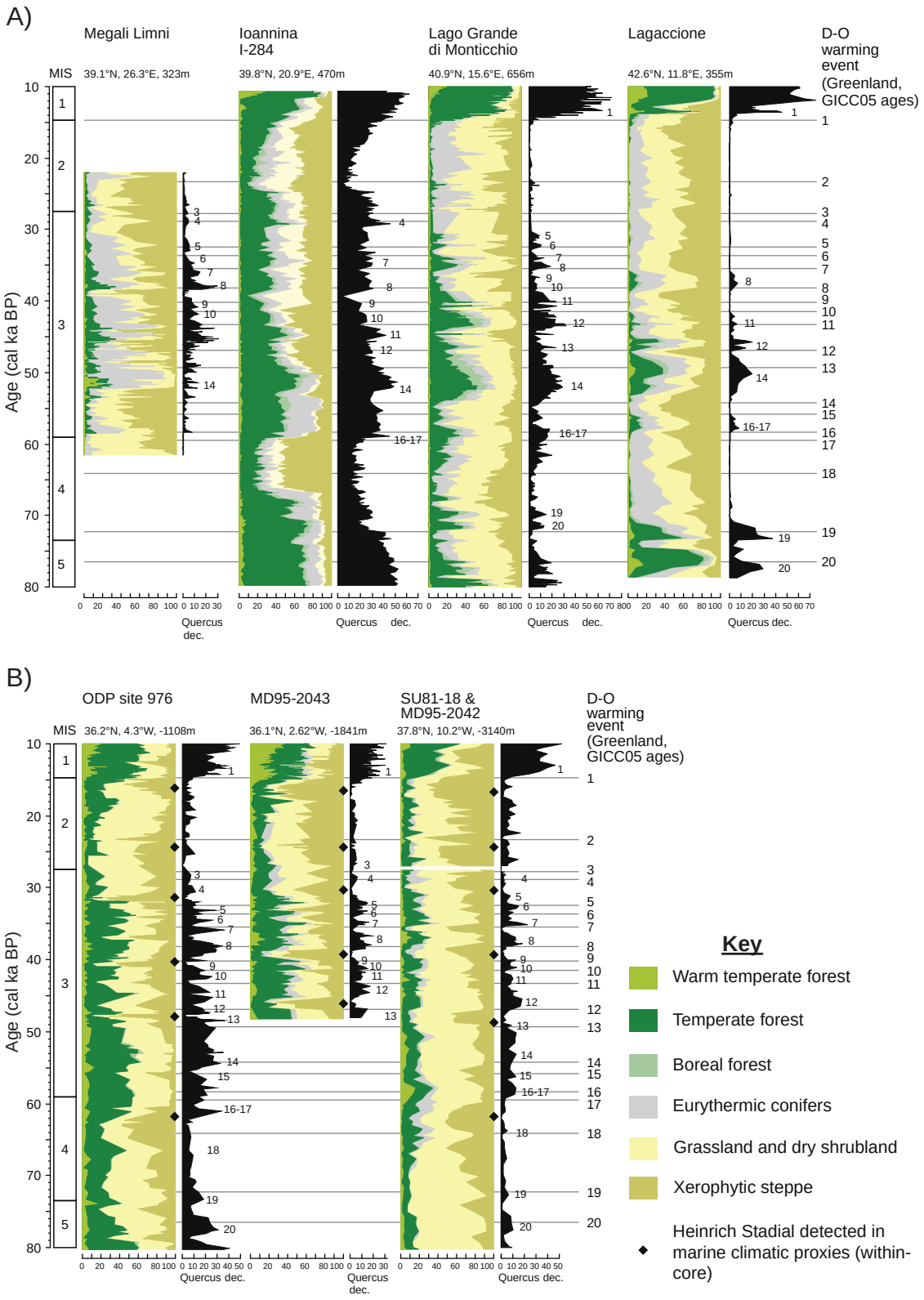

Figure 1.1: Vegetation changes during MIS 4, 3 and 2 in several high resolution records from the Mediterranean region, where correlations of assumed D-O cycles have been made. Each site shows a summary diagram with taxa consistently assigned to a simple biome scheme and a single curve (filled in black) showing the percentage values of deciduous *Quercus* that displays distinct millennial-scale variability. All records are plotted using the best available chronology for each individual site. a) Terrestrial records and b) Marine records. Diagram adapted from Fletcher et al. (2010).

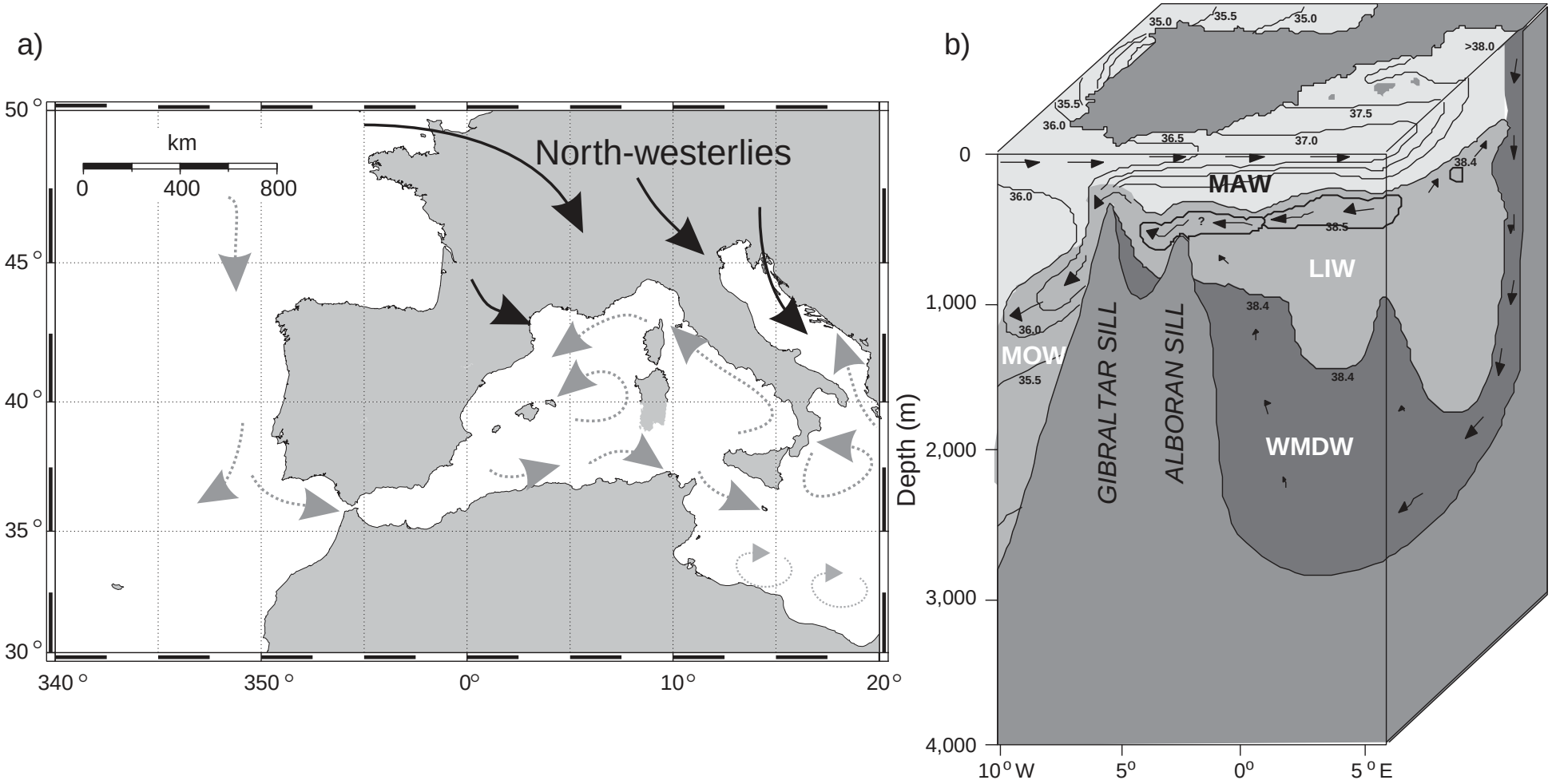

Figure 1.2: a) Present-day dominant oceanographic circulation (dashed arrows) showing the connection of the North Atlantic to the Mediterranean Sea through the flow of surface waters into the Mediterranean through the Strait of Gibraltar. b) 3D illustration of the water masses that link the Atlantic Ocean and Western Mediterranean Sea. MAW = Modified Atlantic Water, LIW = Levantine Intermediate Water, WMDW = Western Mediterranean Deep Water and MOW = Mediterranean Overflow Water. Diagram adapted from Moreno et al. (2005)

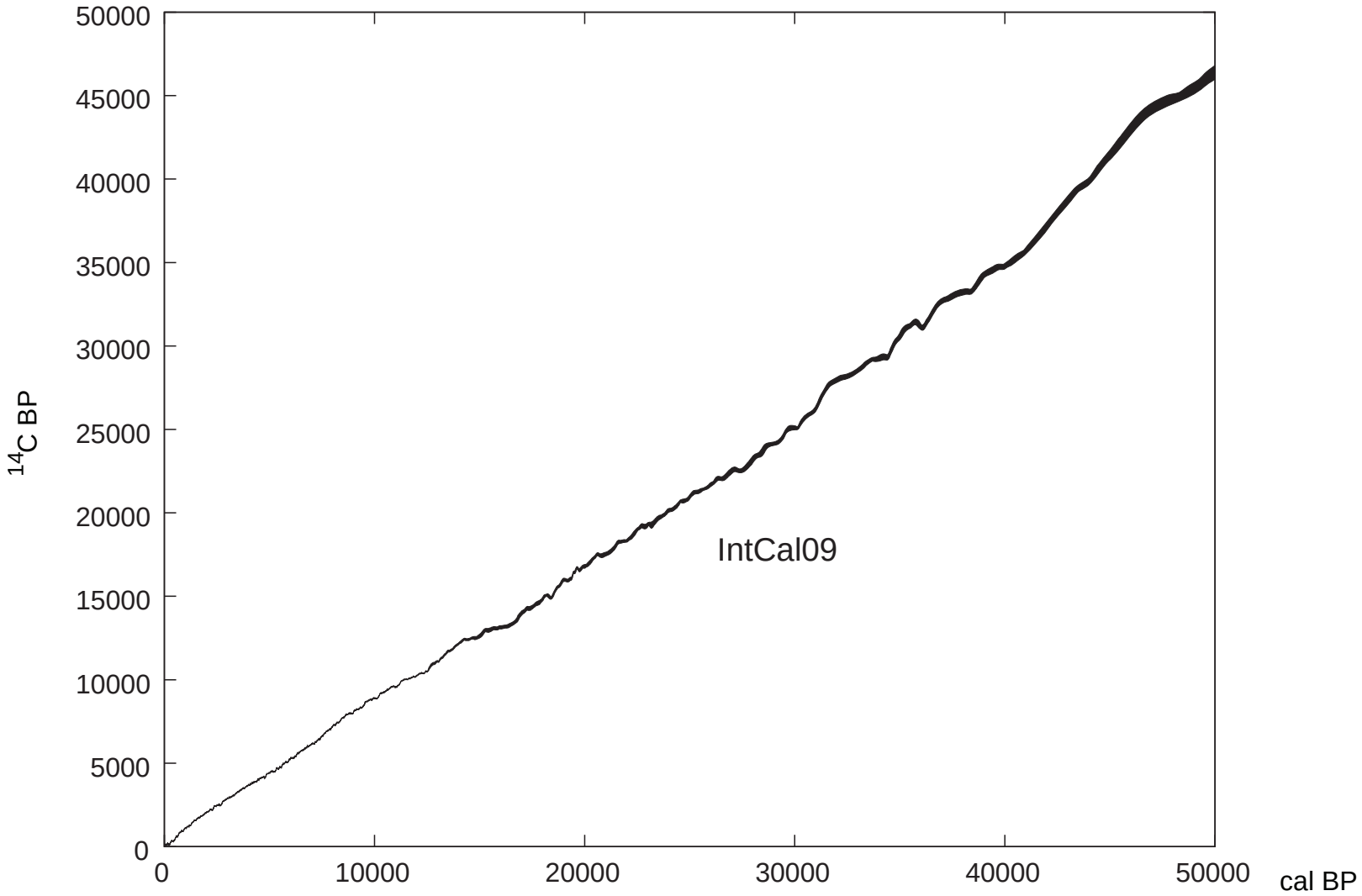

Figure 1.3: IntCal09 calibration curve with 1-standard deviation envelopes (Reimer *et al.,* 2009), showing how the errors of calibration increase with age. It is also clear that this technique is not applicable to the whole time-frame (last glacial-interglacial cycle) of interest in this study.

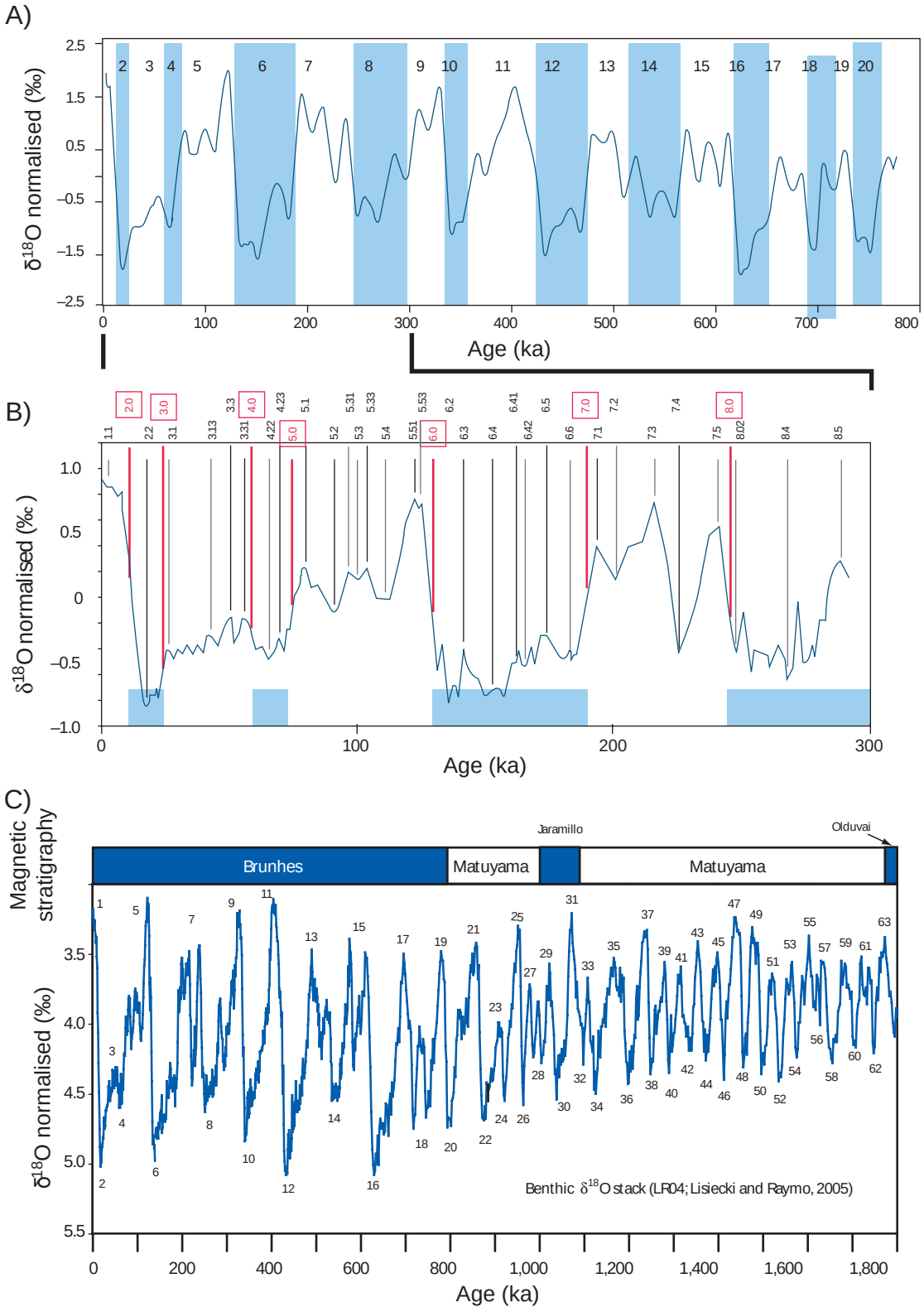

Figure 1.4: A) The reference oxygen isotope record established by the SPECMAP group by stacking five planktonic isotopic records (Pisias *et al.,* 1984). The age model was developed by phase-locking oxygen isotope oscillations to an orbital forcing function (Imbrie *et al.,* 1984). B) Detailed oxygen-isotopic record from the last 300 kyr obtained by stacking benthic records and tied to orbital-forcing functions (Martinson *et al.,* 1987). C) Isotopic curve LR04 obtained by stacking 57 global benthic isotopic records with age modelling obtained through orbital tuning (Lisiecki and Raymo, 2005) Diagrams adapted from Bassinot (2007).

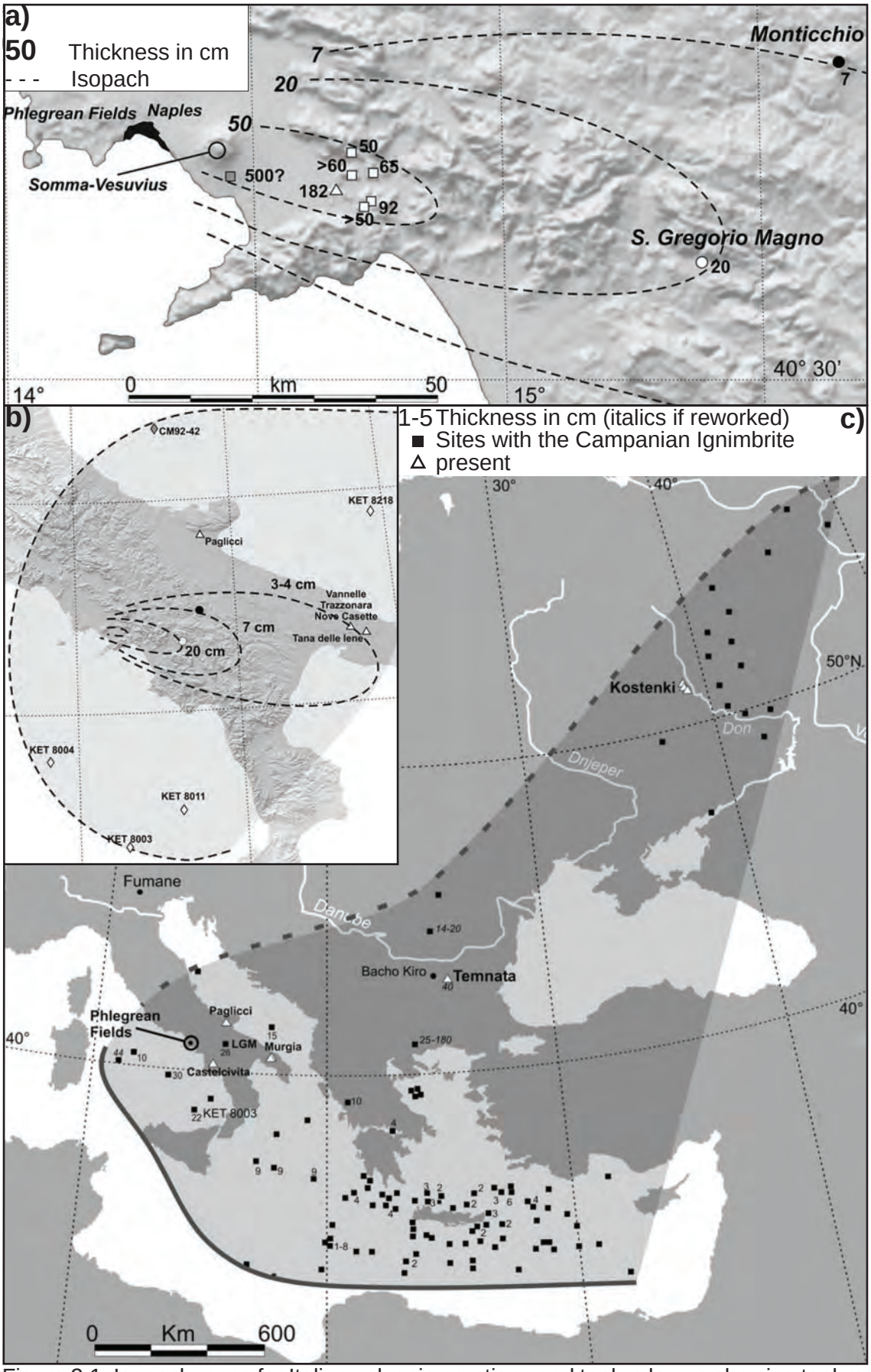

Figure 2.1: Isopach maps for Italian volcanic eruptions and tephra layers showing tephra fall out over Southern Europe. a) Inferred isopach map of the proximal and medial Codola deposits; b) Isopach map for the Codola tephra layer (and its marine equivalent) including distal tephra layers; c) Distribution of the Campanian Ignimbrite (CI) at distal sites (reproduced from Giaccio *et al.,* 2008).

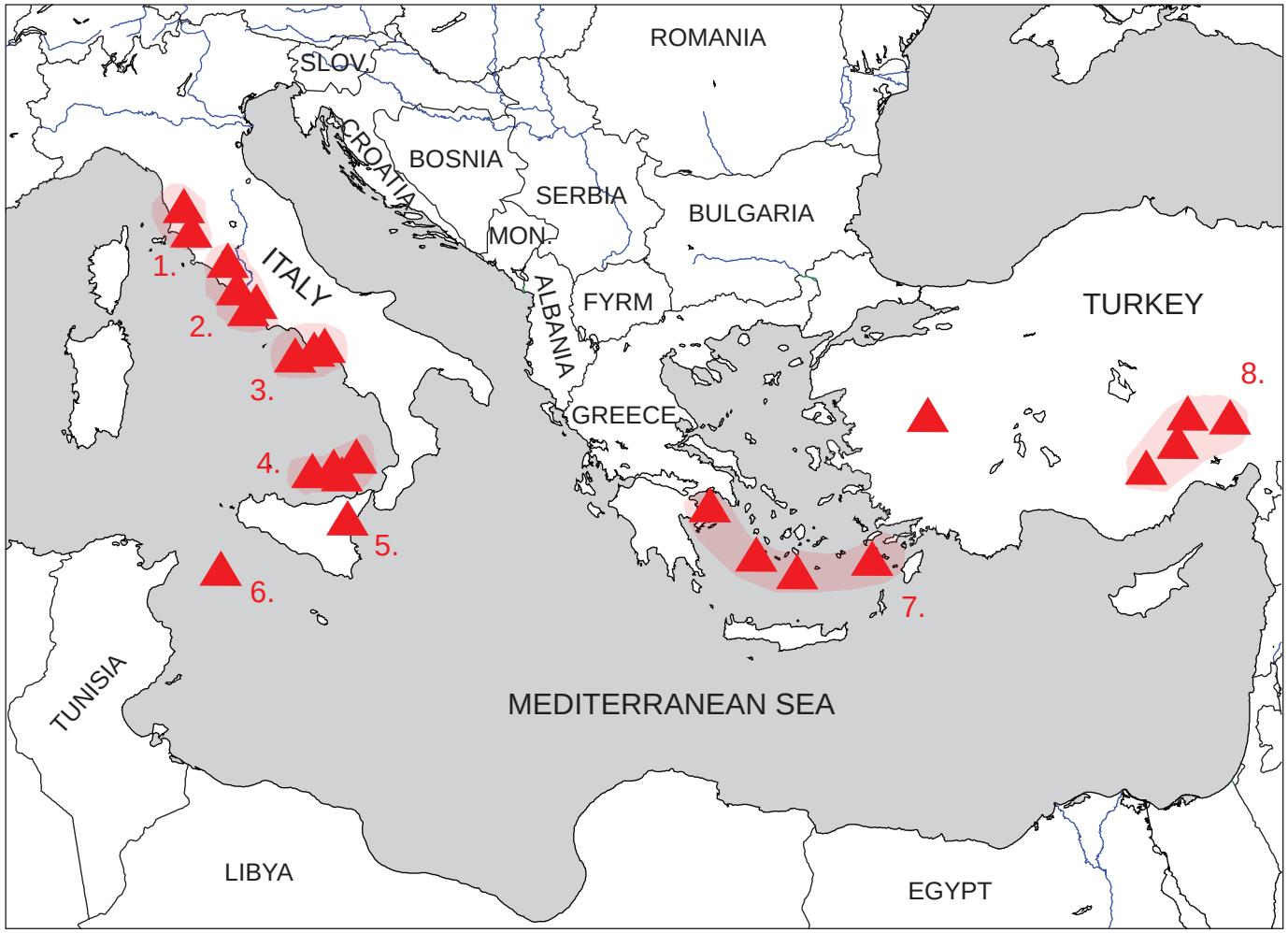

Figure 2.2: Major volcanic source areas that have been identified as preserving tephra layers around the Mediterranean Region during the Quaternary. 1. Tuscan Province, 2. Roman Province, 3. Campanian Province, 4. Aeolian Province, 5. Etna, 6. Pantelleria, 7. Hellenic Arc, 8. Central Anatolia. (Base map from NOAA MapPad, 2011).

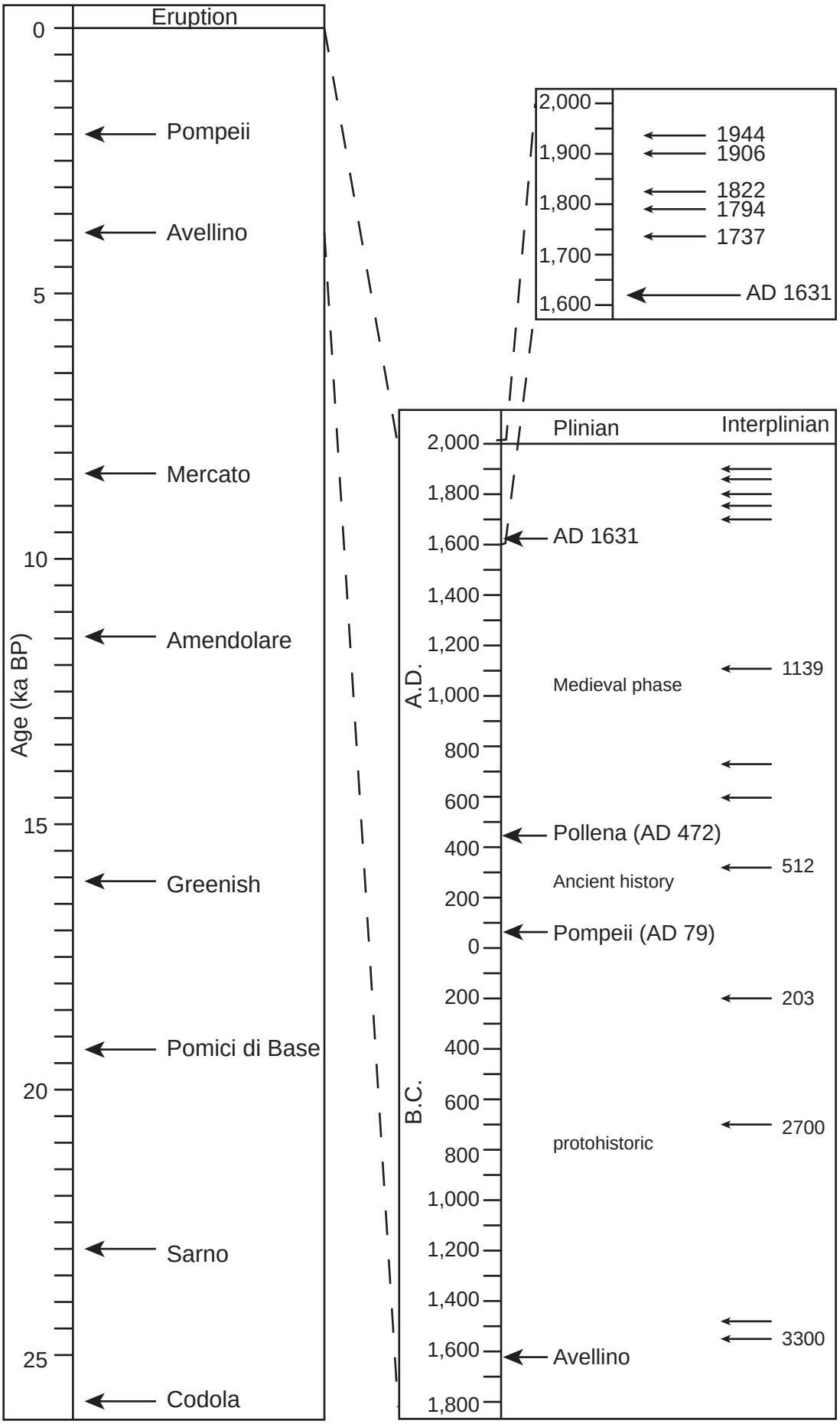

Figure 2.3: Chronological chart of the eruptions from Somma-Vesuvius (adapted from Guest *et al.,* 2003). Only approximate dates of eruptions are shown to indicate the sequence of eruptions from Somma-Vesuvius.

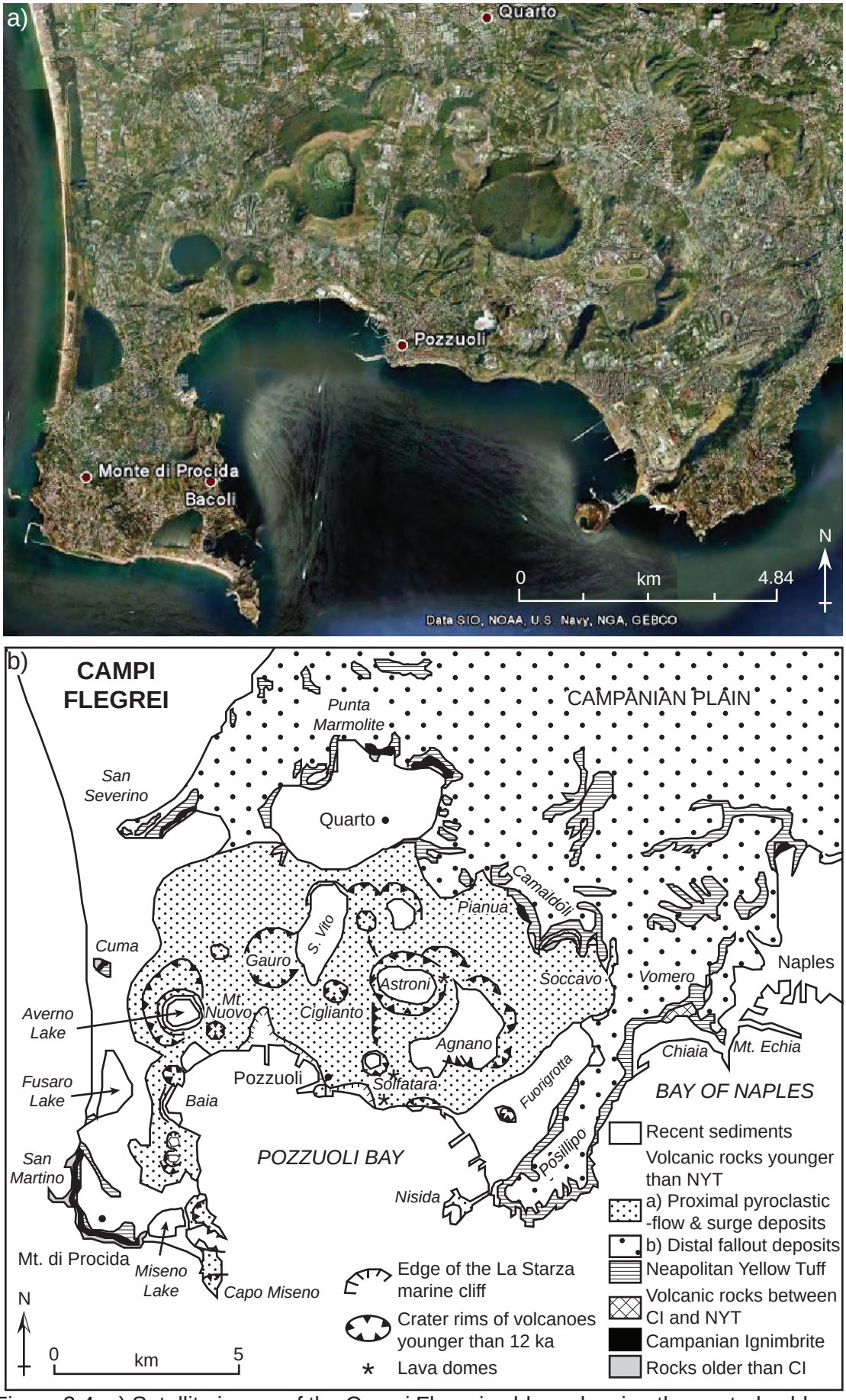

Figure 2.4: a) Satellite image of the Campi Flegrei caldera showing the nested calderas and craters (Google Earth, 2010). b) Geological map of the Campi Flegrei, showing the names of the calderas and major deposits (modified from Guest *et al.,* 2003).

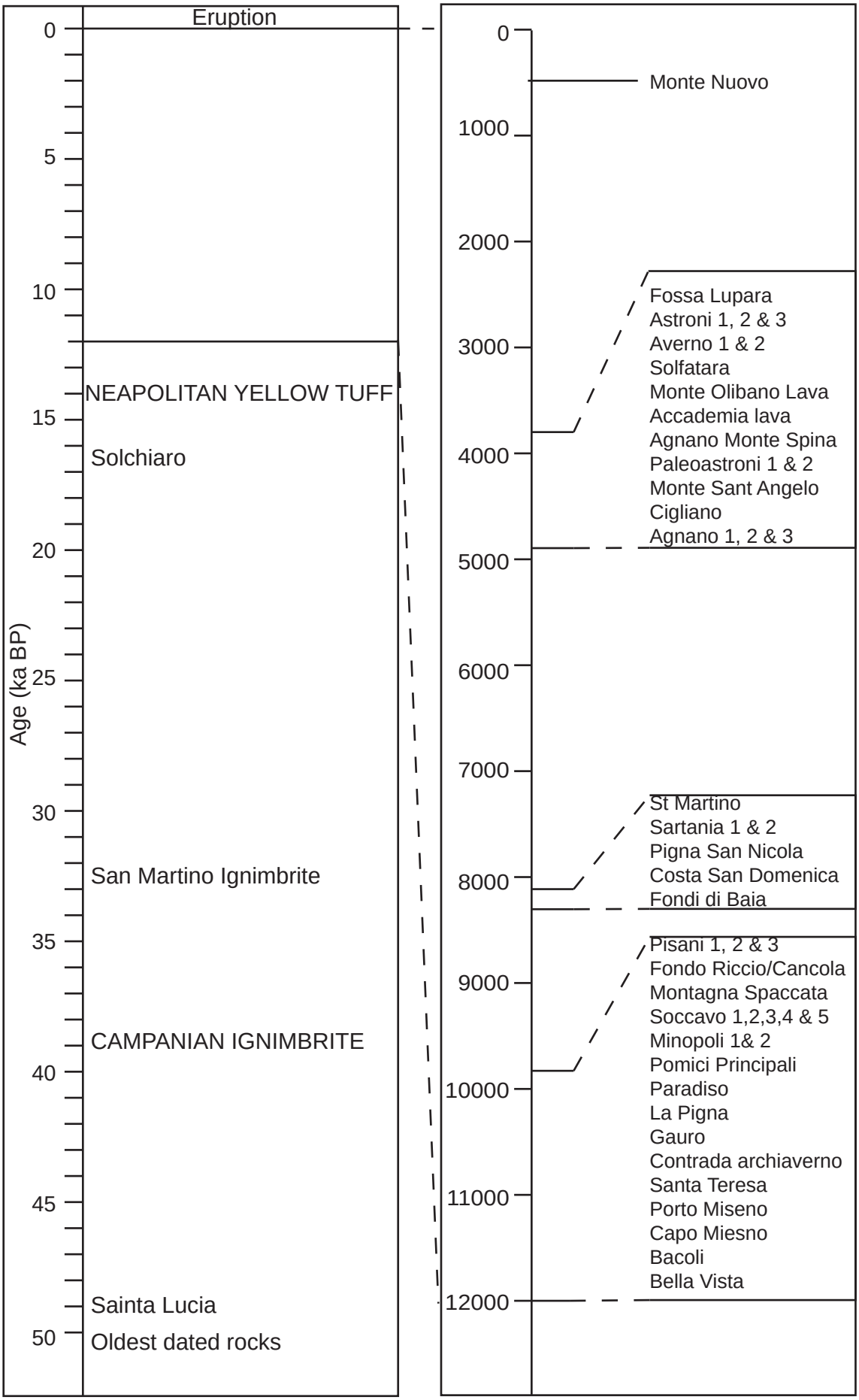

Figure 2.5: Chronological chart of the eruptions from the Campi Flegrei (adapted from Guest *et al.,* 2003). Only approximate dates of eruptions are shown to indicate the sequence of eruptions from the Campi Flegrei.

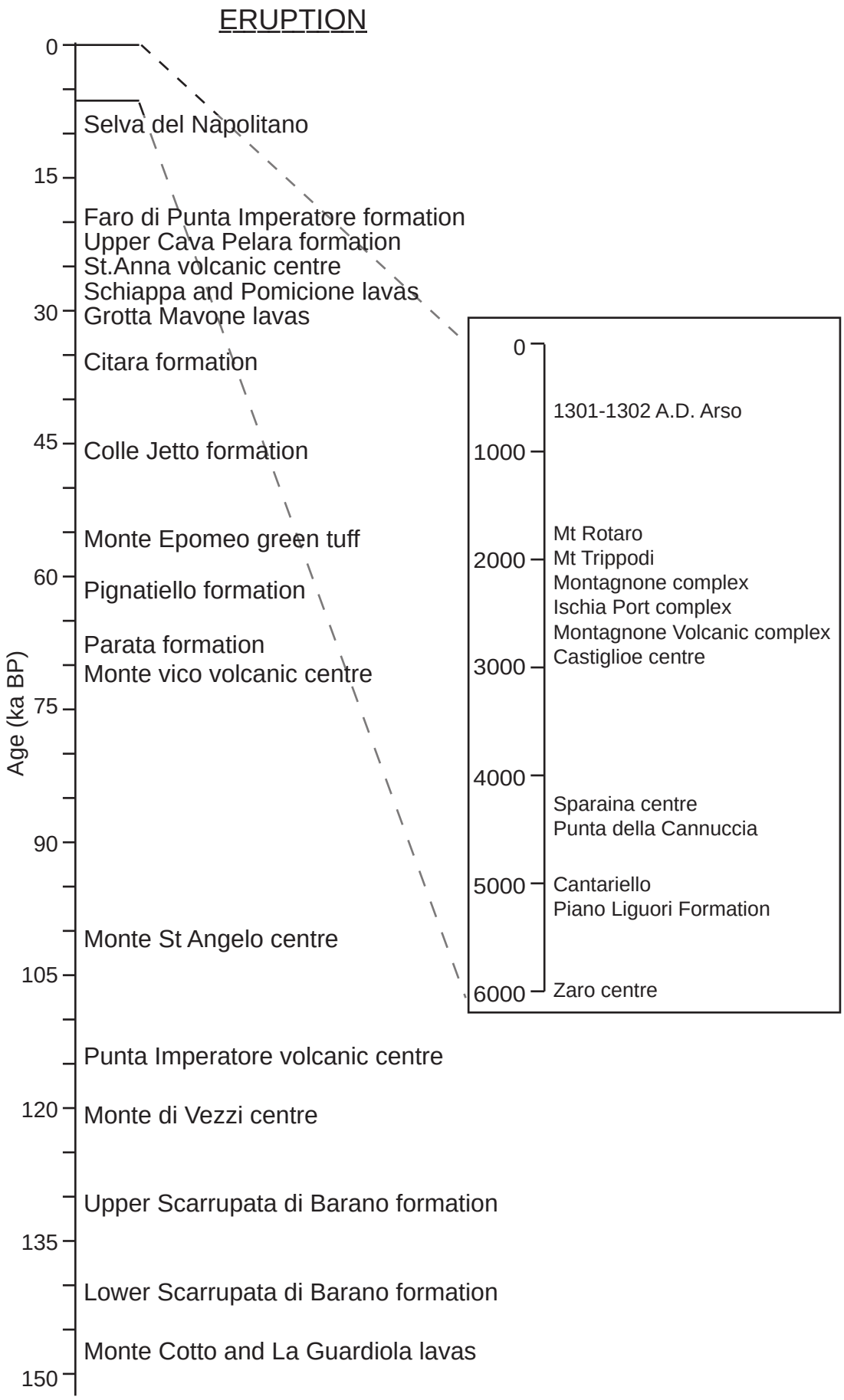

Figure 2.6: Chronological chart of the eruptions from Ischia Island (adapted from Guest *et al.,* 2003). Only approximate dates of eruptions are shown to indicate the sequence of eruptions from Ischia Island.

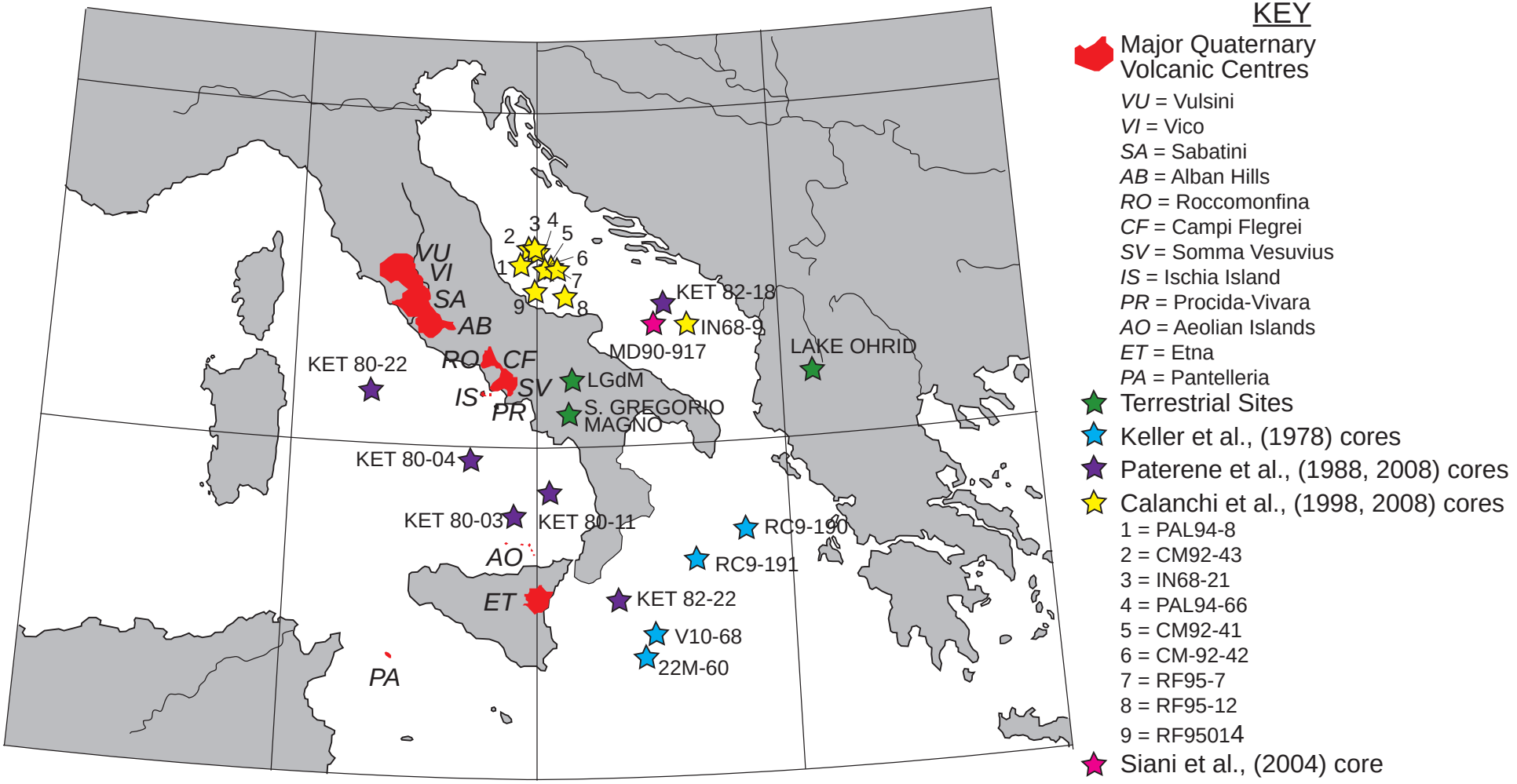

Figure 2.7: Location of the main Italian volcanic centres that were active during the Quaternary. The locations of the terrestrial and marine tephra studies discussed in the text are also shown. LGdM = Lago Grande di Monticchio. Marine core locations from Keller *et al.* (1978), Paterne *et al.* (1988, 2008), Calanchi *et al.* (1998, 2008), Siani *et al.* (2004). Terrestrial site locations from Wulf *et al.* (2004) (LGdM), Munno and Petrosini. (2007) (San Gregorio Magno Basin), Wagner *et al.* (2008) (Lake Ohrid).

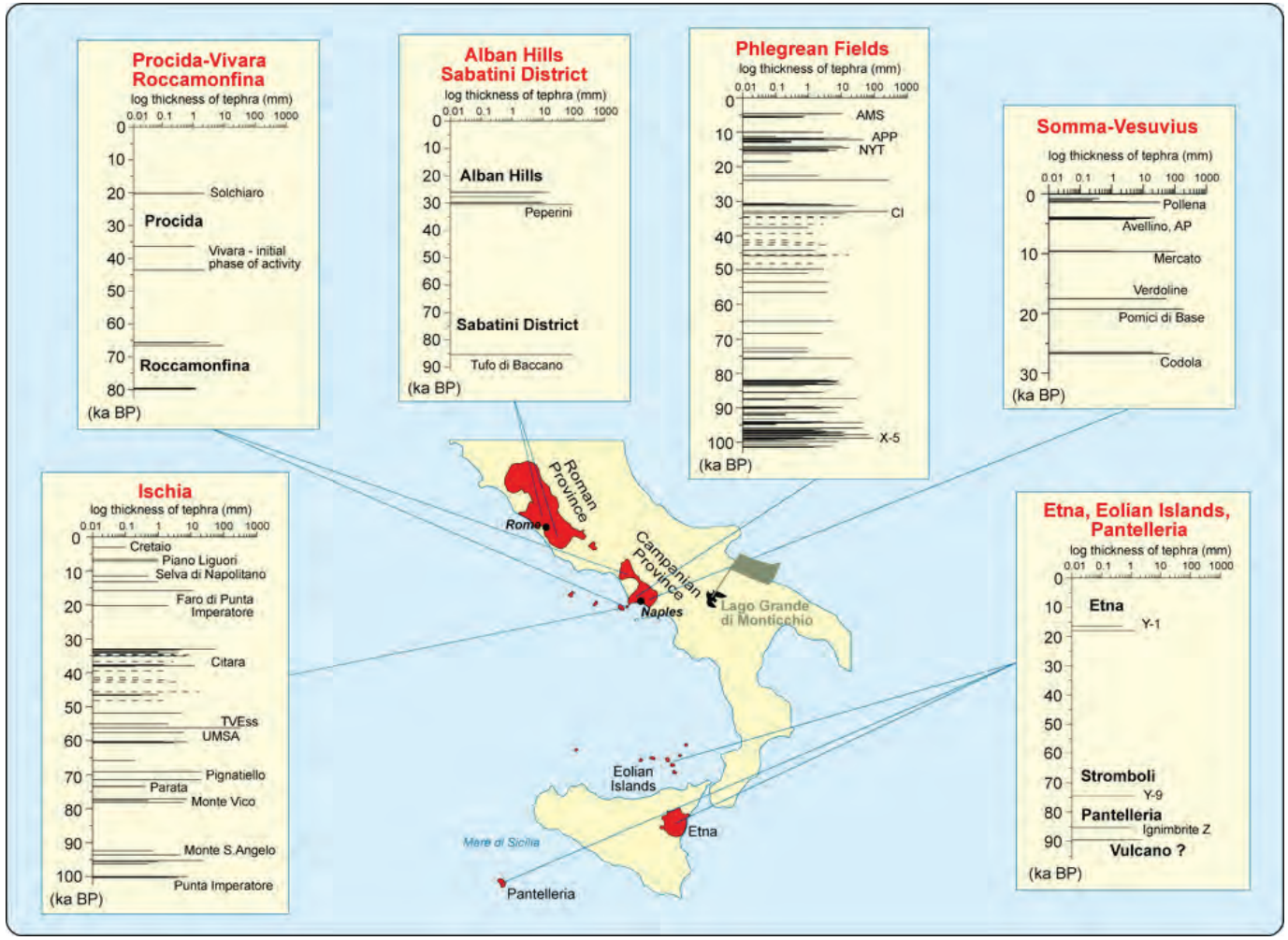

Figure 2.8: Location of Lago Grande di Monticchio and the main Italian Volcanic Centres. The LGdM tephra layers are grouped by source volcano with the tephra layers plotted through time and the main volcanic eruptions highlighted (reproduced from Wulf *et al.,* 2004).

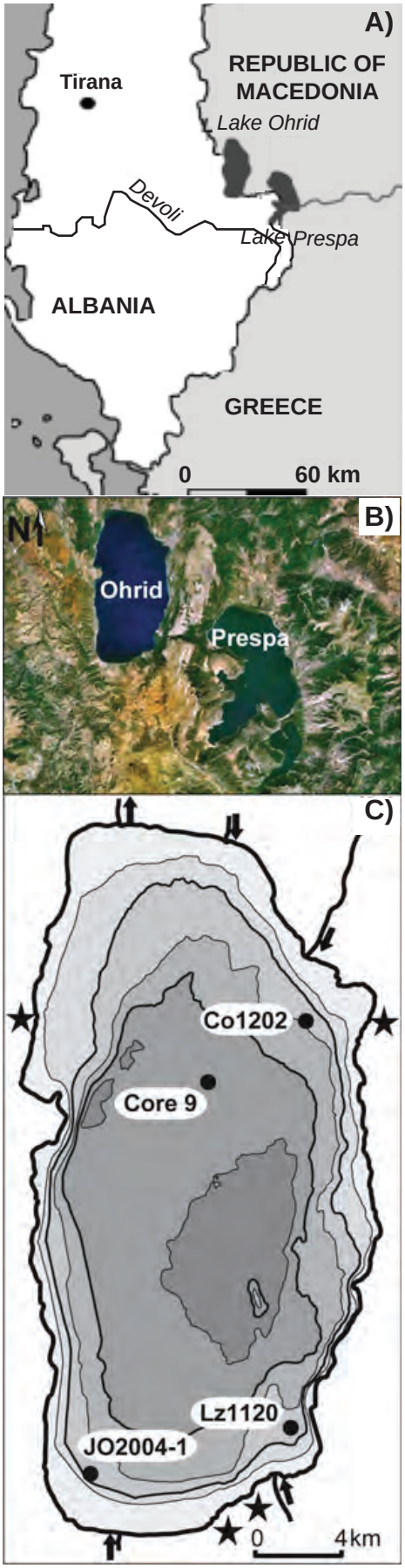

Figure 2.9: A) Location of Lake Ohrid on the Albanian/Macedonian border. B) Satellite image showing Lakes Ohrid and Prespa. C) Bathymetric map of Lake Ohrid showing the coring sites for the different tephra studies conducted. Co1202 (Vogel *et al.,* 2010a and b), Lz1120 (Wagner *et al.,* 2008) and JO2004-1 (Lézine *et al.,* 2010).

Table 2.8: Tephra layers from terrestrial and marine records, their stratigraphic order, their source volcano and correlation to known volcanic eruptions. For all studies only tephra layers that have at least one other correlative within the region are shown and for Keller *et al.* (1978) only layers from an Italian volcanic province are shown. Sources: SV Somma-Vesuvius, IS Ischia, CF Campi Flegrei, ET Etna, PR Procida-Vivara, AB Alban Hills, EO Aeolian Islands, PA Pantelleria, CAMP Campanian Province, ROME Roman Province.

Age (ka)	Terrestrial Records			Marine Records										Source	Volcanic Eruption
				Mediterranean Studies		Adriatic Cores Calanchi *et al.* (1998, 2008) (Depth of layers in cm)							MD90-917 Siani *et al.* (2004)		
	LGdM Wulf *et al.* (2004)	San Gregorio Magno Basin (Munno & Petrosino, 2007)	Lake Ohrid Wagner *et al.* (2008) Vogel *et al.* (2010) *Caron et al. (2010)*	Keller *et al.* (1978)	Paterne *et al.* (1988, 2008)	CM92-43 *IN68-21*	PAL94-66 *CM92-41*	PAL94-8 *CM92-42*	RF95-7	RF95-12	RF95-14	IN68-9			
1.5	TM-2a, b		OT0702-1											SV	a=AD-472, b=AD-512
3			**310 cm** OT0702-1 *JO-42*											ET	FL eruption
4	TM-3b									200	240			SV	AP3
	TM-3c											20		SV	AP2
	TM-4			Z-1										SV	Avellino
	TM-5a,b												140 cm	CF	Astroni
5	TM-5c					150 *100*	64 *70*	128		260	250	30	167 cm	CF	AMS
9	TM-6		OT0702-3		V-1							125		SV	Mercato
12	TM-7				C-1						550	178	305 cm	CF	Pomici Principali
14	TM-8	S21			C-2	605 *402*	214 *260*	208 *200*		560		225	295 cm	CF	NYT
	TM-9												405 cm	CF	Tufi Biancastri/GM1
15	TM-10						266 *270*						435 cm	CF	Lagno Amendolare
16	TM-11			Y-1	Et-1		358 *420*	353					490 cm	ET	Biancavilla
17	TM-12	S20												SV	Greenish
19	TM-13											525	595 cm	SV	Pomici di Base
	TM-14				C-4									PR	Solchiaro

Age (ka)	Terrestrial Records			Marine Records										Source	Volcanic Eruption
				Mediterranean Studies		Adriatic Cores Calanchi *et al.* (1998, 2008) (Depth of layers in cm)							MD90-917 Siani *et al.* (2004)		
	LGdM Wulf et al. (2004)	San Gregorio Magno Basin (Munno & Petrosino, 2007)	Lake Ohrid Wagner *et al.* (2008) Vogel *et al.* (2010) *Caron et al. (2010)*	Keller *et al.* (1978)	Paterne *et al.* (1988, 2008)	CM92-43 *IN68-21*	PAL94-66 *CM92-41*	PAL94-8 *CM92-42*	RF95-7	RF95-12	RF95-14	IN68-9			
30	TM-15	S19	**896cm** OT0702-4 *JO-187*	Y-3	C-7									CF	Unknown, distally described layer (Y-3)
	TM-16	S18	OT0702-5		C-10			*400*						SV	Codola
	TM-17-2				C-9									CF	Schiava
40	TM-18	S17	**1075cm** OT0702-6 *JO-244*	Y-5	C-13			*450*						CF	CI
45			OT0702-7	Y-6										PA	Green Tuff
55	TM-19	S16			C-16									IS	MEGT
					C-17									IS	Barano tuff
	TM-20	S15		Y-7	C-18									IS	UMSA
70	TM-21			Y-9/X-1										EO	Petrazza Tuffs
	TM-22				P-10									PA	Ante Green Ignimbrite
		S14		X-2					80					CAMP	Unknown
89					C-22									CAMP	Unknown
90				X-3										EO	Unknown
				X-4										ET	Unknown
105	TM-24	S11	OT0702-8	X-5	C-27			*710*						CAMP	Unknown (X-5)
107	TM-27	S10	OT0702-9 *JO-575*	X-6	C-31									CAMP	Unknown (X-6)
		S9			C-36									?	Unknown
131			OT0702-10 *JO-941*		P-11									PA	Unknown
145		S7		W-1	C-41				335					ROME	Unknown (W-1)
182		S6			C-50									?	Unknown
		S5		V-2					450					ROME	Unknown (V-2)

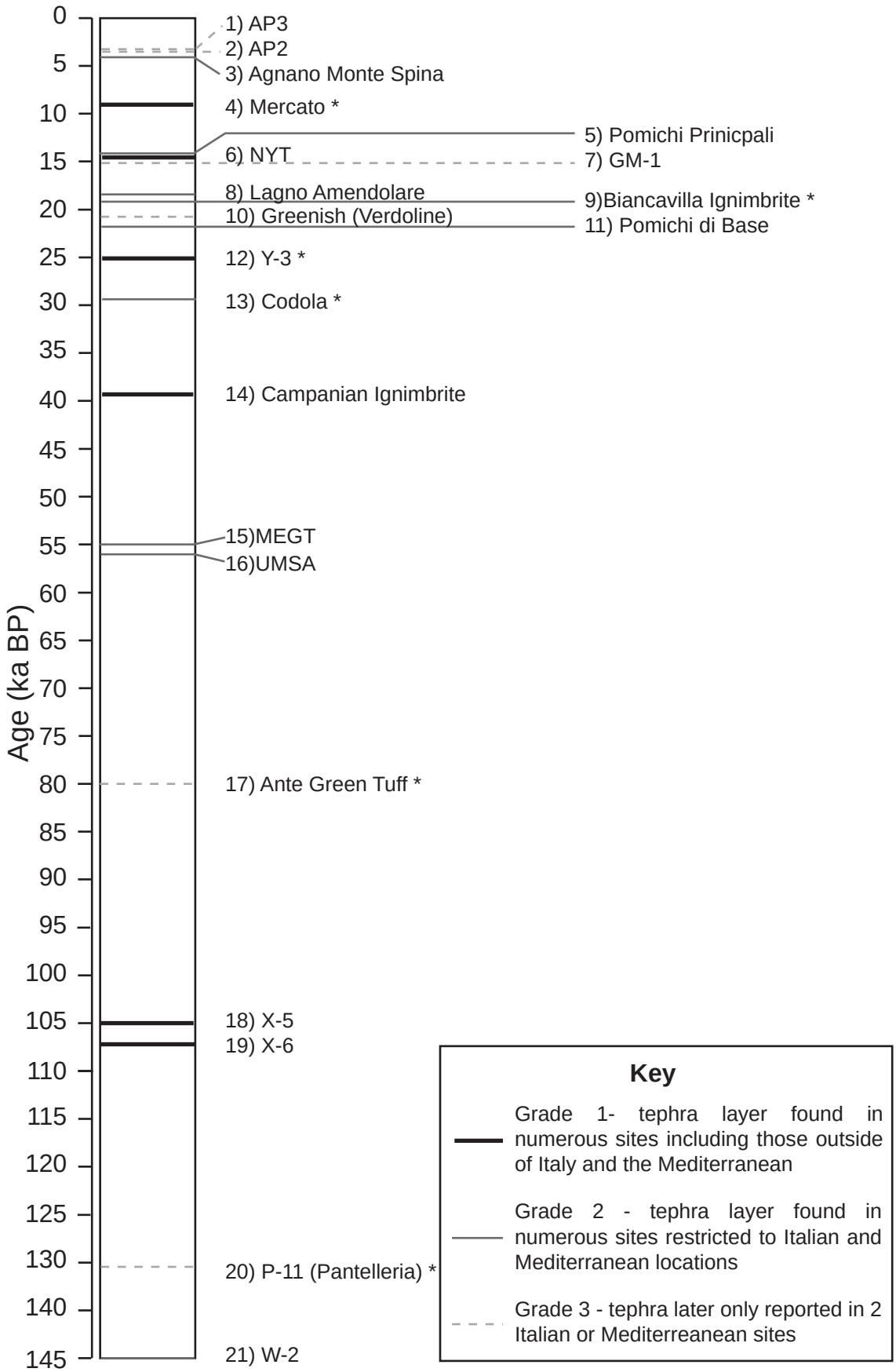

Figure 2.10: Tephra layer predictions for Adriatic marine cores in this study based on the regional tephrostratigraphy and occurrence of tephra layers in other sites. * denotes layers useful for correlation due to their stratigraphic or geochemical distinctiveness

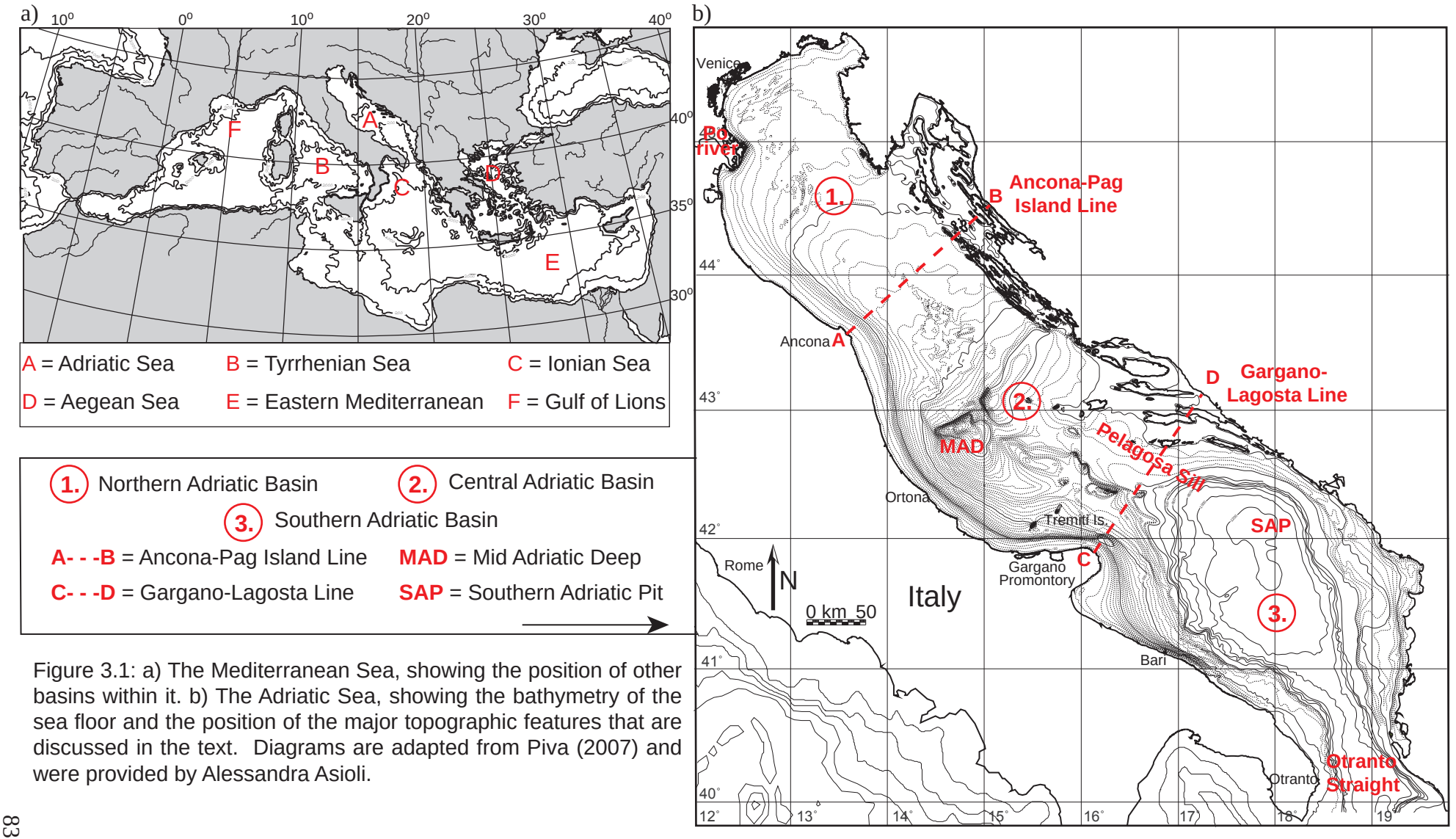

Figure 3.1: a) The Mediterranean Sea, showing the position of other basins within it. b) The Adriatic Sea, showing the bathymetry of the sea floor and the position of the major topographic features that are discussed in the text. Diagrams are adapted from Piva (2007) and were provided by Alessandra Asioli.

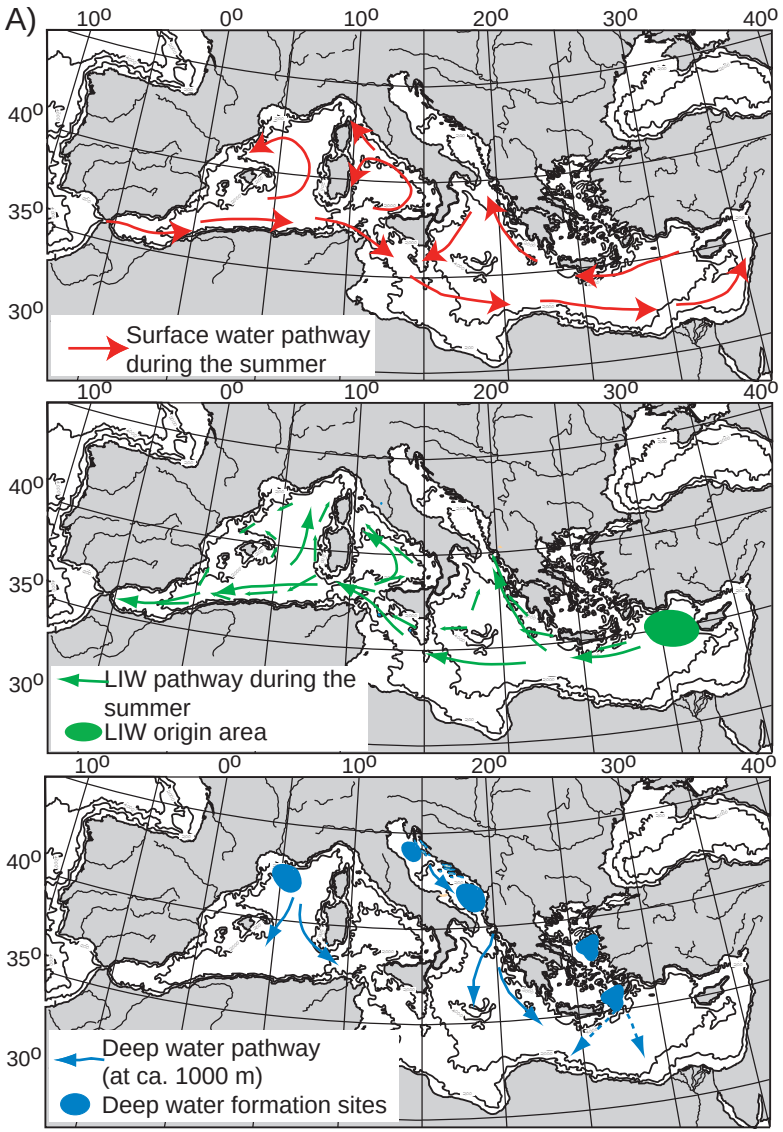

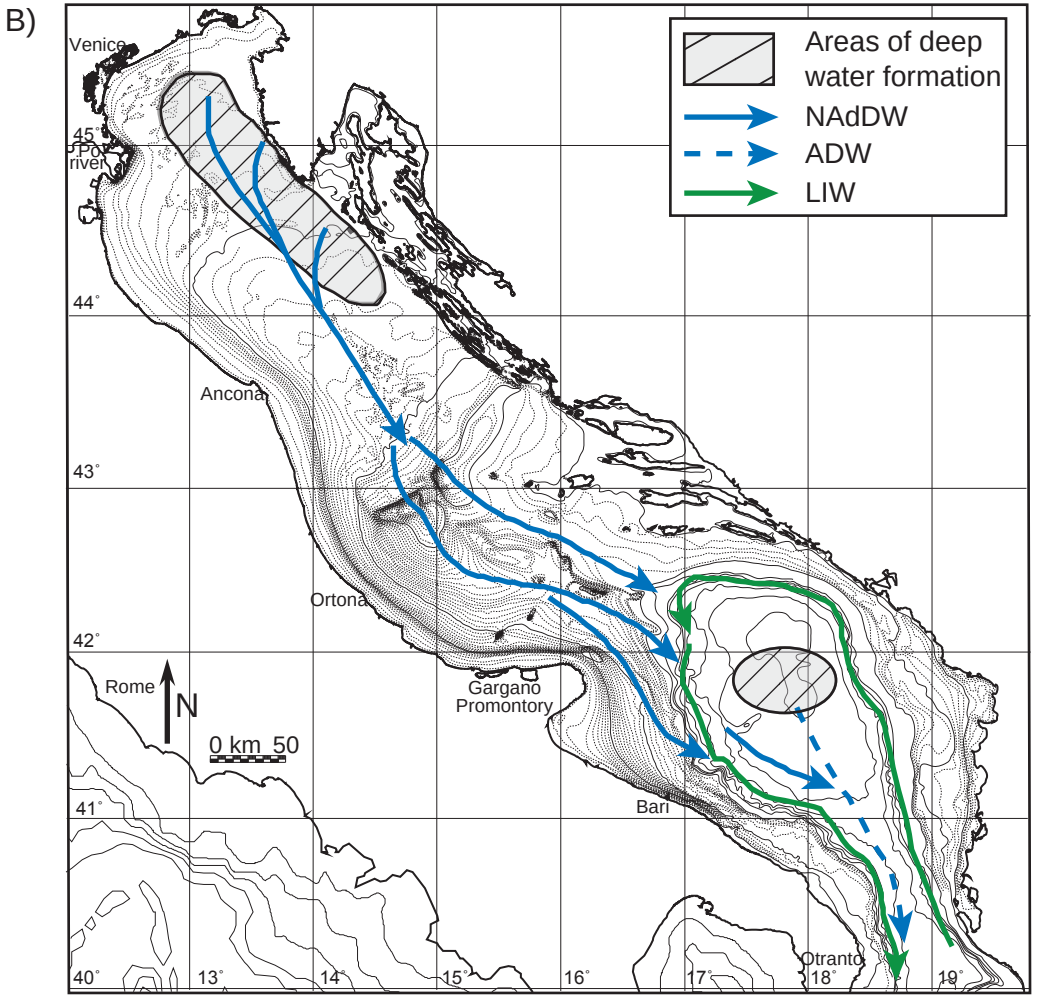

Figure 3.2: A) Ocean currents and water formation sites in the Mediterranean Sea. B) Intermediate and deep water currents and formation sites within the Adriatic Sea. NAdDW=North Adriatic Dense Water, ADW=Adriatic Dense Water, LIW=Levantine Intermediate Water.

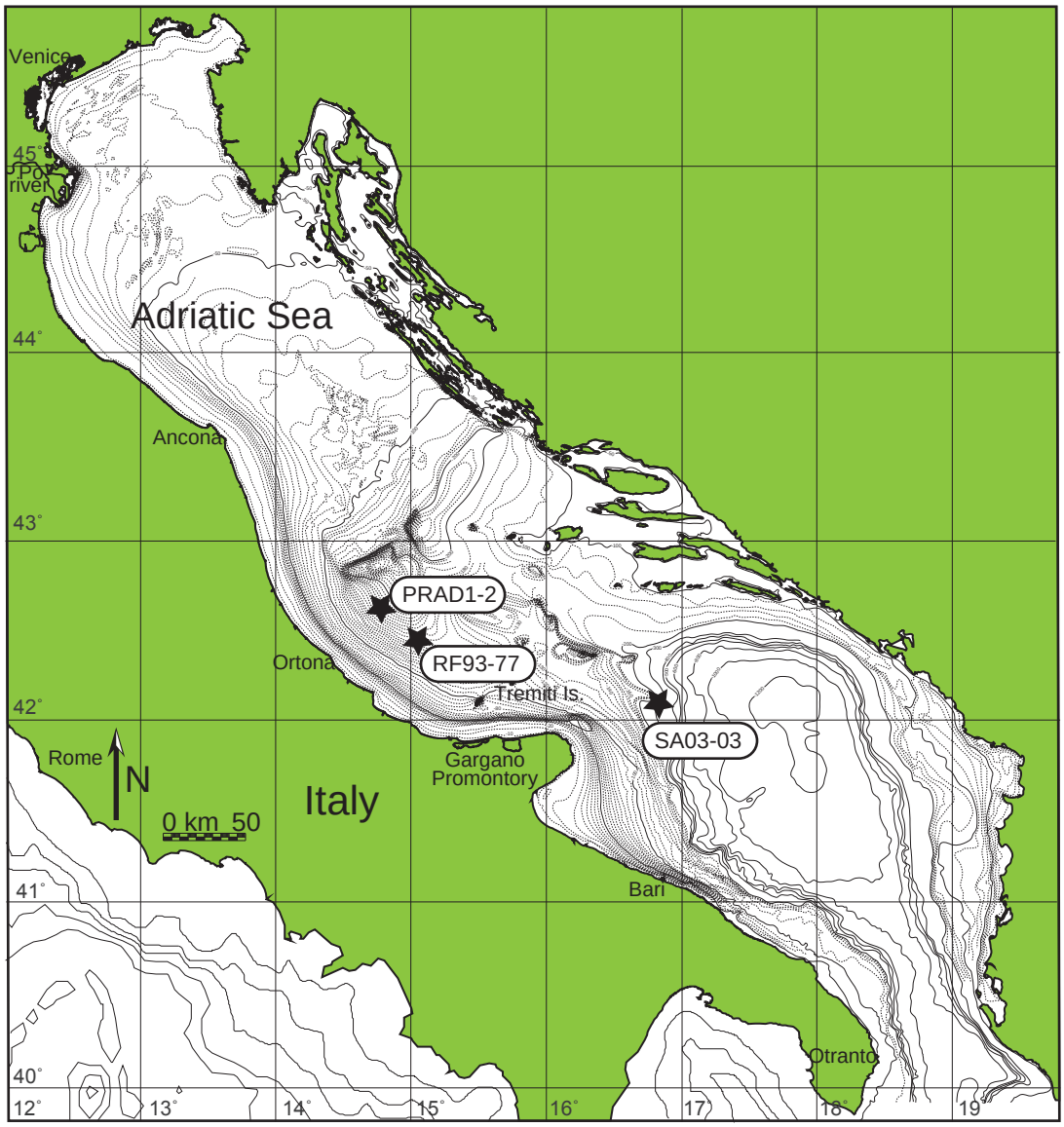

Figure 3.3: Location of core-sites PRAD 1-2 and RF93-77 in the Central Adriatic Basin and SA03-03 in the Southern Adriatic Basin. The bathymetry of the Adriatic Sea is also shown, along with key features of the basin that are referred to in the text. Diagram is adapted from Piva (2007).

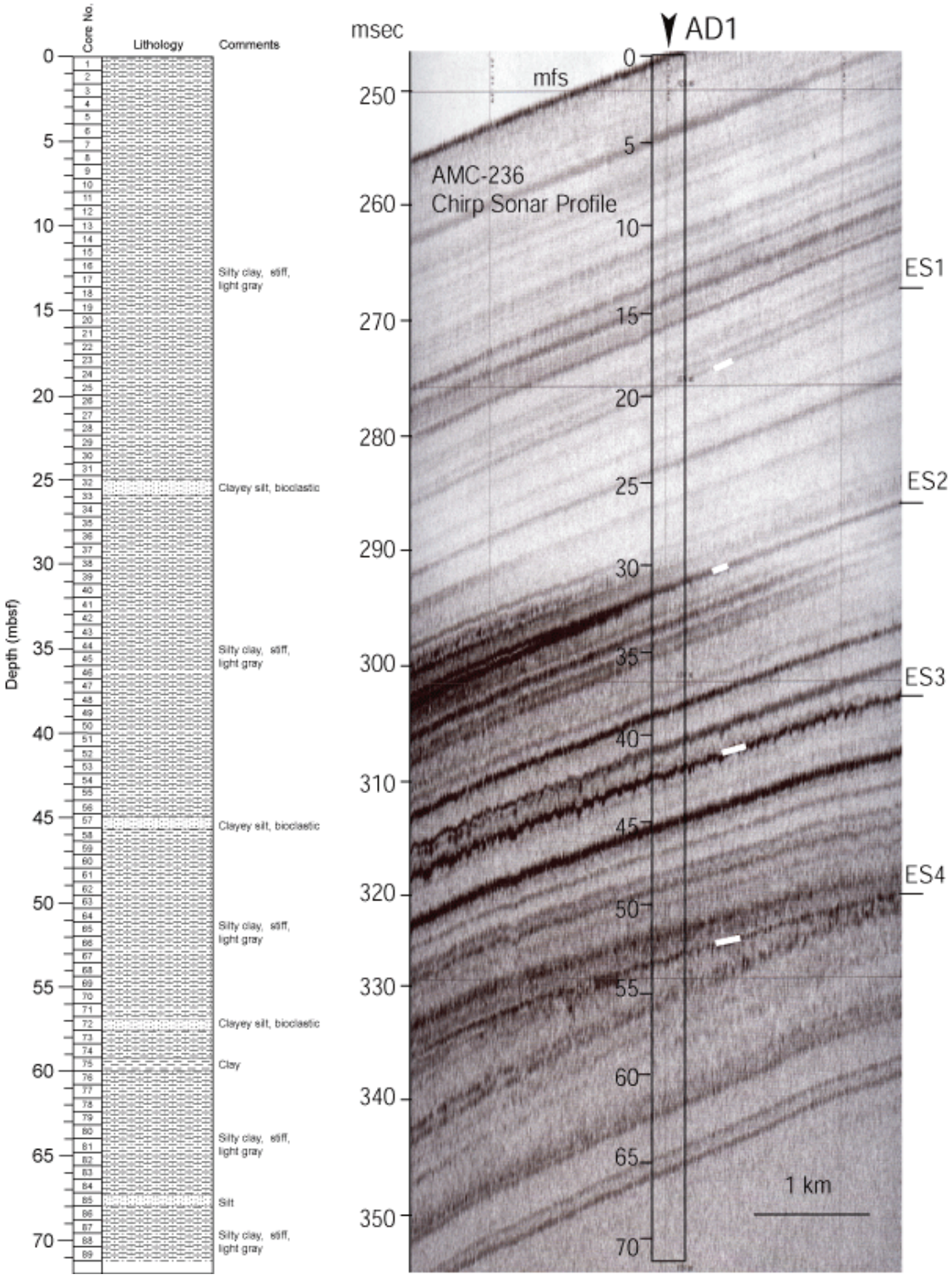

Figure 3.4: CHIRP sonar profile (AMC-236) taken along a transect in the locality of PRAD 1-2, showing the profile of underlying seismic facies around the PRAD 1-2 core site.

Figure 3.5: PRAD 1-2 Core photographs for Section 1 - Section 46, the sections analysed as part of this study. Core length is 75 - 80cm and core diameter is 6 cm

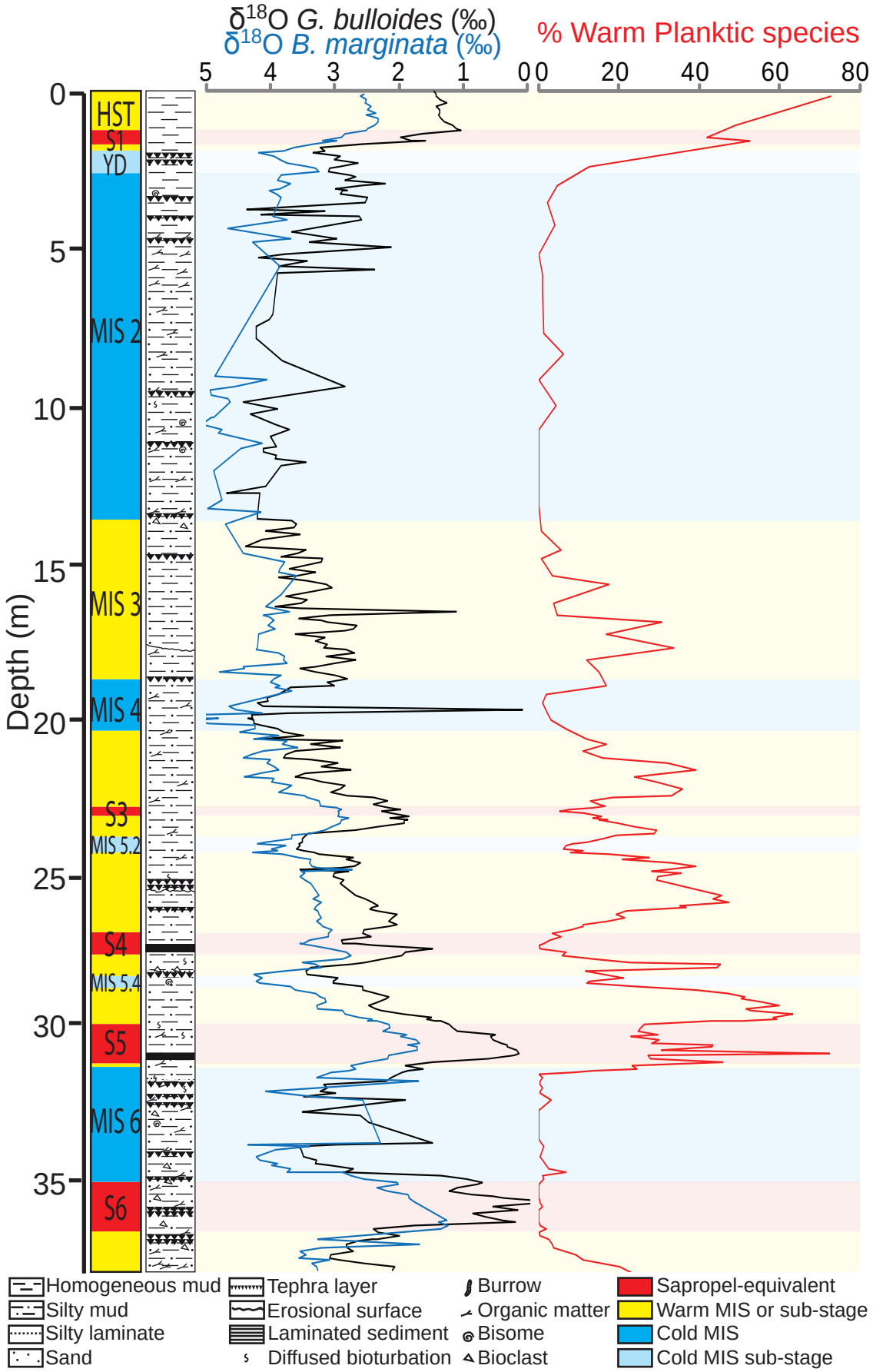

Figure 3.6: PRAD 1-2 Stratigraphic scheme, lithology, planktic (black curve) and benthic (blue curve) foram-based oxygen isotope record and percentage of warm planktic Foraminifera species (red curve) for the section of PRAD 1-2 investigated in this study. Shading extends the MIS stratigraphic scheme across the diagram as a visual aid. Data provided by A. Asioli and A. Piva and reported in Piva *et al.* (2008a).

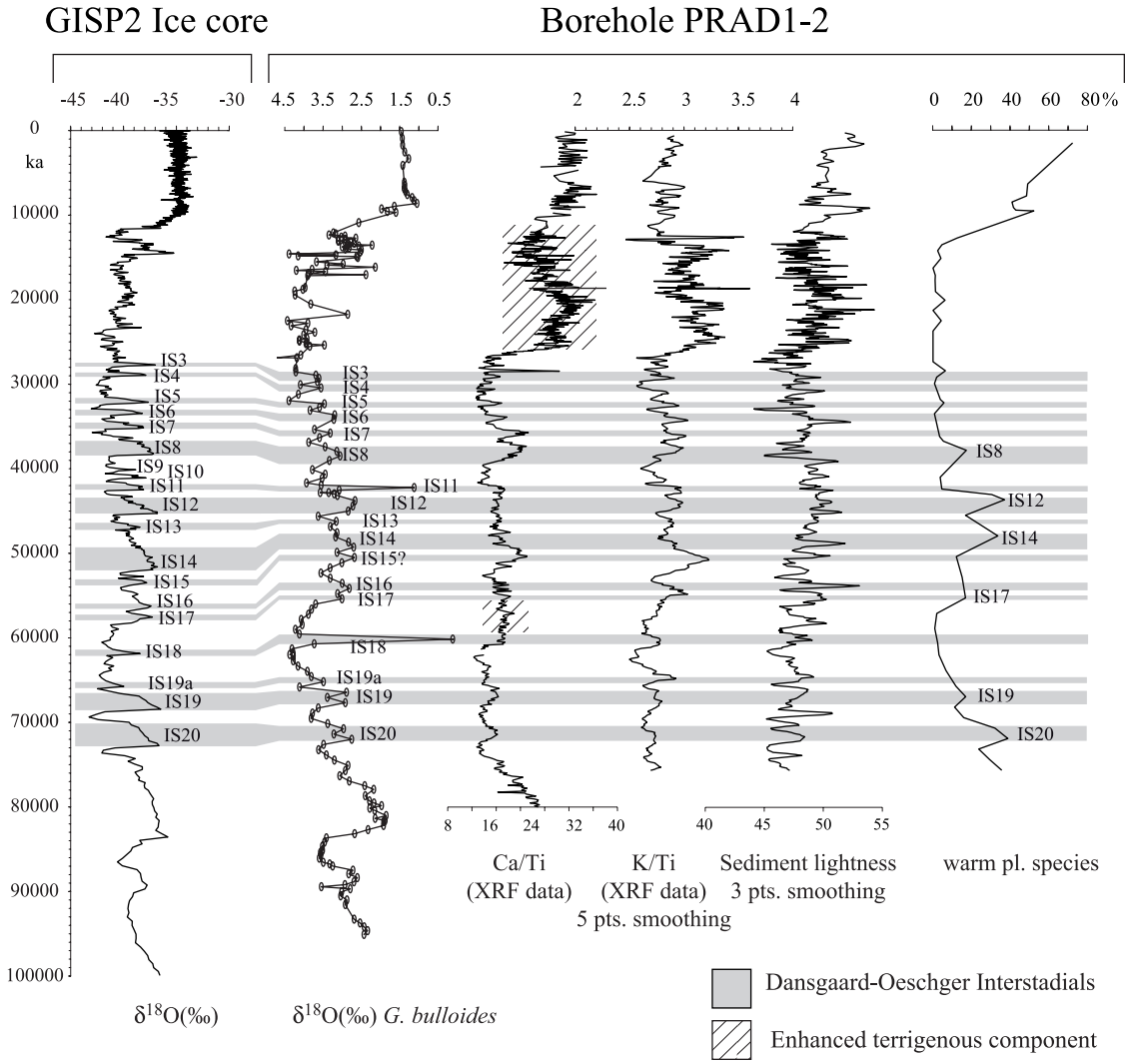

Figure 3.7: Reproduction of Figure 7 in Piva *et al.* (2008a) showing the wiggle-matched correlation of the PRAD 1-2 *G. bulloides* δ18O record, XRF data, sediment lightness and % warm planktic species with the GISP2 δ18O record to show the proposed correlation of Dansgaard-Oeschger (D-O) cycles between the records. The D-O interstadials are highlighted in grey.

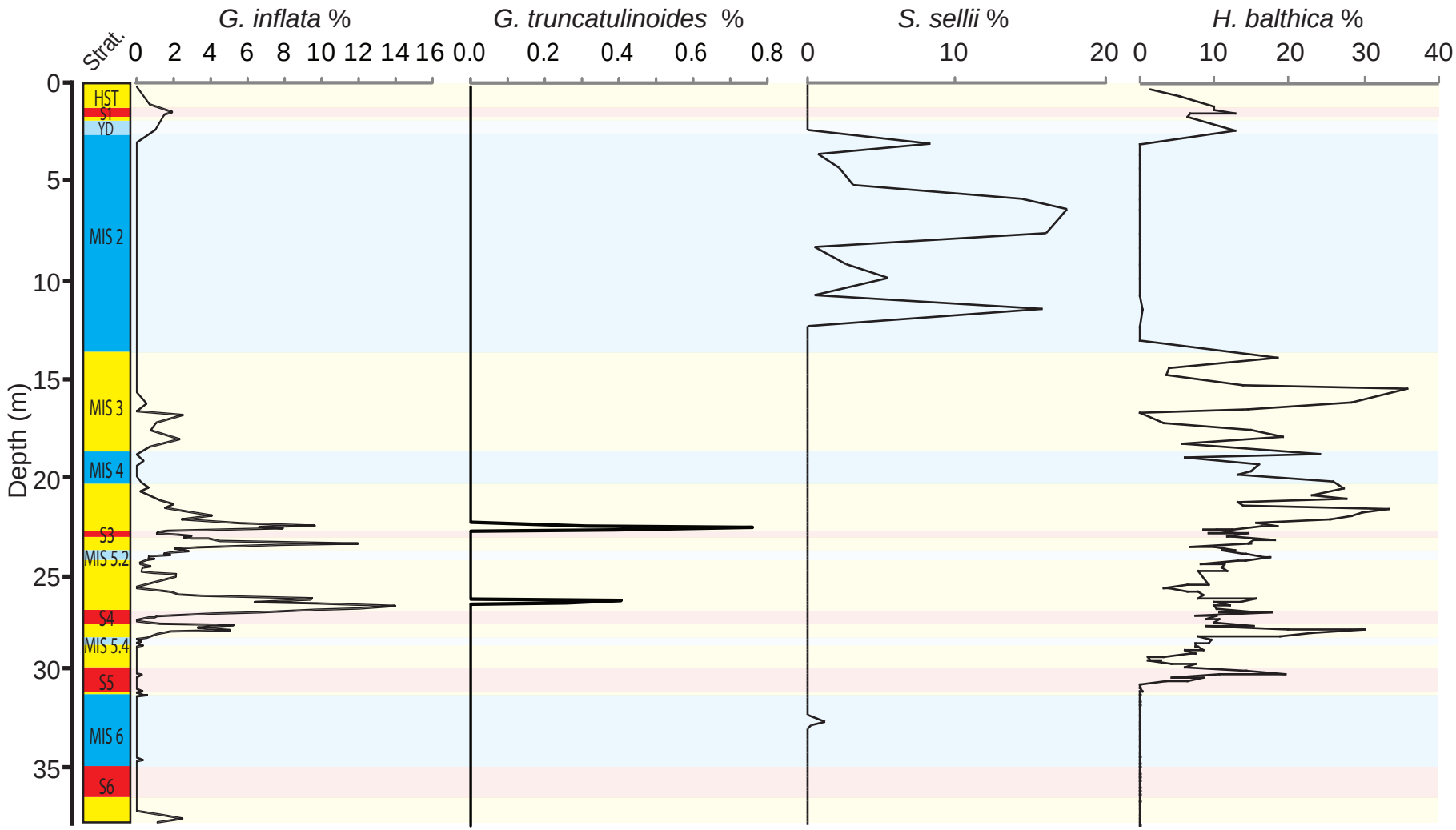

Figure 3.8: Variations in abundance of foraminiferal species that form the basis of bioevents identified in PRAD 1-2. *G. inflata* and *G. truncatulinoides* are both planktonic species whilst *S. sellii* and *H. balthica* are both benthic species. The PRAD 1-2 stratigraphic scheme is also shown with shading extended across the diagram as a visual aid (see Figure 3.6).

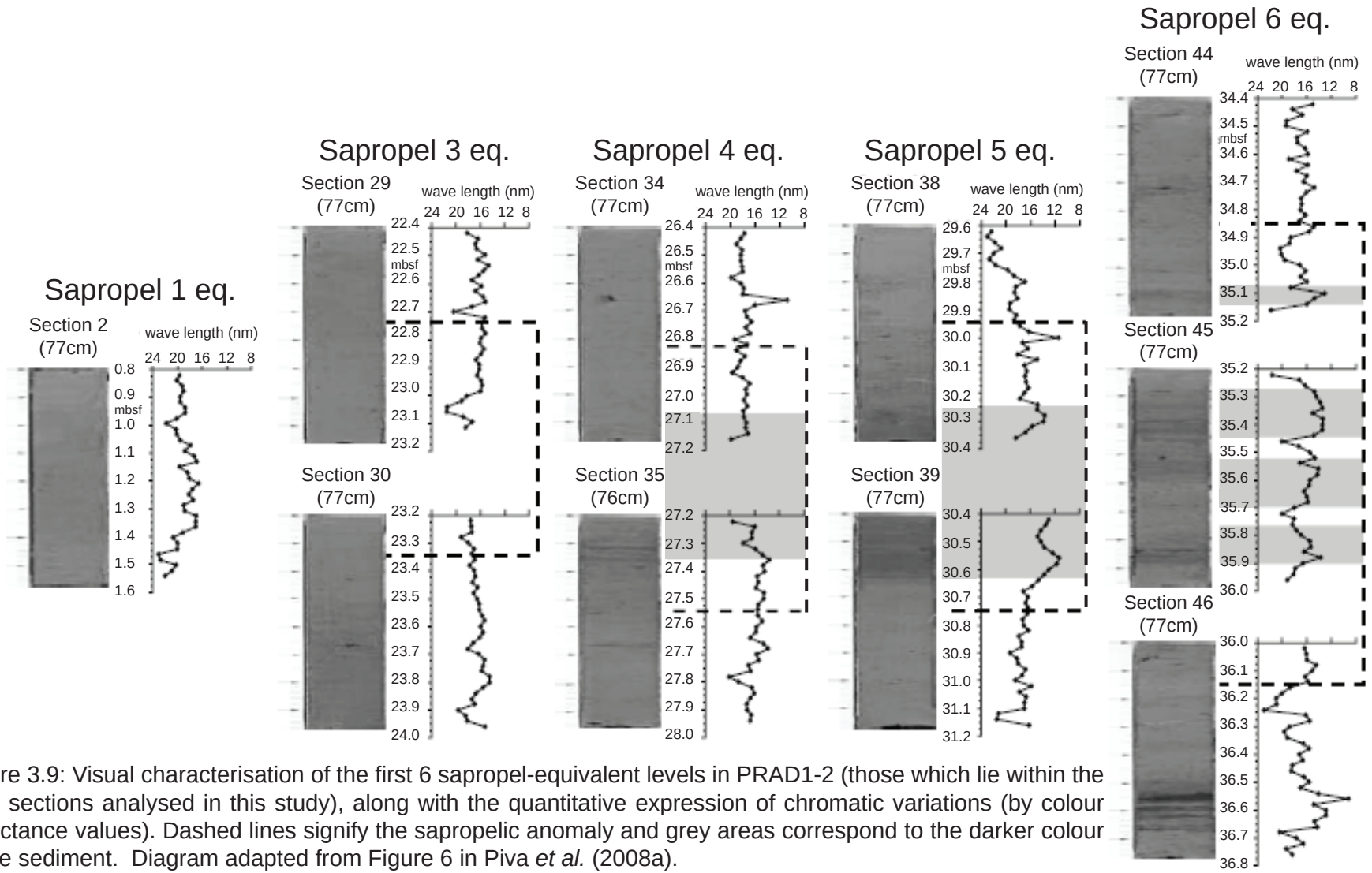

Figure 3.9: Visual characterisation of the first 6 sapropel-equivalent levels in PRAD1-2 (those which lie within the core sections analysed in this study), along with the quantitative expression of chromatic variations (by colour reflectance values). Dashed lines signify the sapropelic anomaly and grey areas correspond to the darker colour in the sediment. Diagram adapted from Figure 6 in Piva *et al.* (2008a).

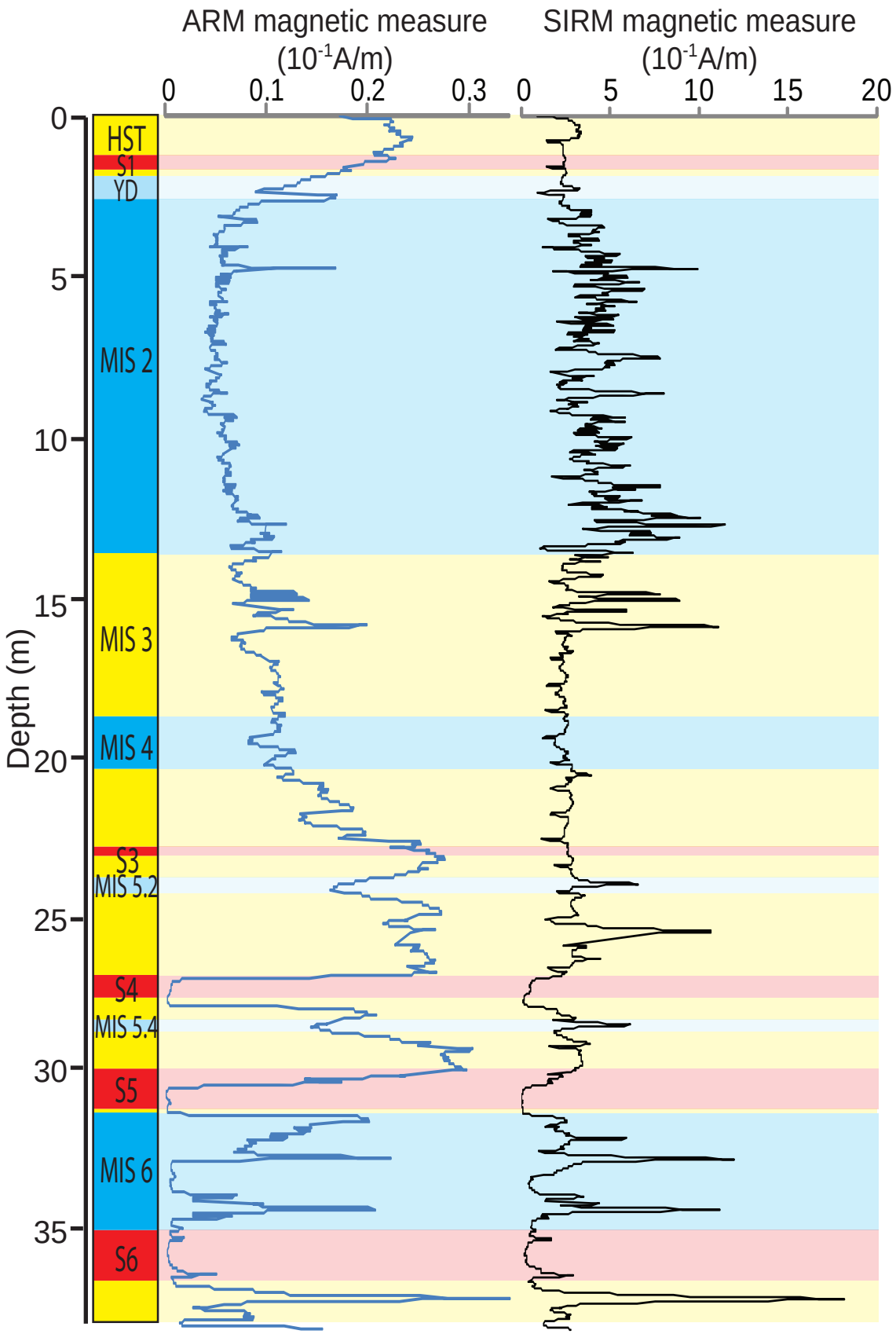

Figure 3.10: PRAD 1-2 ARM (blue curve) and SIRM (black curve) magnetic measures for the section of PRAD 1-2 investigated in this study. The PRAD 1-2 stratigraphic scheme is also shown with shading extended the diagram as a visual aid (see Figure 3.6). Data provided by Luigi Vigliotti and reported in Piva *et al.* (2008a).

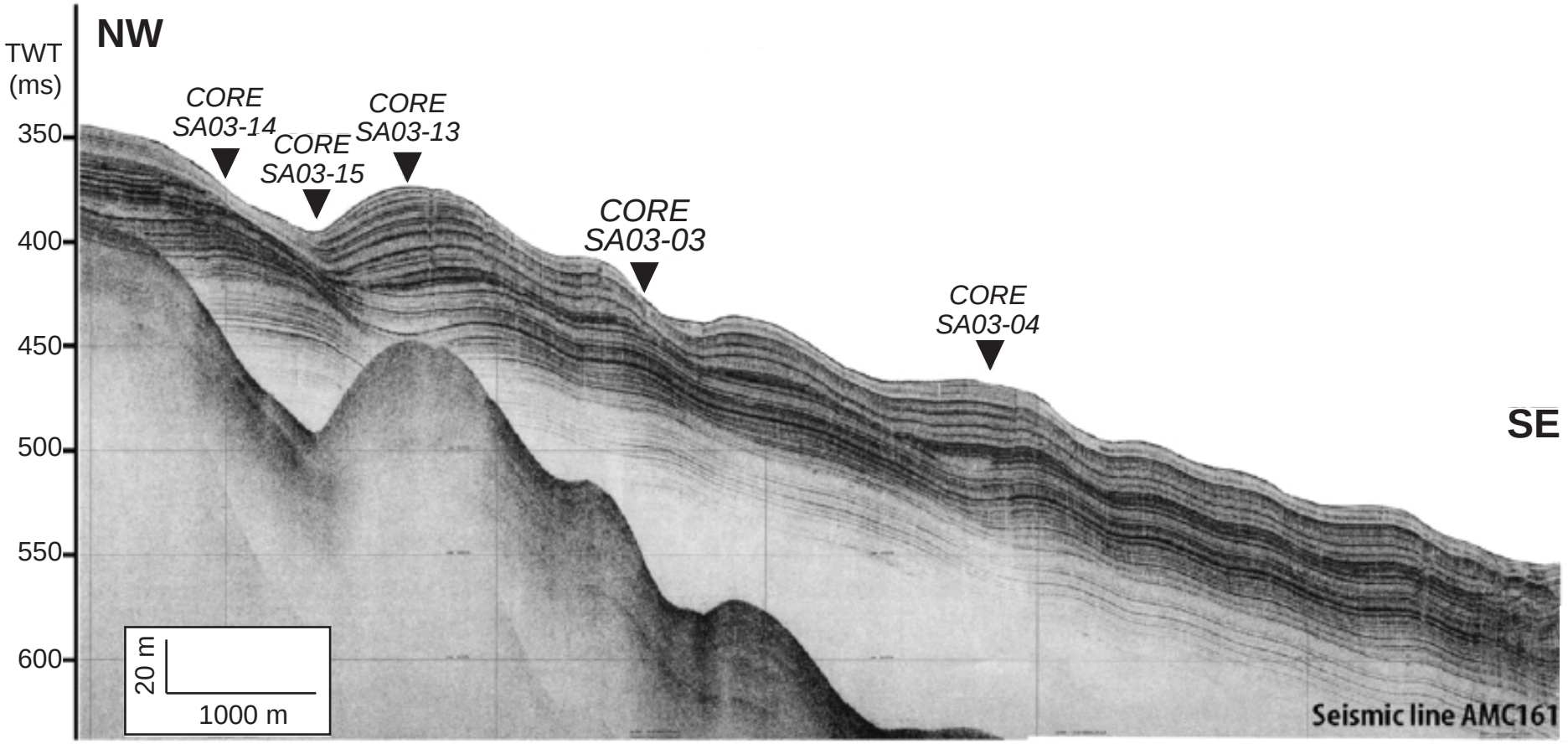

Figure 3.11: CHIRP-sonar profile across a large sediment wave in the northern sector of the Southwestern Adriatic Margin (SAM) showing the position of core SA03-03 and others taken during the SAGA-2003 cruise. Diagram adapted from Figure 11 in Verdicchio *et al.* (2006).

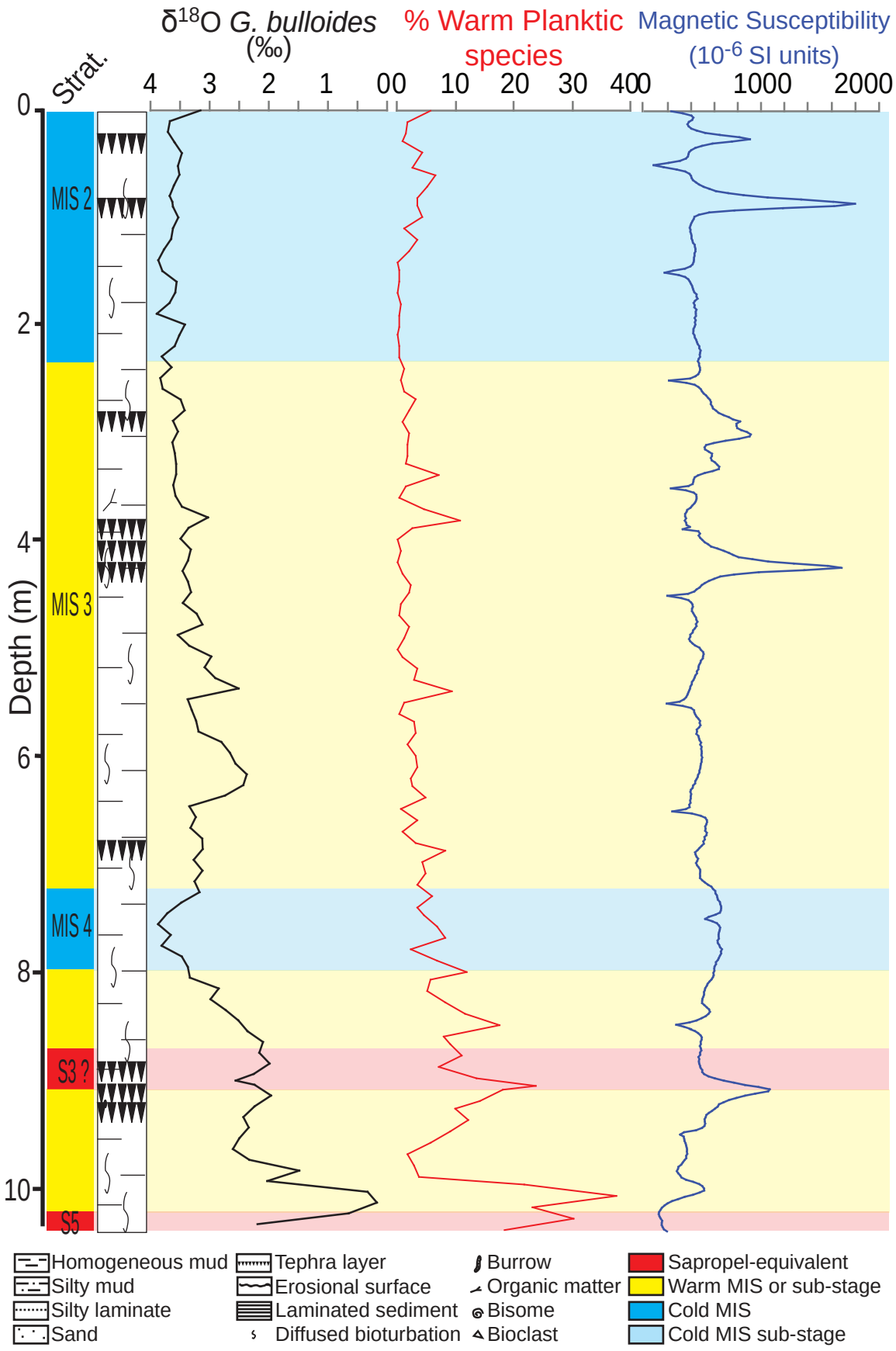

Figure 3.12: SA03-03 Stratigraphic scheme, lithology, planktic oxygen isotope record (black curve), percentage of warm planktic foraminiferal species (red curve) and magnetic susceptibility measurements (blue curve). Shading extends the MIS stratigraphic scheme across the diagram as a visual aid. Data provided by A. Asioli, A. Piva and L. Vigliotti and reported in Piva (2007).

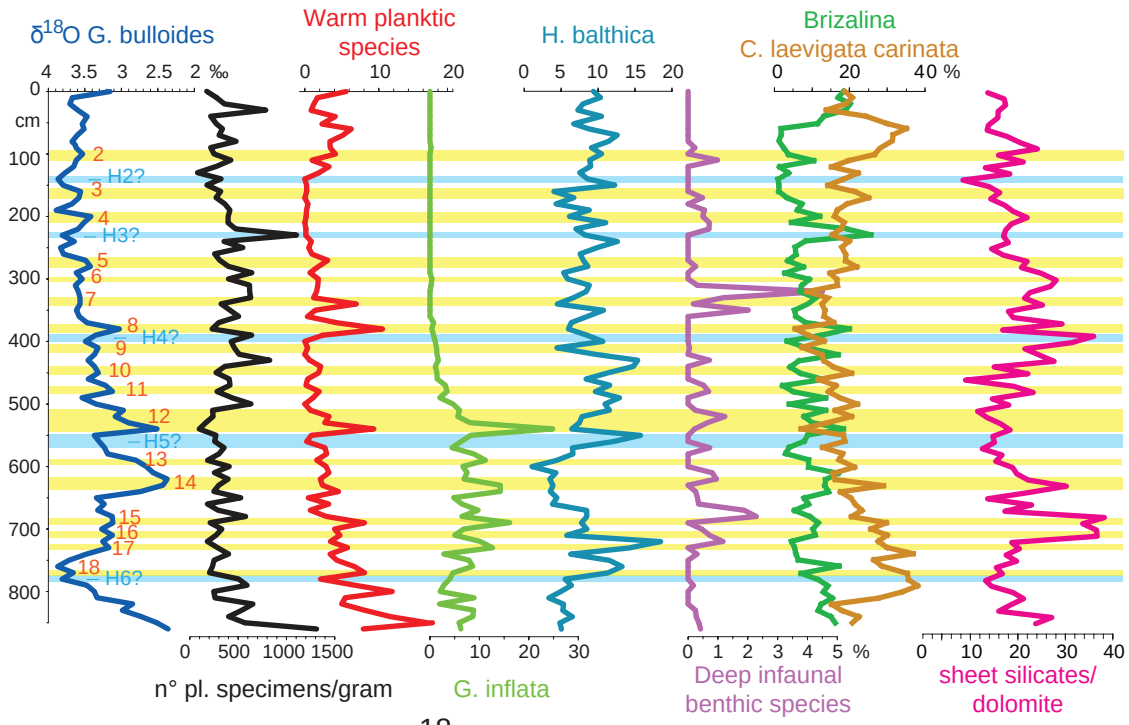

Figure 3.13: SA03-03 planktic $\delta^{18}O$ record and foraminifera species percentages and their proposed matching to GISP2 D-O Interstadials. The matched interstadials are numbered in red on the $\delta^{18}O$ G. bulloides record (dark blue curve) and traced through the other records in yellow. Figure adapted from Piva *et al.* (2008c).

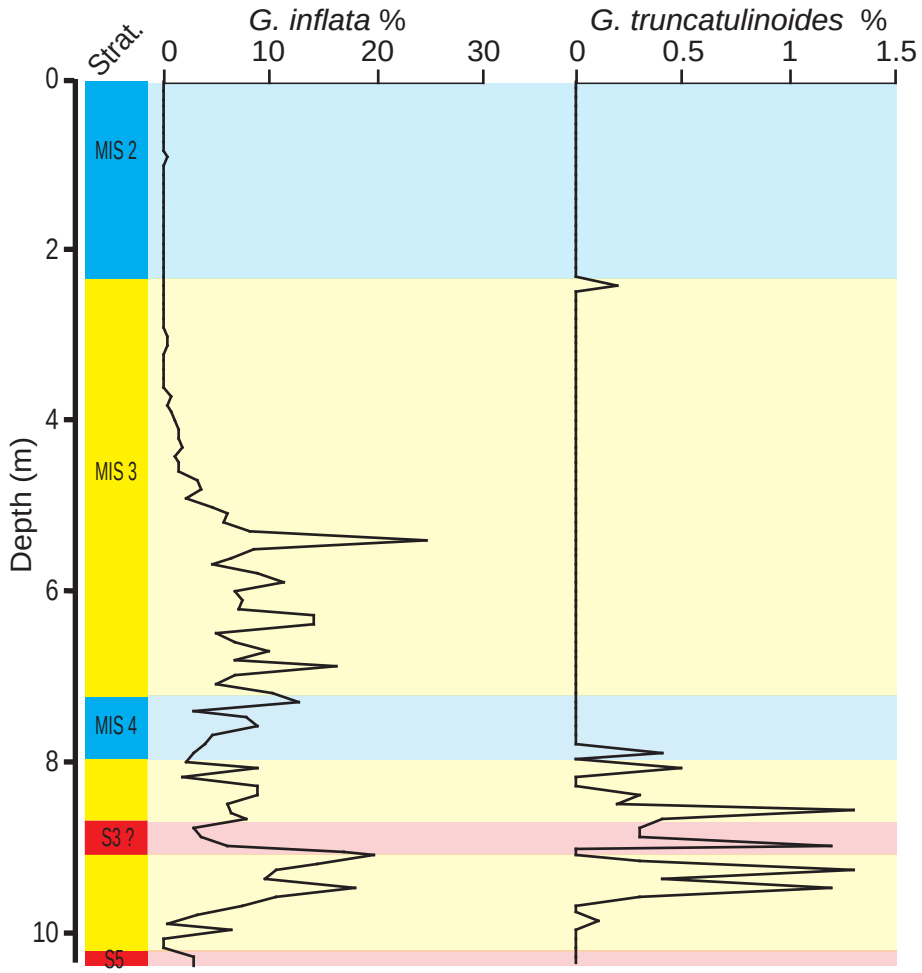

Figure 3.14: Variations in abundance of foraminiferal species that form the basis of bioevents identified in SA03-03. The SA03-03 stratigraphic scheme is also shown with shading extended across the diagram as a visual aid (see Figure 3.12).

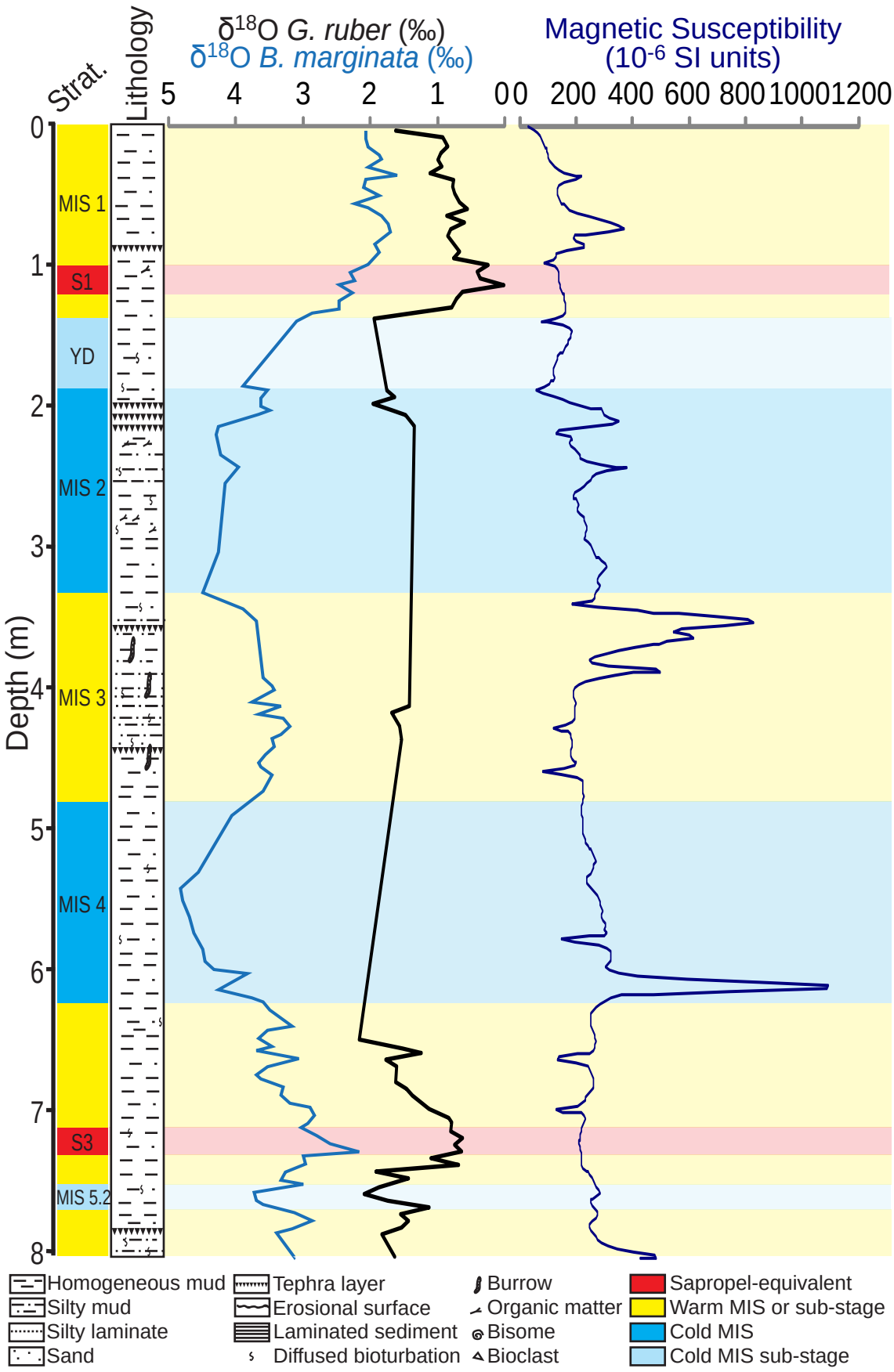

Figure 3.15: RF93-77 Stratigraphic scheme, lithology, planktic (black curve) and benthic (blue curve) foram-based oxygen isotope record and magnetic susceptibility measurements (dark blue curve). Shading extends the MIS stratigraphic scheme across the diagram as a visual aid. Data provided by A. Asioli and L. Vigliotti and reported in Ariztegui *et al.* (1996).

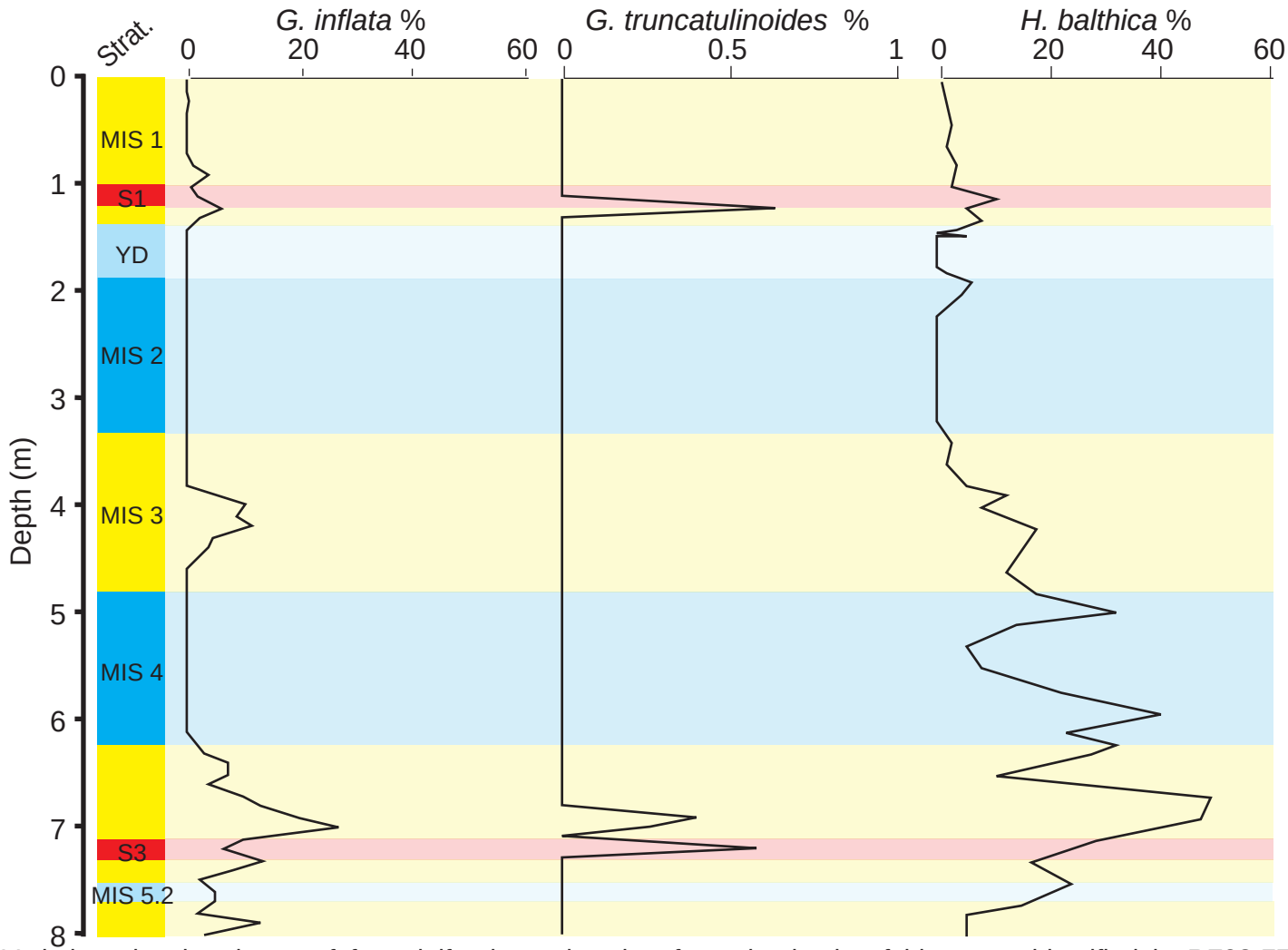

Figure 3.16: Variations in abundance of foraminiferal species that form the basis of bioevents identified in RF93-77. *G. inflata* and *G. truncatulinoides* are both planktonic species and *H. balthica* is a benthic species. The RF93-77 stratigraphic scheme is also shown with shading extended across the diagram as a visual aid (see Figure 3.15).

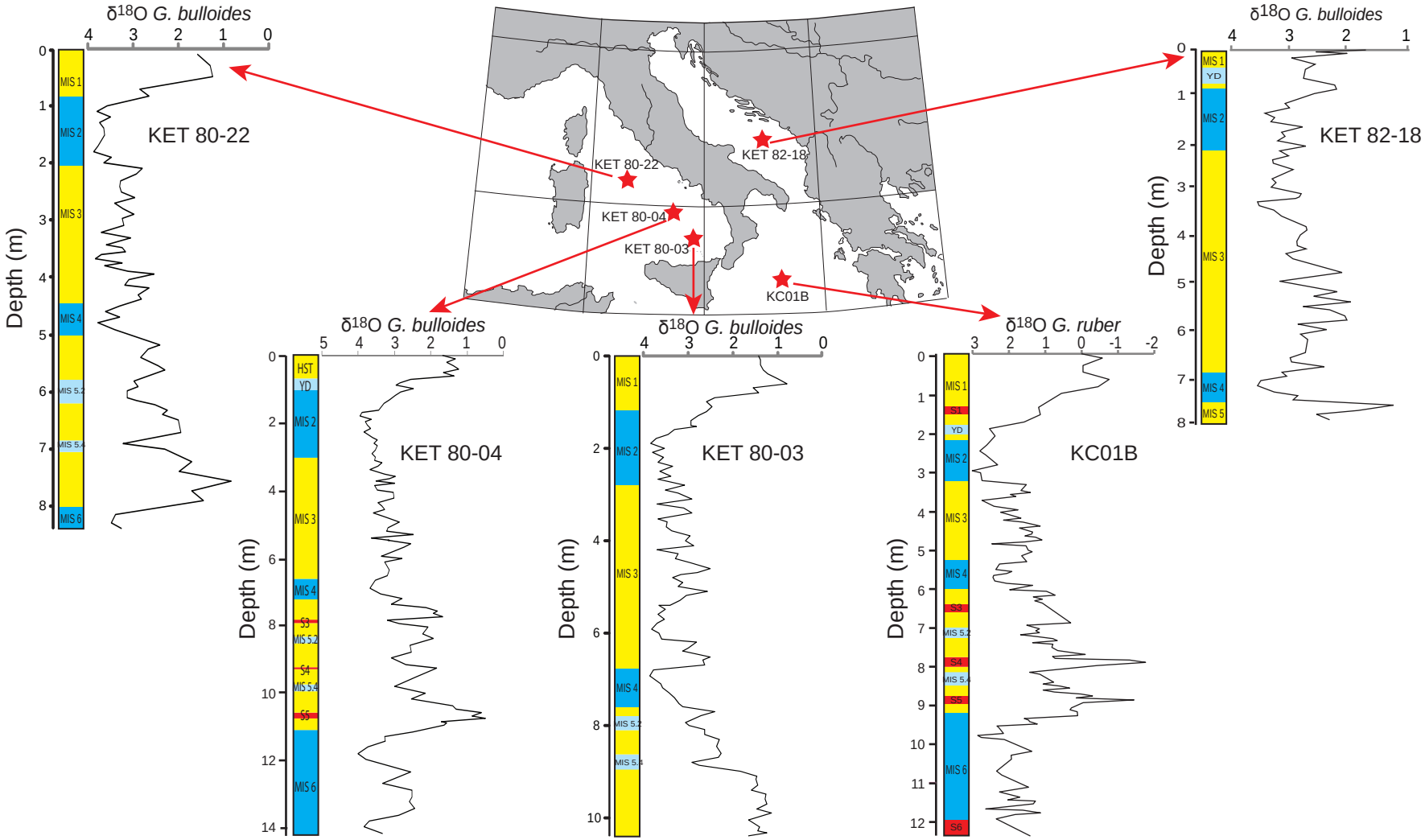

Figure 3.17: Central Mediterranean planktic oxygen isotope records. The MIS scheme is shown to the left of the curve and sapropel layers are marked in red where they are identified in the core. Cores KET 80-22, KET 80-04, KET 80-03 and KET 82-18 are after Paterne *et al.* (1986) and isotope measurements are on the foram species *G. bulloides*. Core KC01B is after Lourens (2004) and isotope measurements are on foram species *G. ruber*.

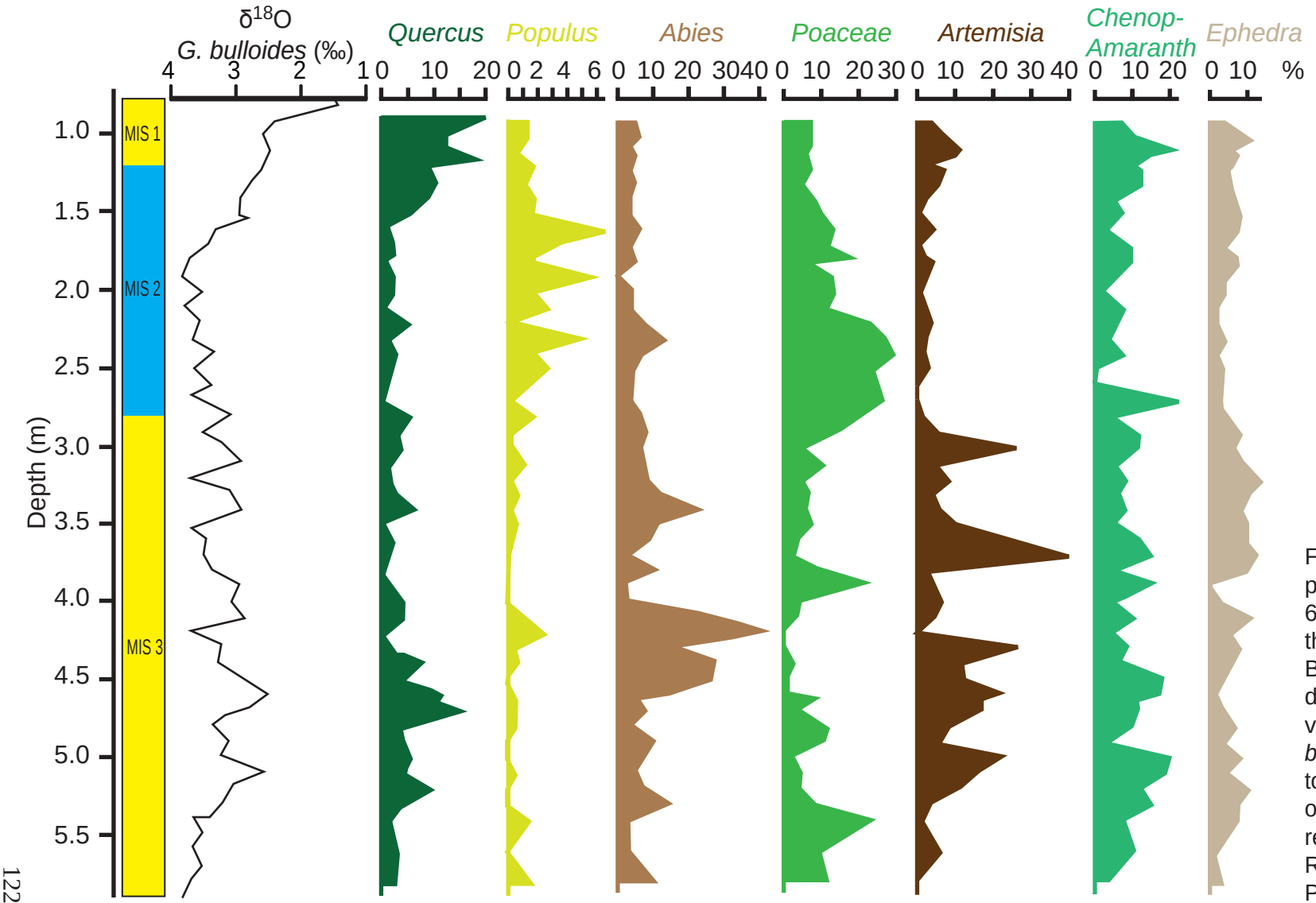

Figure 3.18: KET 80-03 pollen diagram for the top 6 m of the core covering the period from 55 - 9 ka BP. *Quercus* abundance data are compared with variations in the $\delta^{18}O$ *G. bulloides* (‰) and thought to co-vary in phase with one another. Diagram redrawn from Rossignol-Strick and Planchais (1989).

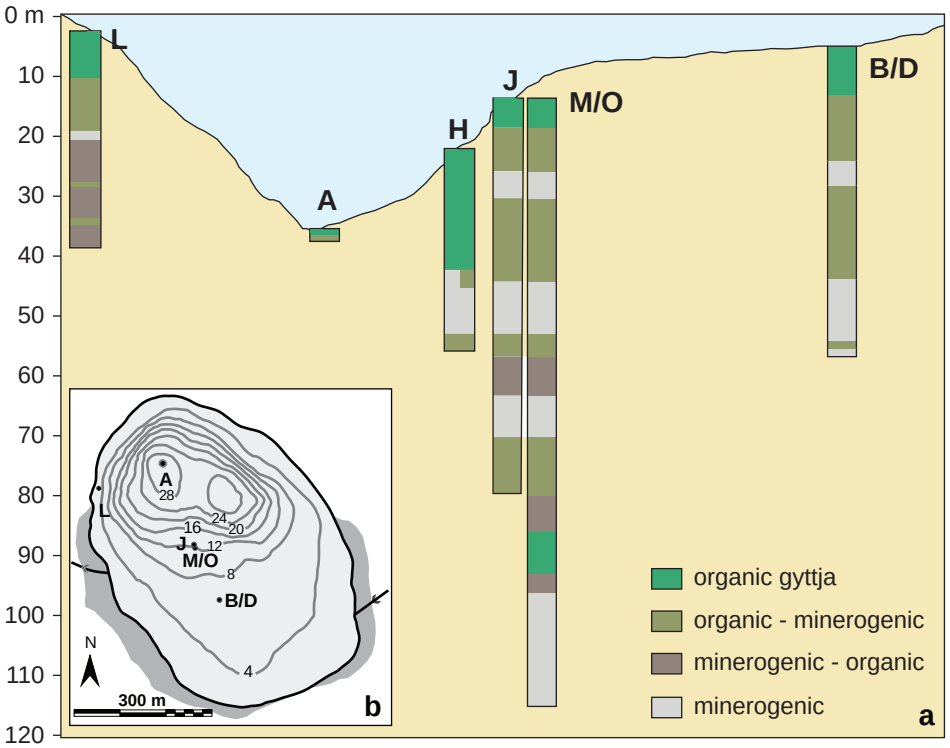

Figure 3.19: Location and depth of sediment profiles from Lago Grande di Monticchio. Cores A and B/D were acquired in 1990, Cores H, J and L in 1994 and Core M and O in 2000. a) Position of cores on the lake slope and core lithology (adapted from Brauer *et al*., 2000). b) Bathymetry of the lake and core locations, bathymetric contour depths in metres (adapted from Allen and Huntley, 2009).

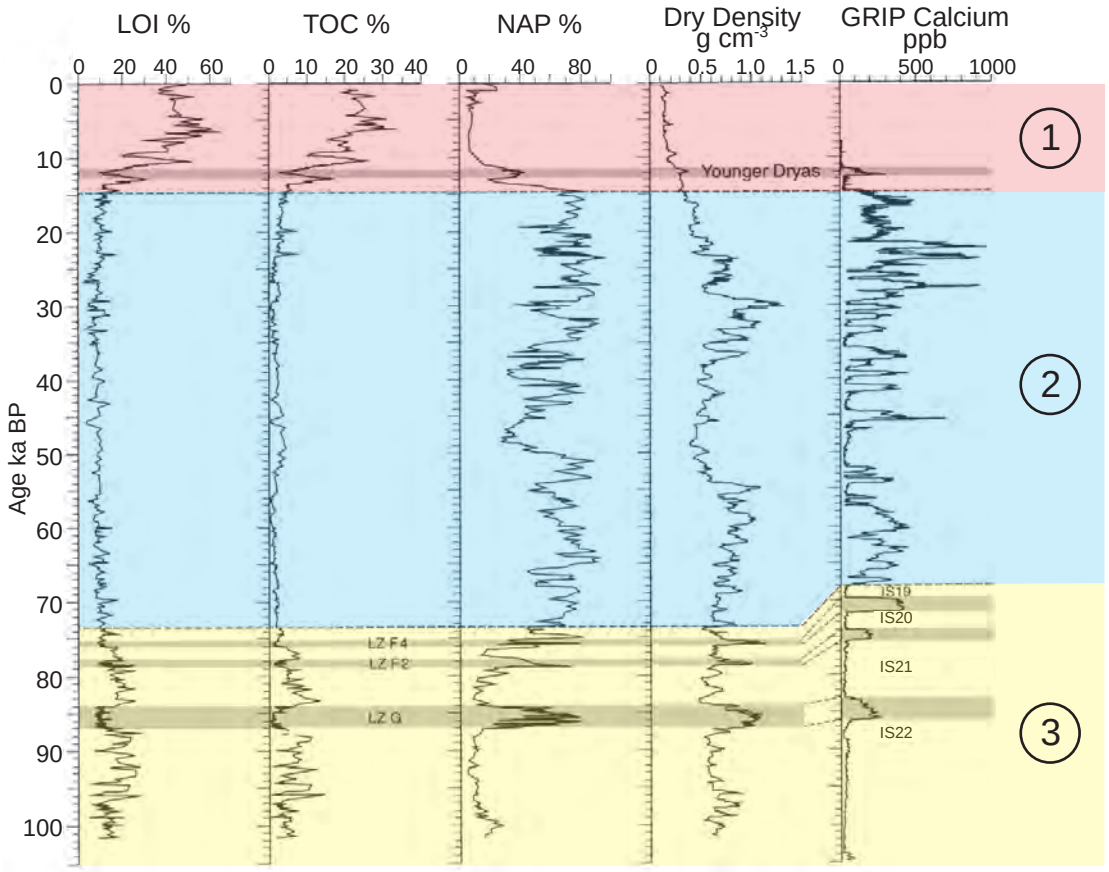

Figure 3.20: Proxy data of the LGdM L/J record compared with non-arboreal pollen (NAP) data from the same core and the GRIP calcium record. Dashed lines indicate transitions from interstadial to full glacial and from full glacial to Lateglacial conditions. Shaded areas mark abrupt cold periods during the Lateglacial and early Weichselian. Adapted from Brauer *et al.* (2000).

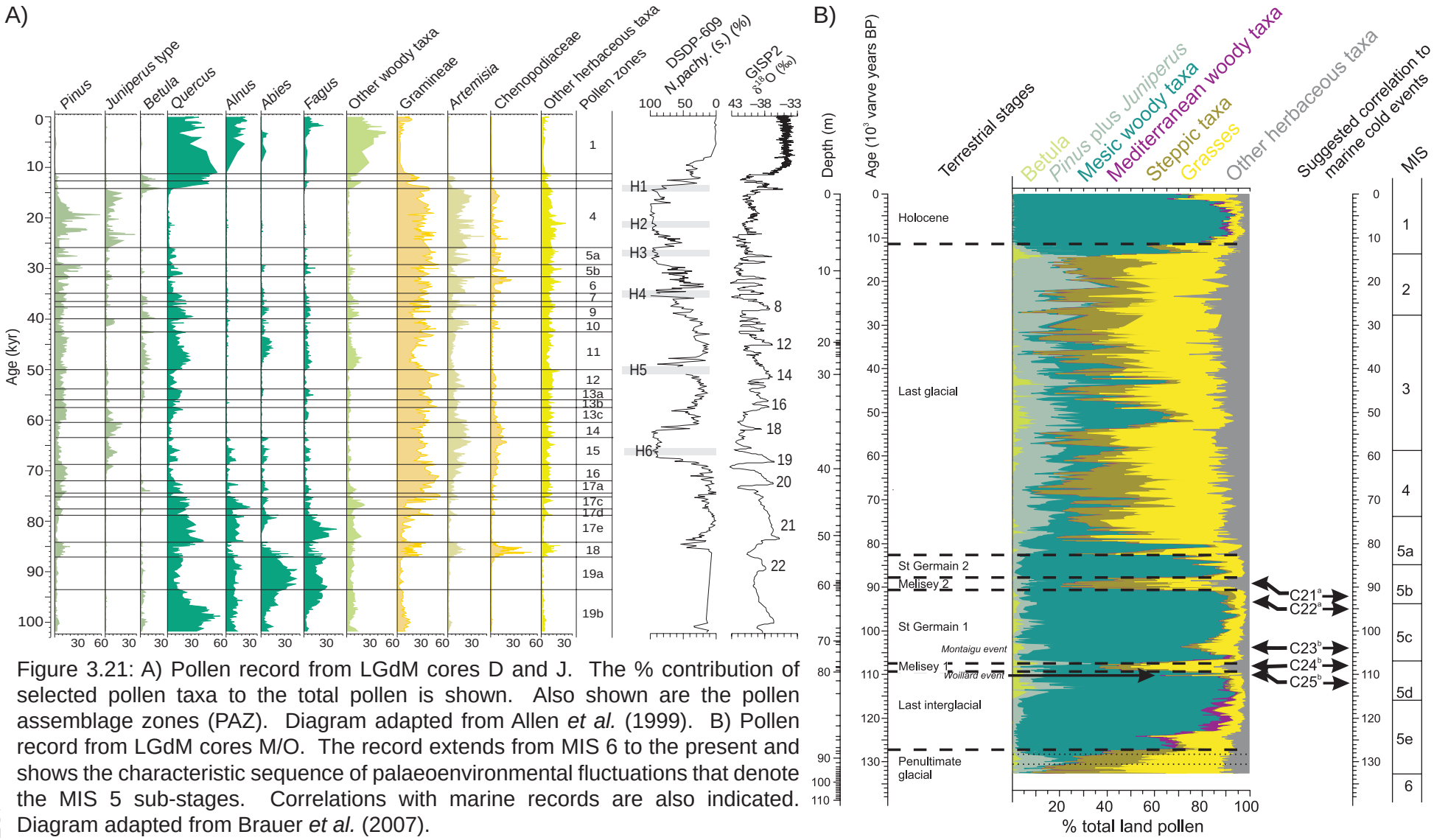

Figure 3.21: A) Pollen record from LGdM cores D and J. The % contribution of selected pollen taxa to the total pollen is shown. Also shown are the pollen assemblage zones (PAZ). Diagram adapted from Allen *et al.* (1999). B) Pollen record from LGdM cores M/O. The record extends from MIS 6 to the present and shows the characteristic sequence of palaeoenvironmental fluctuations that denote the MIS 5 sub-stages. Correlations with marine records are also indicated. Diagram adapted from Brauer *et al.* (2007).

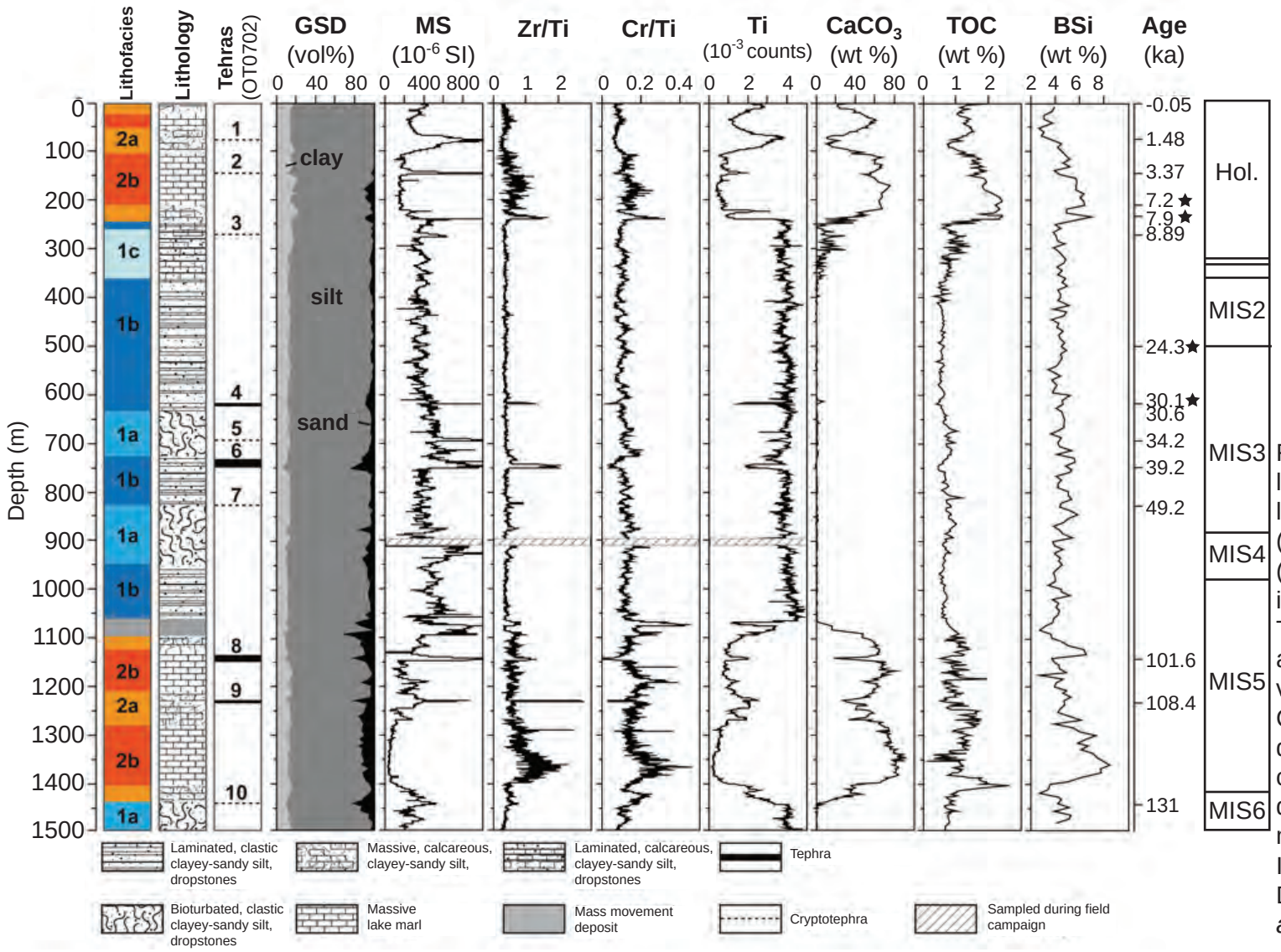

Figure 3.22: Lithofacies, lithology, positions of tephra layers, grain-size distribution (GSD), magnetic susceptibility (MS), Zr/Ti, Cr/Ti ratios, Ti intensities, calcite (CaCO3), Total Organic Carbon (TOC) and biogenic silica (BSi) variations in Lake Ohrid core Co1202. Ages on the right are derived through tephra correlations and radiocarbon dates (stars). Correlations made with Marine Oxygen Isotope Stages are also shown. Diagram adapted from Vogel *et al.* (2010b).

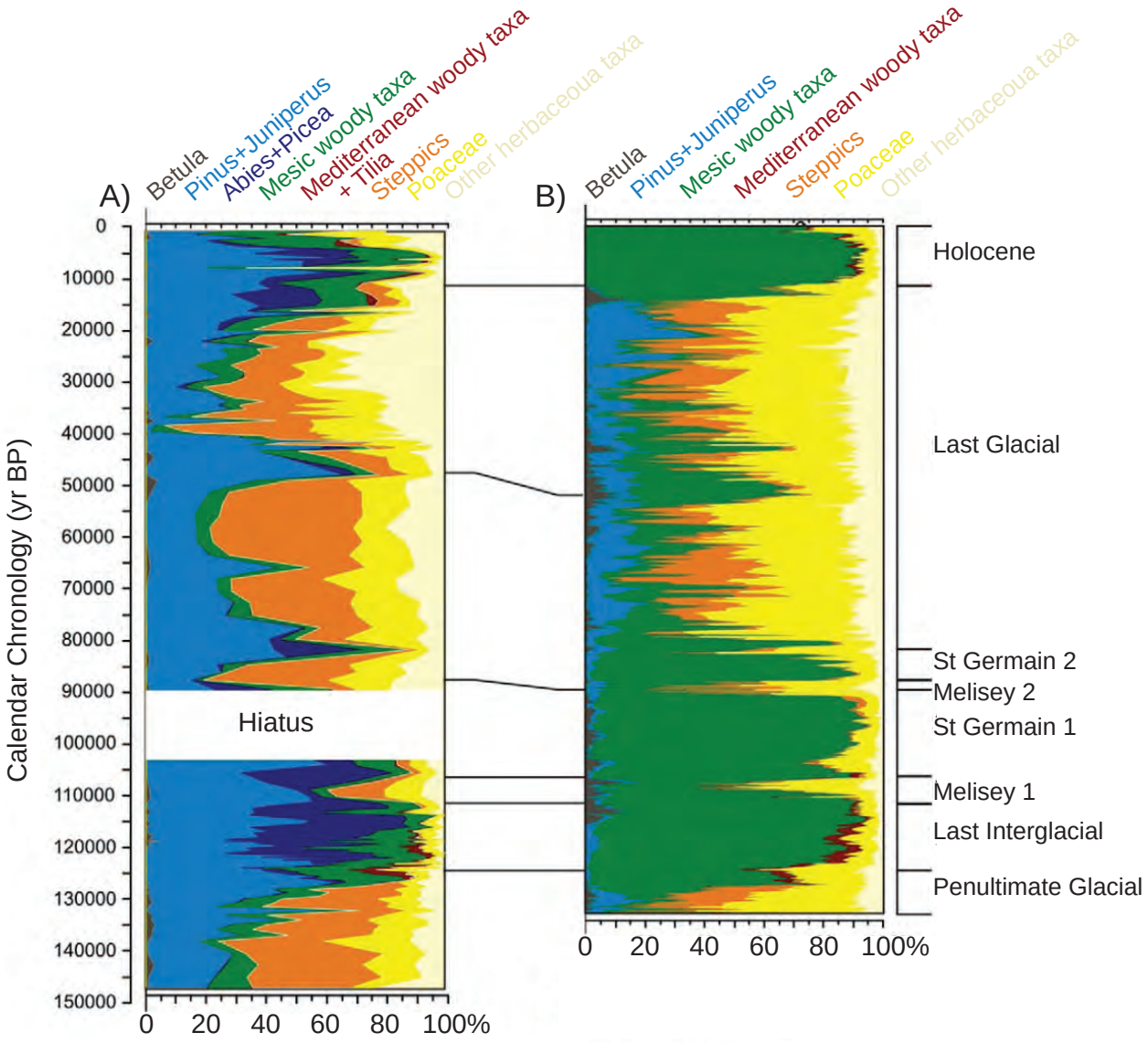

Figure 3.23: A) Lake Ohrid pollen record from Core JO2004-1. The main vegetation types encountered at the site reflect the near continuous dominance of mountain vegetation types at Lake Ohrid due to the steep altitudinal gradient in the catchment area (Lézine *et al.,* 2010). B) Comparison with the LGdM pollen record of Brauer *et al.* (2007). The overall development of vegetation (e.g. tree percentages variations, changes in Mediterranean vegetation types) are consistent between the records. Diagram adapted from Figure 6, Lézine *et al.* (2010).

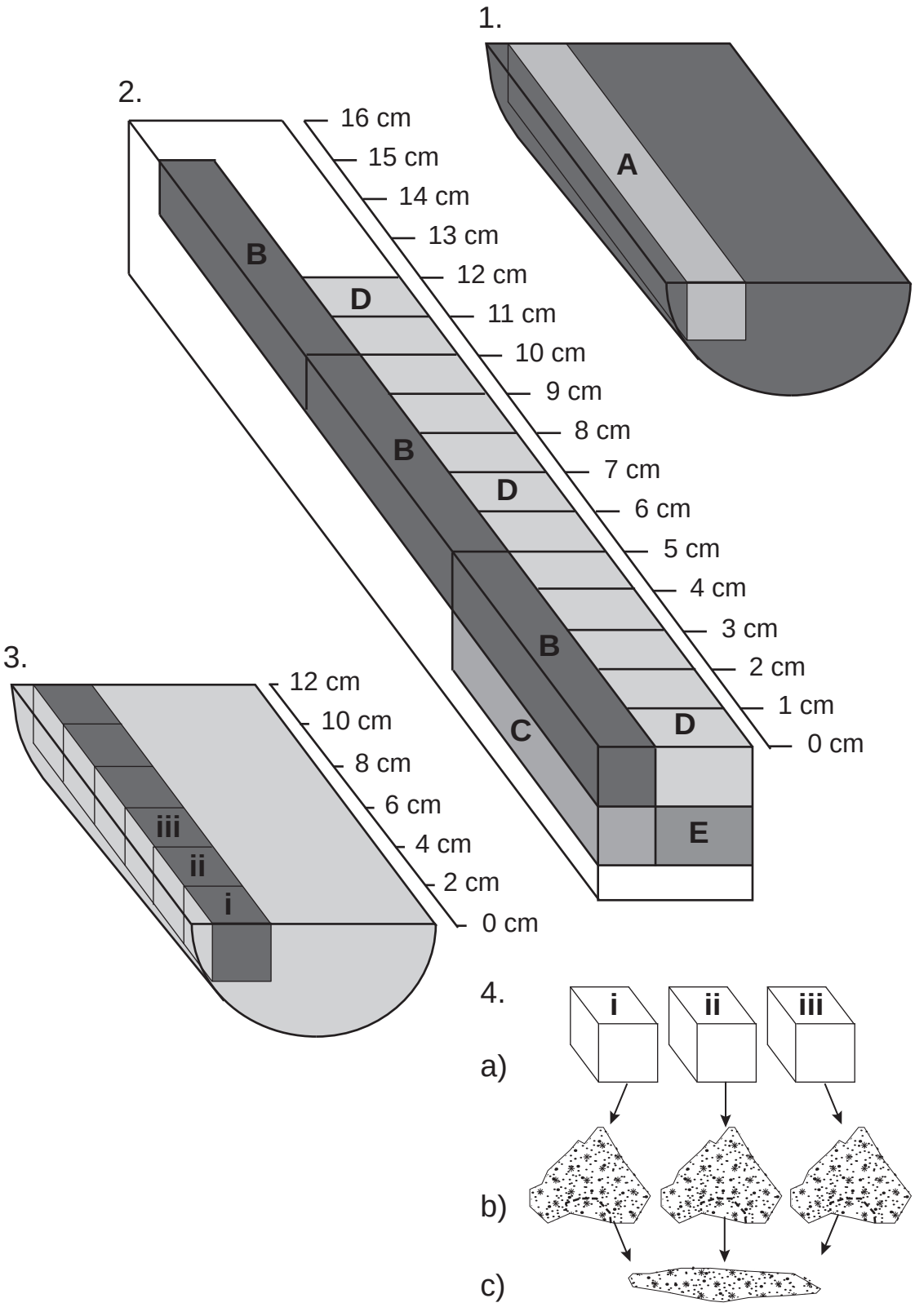

Figure 4.1: Core sub-sampling strategy 1. PRAD 1-2/SA03-03 cores, with U-channel for tephra sub-sampling removed from it (A). 2. U-channel with 5 cm contiguous tephra scan sample (B), 5 cm geochemical samples (C), 1 cm refined tephra samples (D) and 1 cm geochemical samples (E). 3. RF93-77 core with 2 cm^3 blocks removed. 4. a) 2 cm resolution blocks from core in 3. b) Each 2 cm^3 block was homogenised and part of it removed. c) Removed parts of sample combined to form a 6 cm resolution sample.

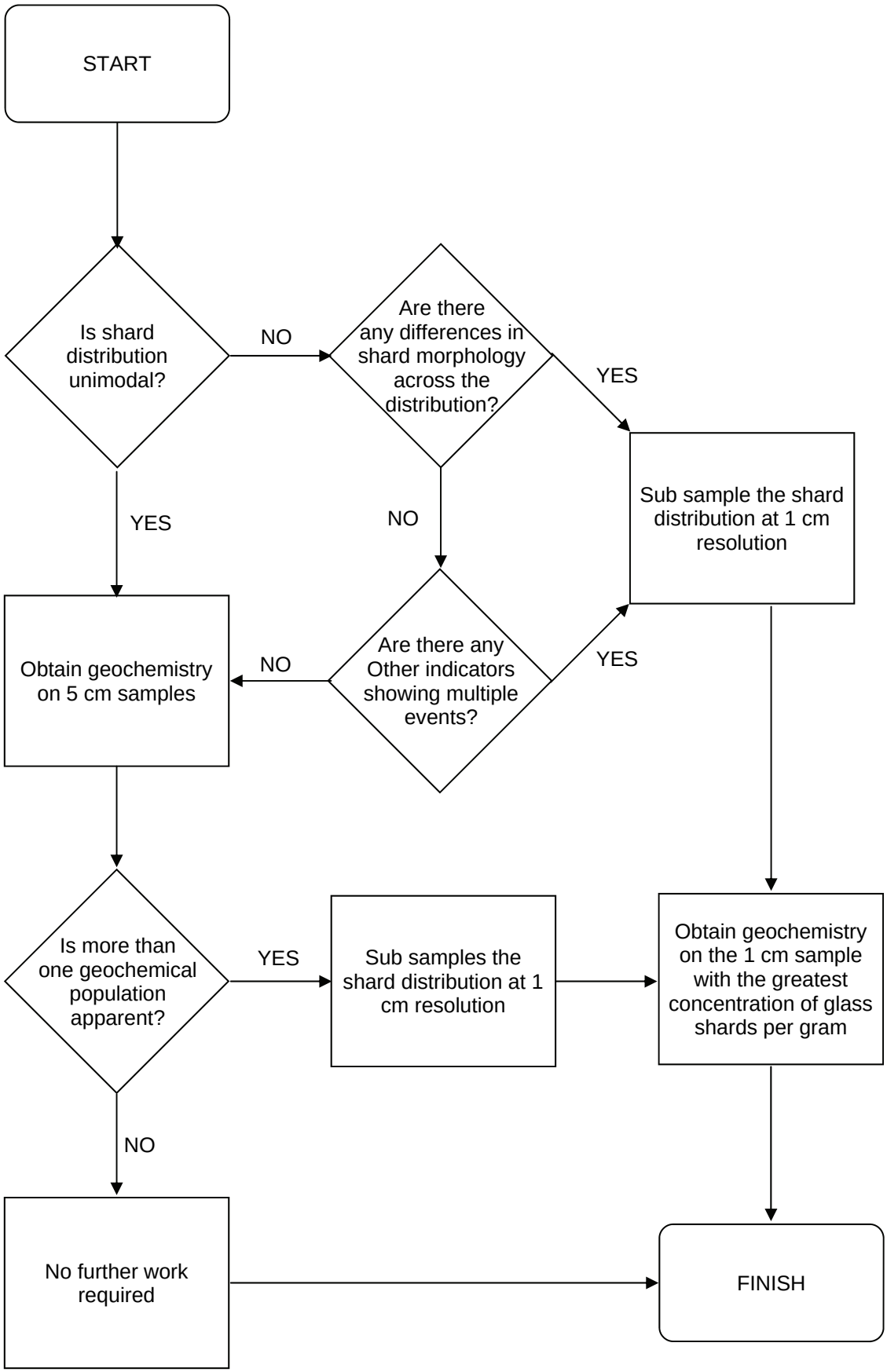

Figure 4.2: Flowchart for sub-sampling decisions after 5 cm scan samples

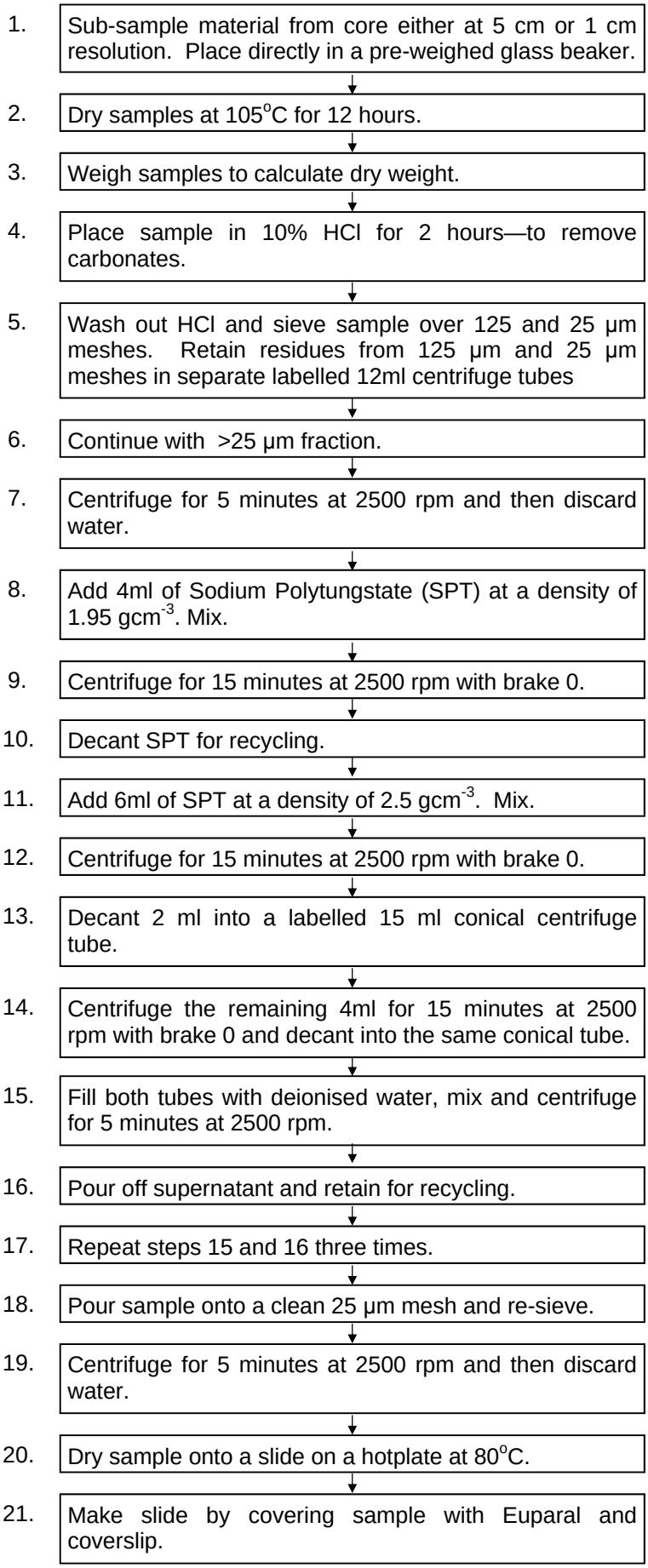

Figure 4.3: Glass shard extraction and slide preparation protocol.

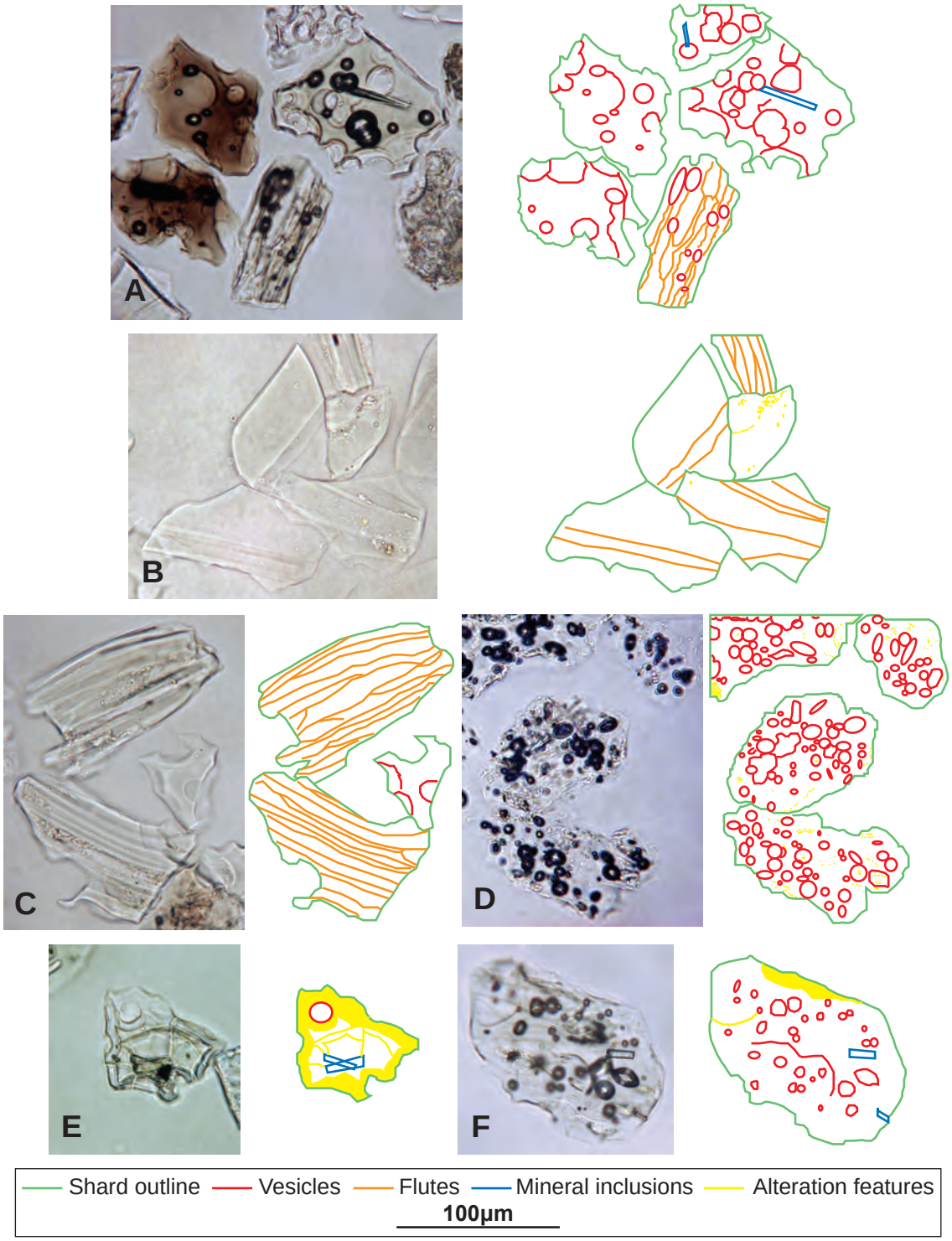

Figure 4.4: Photomicrographs and associated schematics of tephra shards. The schematics highlight the primary diagnostic morphological features of tephra shards. A = brown and colourless shards from the AP3 eruption with very irregular concave-convex outlines. Closed vesicles which are circular to ovoid are present. Microlite inclusions are present in two shards and one shard show fluting (tracks left as gas bubbles escape). B = Colourless shards from the Monte Epomeo Green Tuff eruption that show a dominant platy morphology with a little fluting present and convex fractures on the shard outline. C = Colourless, fluted shards from the Agnano Monte Spina eruption. D = Highly vesicular, colourless shards from the Codola eruption, some shards show evidence of alteration through chemical attack. E = Shard showing a hydration rim and evidence of cracking, microlite inclusions are also present. F = Colourless, vesicular shard with microlite inclusions and signs of physical and chemical alteration.

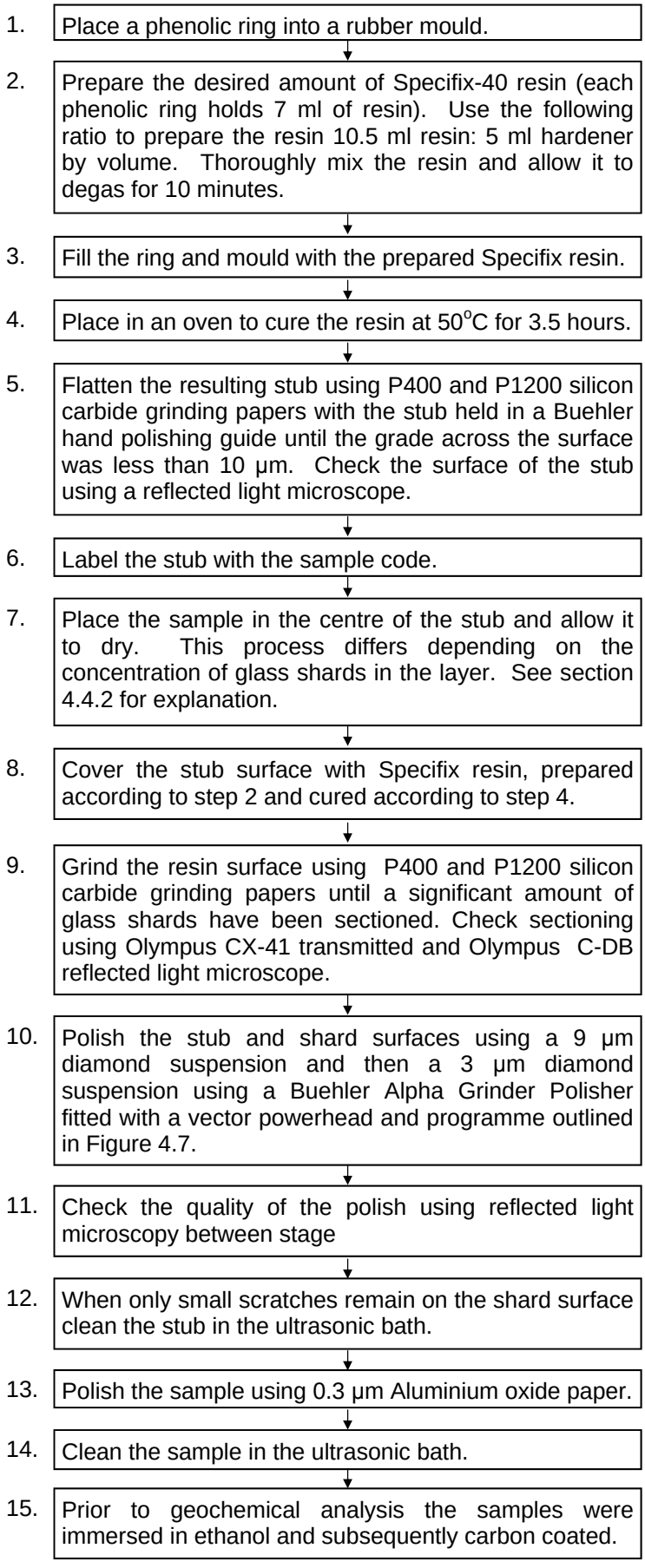

Figure 4.6: Flowchart for the preparation of geochemical stubs and samples

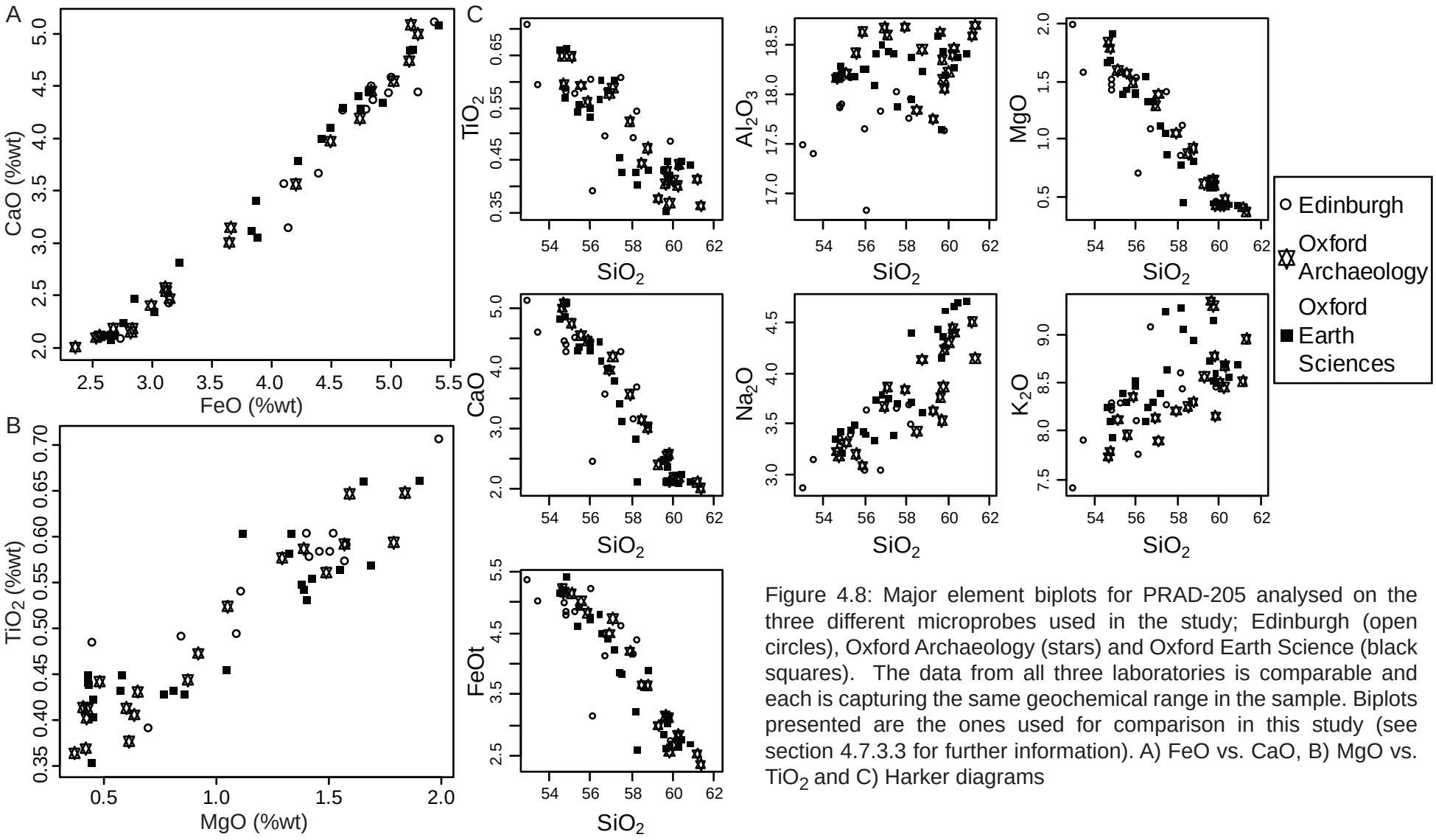

Figure 4.8: Major element biplots for PRAD-205 analysed on the three different microprobes used in the study; Edinburgh (open circles), Oxford Archaeology (stars) and Oxford Earth Science (black squares). The data from all three laboratories is comparable and each is capturing the same geochemical range in the sample. Biplots presented are the ones used for comparison in this study (see section 4.7.3.3 for further information). A) FeO vs. CaO, B) MgO vs. TiO_2 and C) Harker diagrams

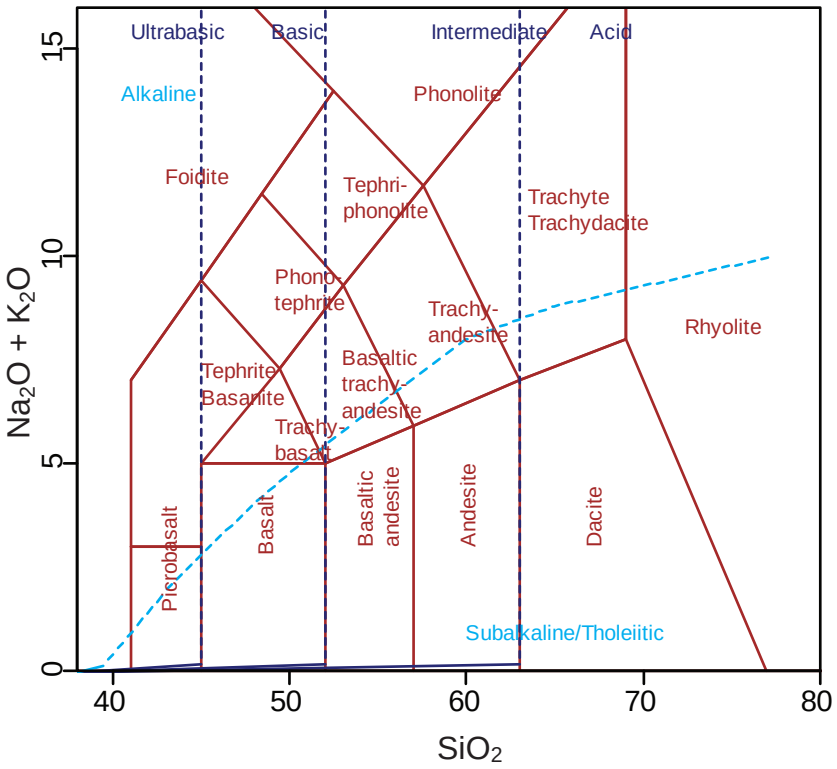

Figure 4.9: Total Alkalis vs. Silica (TAS) diagram with divisions specified by Le Bas *et al.* (1986). The light blue dashed line delimits the lower subalkaline and higher alkaline chemistries.

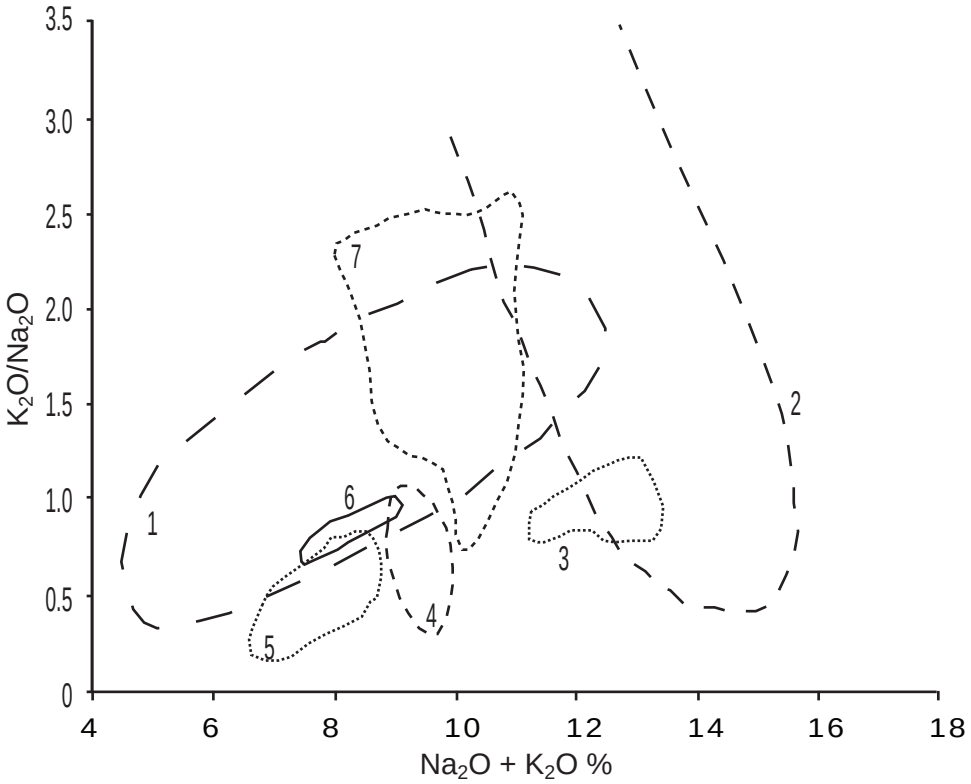

Figure 4.10: Alkali ratio diagram showing distinctive groupings for Mediterranean volcanic systems. Volcanic system 1 = Aeolian, 2 = Campanian Volcanic Zone, 3 = Ischia, 4 = Pantelleria, 5 = Etna, 6 = Procida and 7 = Alban Hills, based on data from Paterne *et al.* (1988) and Wulf *et al.* (2004).

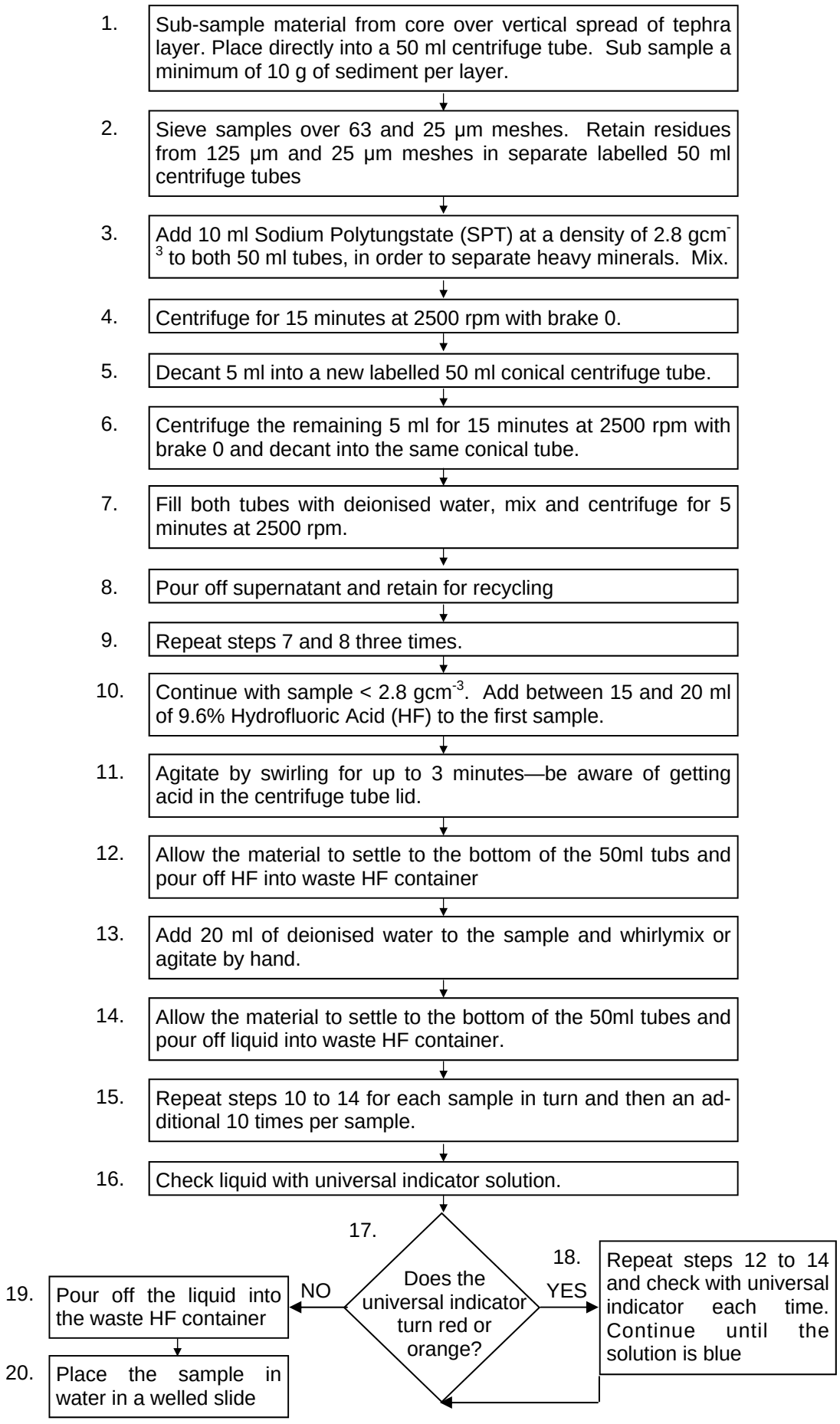

Figure 4.12: Sample preparation procedure for Argon-Argon dating

Table 5.1: Summary of PRAD 1-2 tephra layers identified at 5 cm resolution in this study including shard content, number of geochemical determinations obtained, classification of glass shards where applicable, and descriptions of shard characteristics. All samples were coded by depth to allow for possible addition of new horizons to the sequence. Classifications (based on Le Bas et al., 1986): Tr = trachyte, P = phonolite, TP = tephriphonolite.

Layer code	Shards/g dry wt.	Total analyses	Classification	Shard morphological characteristics
PRAD 055	1095	29	P/Tr	Clear mainly fluted shards, with some large open vesicles. Few inclusions, fairly large shards.
PRAD 120	200	15	Tr/P	Small clear fluted and platy shards. Few inclusions.
PRAD 203	746	23	Tr/P	Clear fluted shards, some more intermediate in colour. Large shards with some mineral inclusions
PRAD 218	> 10000	26	Tr/P	Clear fluted shards, some more intermediate in colour. Large shards with some mineral inclusions
PRAD 268	1238	21	Tr/P/TP	Clear fluted shards, some more intermediate in colour. Large shards with some mineral inclusions
PRAD 324	> 10000	19	Tr/P/TP	Large clear fluted shards, some more intermediate in colour. Large shards with some mineral inclusions
PRAD 404	3187	17	Tr/P/TP	Clear fluted shards, some more intermediate in colour. Large shards with some mineral inclusions
PRAD 480	308	16	P/Tr	Brown and intermediate small shards, some closed vesicles, platy shards
PRAD 566	26	N/A	N/A	Small clear/intermediate shards. Evidence of alteration
PRAD 608	17	N/A	N/A	Small clear/intermediate shards. Evidence of alteration
PRAD 650	36	20	P/Tr	Small clear/intermediate shards. Evidence of alteration
PRAD 784	359	18	P/Tr	Very vesicular shards
PRAD 845	156	13	P/Tr	Shards with a large number of closed vesicles.
PRAD 875	178	11	Tr	Shards with a large number of closed vesicles.
PRAD 1100	> 10000	29	Tr	All clear shards, mainly platy and few mineral inclusions. No intermediate shards
PRAD 1125	145	10	Tr/P	All clear shards, mainly platy and few mineral inclusions. No intermediate shards
PRAD 1332	53	23	Tr	All clear shards, vesicular and few mineral inclusions. No intermediate shards
PRAD 1474	204	10	Tr/P	Very pumiceous layer, small, clear vesicular shards that may have been altered

PRAD 1494	1878	17	Tr/P	Very small clear, platy shards, no mineral inclusions, some closed vesicles.
PRAD 1653	> 10000	14	P/Tr	Large clear and some intermediate shards, highly fluted shards with some open vesicles.
PRAD 1752	5448	29	Tr	Clear and some intermediate shards, highly fluted shards with some open vesicles.
PRAD 1870	> 10000	30	Tr	All clear shards, vesicular and few mineral inclusions. No intermediate shards
PRAD 2040	1931	23	P/Tr	All clear shards, vesicular and few mineral inclusions. No intermediate shards
PRAD 2375	217	8	Unknown	Shards are hydrated with evidence of alteration.
PRAD 2525*	7390076	92	P/Tr	Large clear and some intermediate shards, highly fluted shards with some open vesicles.
PRAD 2605	> 10000	28	P	Only clear shards, predominantly fluted.
PRAD 2812*	24755166	27	P/Tr	Large shards, fluted and platy shards.
PRAD 3065	843	N/A	N/A	Clear platy shards, some shards with closed vesicles.
PRAD 3225*	>10000	13	P	Mix of platy and fluted shards which are predominantly clear in colour.
PRAD 3336	>10000	10	P	Clear shards, platy morphology, some open vesicles.
PRAD 3383*	>10000	11	P/Tr	Clear shards which are highly fluted and vesicular, with a large number of closed vesicles.
PRAD 3472*	>10000	11	Tr	Clear shards with a dominant platy morphology, small number of brown shards present have small closed vesicles
PRAD 3586*	>10000	10	P	Mainly clear platy shards, very few brown shards
PRAD 3666*	>10000	10	P	Highly vesicular shards, mainly clear but brown shards also present

* Denotes visible tephra layer

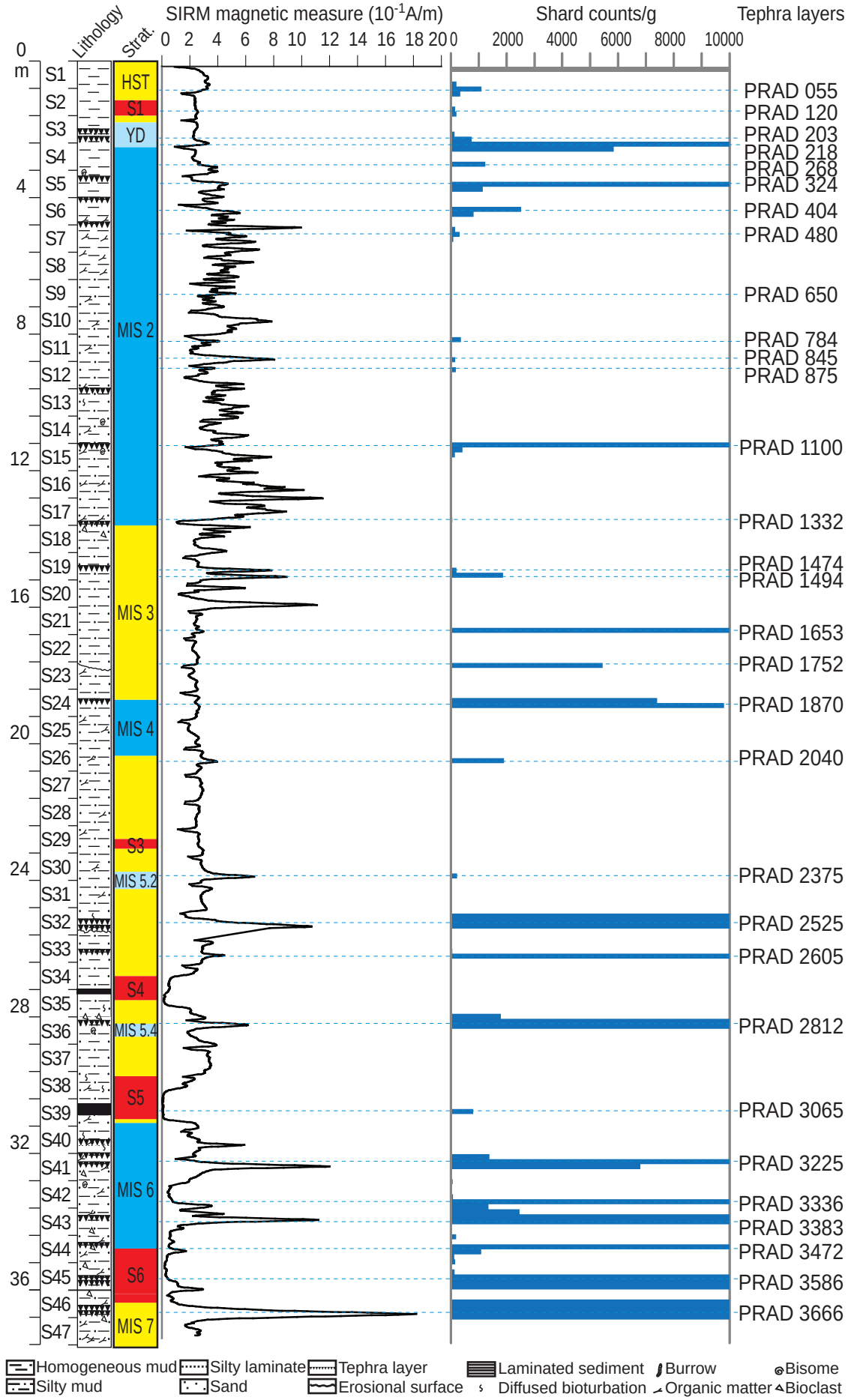

Figure 5.1: PRAD 1-2 stratigraphic, magnetic and shard concentration information. Stratigraphic subdivisions on the left are based on oxygen isotope stratigraphy.

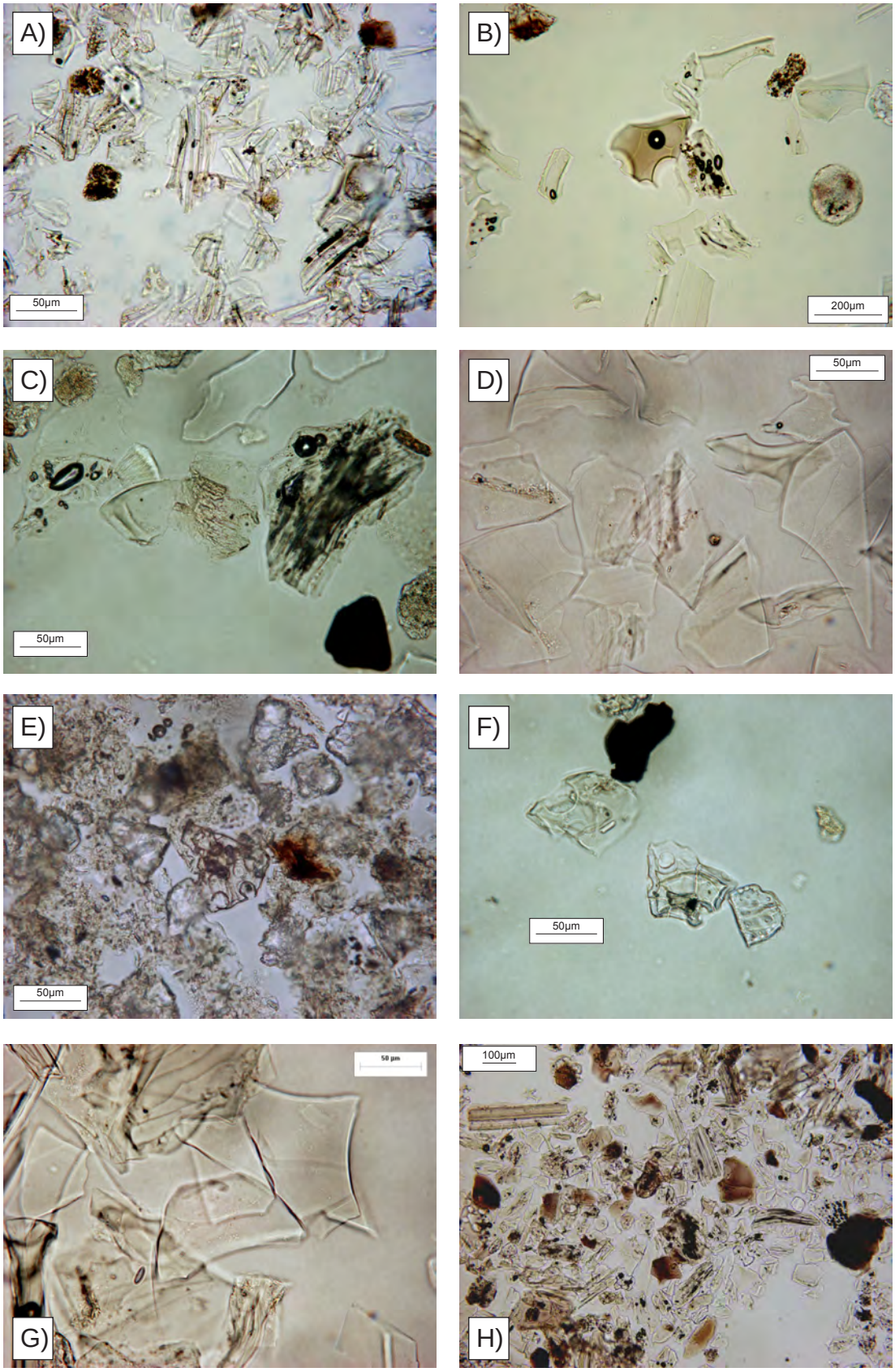

Figure 5.2: Photomicrographs showing the shard morphologies and characteristics of the PRAD 1-2 tephra layers. A) Clear, fluted shards from PRAD-1653. B) Intermediate shard with vesicle from PRAD-324. C) Highly vesicular shard from PRAD-784. D) Clear, platy shards from PRAD-2812. E) Clear, vesicular shard (in the centre) from PRAD-1474 with pumice fragments around it. F) Shard with a hydration ring and evidence of alteration from PRAD-2375. G) Clear, platy shards from PRAD-3472 and H) Highly vesicular and fluted brown and clear shards from PRAD-3666.

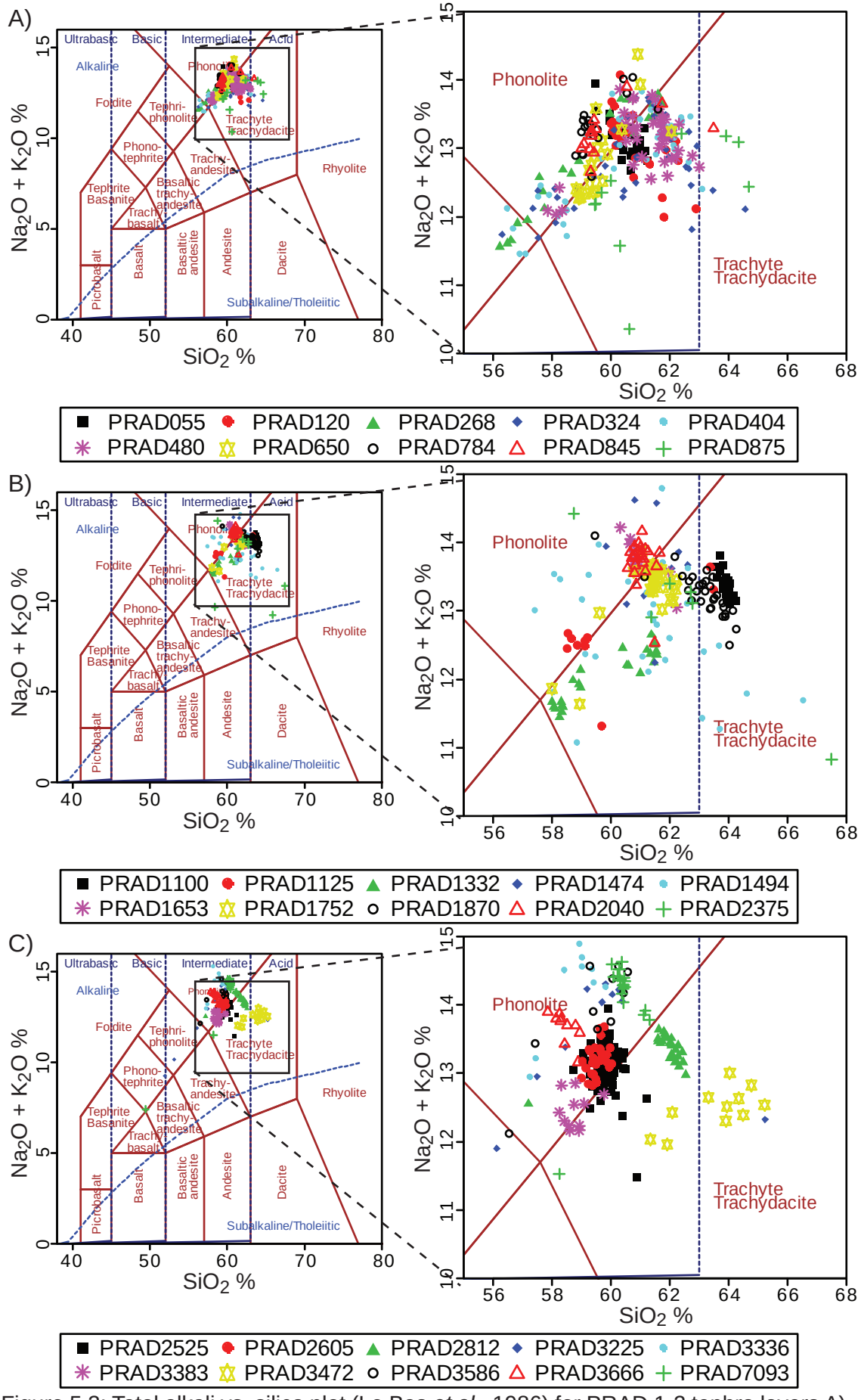

Figure 5.3: Total alkali vs. silica plot (Le Bas *et al.*, 1986) for PRAD 1-2 tephra layers A) PRAD-055 to PRAD-875, B) PRAD-1100 to PRAD-2375, C) PRAD-2525 to PRAD-7093.

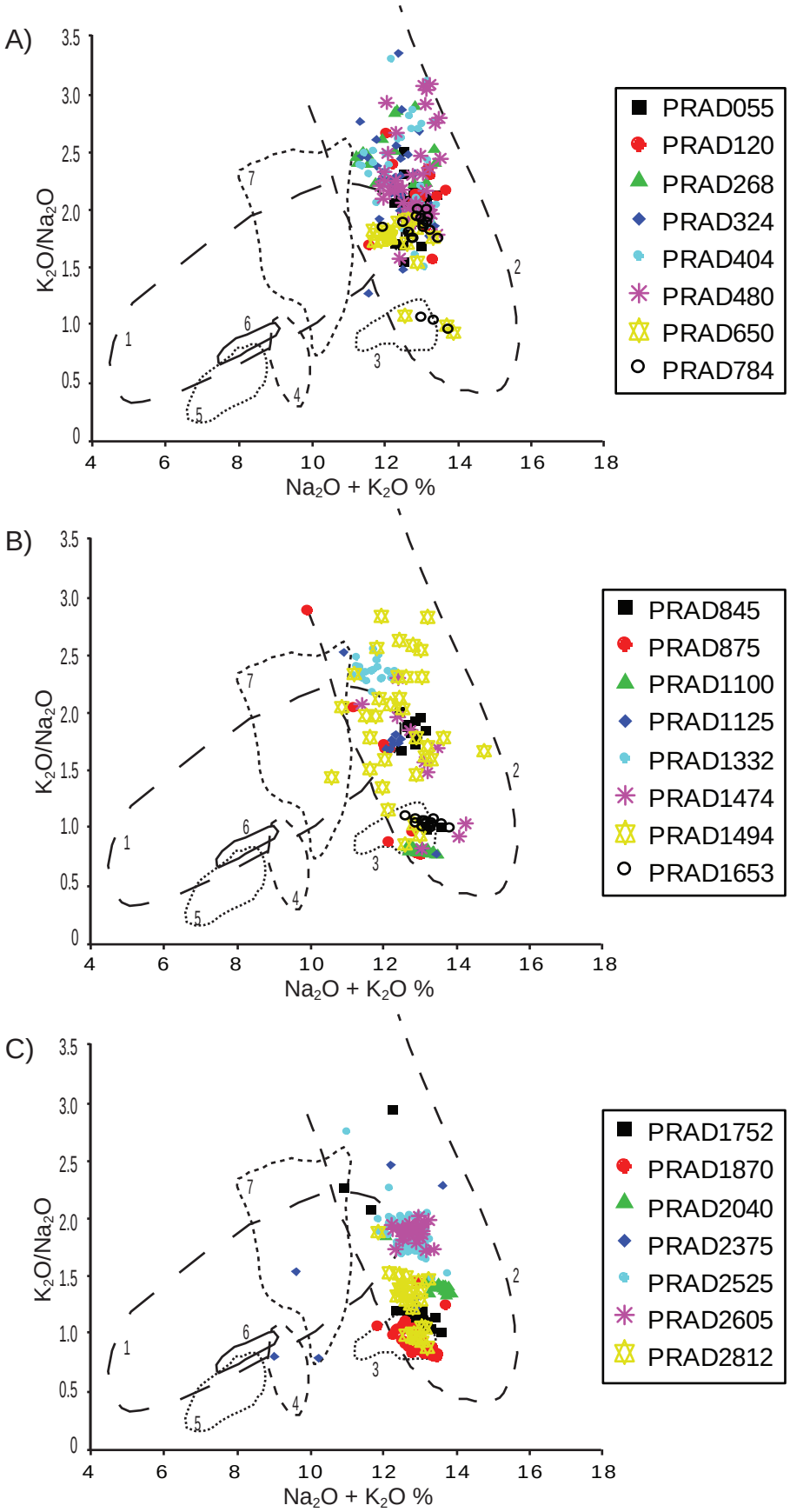

Figure 5.4: Comparison of PRAD layers with distinctive groupings of ash layers determined by alkali data. Volcanic system 1=Aeolian, 2=Campanian Volcanic Zone, 3=Ischia, 4=Pantelleria, 5=Etna, 6=Procida and 7=Alban Hills (Diagram reproduced from Paterne *et al.,*1988 and Wulf *et al.,* 2004) A) PRAD-055 to PRAD-784, B) PRAD-845 to PRAD-1653, C) PRAD-1752 to PRAD-2812.

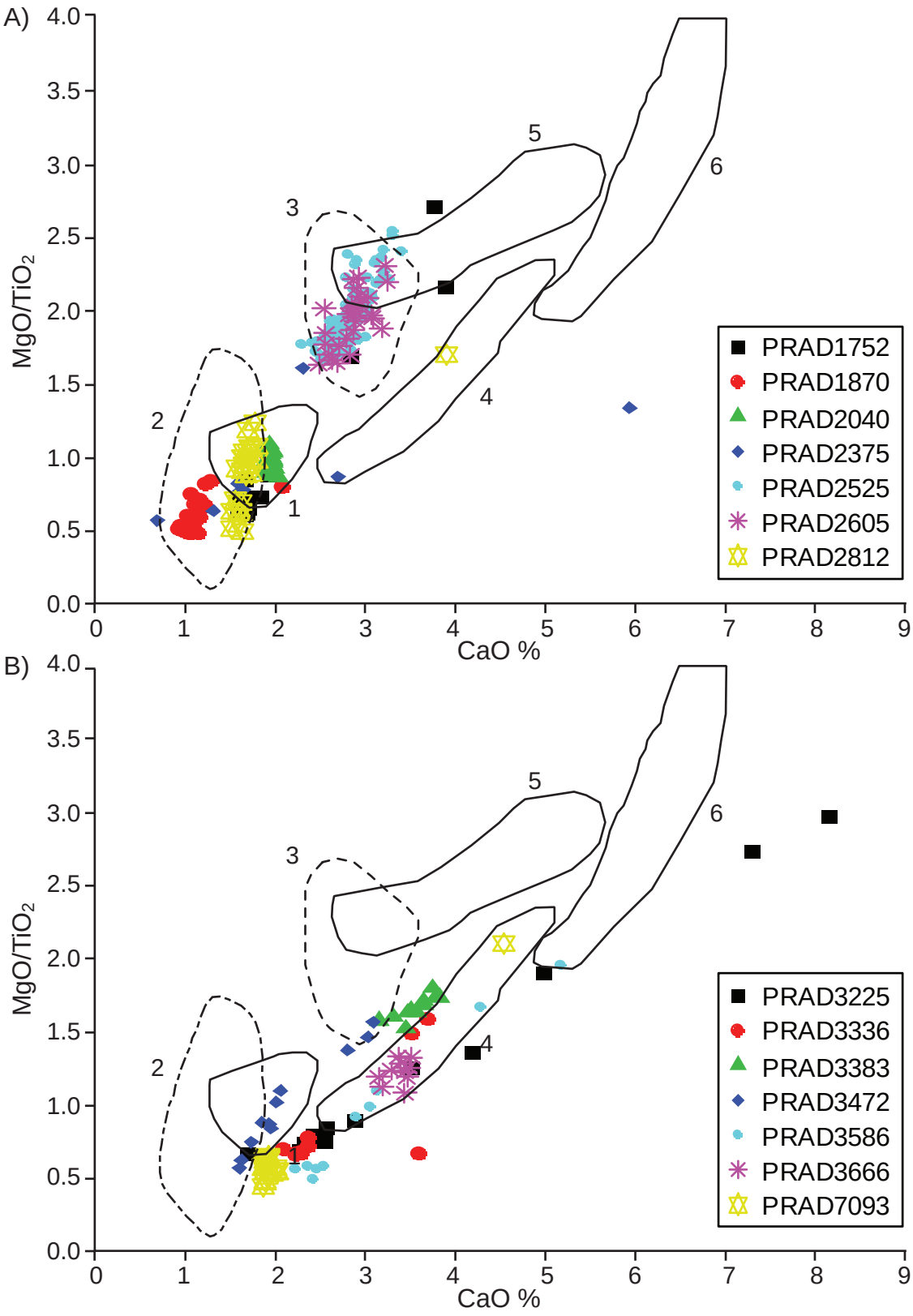

Figure 5.5: CaO vs. MgO/TiO_2 used to discriminate the sources of PRAD 1-2 tephra layers. Fields 1-6 are defined by on-land volcanic products older than 60 ka BP based on data from (1) the Campi Flegrei pre-Campanian Ignimbrite deposits, (2) Ischia pre-Monte Epomeo Green Tuff (Rosi and Sbrana (1987); Pappalardo *et al.* (1999); Webster *et al.* (2003); Vezzoli (1988)); (3) the average composition of tephra layer X5 (Vezzoli (1991); Calanchi *et al.* (2008)): (4) Vico (Perini *et al.,* 2004); (5) Vulsini (Tubeville (1992); Palladino *et al.* (1994)); and (6) Alban Hills (Trigila (1995); Peccerillo (2005)) for the Roman area. A) PRAD 1752 to PRAD 2812, B) PRAD 3225 to PRAD 7093 (adapted from Calanchi *et al.* 2008).

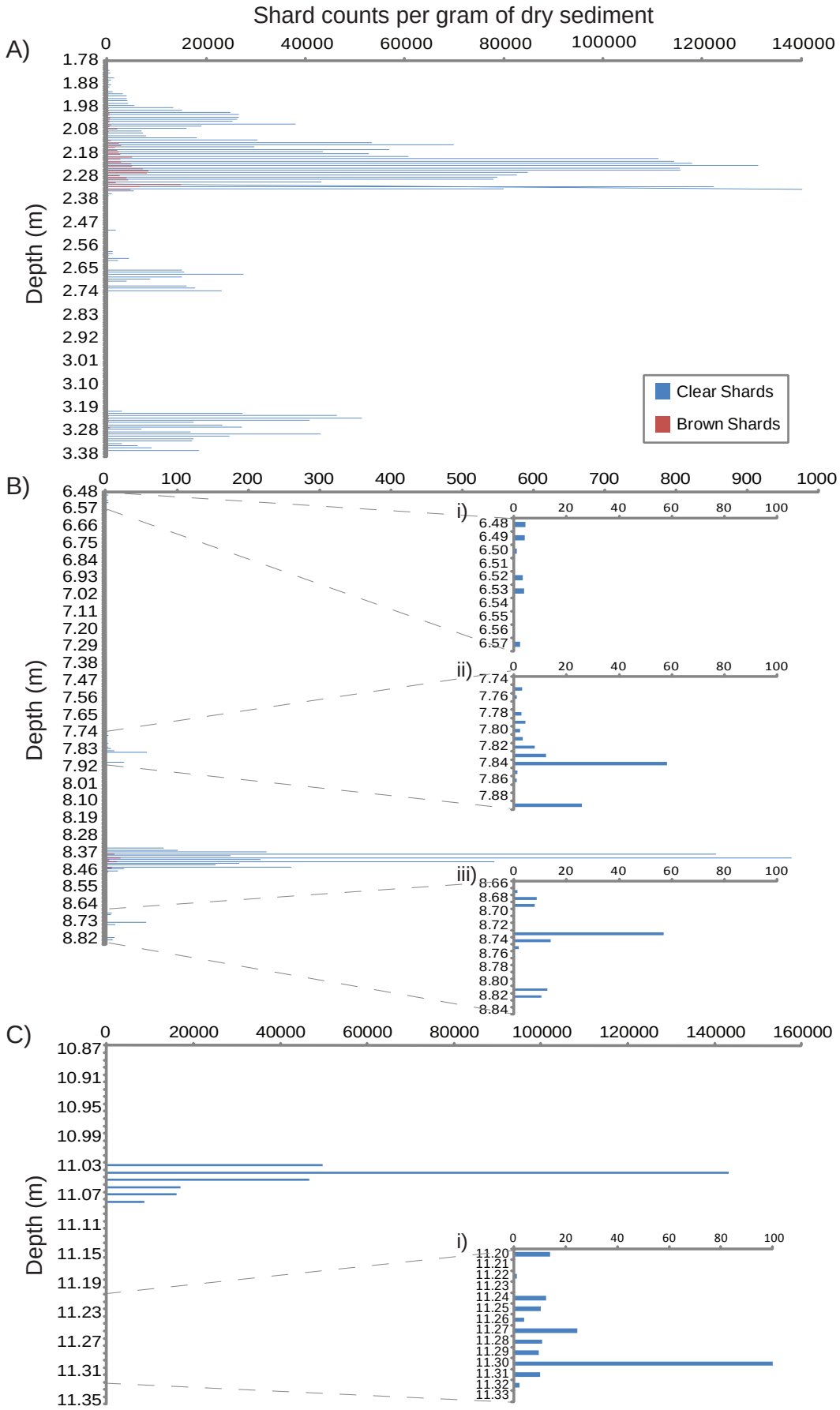

Figure 5.6: PRAD 1 cm shard counts for A) PRAD 178 - 277 cm and 306 - 338 cm; B) PRAD 648 - 657 cm, 774 - 789 cm and 834 - 884 cm and C) PRAD 1087 - 1135 cm. Zoomed in sections Bi) PRAD 648 - 657 cm, Bii) PRAD 774 - 789 cm, Biii) PRAD 866 - 884 and Ci) PRAD 11.20 - 11.33

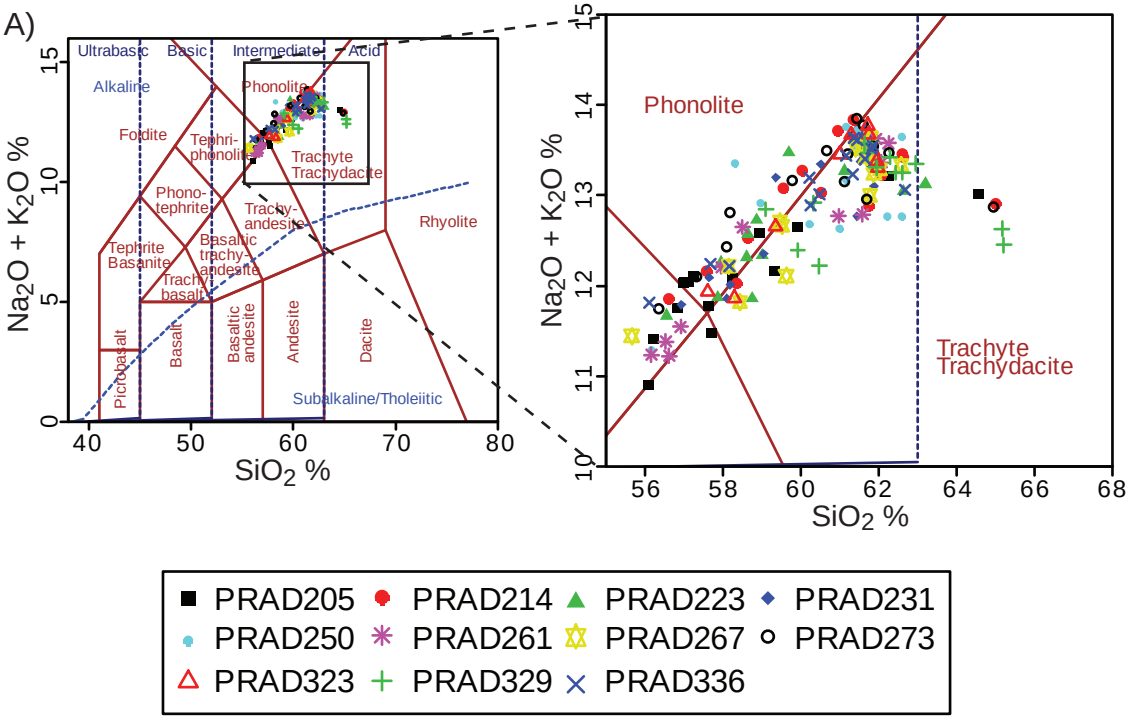

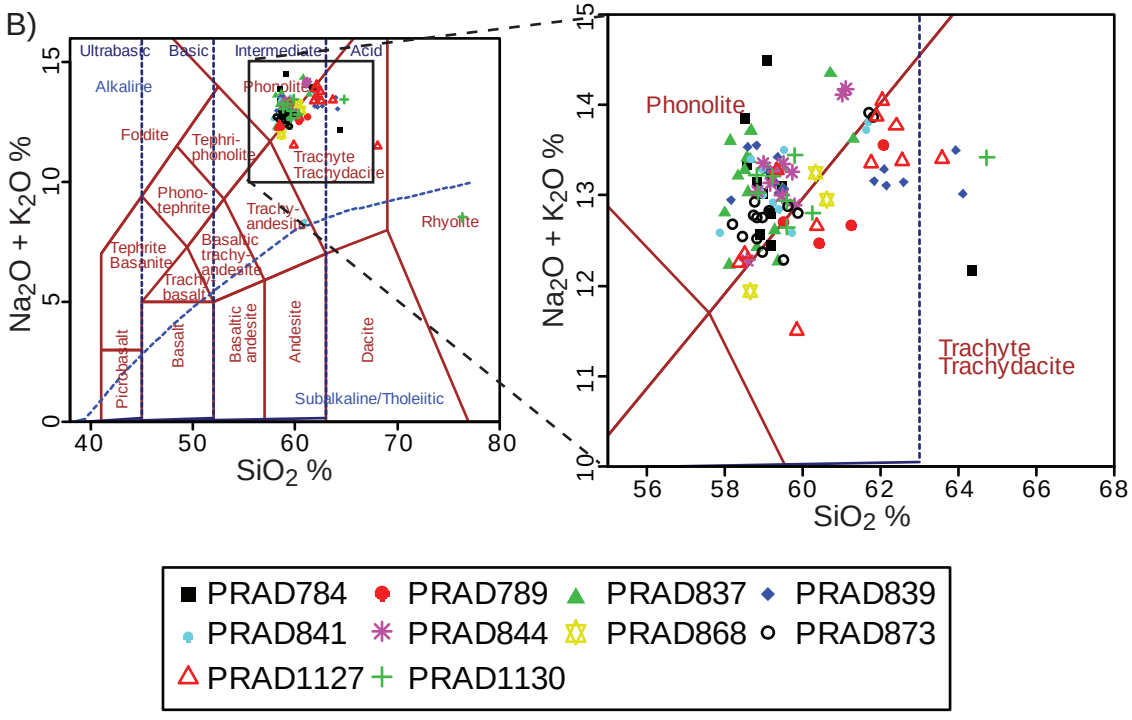

Figure 5.7: Total alkali vs. silica plot (Le Bas *et al.*, 1986) for 1 cm resolution PRAD 1-2 tephra layers A)PRAD-205 to PRAD-336 and B) PRAD-784 to PRAD-1130

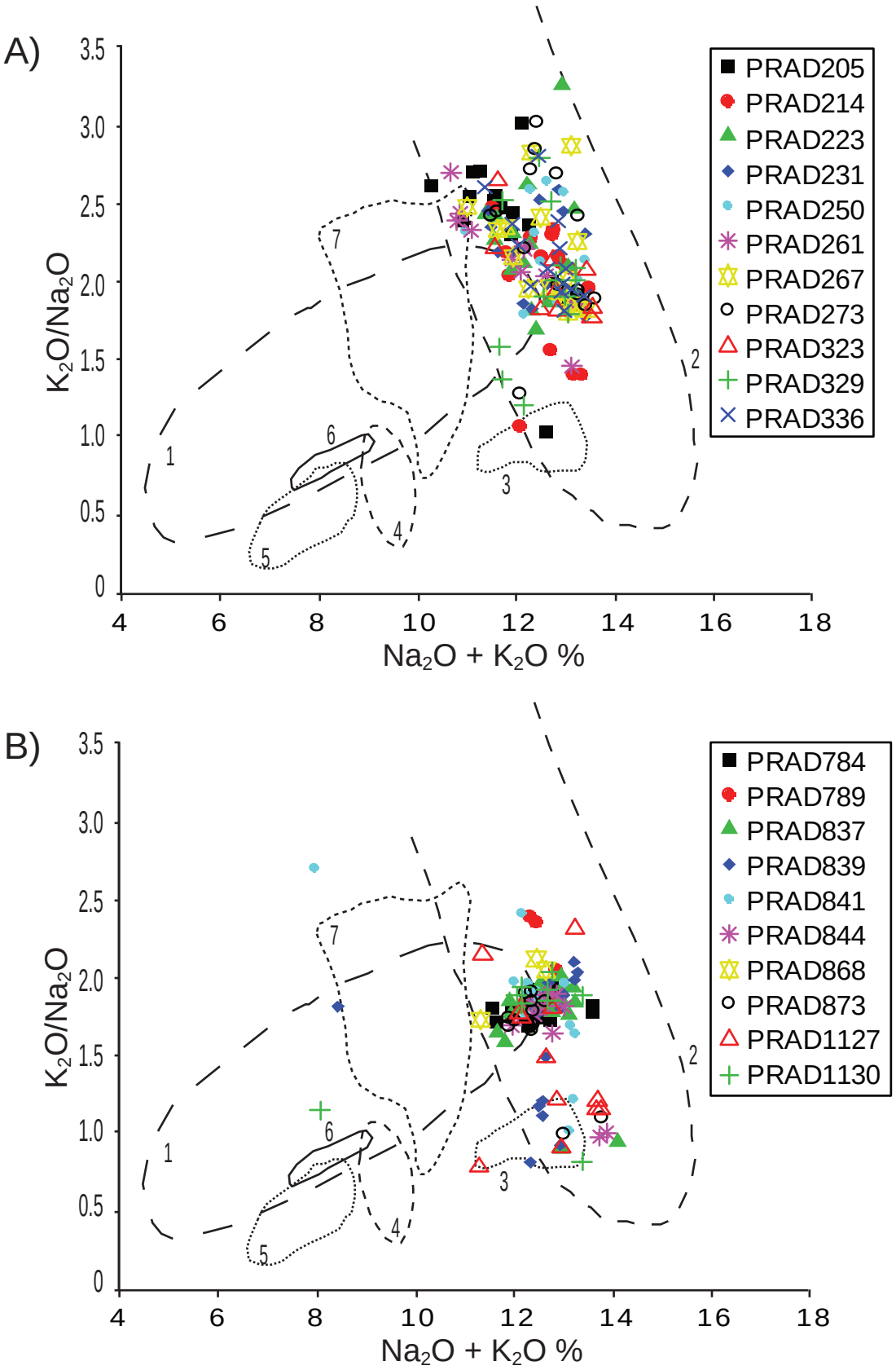

Figure 5.8: Comparison of 1 cm resolution PRAD layers with distinctive groupings of ash layers determined by alkali data. Volcanic system 1=Aeolian, 2=Campanian Volcanic Zone, 3=Ischia, 4=Pantelleria, 5=Etna, 6=Procida and 7=Alban Hills (Diagram reproduced from Paterne *et al.,*1988 and Wulf *et al.,* 2004) A) PRAD-205 to PRAD-336 and B) PRAD-784 to PRAD-1130

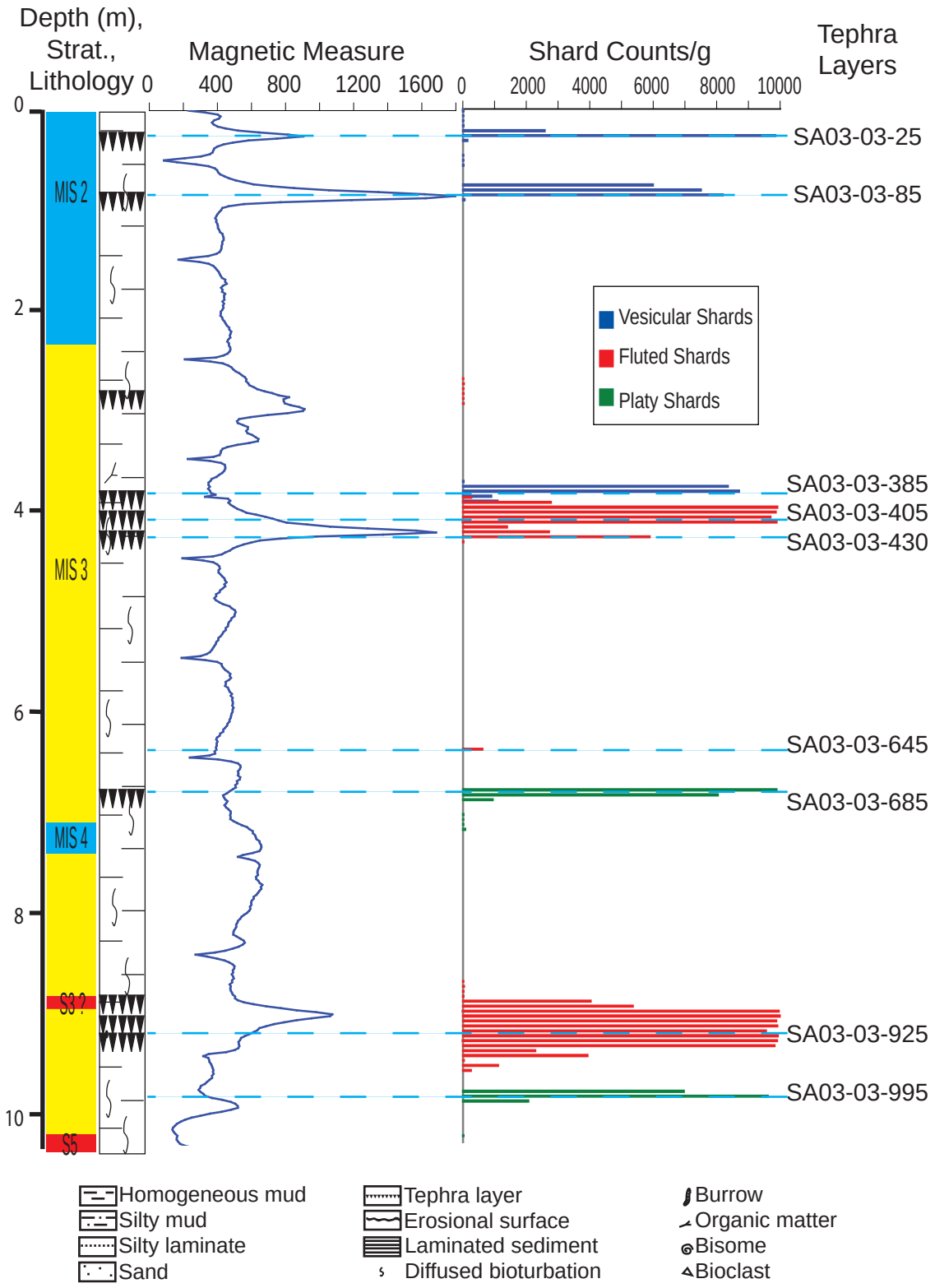

Figure 5.9: SA03-03 stratigraphic, magnetic and shard concentration information. Stratigraphic subdivisions on the left are based on oxygen isotope stratigraphy (Piva, 2007).

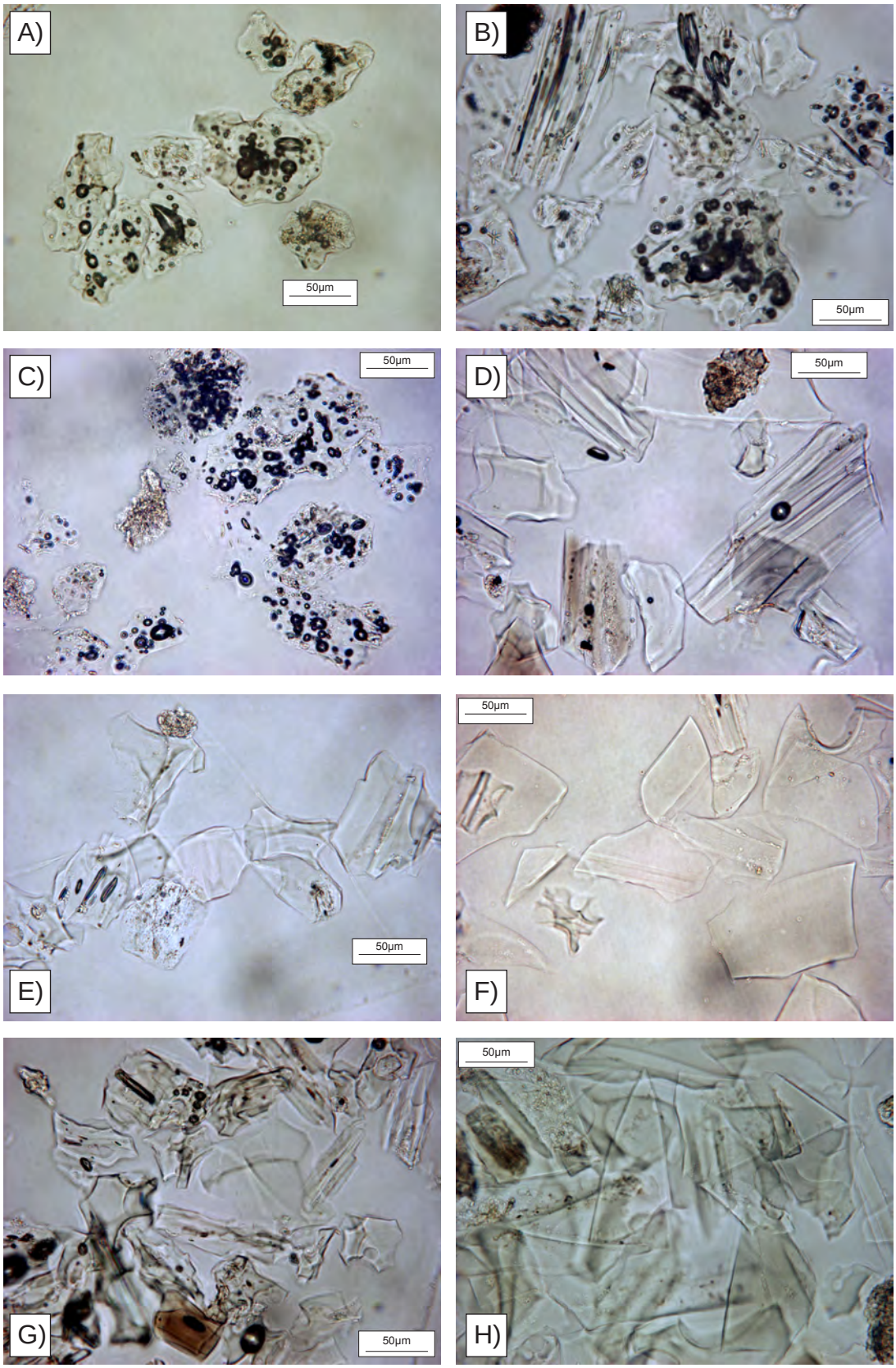

Figure 5.10: Photomicrographs showing the shard morphologies and characteristics of the SA03-03 tephra layers. A) Clear, highly vesicular shards from SA03-03-25. B) Clear, highly vesicular shards from SA03-03-85 C) Clear, highly vesicular shards from SA03-03-383 D) Clear, fluted shards from SA03-03-413. E) Predominantly clear, fluted shards from SA03-03-427. F) Clear, platy shards from SA03-03-685. G) Clear, fluted and vesicular shards from SA03-03-925 and H) Clear, platy shards from SA03-03-995.

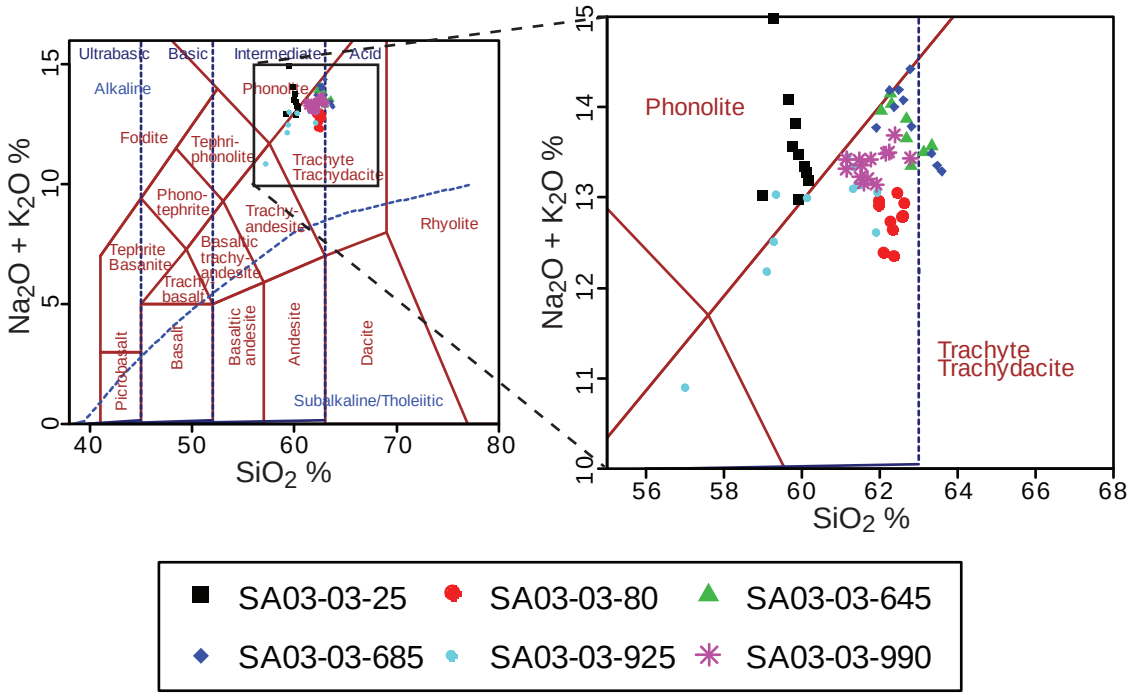

Figure 5.11: Total alkali vs. silica plot (Le Bas *et al.,* 1986) for SA03-03 tephra layers

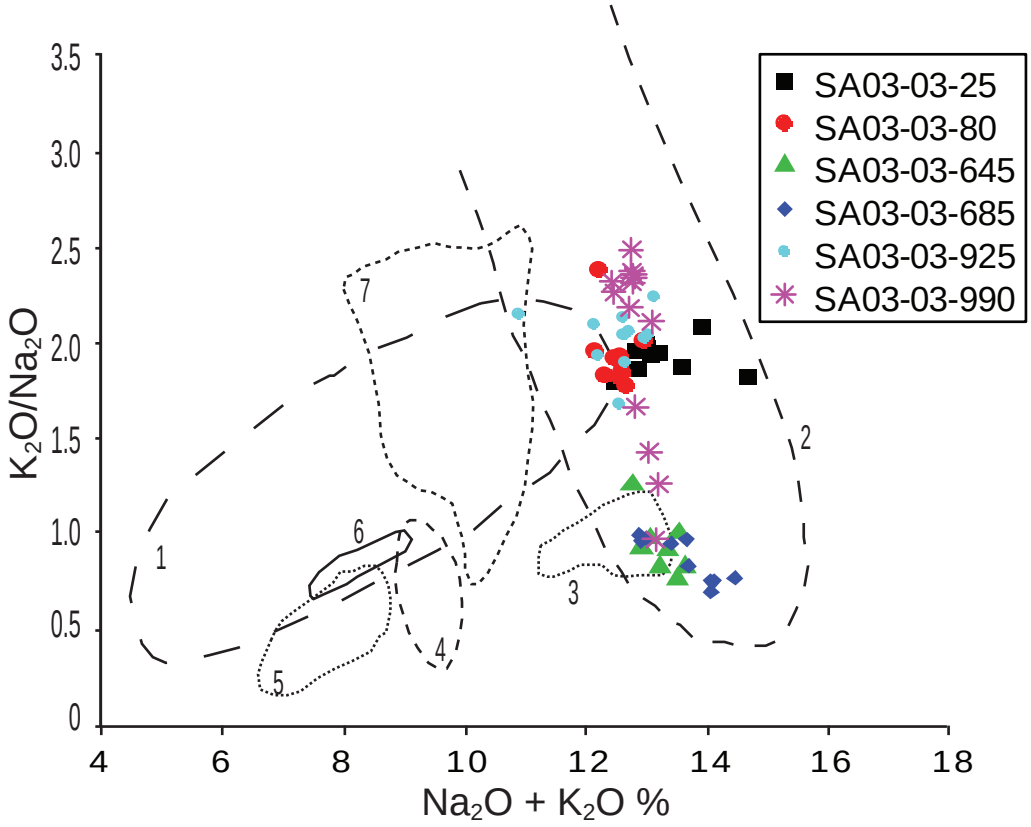

Figure 5.12: Comparison of SA03-03 layers with distinctive groupings of ash layers determined by alkali data. Volcanic system 1=Aeolian, 2=Campanian Volcanic Zone, 3=Ischia, 4=Pantelleria, 5=Etna, 6=Procida and 7=Alban Hills (Paterne *et al.,* 1988 and Wulf *et al.,* 2004)

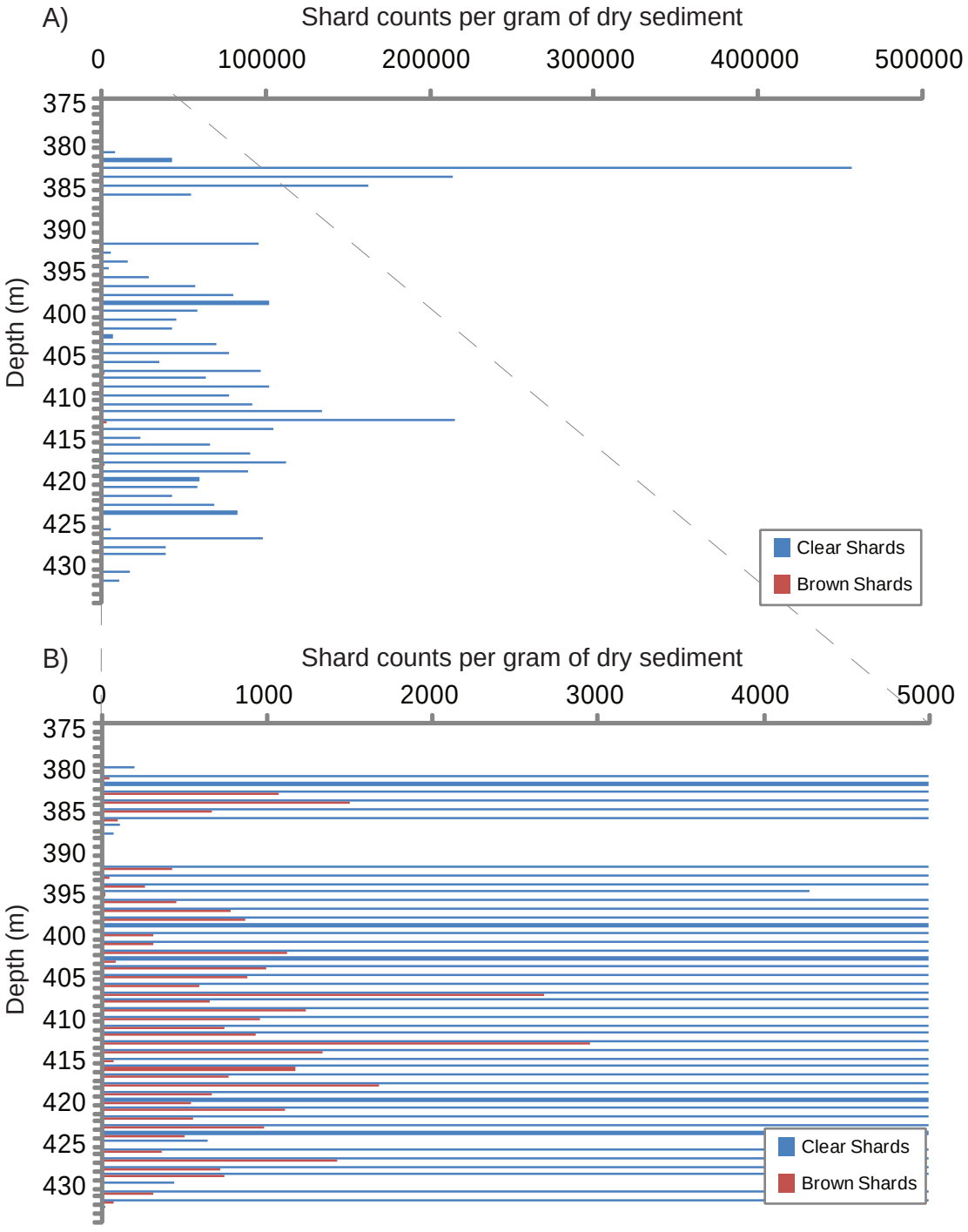

Figure 5.13: A) SA03-03 1 cm shard counts for SA03-03 375 - 434 cm. B) SA03-03 1 cm shard counts for SA03-03 375 - 434 cm at expanded scale to show variations in the number of brown shards.

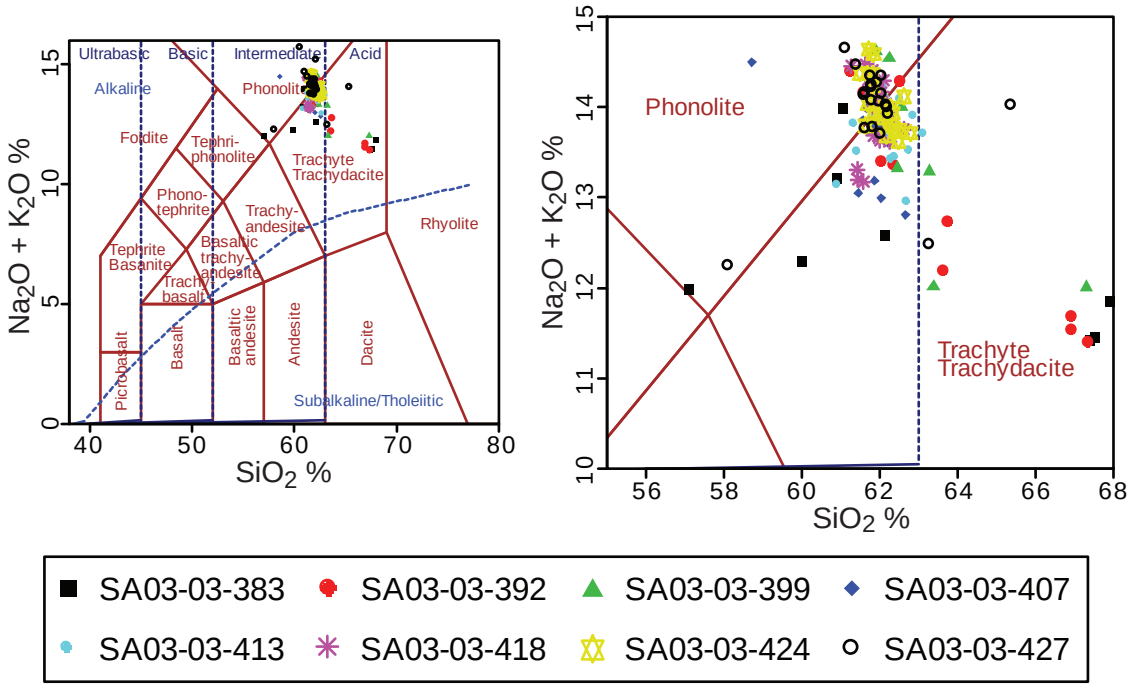

Figure 5.14: Total alkali vs. silica plot (Le Bas *et al.,* 1986) for 1 cm resolution SA03-03 tephra layers

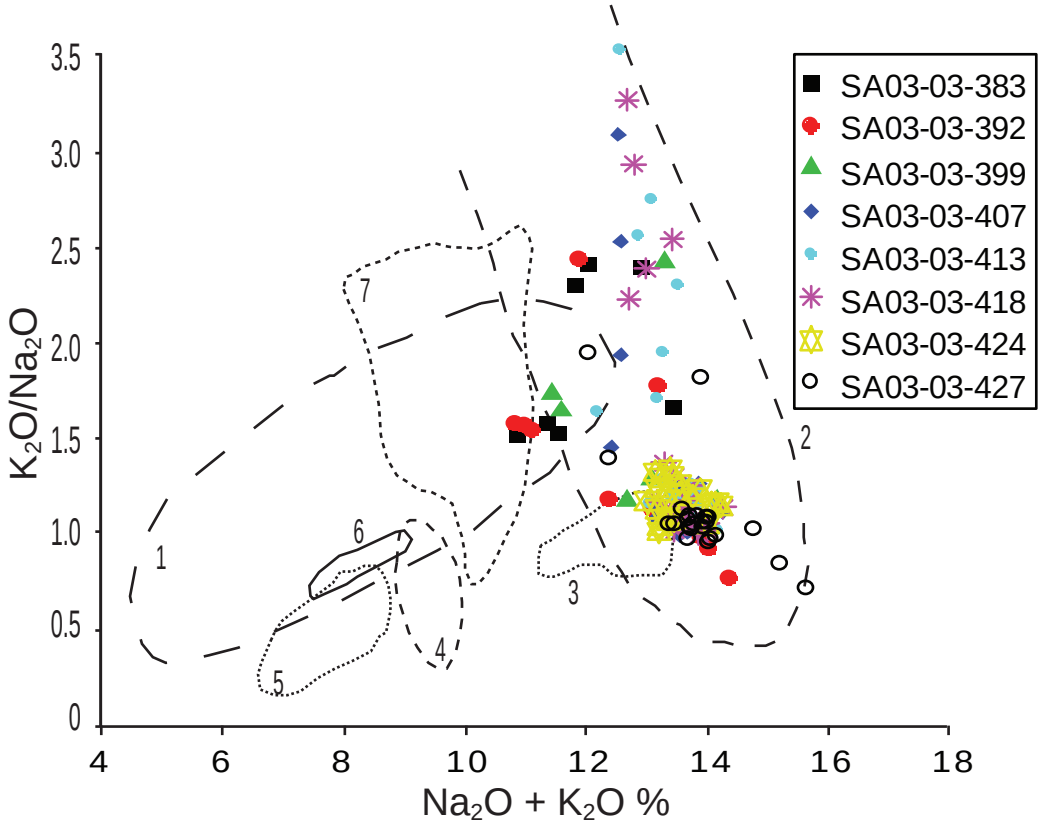

Figure 5.15: Comparison of 1 cm resolution SA03-03 layers with distinctive groupings of ash layers determined by alkali data. Volcanic system 1=Aeolian, 2=Campanian Volcanic Zone, 3=Ischia, 4=Pantelleria, 5=Etna, 6=Procida and 7=Alban Hills (Paterne *et al.,* 1988 and Wulf *et al.,* 2004)

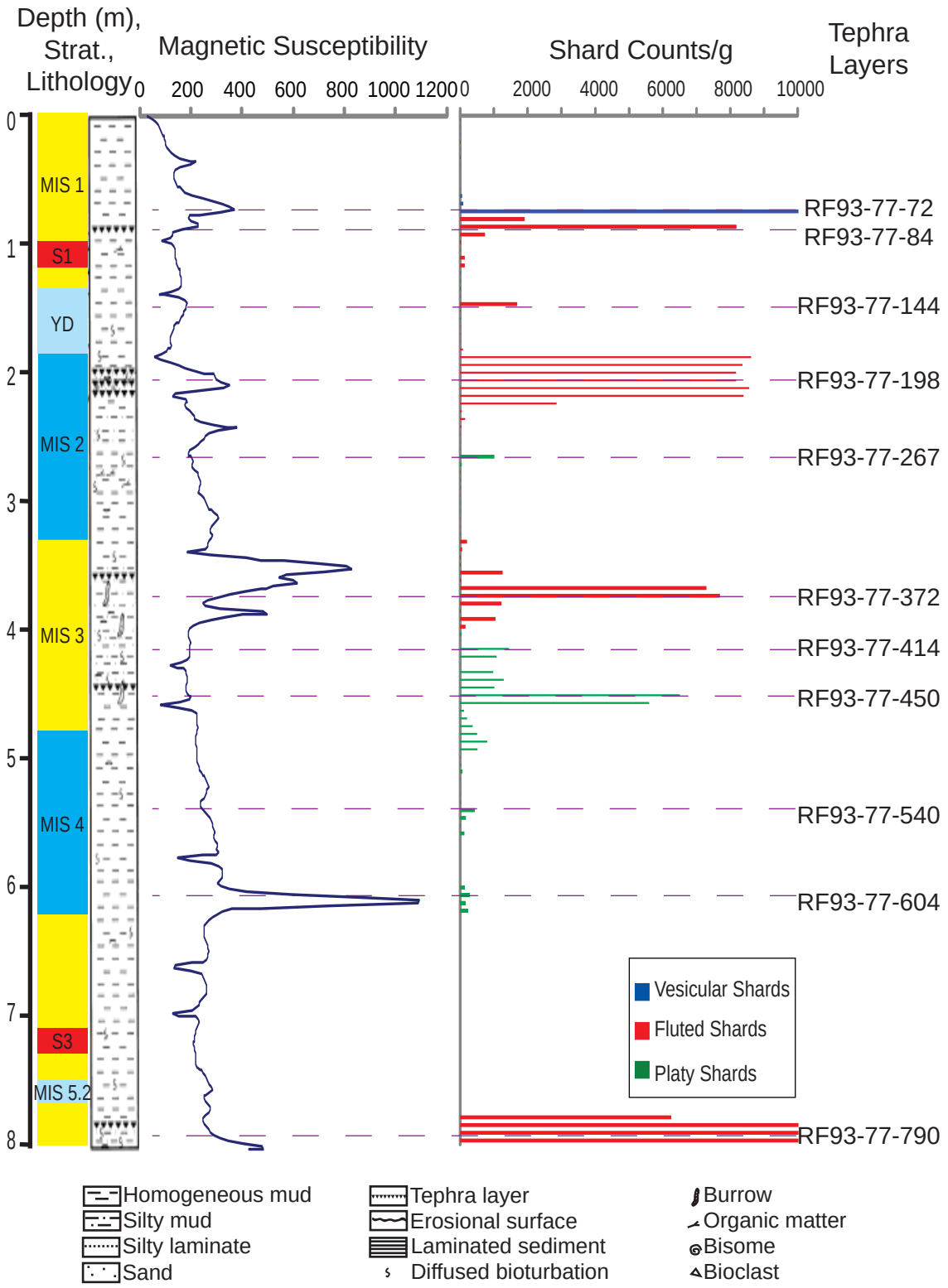

Figure 5.16: RF93-77 stratigraphic, magnetic and shard concentration information. Stratigraphic subdivisions on the left are based on oxygen isotope stratigraphy.

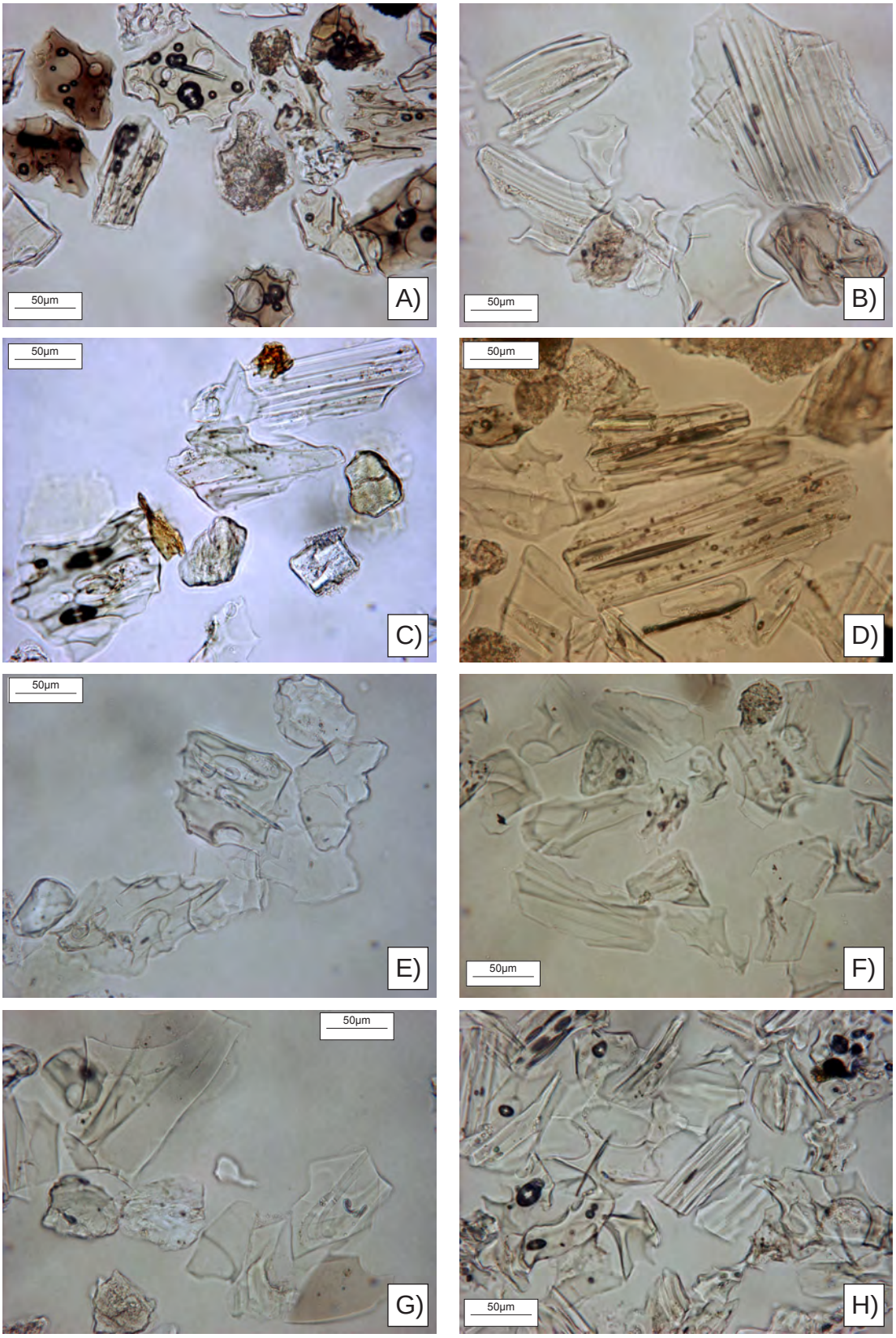

Figure 5.17: Photomicrographs showing the shard morphologies and characteristics of the RF93-77 tephra layers. A) Brown and clear shards with numerous open and closed vesicles from RF93-77-68. B) Predominantly clear, fluted shards from RF93-77-88 C) Clear, fluted shards from RF93-77-144. D) Clear, highly fluted shards from RF93-77-198. E) Clear, predominantly platy shards, with some large open vesicles from RF93-77-267. F) Clear, fluted shards from RF93-77-372. G) Clear, platy shards from RF93-77-450 and H) Clear, fluted shards with some closed vesicles from RF93-77-790.

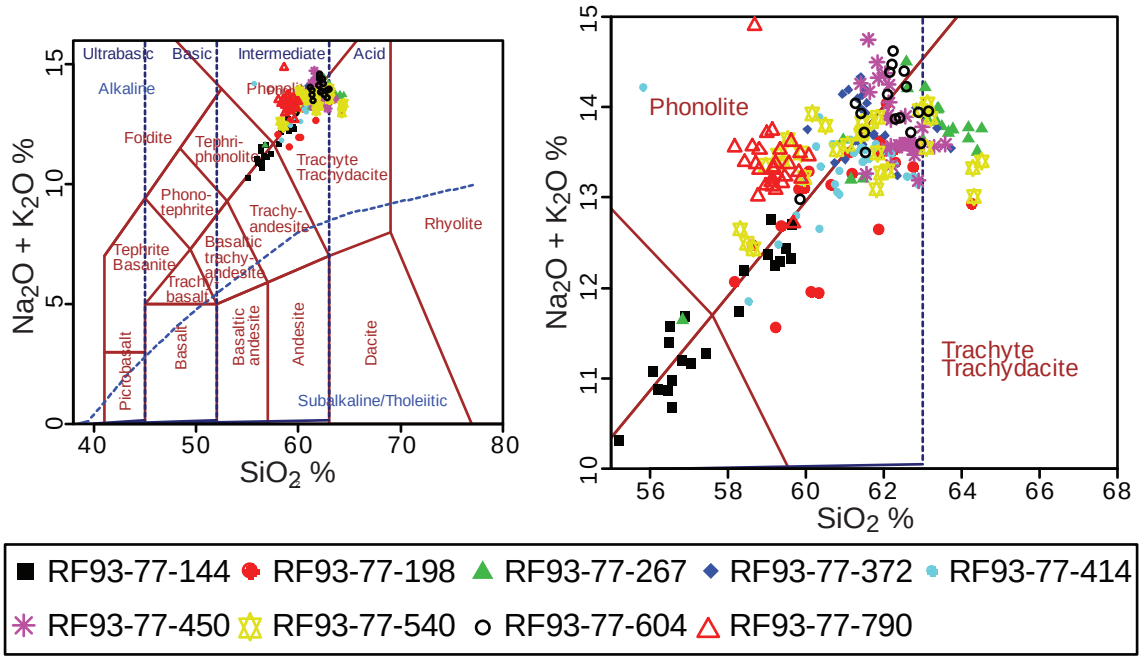

Figure 5.18: Total alkali vs. silica plot (Le Bas *et al.,* 1986) for RF93-77 tephra layers

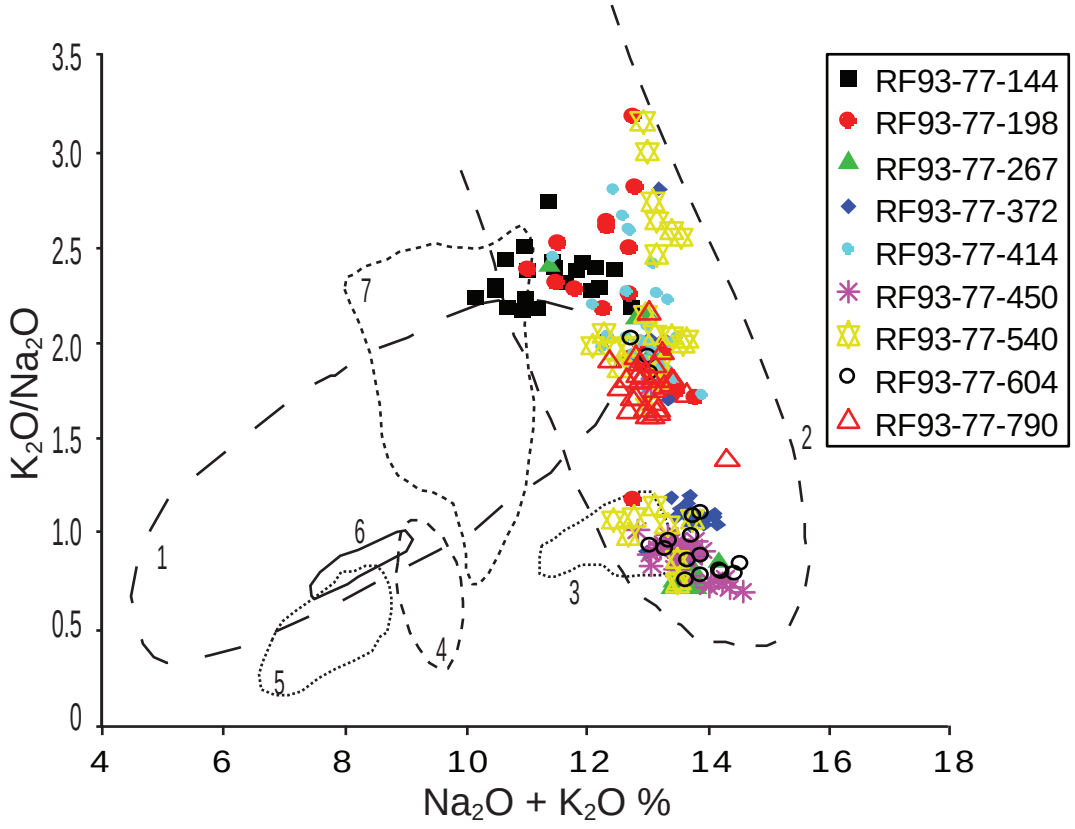

Figure 5.19: Comparison of RF93-77 layers with distinctive groupings of ash layers determined by alkali data. Volcanic system 1=Aeolian, 2=Campanian Volcanic Zone, 3=Ischia, 4=Pantelleria, 5=Etna, 6=Procida and 7=Alban Hills (Diagrams reproduced from Paterne *et al.,* 1988 and Wulf *et al.,* 2004)

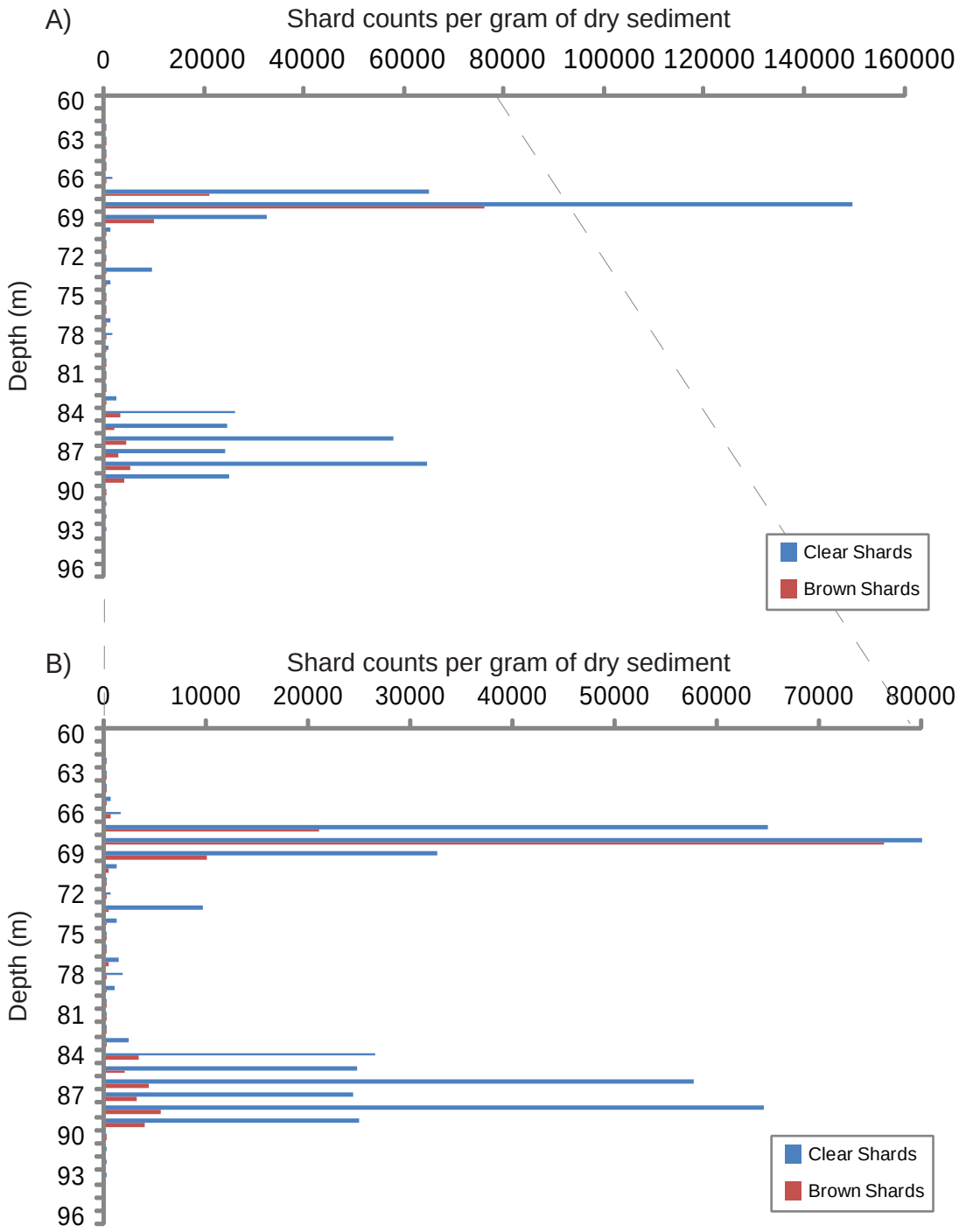

Figure 5.20: A) RF93-77 1 cm shard counts for RF93-77 60 - 96 cm. B) RF93-77 1 cm shard counts for RF93-77 60 - 96 cm at an expanded scale to show variations in number of brown shards.

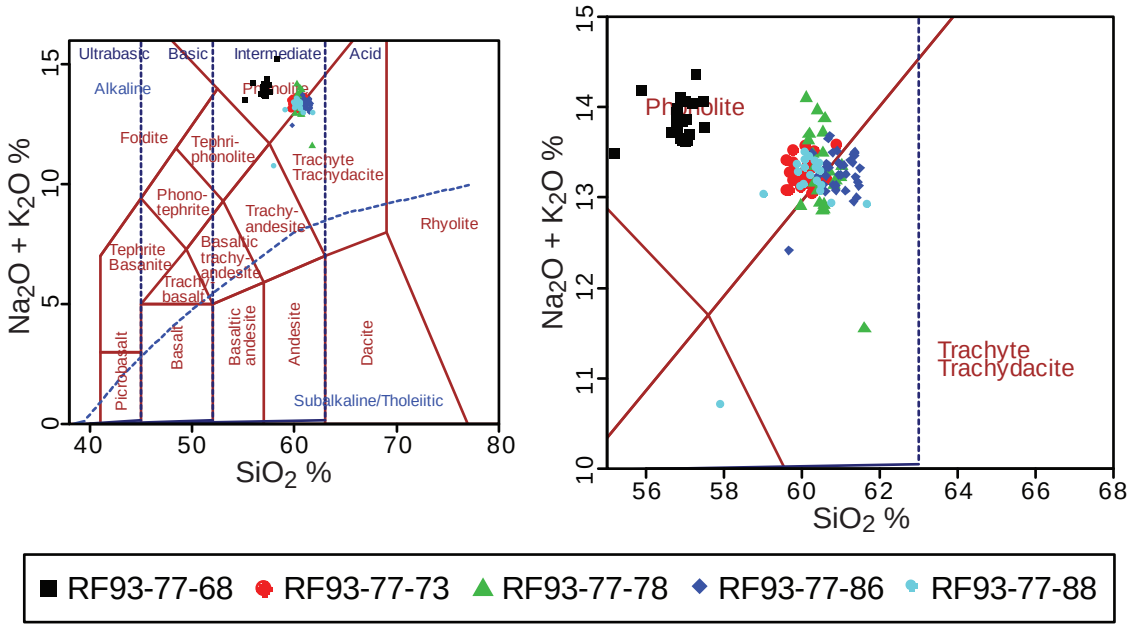

Figure 5.21: Total alkali vs. silica plot (Le Bas *et al.,* 1986) for 1 cm resolution RF93-77 tephra layers

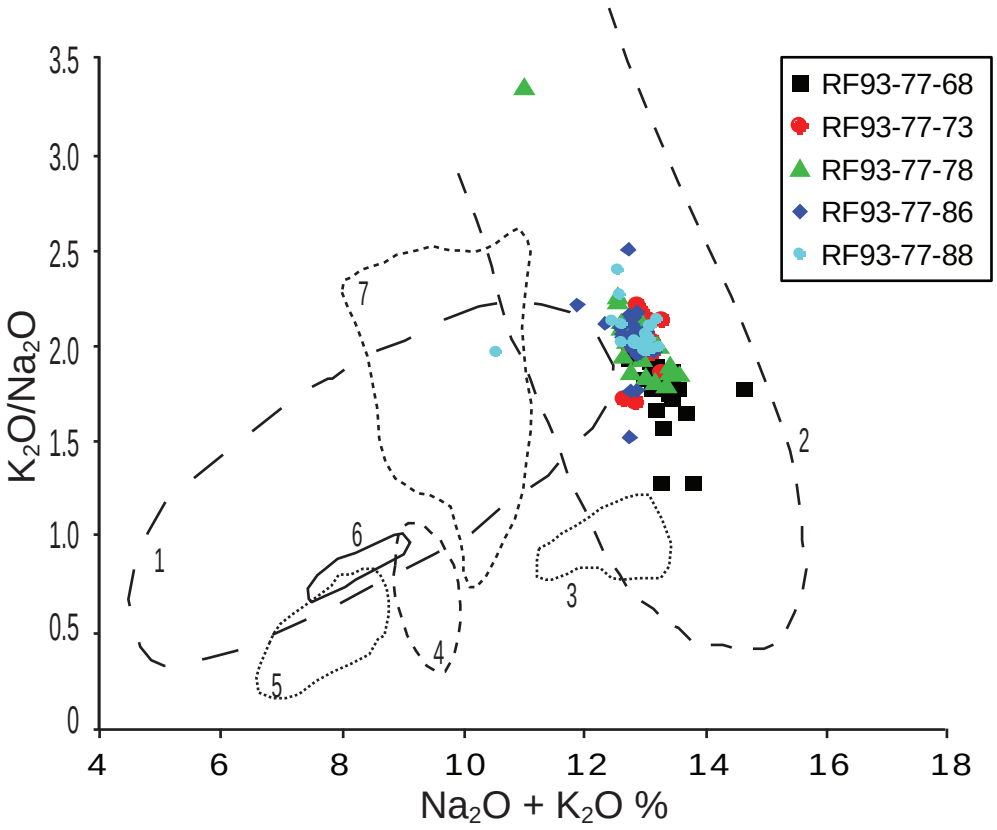

Figure 5.22: Comparison of 1 cm resolution RF93-77 layers with distinctive groupings of ash layers determined by alkali data. Volcanic system 1=Aeolian, 2=Campanian Volcanic Zone, 3=Ischia, 4=Pantelleria, 5=Etna, 6=Procida and 7=Alban Hills (Diagram reproduced from Paterne *et al.,* 1988 and Wulf *et al.,* 2004).

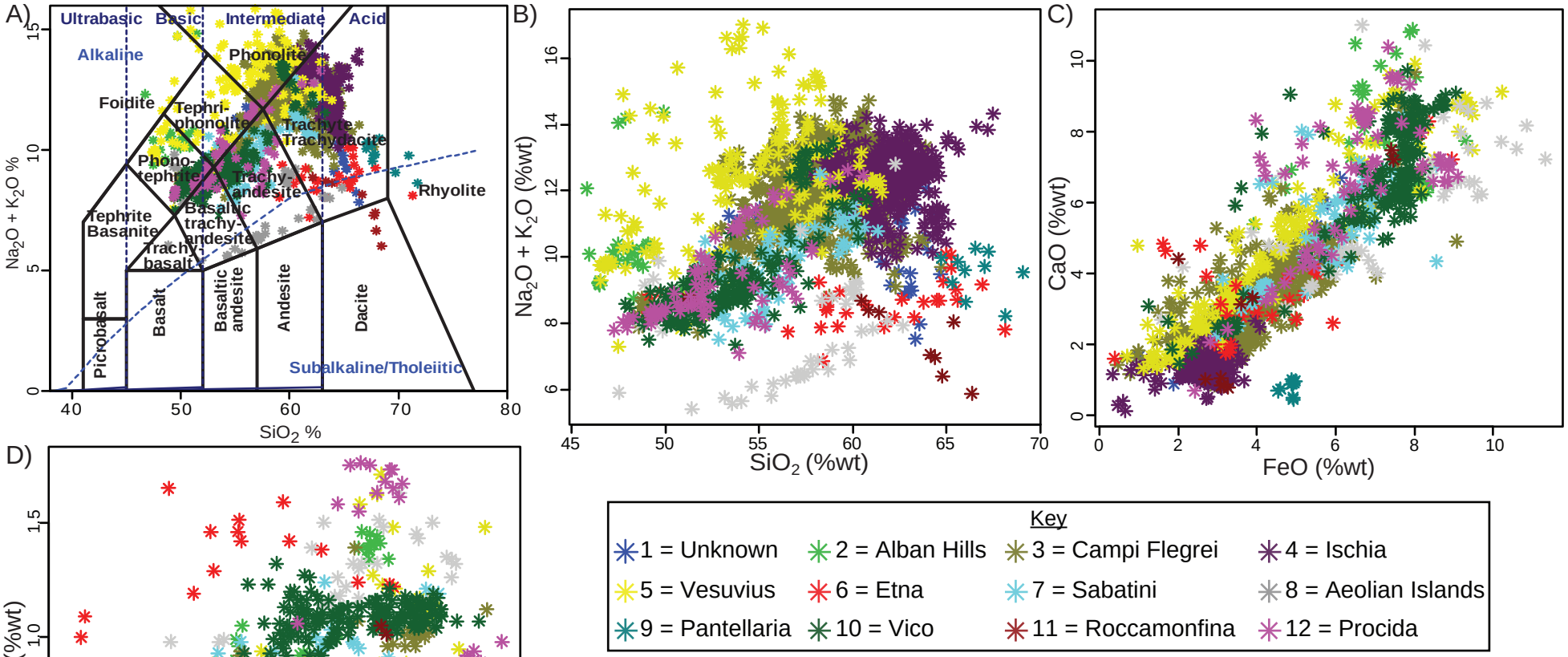

Figure 6.1: Biplots of LGdM major element data, grouped by volcanic system (assigned by Wulf *et al.,* 2004, 2008 and unpublished) A) Total Alkali vs. Silca (TAS) diagram for the whole LGdM dataset with divisions after Le Bas *et al.* (1986). B) TAS diagram scaled to fit data, no divisions. C) FeO vs. CaO. D) MgO vs TiO_2. In A) and B) the volcanic systems of Etna, the Aeolian Islands and Pantelleria (Subset A) can be discriminated from the remainder of the data. However Panterlleria can be discriminated from the other data in C) and only Etna layers can be discriminated from the other data in D). The Ischia data (major cluster B1) can also be discriminated from the other data in A), B) and D).

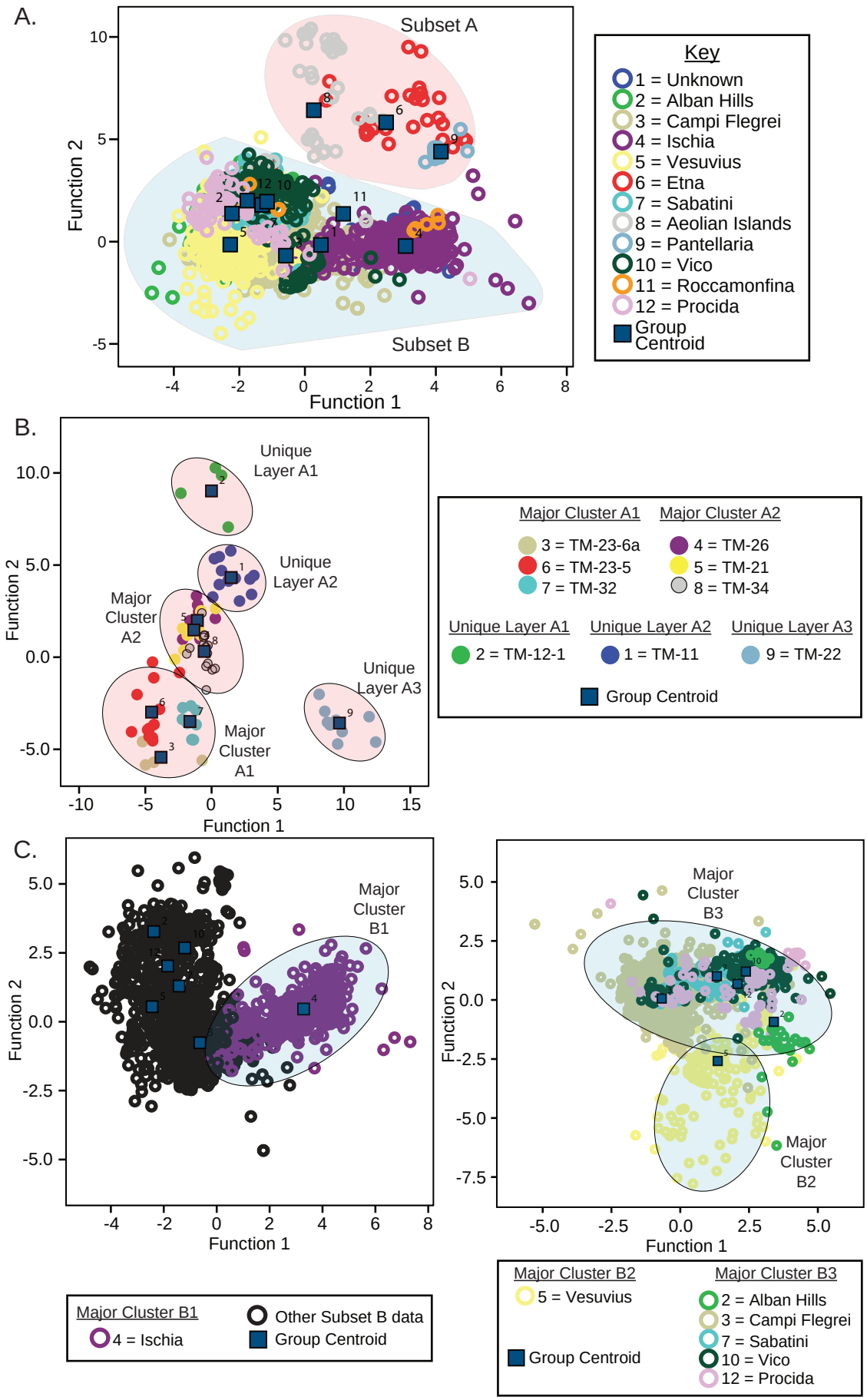

Figure 6.2: A) The first two canonical axes generated from the entire LdGM dataset, divided into 2 subsets. B) Subset A divided into 2 major clusters and 3 unique layers. C) Subset B divided into major clusters 1 - 3 (see text for full details). Envelopes are drawn around the clusters simply to aid with their visualisation.

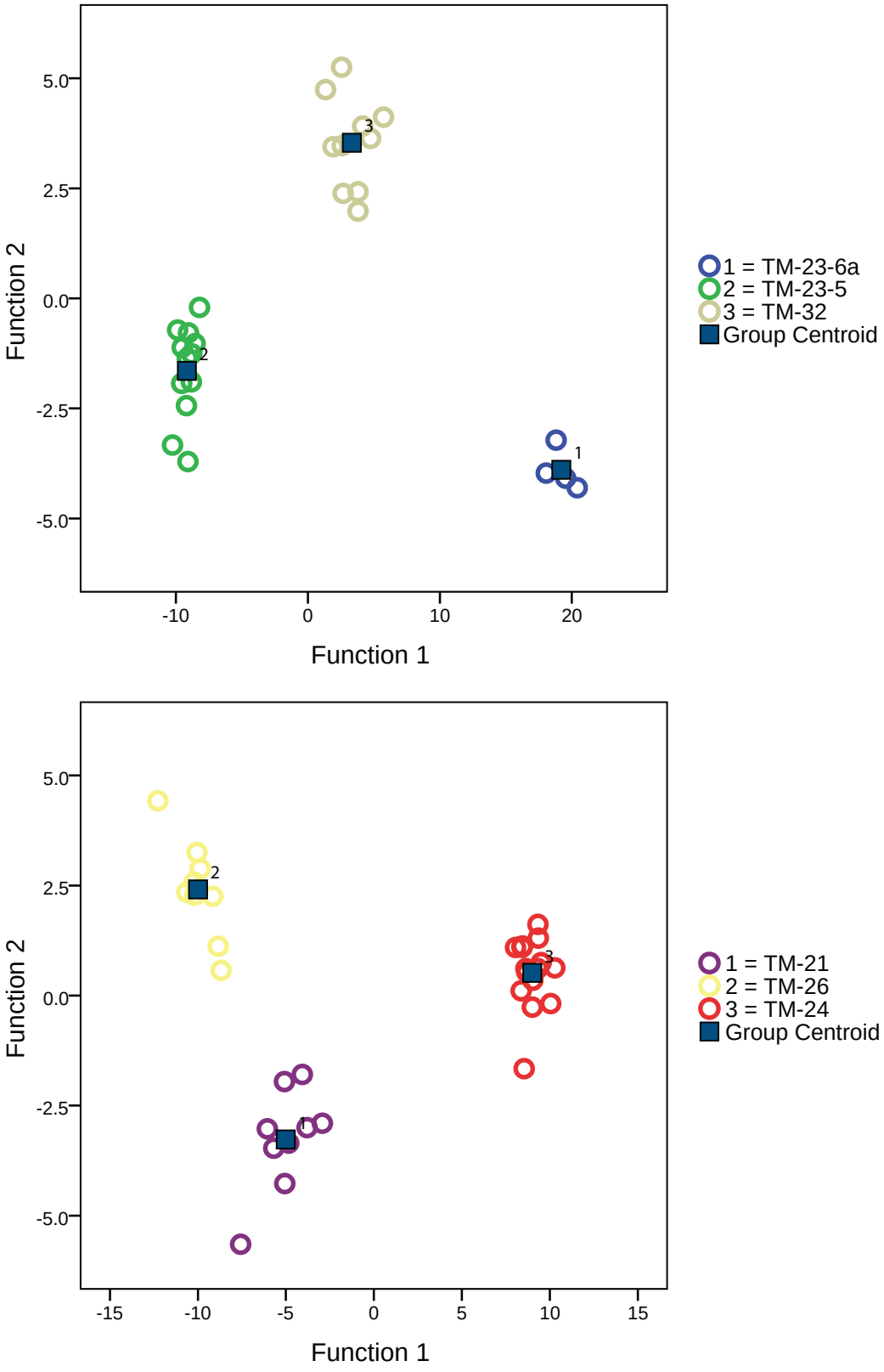

Figure 6.3: A) The first two canonical axes generated for Major Cluster A1 indicating that each of these 3 layers are unique. B) The first two canonical axes generated for Major Cluster A2 indicating that each of the layers in the cluster are unique.

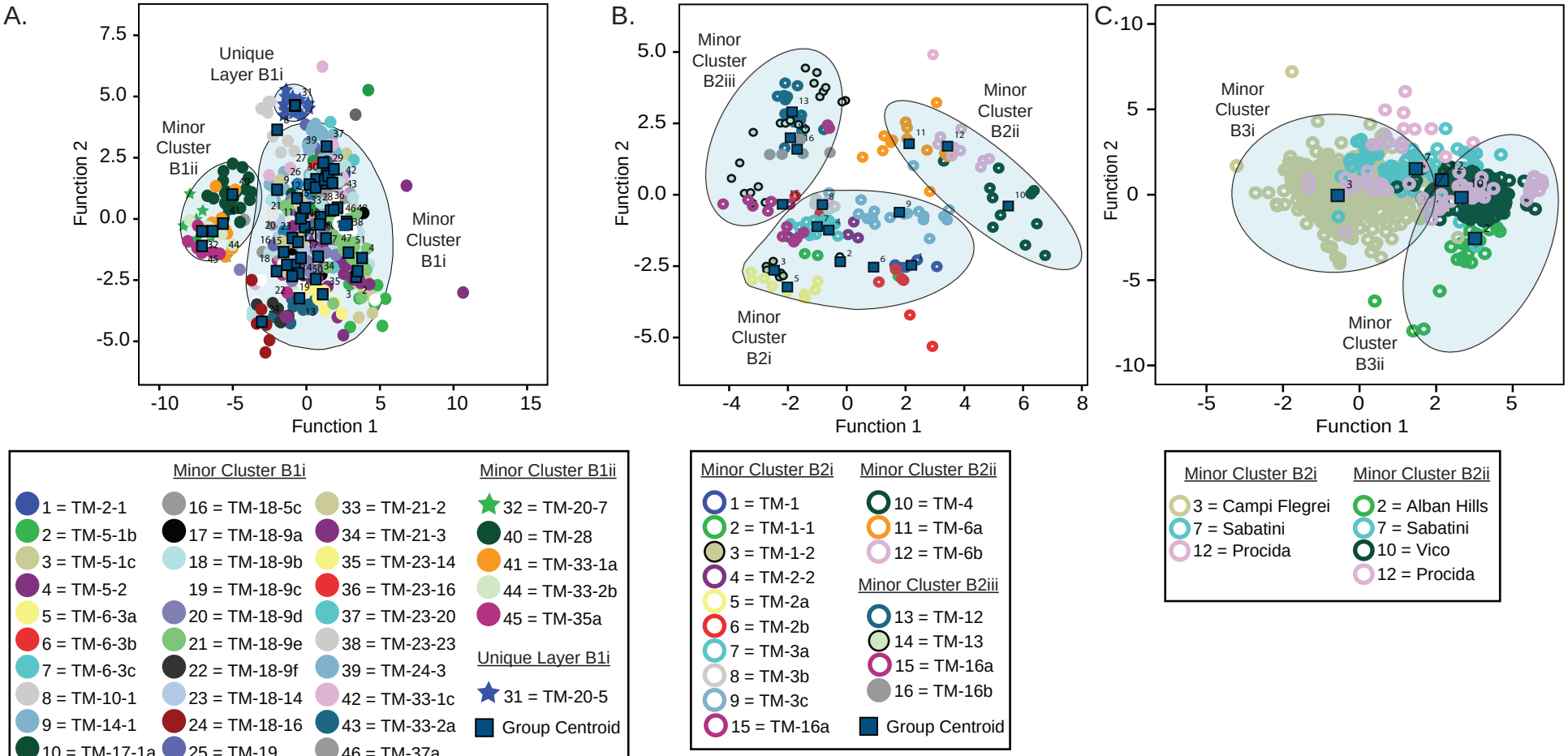

Figure 6.4: Plots of the 1st and 2nd canonical axes used to establish geochemical groupings in the LGdM dataset. A: Major cluster B1 with minor clusters B1i and B1ii highlighted. B: Major Cluster B2 with minor clusters B2i - B2iii highlighted and C: Major cluster B3 with minor clusters B3i and Bii highlighted. Envelopes are drawn around the clusters simply to aid with their visualisation.

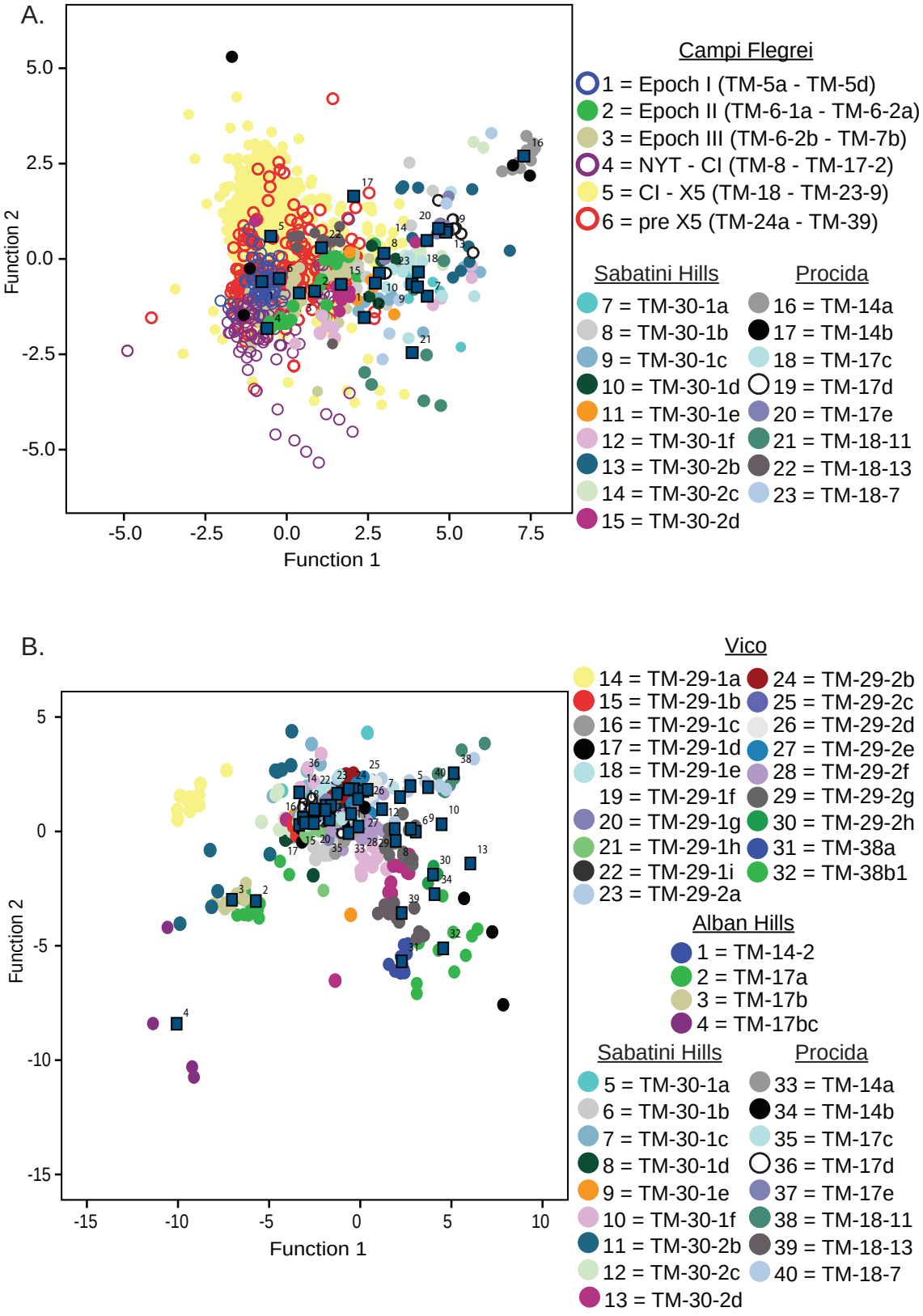

Figure 6.5: A) Minor Cluster B3i but due to the large number of layers from the Campi Flegrei, the data are presented as groups of layers from different time periods of Campi Flegrei activity. Epochs I, II and III as defined by de Vito *et al.,* 1999 and then layers between major eruptions, the Neapolitan Yellow Tuff, the Campanian Ignimbrite and the X5. B) Minor Cluster B3ii. Layers from the Sabatini Hills and Procida are represented in both A and B.

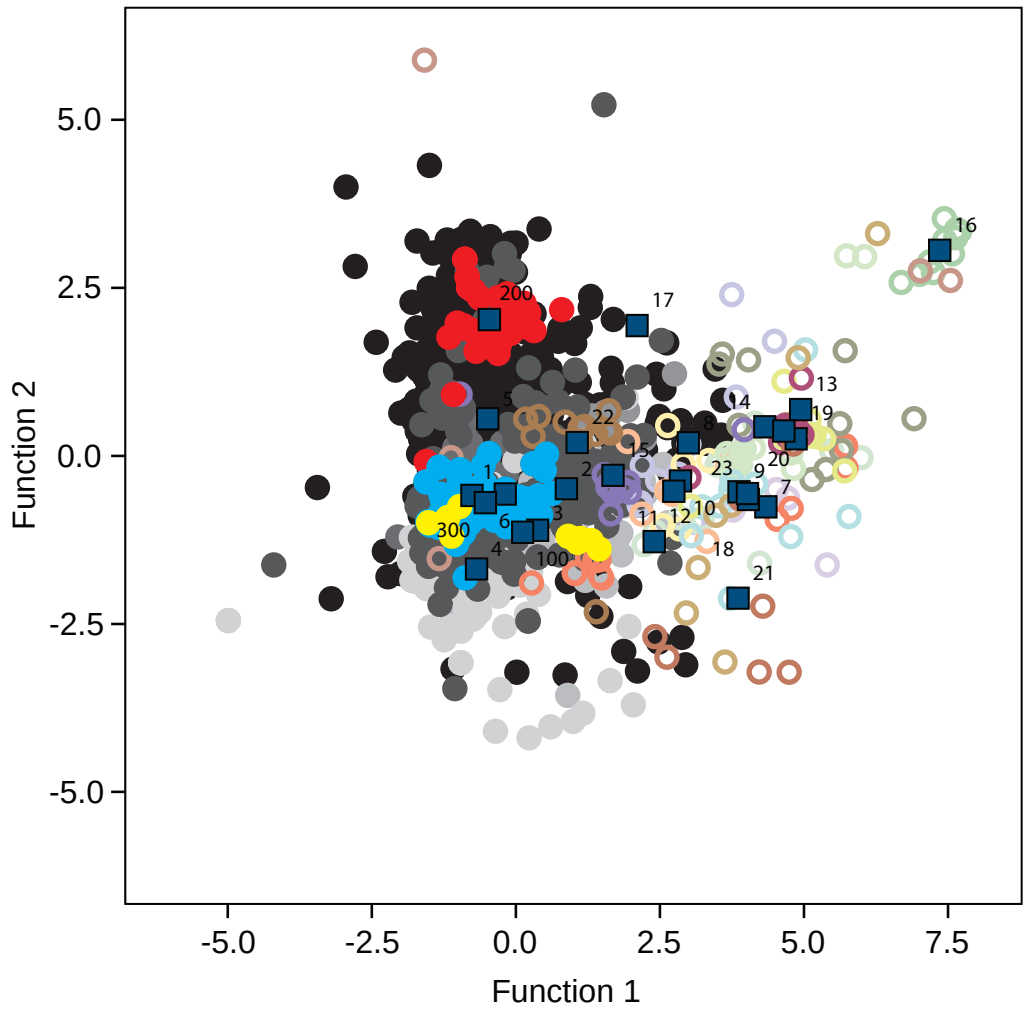

Campi Flegrei

1 = Epoch I (TM-5a - TM-5d)
2 = Epoch II (TM-6-1a - TM-6-2a)
3 = Epoch III (TM-6-2b - TM-7b)
4 = NYT - CI (TM-8 - TM-17-2)
5 = CI - X5 (TM-18 - TM-23-9)
6 = pre X5 (TM-24a - TM-39)
100 = TM-8
200 = TM-18
300 = TM-24a

Sabatini Hills

7 = TM-30-1a
8 = TM-30-1b
9 = TM-30-1c
10 = TM-30-1d
11 = TM-30-1e
12 = TM-30-1f
13 = TM-30-2b
14 = TM-30-2c
15 = TM-30-2d

Procida

16 = TM-14a
17 = TM-14b
18 = TM-17c
19 = TM-17d
20 = TM-17e
21 = TM-18-11
22 = TM-18-13
23 = TM-18-7

Figure 6.6: Minor Cluster B3i with specific Campi Flegrei layers highlighted. TM-8 (yellow), TM-18 (red) and TM-24a (blue) are all layers within the Lago Grande di Monticchio sequence which have been widely reported in other sequences in the Mediterranean region.

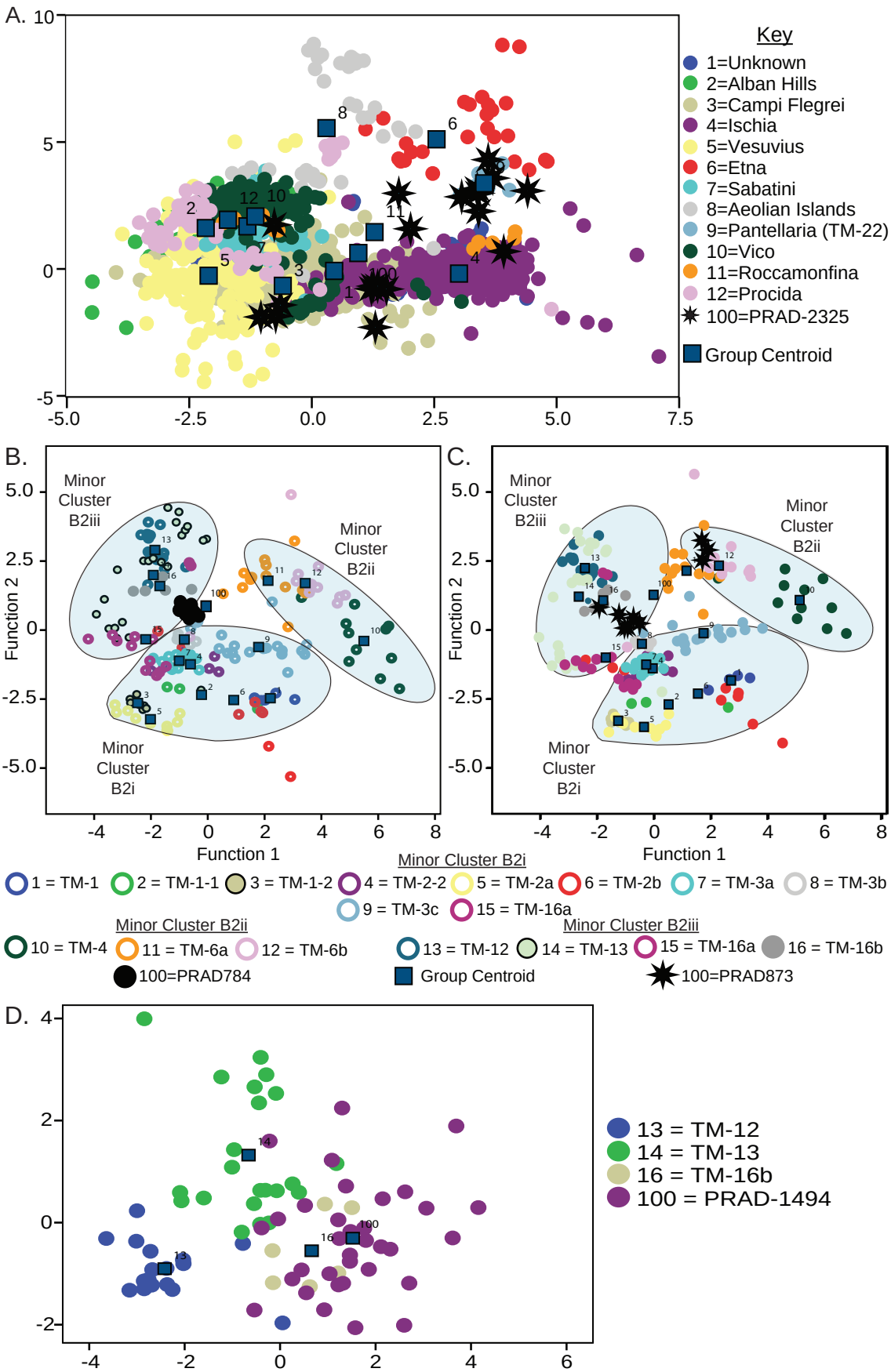

Figure 6.7: Plots of the 1st and 2nd canonical discriminant function axes. A) PRAD-2325 and the entire LGdM dataset, showing the grouping with TM-22 in Subset A. B) PRAD-784 and major cluster B2, showing grouping with minor cluster B2iii. C) PRAD-873 and major cluster B2, showing grouping with minor cluster B2iii. D) PRAD-1494 and minor cluster B2iii, showing grouping with TM-16b. Envelopes are drawn around the clusters simply to aid with their visualisation.

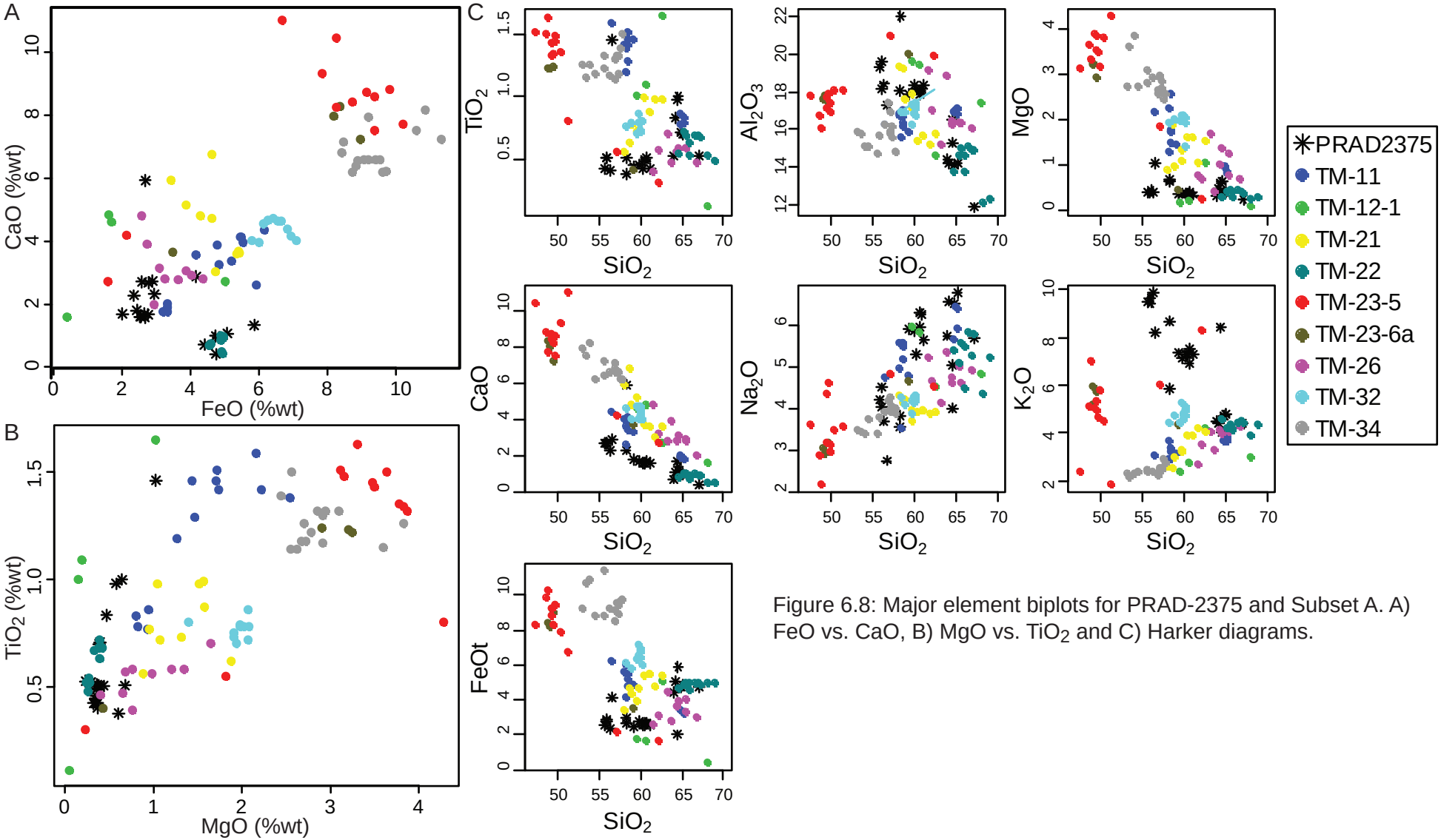

Figure 6.8: Major element biplots for PRAD-2375 and Subset A. A) FeO vs. CaO, B) MgO vs. TiO_2 and C) Harker diagrams.

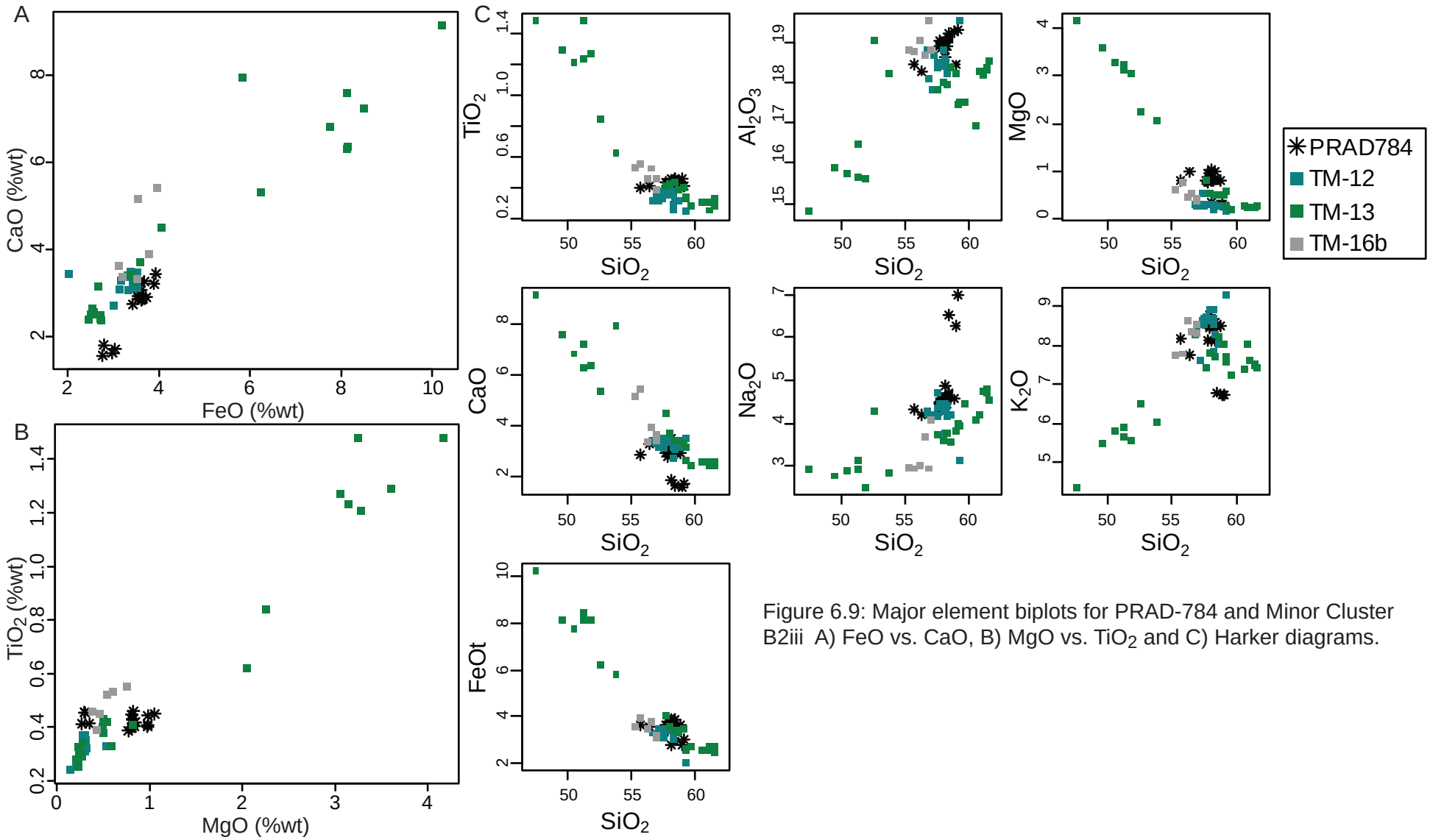

Figure 6.9: Major element biplots for PRAD-784 and Minor Cluster B2iii A) FeO vs. CaO, B) MgO vs. TiO_2 and C) Harker diagrams.

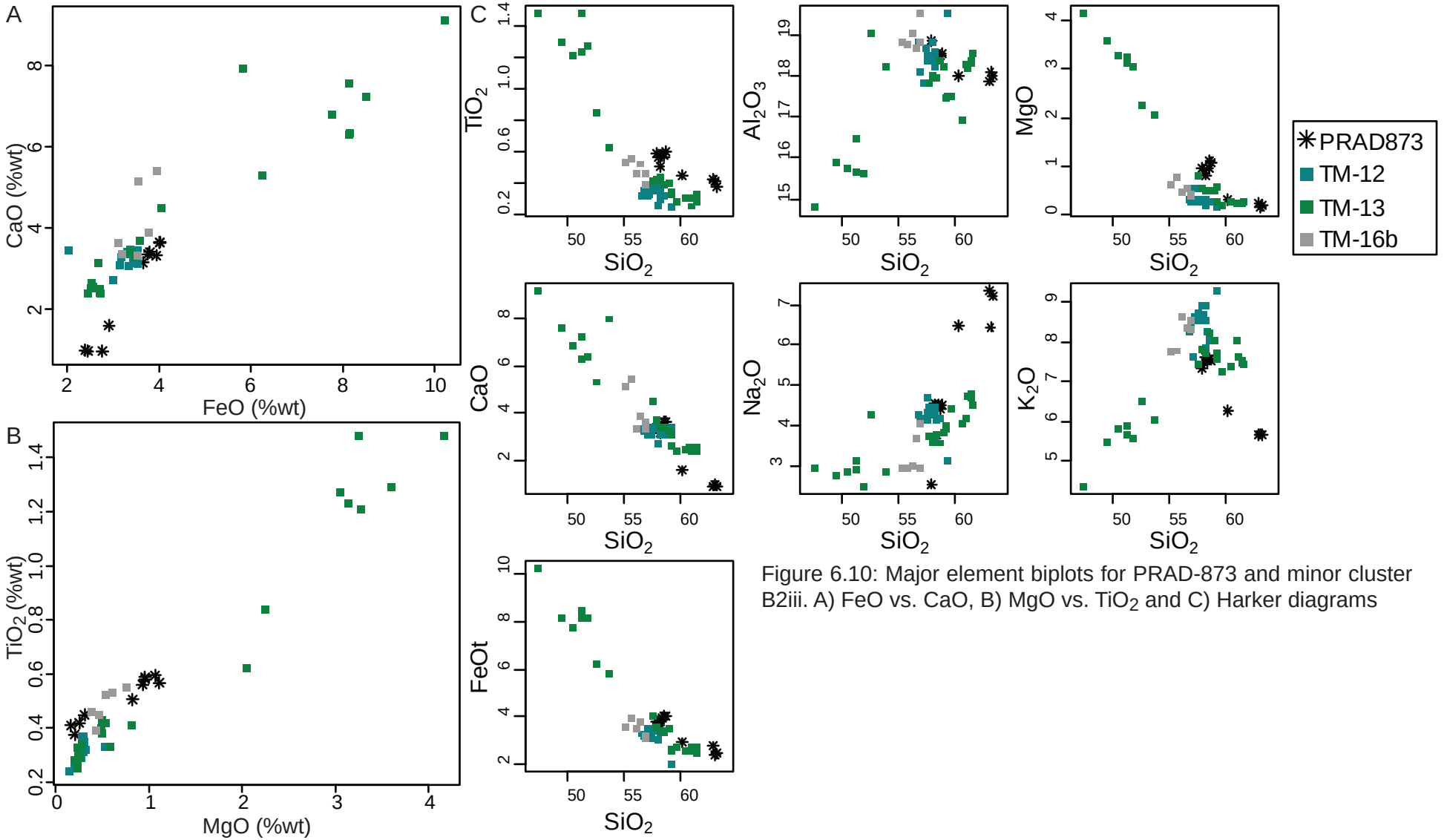

Figure 6.10: Major element biplots for PRAD-873 and minor cluster B2iii. A) FeO vs. CaO, B) MgO vs. TiO_2 and C) Harker diagrams

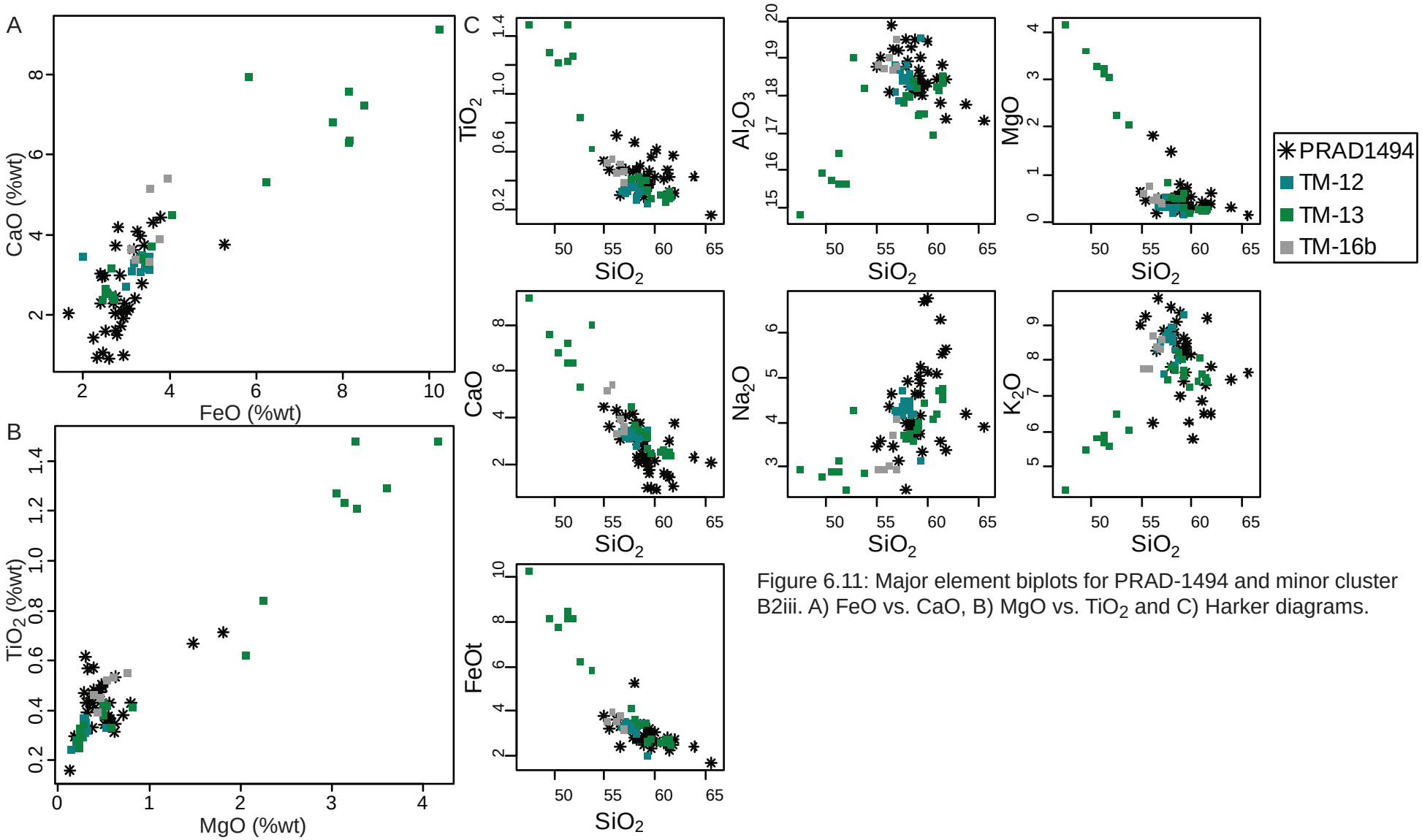

Figure 6.11: Major element biplots for PRAD-1494 and minor cluster B2iii. A) FeO vs. CaO, B) MgO vs. TiO_2 and C) Harker diagrams.

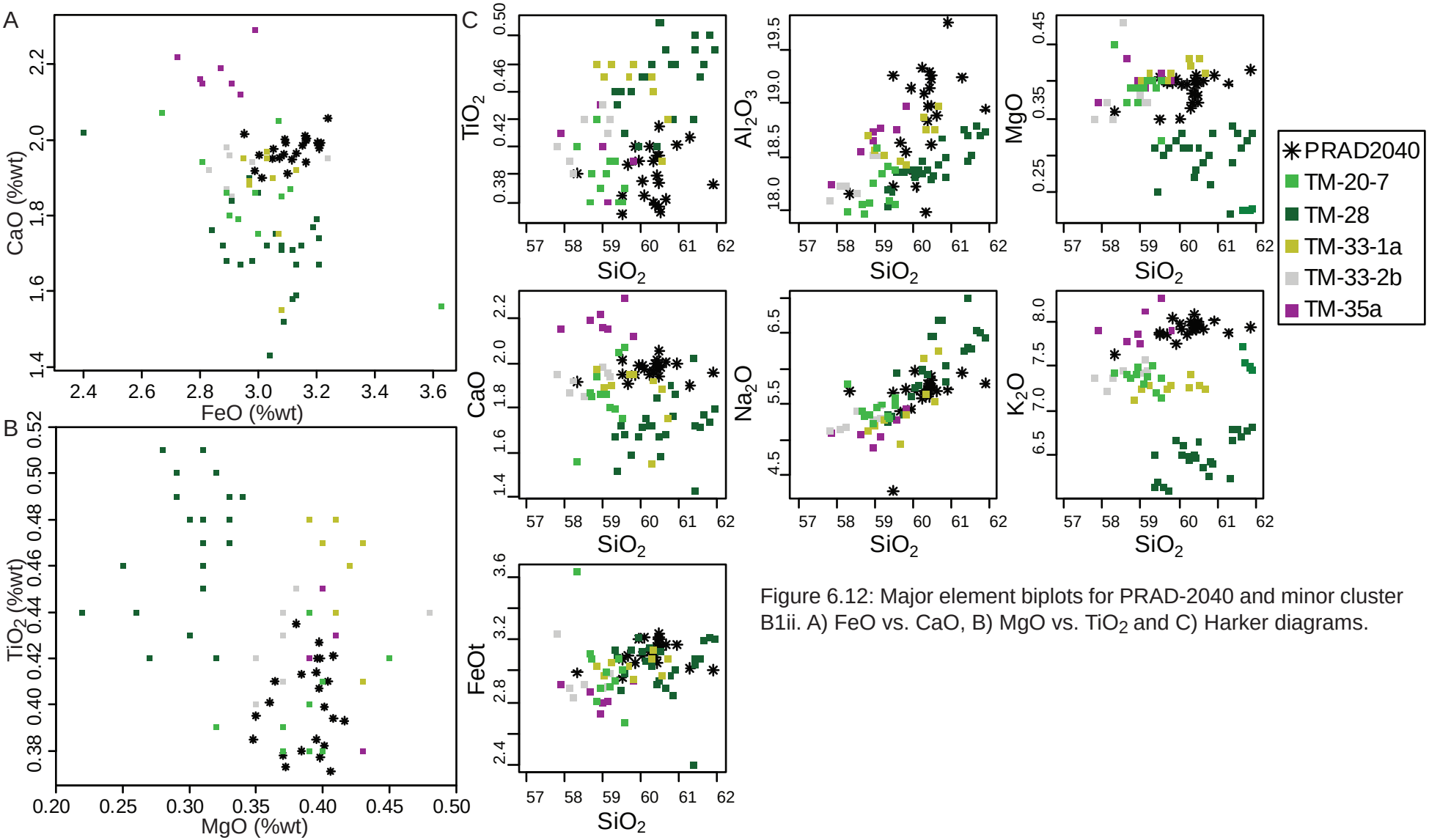

Figure 6.12: Major element biplots for PRAD-2040 and minor cluster B1ii. A) FeO vs. CaO, B) MgO vs. TiO_2 and C) Harker diagrams.

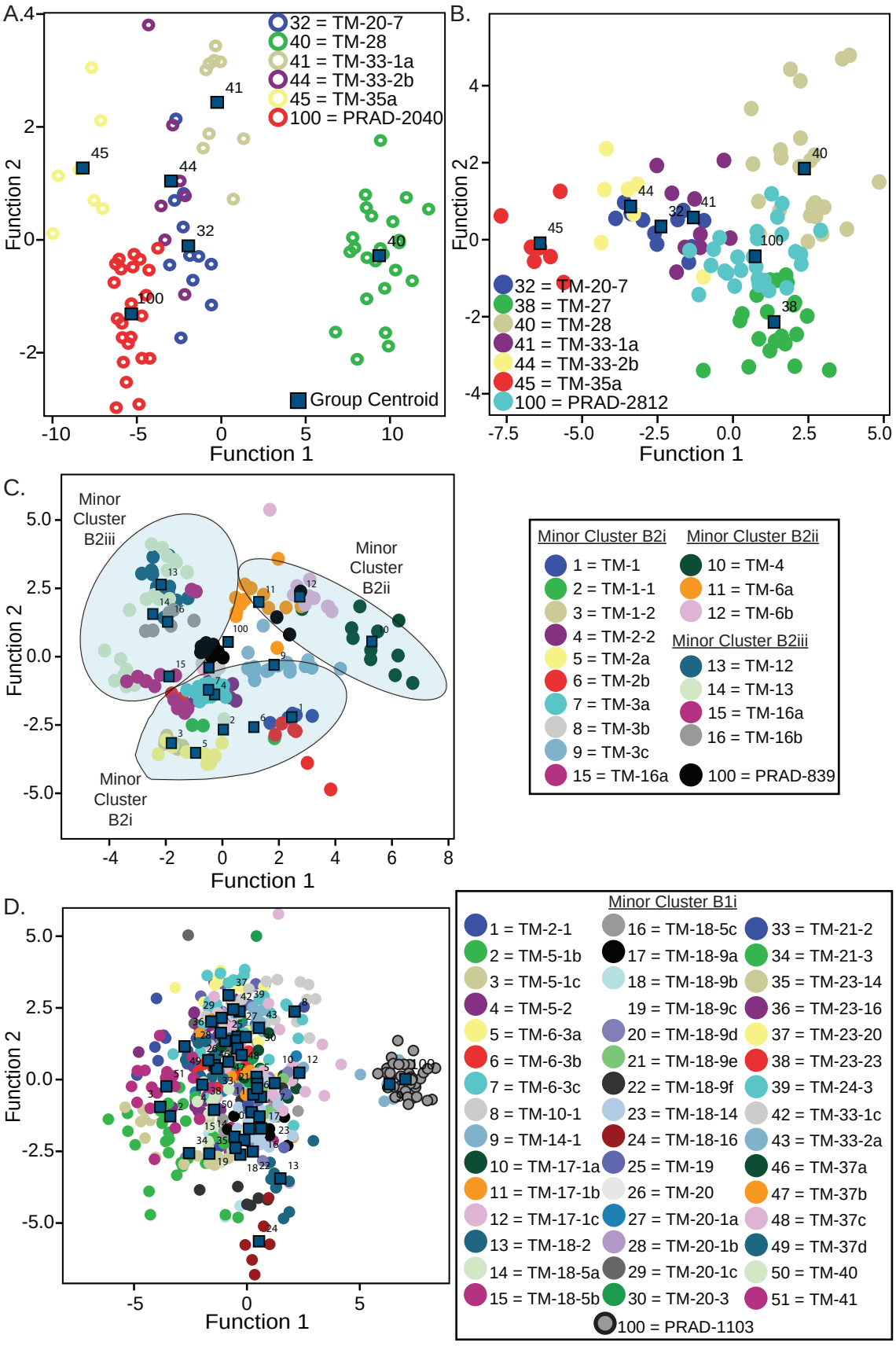

Figure 6.13: Plots of the 1st and 2nd canonical discriminant function axes. A) PRAD-2040 and minor cluster B1ii, showing grouping with TM-20-7. B) PRAD-2812 and minor cluster B1ii, showing grouping with TM-27. C) PRAD-839 and major cluster B2, showing grouping with minor cluster B2iii. D) PRAD-1103 and minor cluster B1i, showing grouping with TM-14-1. Envelopes are drawn around the clusters simply to aid with their visualisation.

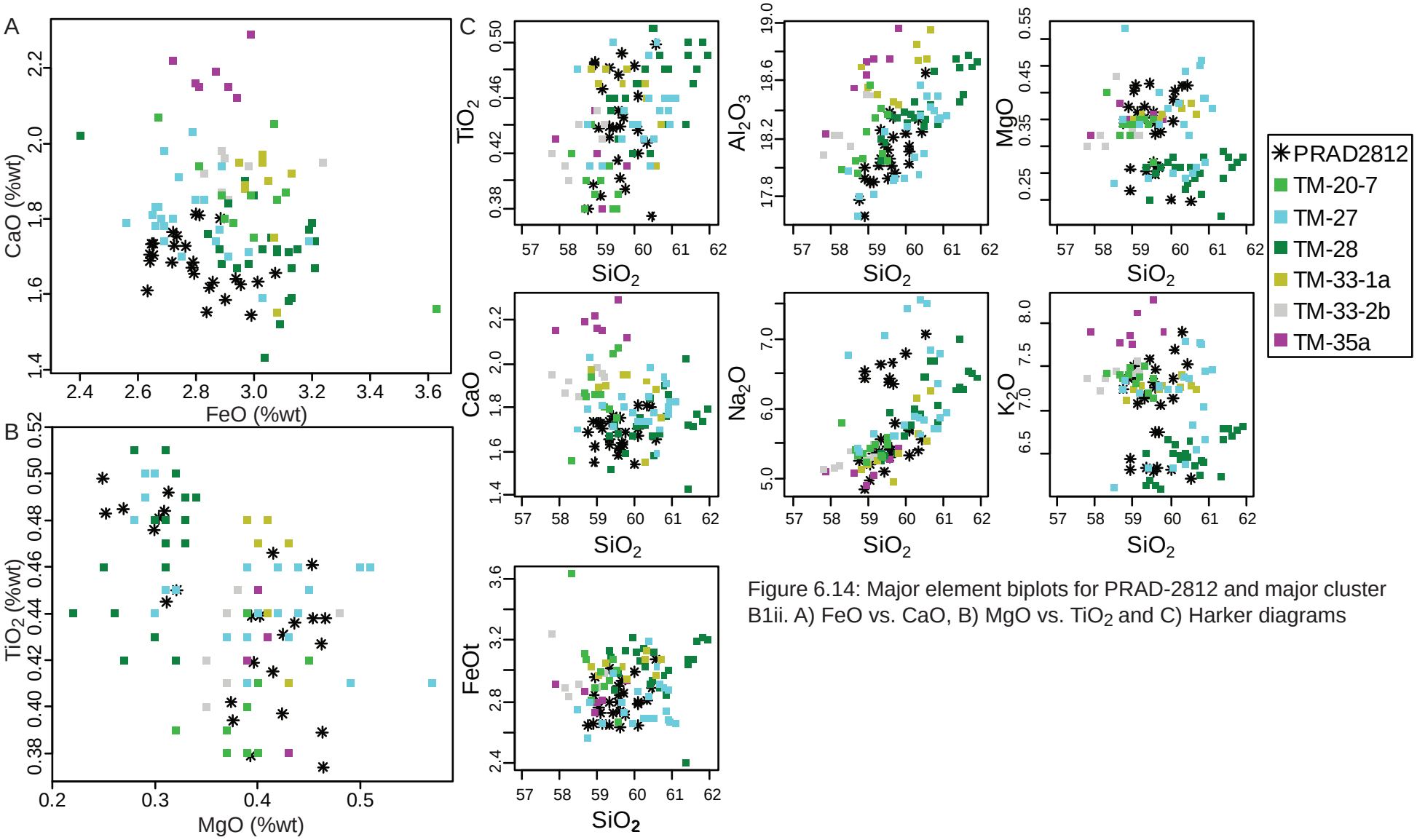

Figure 6.14: Major element biplots for PRAD-2812 and major cluster B1ii. A) FeO vs. CaO, B) MgO vs. TiO_2 and C) Harker diagrams

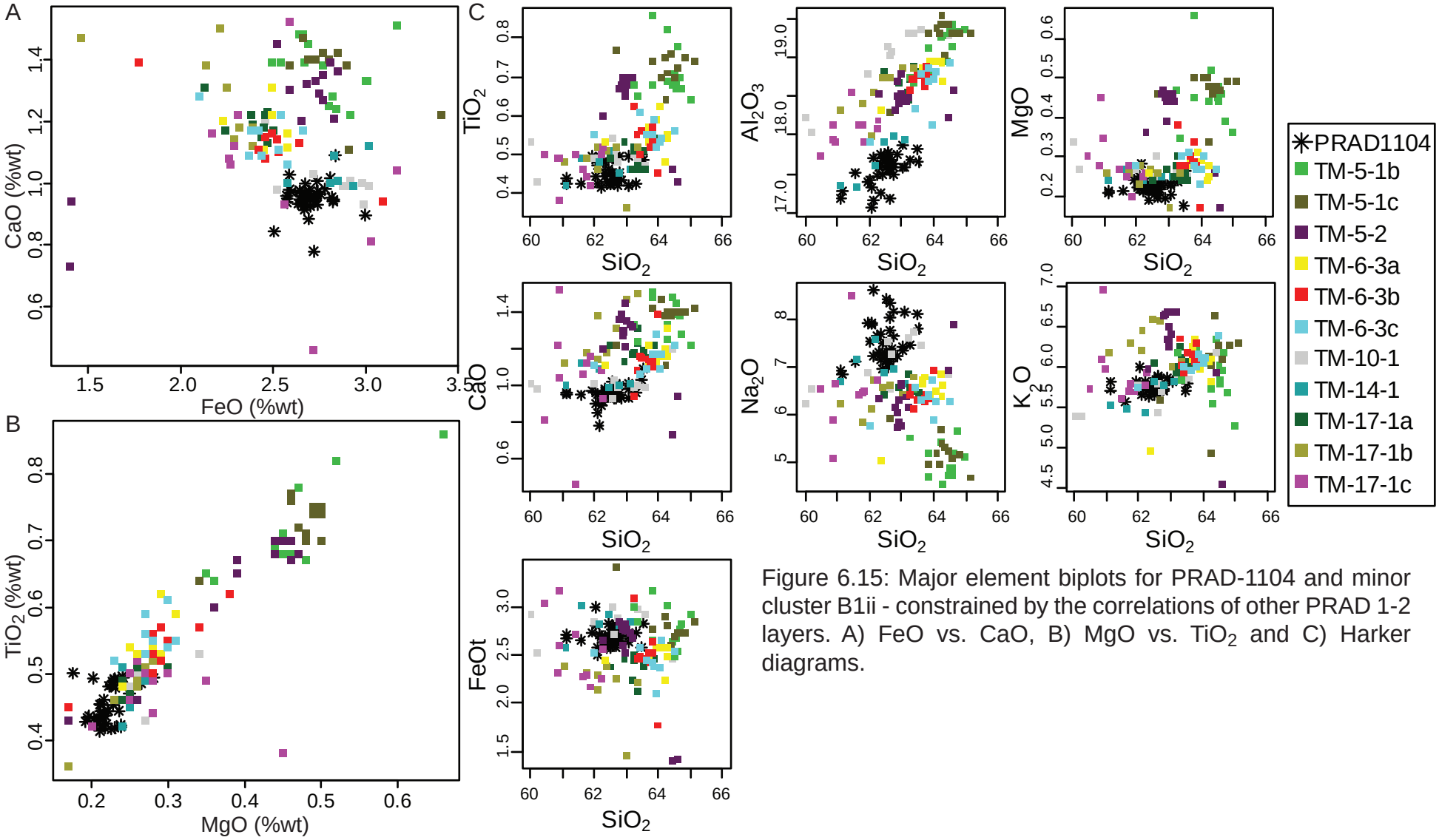

Figure 6.15: Major element biplots for PRAD-1104 and minor cluster B1ii - constrained by the correlations of other PRAD 1-2 layers. A) FeO vs. CaO, B) MgO vs. TiO_2 and C) Harker diagrams.

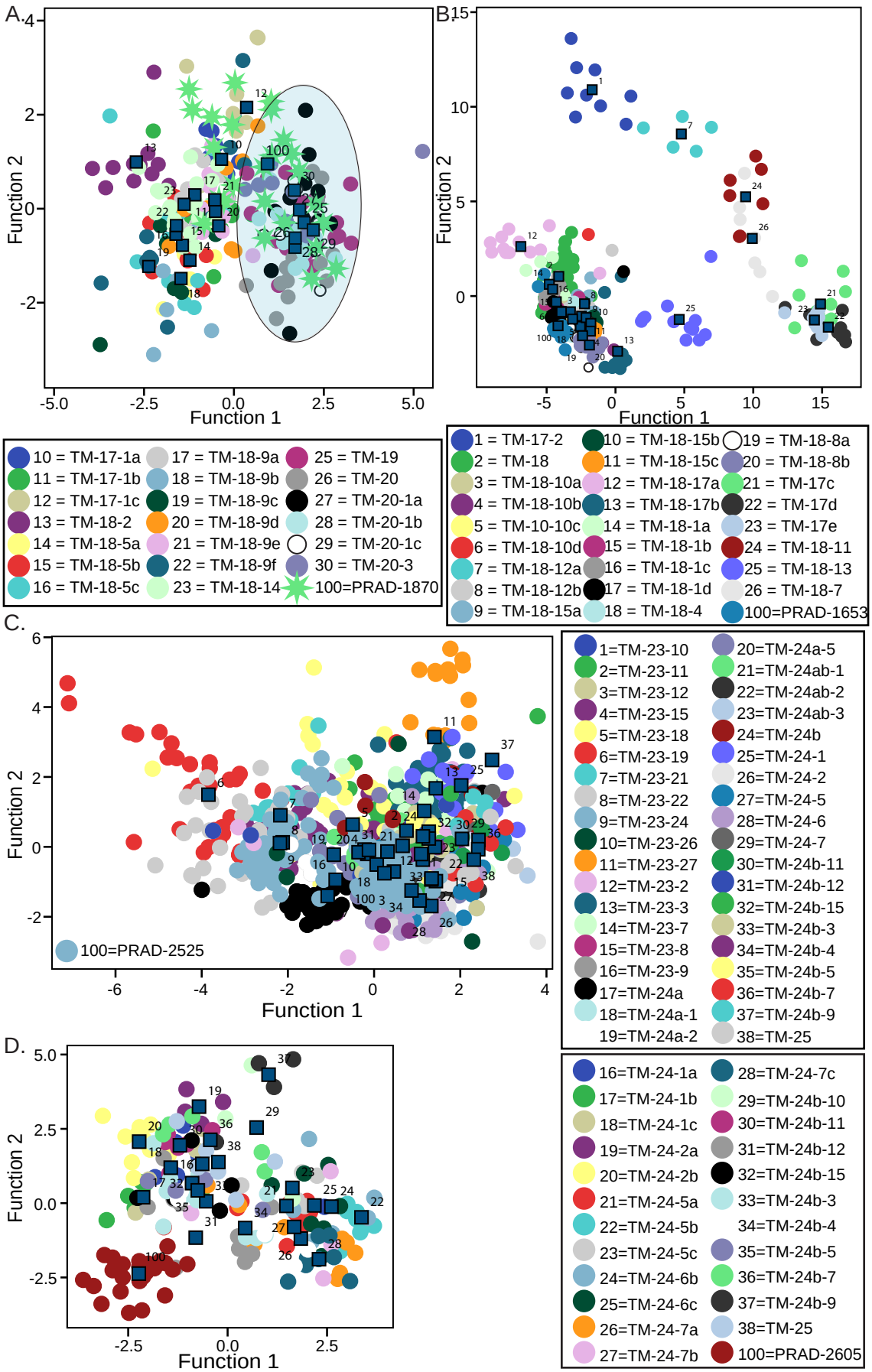

Figure 6.16: Plots of the 1st and 2nd canonical discriminant function axes. A) PRAD-1870 and minor cluster B1i, showing the grouping with TM-19, TM-20 and TM-20-1 (shaded section). B) PRAD-1653 and minor cluster B3i. C) PRAD-2525 and minor cluster B3i. D) PRAD-2605 and minor cluster B3i. Envelopes are drawn around the clusters simply to aid with their visualisation.

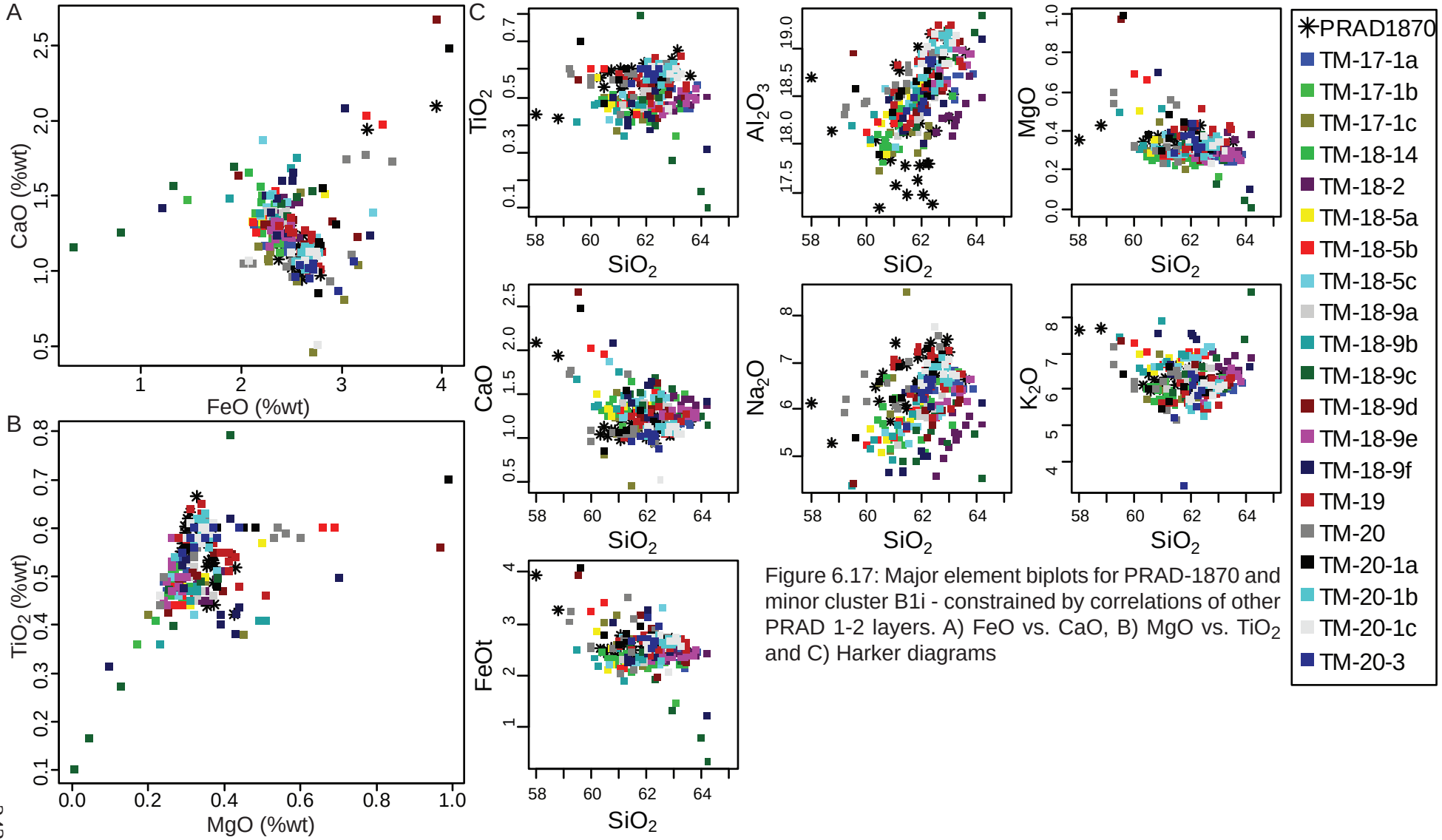

Figure 6.17: Major element biplots for PRAD-1870 and minor cluster B1i - constrained by correlations of other PRAD 1-2 layers. A) FeO vs. CaO, B) MgO vs. TiO_2 and C) Harker diagrams

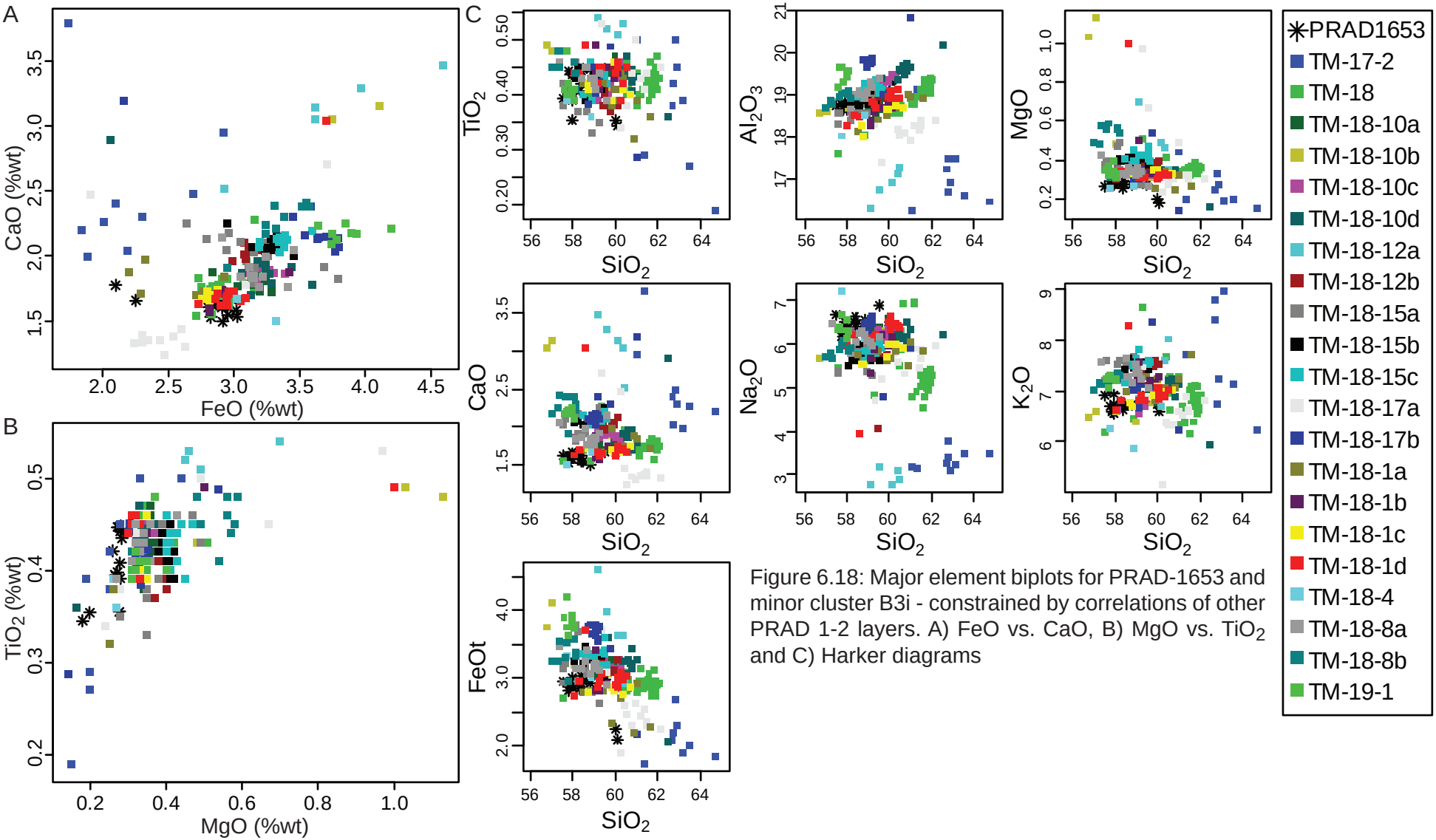

Figure 6.18: Major element biplots for PRAD-1653 and minor cluster B3i - constrained by correlations of other PRAD 1-2 layers. A) FeO vs. CaO, B) MgO vs. TiO_2 and C) Harker diagrams

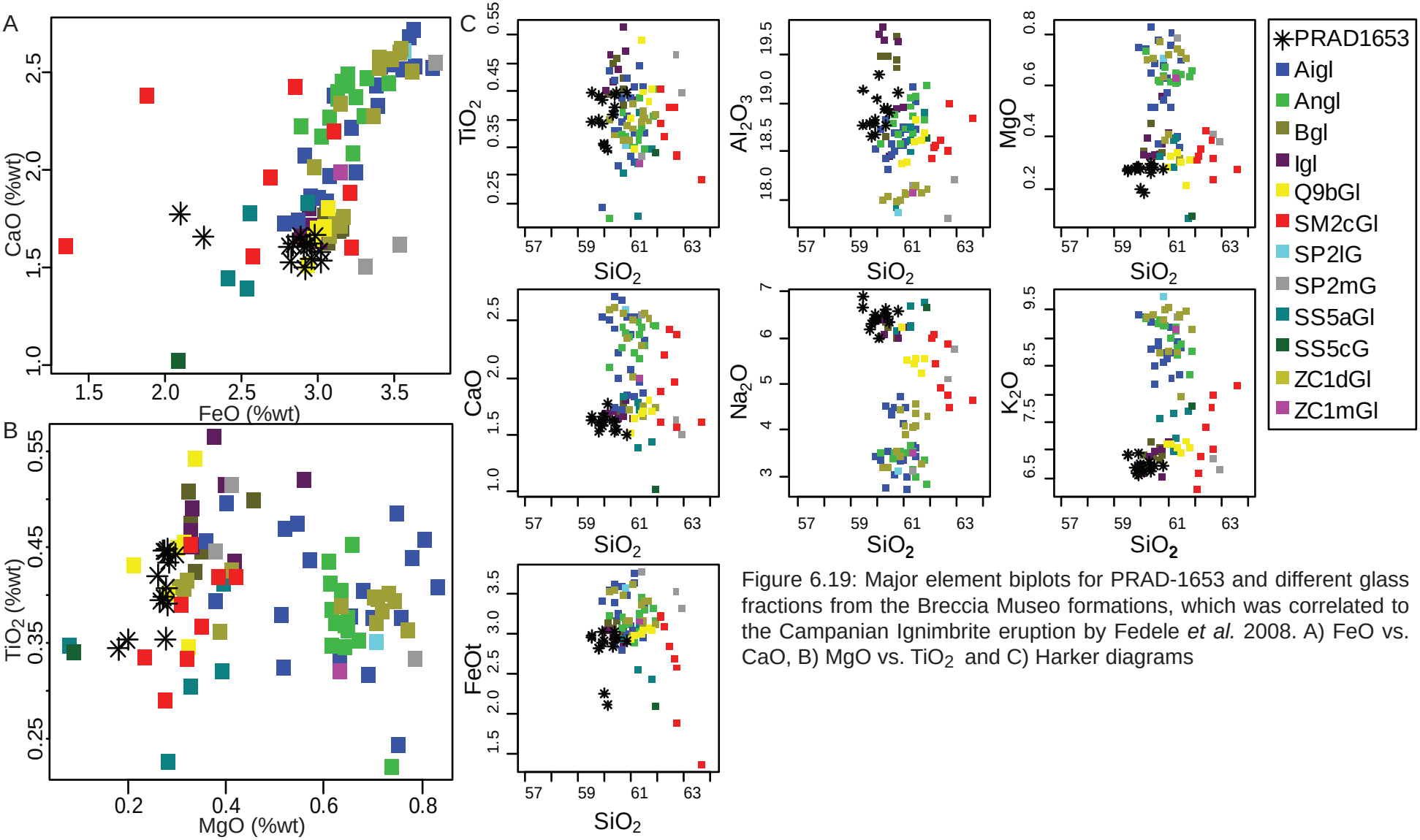

Figure 6.19: Major element biplots for PRAD-1653 and different glass fractions from the Breccia Museo formations, which was correlated to the Campanian Ignimbrite eruption by Fedele *et al.* 2008. A) FeO vs. CaO, B) MgO vs. TiO_2 and C) Harker diagrams

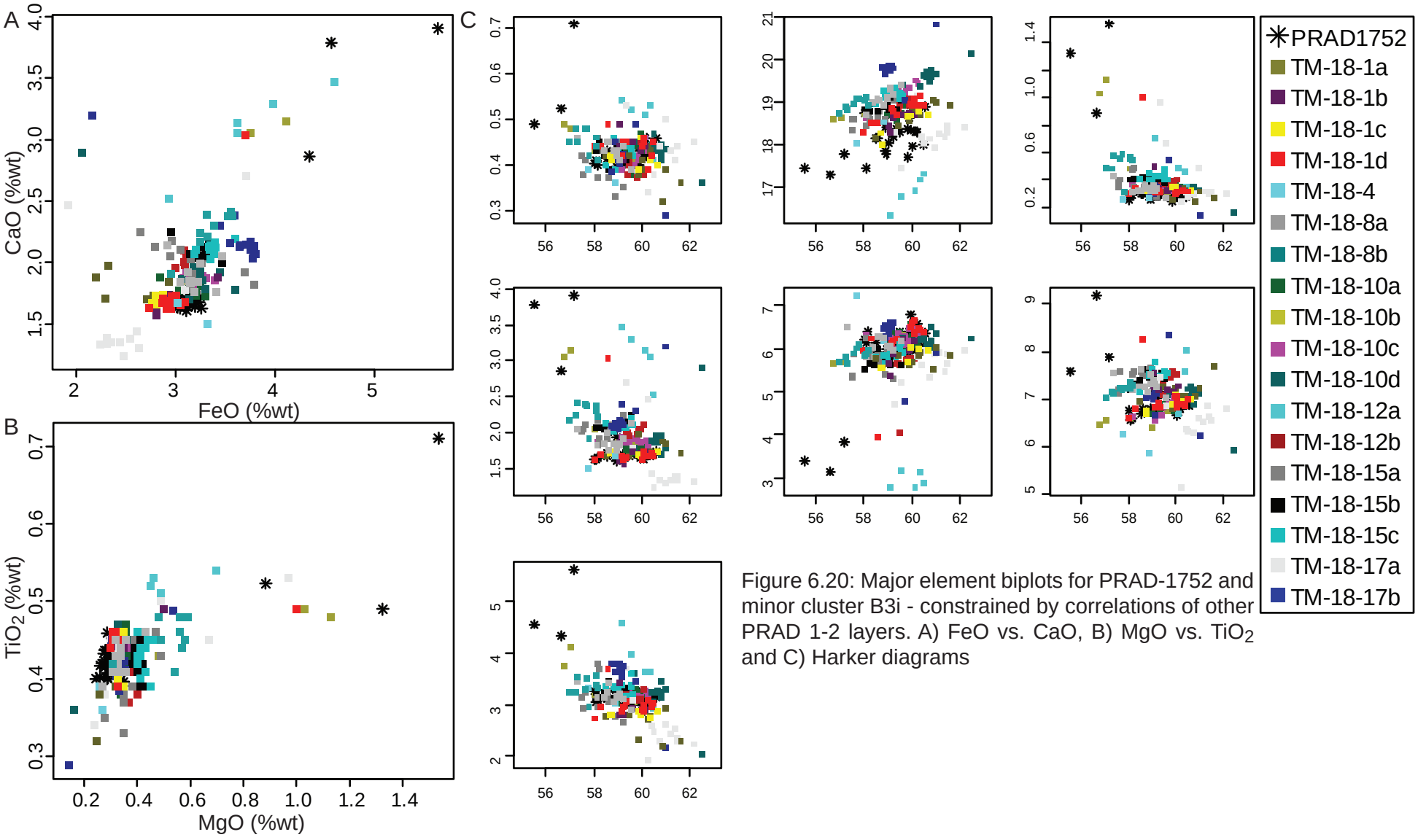

Figure 6.20: Major element biplots for PRAD-1752 and minor cluster B3i - constrained by correlations of other PRAD 1-2 layers. A) FeO vs. CaO, B) MgO vs. TiO_2 and C) Harker diagrams

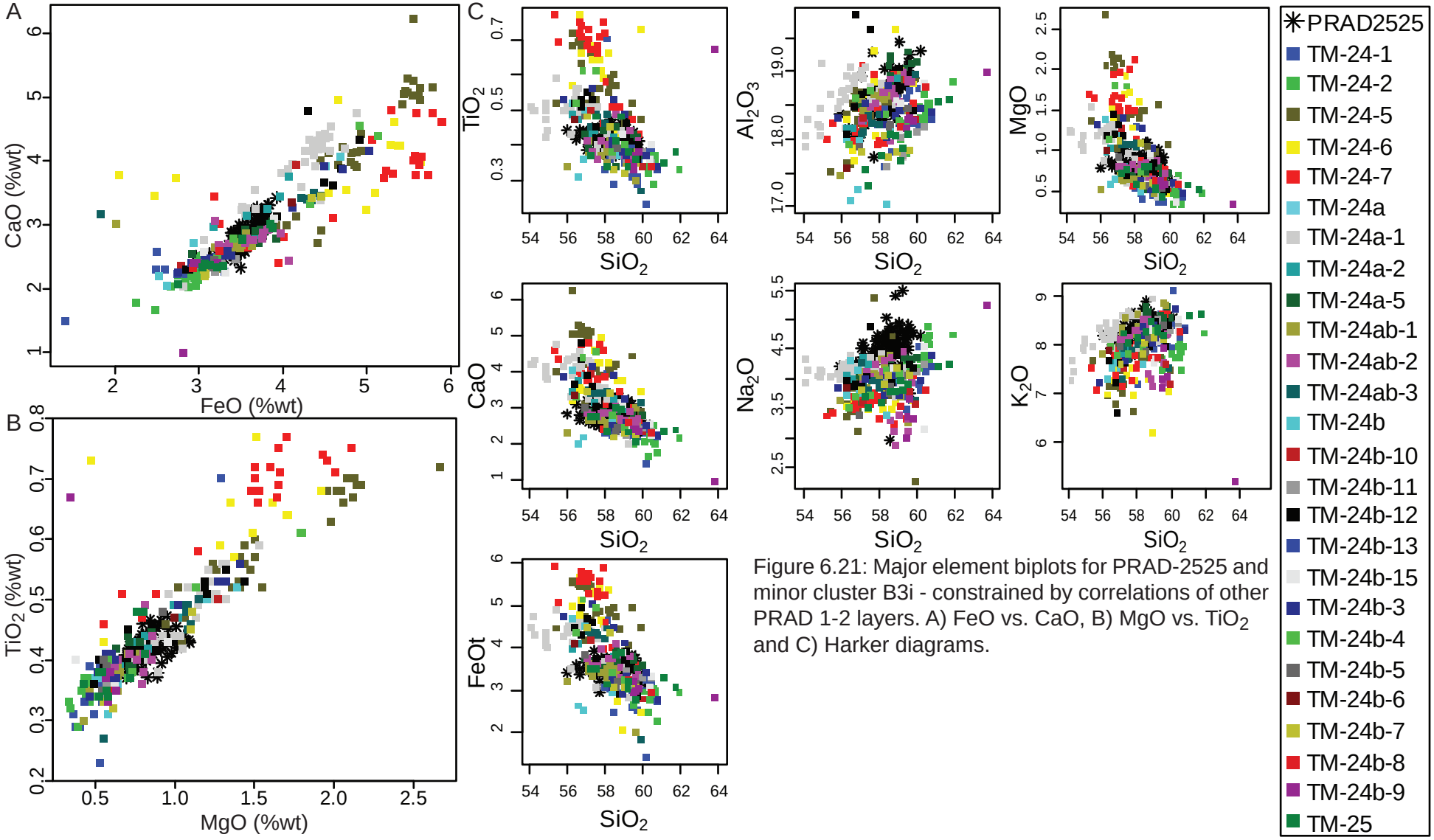

Figure 6.21: Major element biplots for PRAD-2525 and minor cluster B3i - constrained by correlations of other PRAD 1-2 layers. A) FeO vs. CaO, B) MgO vs. TiO_2 and C) Harker diagrams.

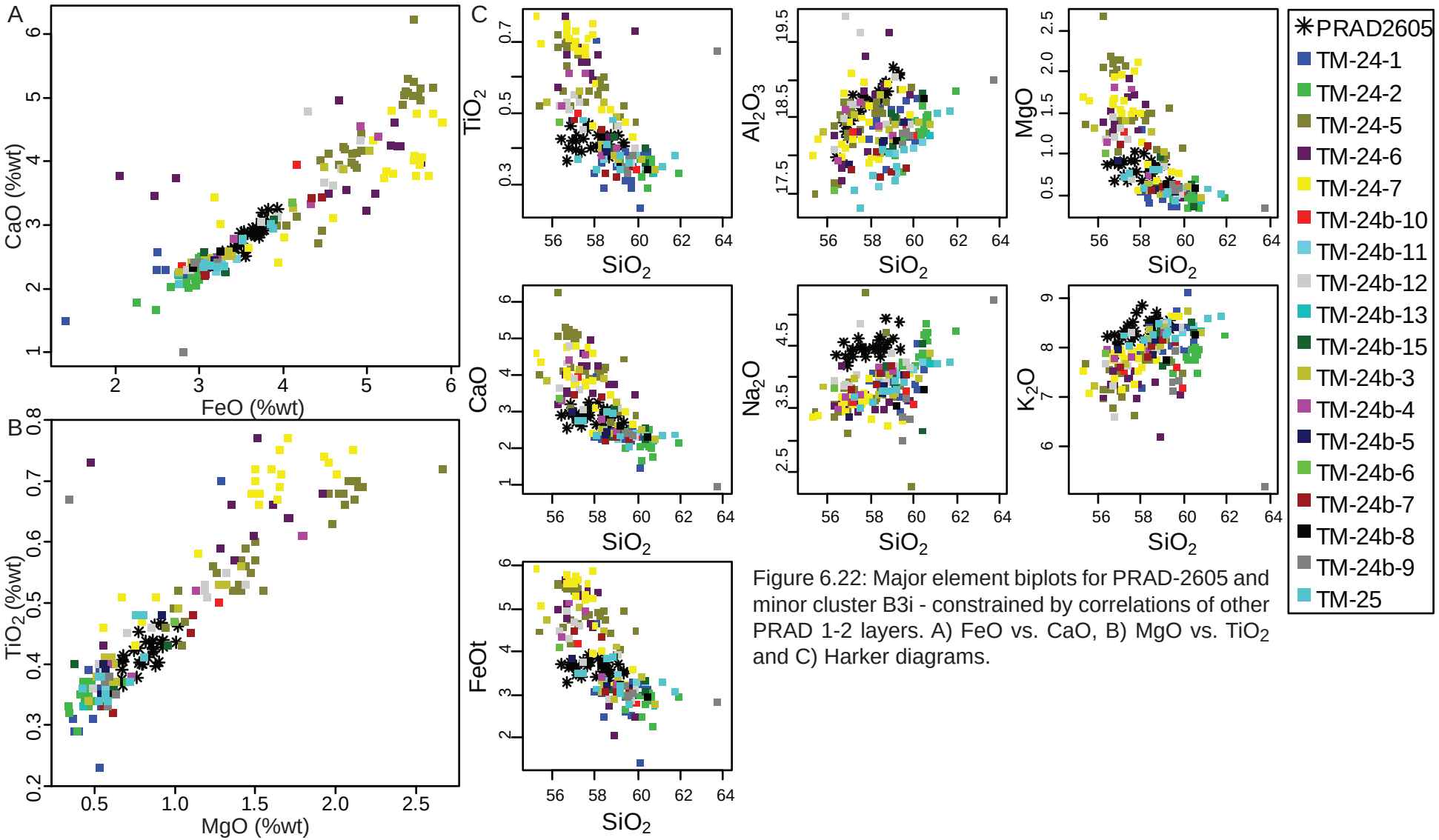

Figure 6.22: Major element biplots for PRAD-2605 and minor cluster B3i - constrained by correlations of other PRAD 1-2 layers. A) FeO vs. CaO, B) MgO vs. TiO_2 and C) Harker diagrams.

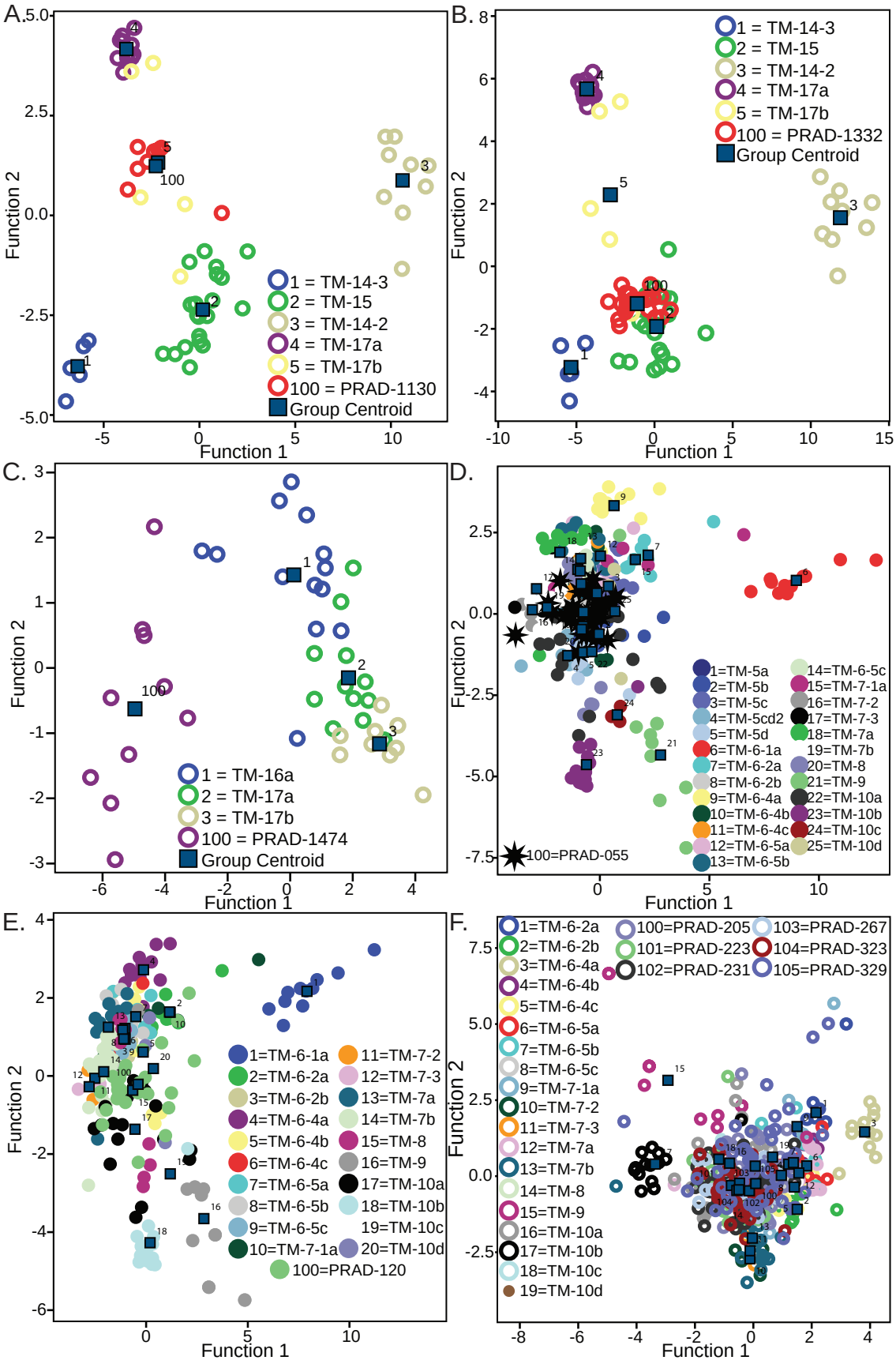

Figure 6.23: Plots of the 1st and 2nd canonical discriminant function axes. A) PRAD-1130 & minor cluster B3i. B) PRAD-1332 & minor cluster B3i, showing grouping with TM-15. C) PRAD-1474 & only stratigraphically possible layers. D) PRAD-055 & minor cluster B3i. E) PRAD-120 & minor cluster B3i. F) PRAD-205, PRAD-223, PRAD-231, PRAD-267, PRAD-323, PRAD-329 & minor cluster B3i. The minor clusters have been constrained based upon correlations of other PRAD 1-2 layers to the LGdM data-set.

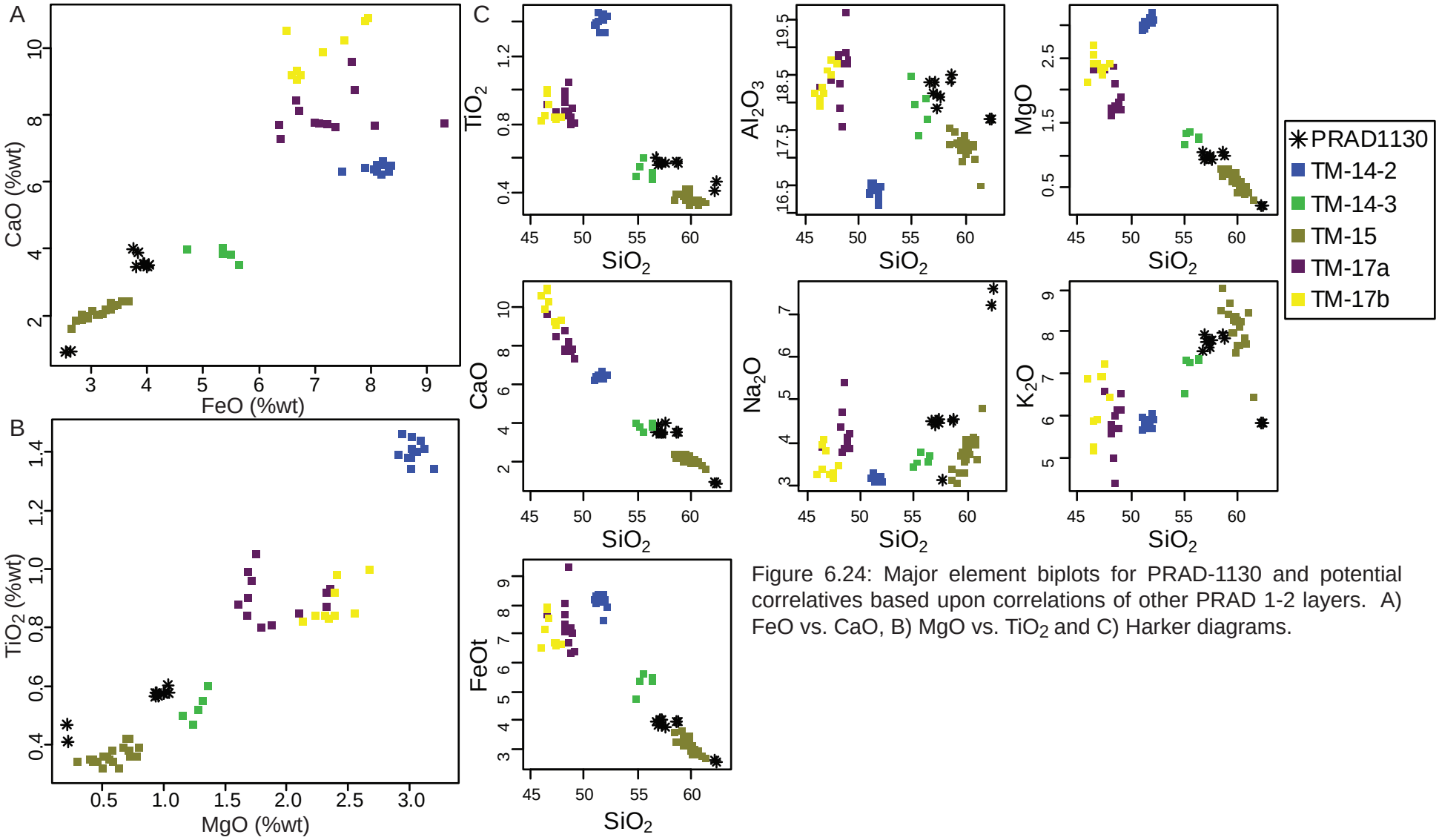

Figure 6.24: Major element biplots for PRAD-1130 and potential correlatives based upon correlations of other PRAD 1-2 layers. A) FeO vs. CaO, B) MgO vs. TiO_2 and C) Harker diagrams.

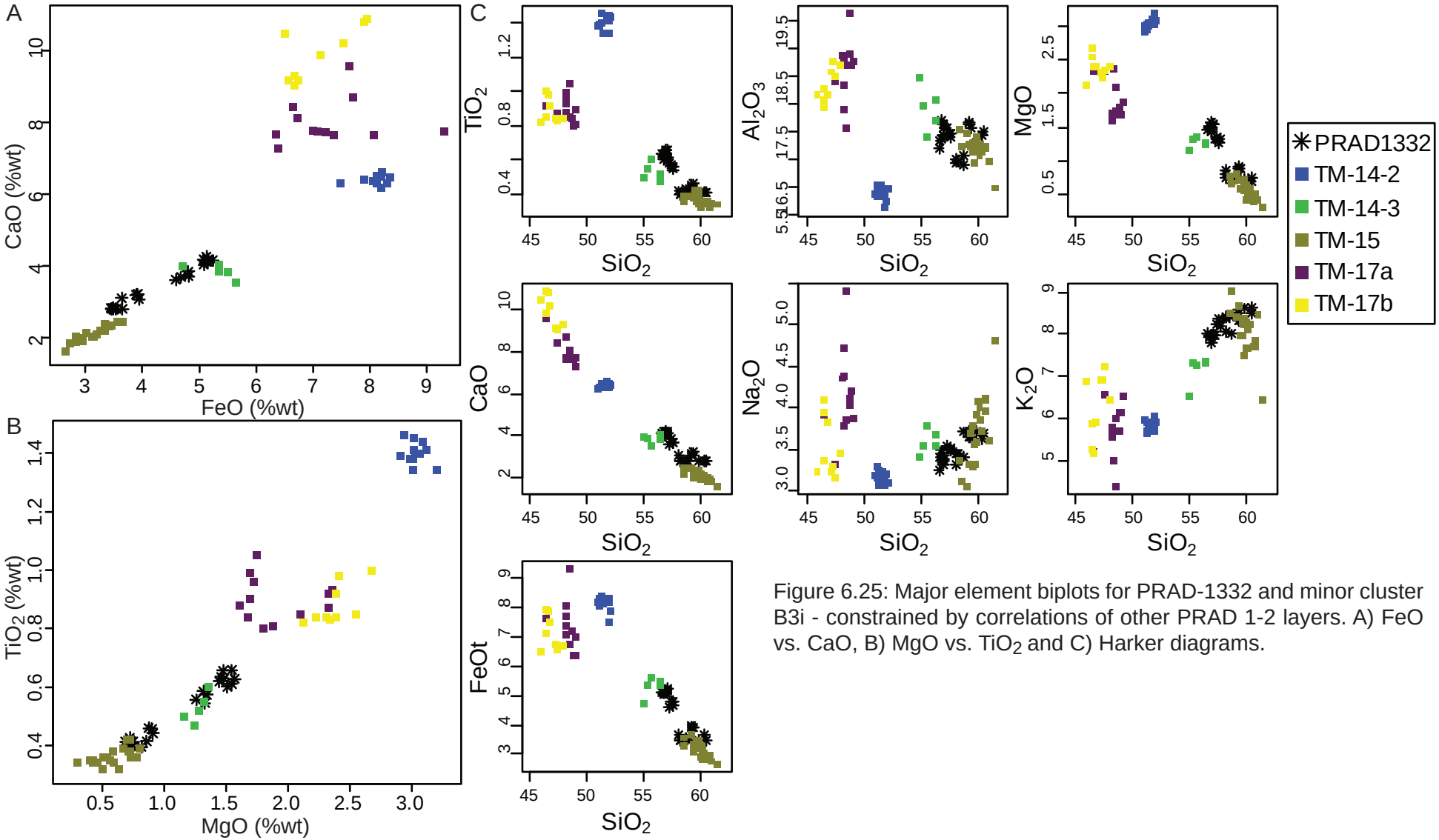

Figure 6.25: Major element biplots for PRAD-1332 and minor cluster B3i - constrained by correlations of other PRAD 1-2 layers. A) FeO vs. CaO, B) MgO vs. TiO_2 and C) Harker diagrams.

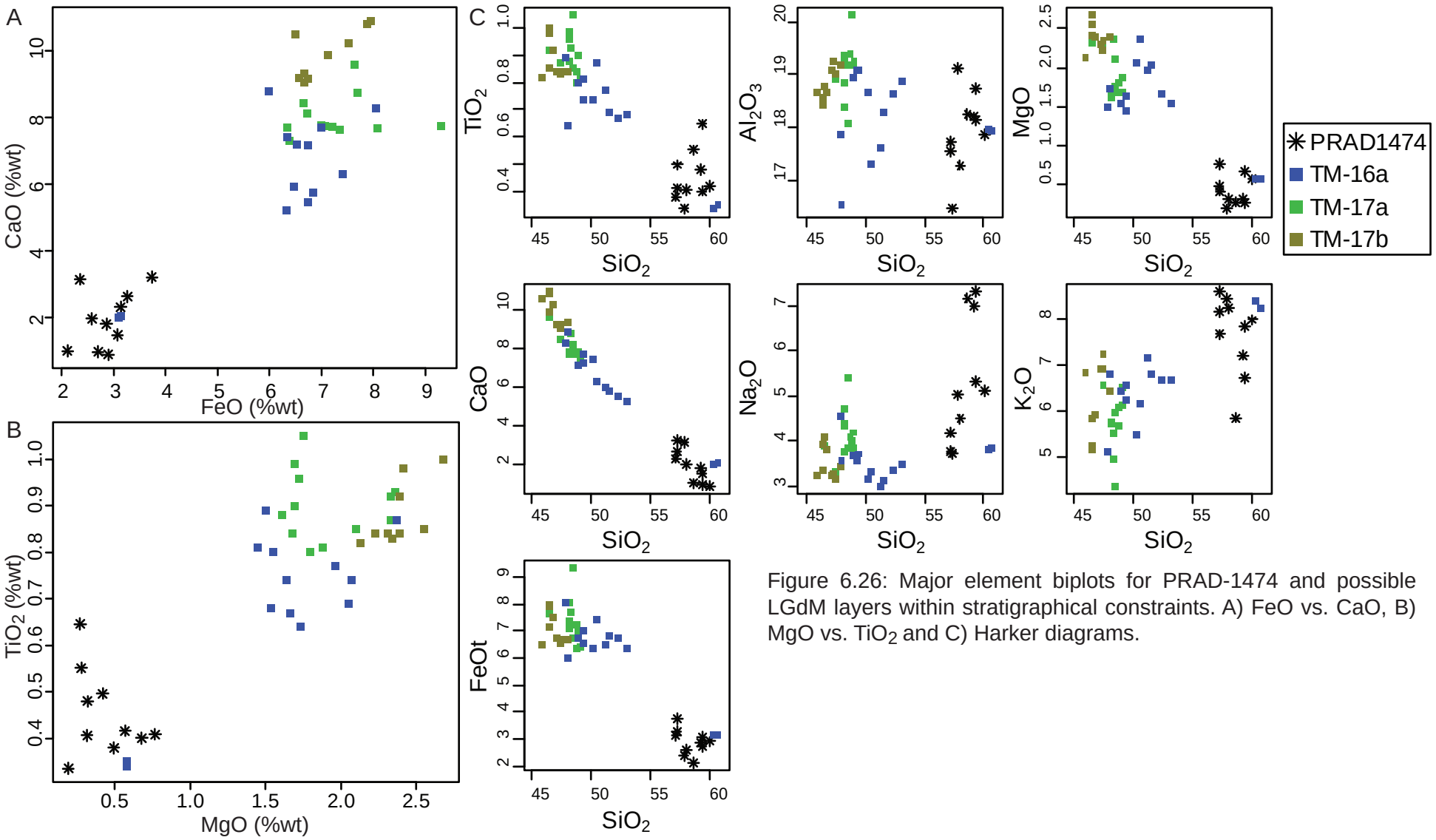

Figure 6.26: Major element biplots for PRAD-1474 and possible LGdM layers within stratigraphical constraints. A) FeO vs. CaO, B) MgO vs. TiO_2 and C) Harker diagrams.

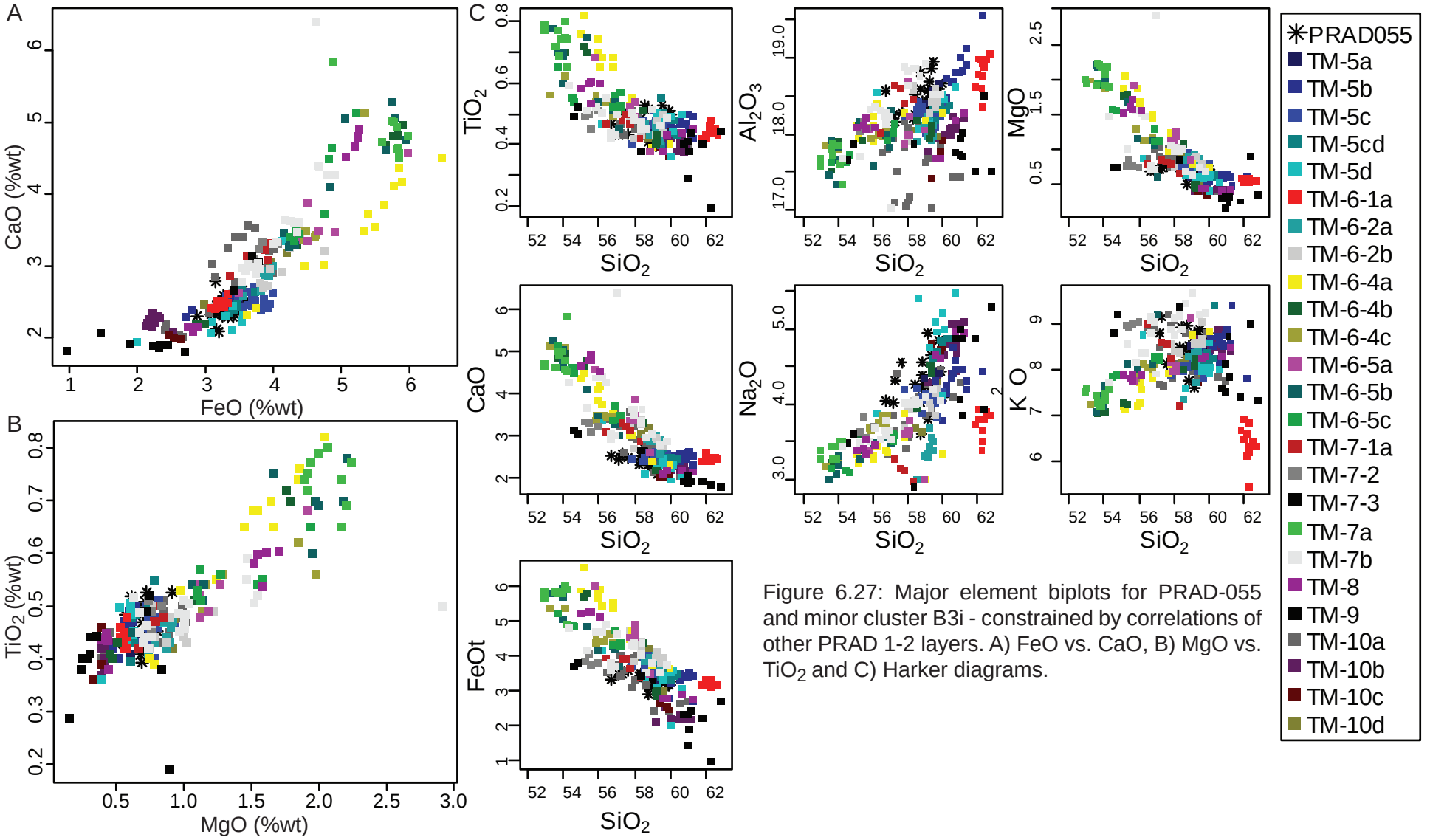

Figure 6.27: Major element biplots for PRAD-055 and minor cluster B3i - constrained by correlations of other PRAD 1-2 layers. A) FeO vs. CaO, B) MgO vs. TiO_2 and C) Harker diagrams.

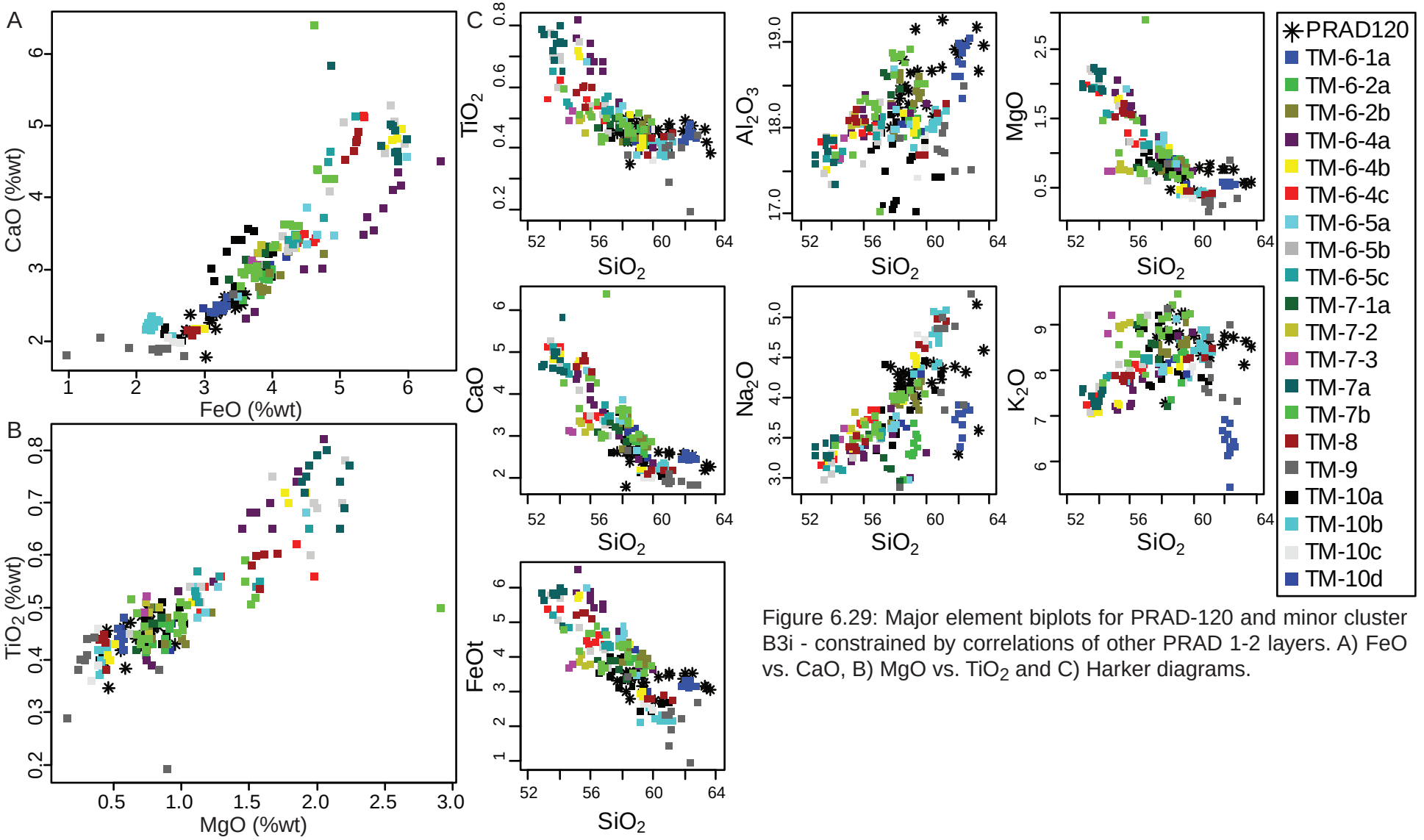

Figure 6.29: Major element biplots for PRAD-120 and minor cluster B3i - constrained by correlations of other PRAD 1-2 layers. A) FeO vs. CaO, B) MgO vs. TiO_2 and C) Harker diagrams.

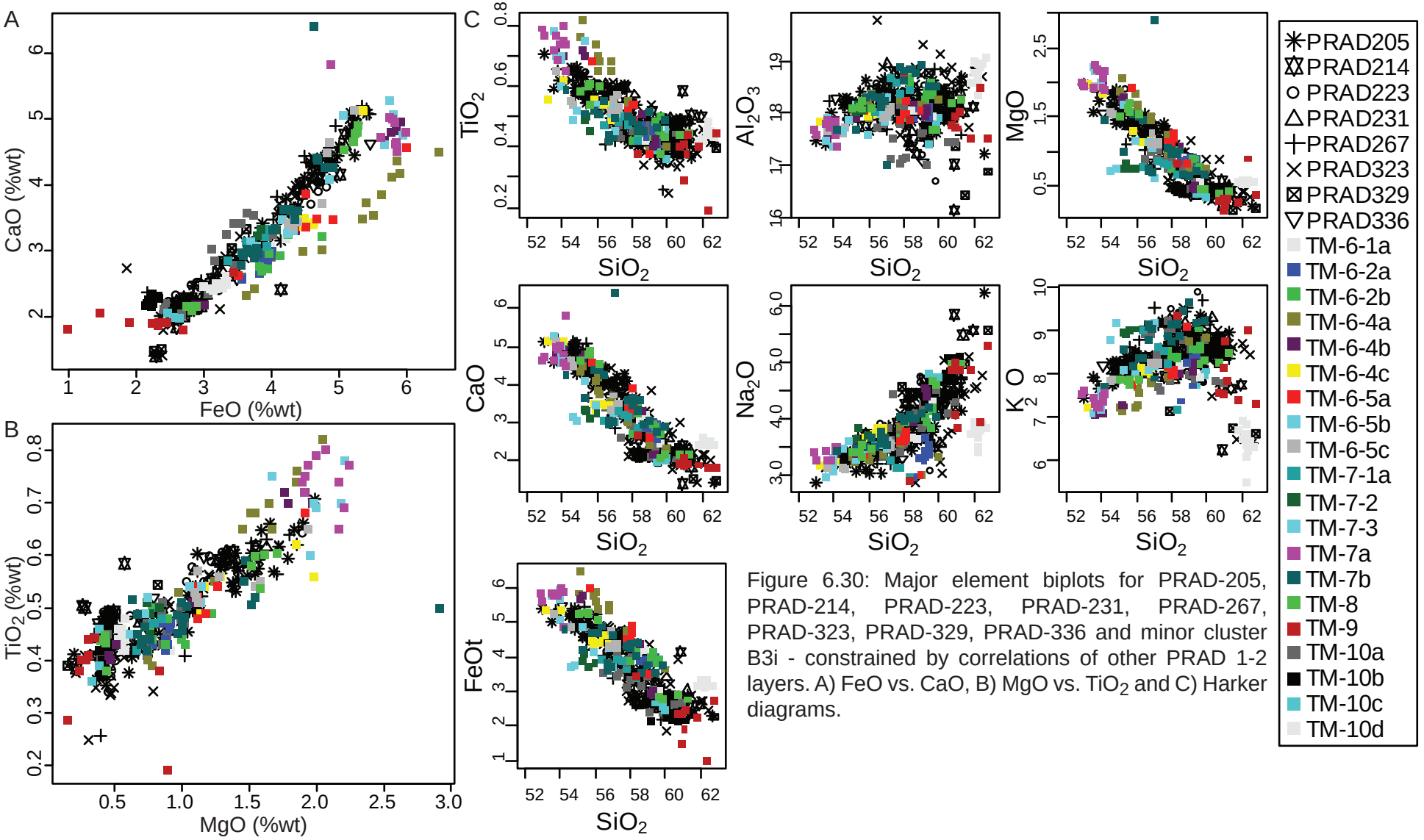

Figure 6.30: Major element biplots for PRAD-205, PRAD-214, PRAD-223, PRAD-231, PRAD-267, PRAD-323, PRAD-329, PRAD-336 and minor cluster B3i - constrained by correlations of other PRAD 1-2 layers. A) FeO vs. CaO, B) MgO vs. TiO_2 and C) Harker diagrams.

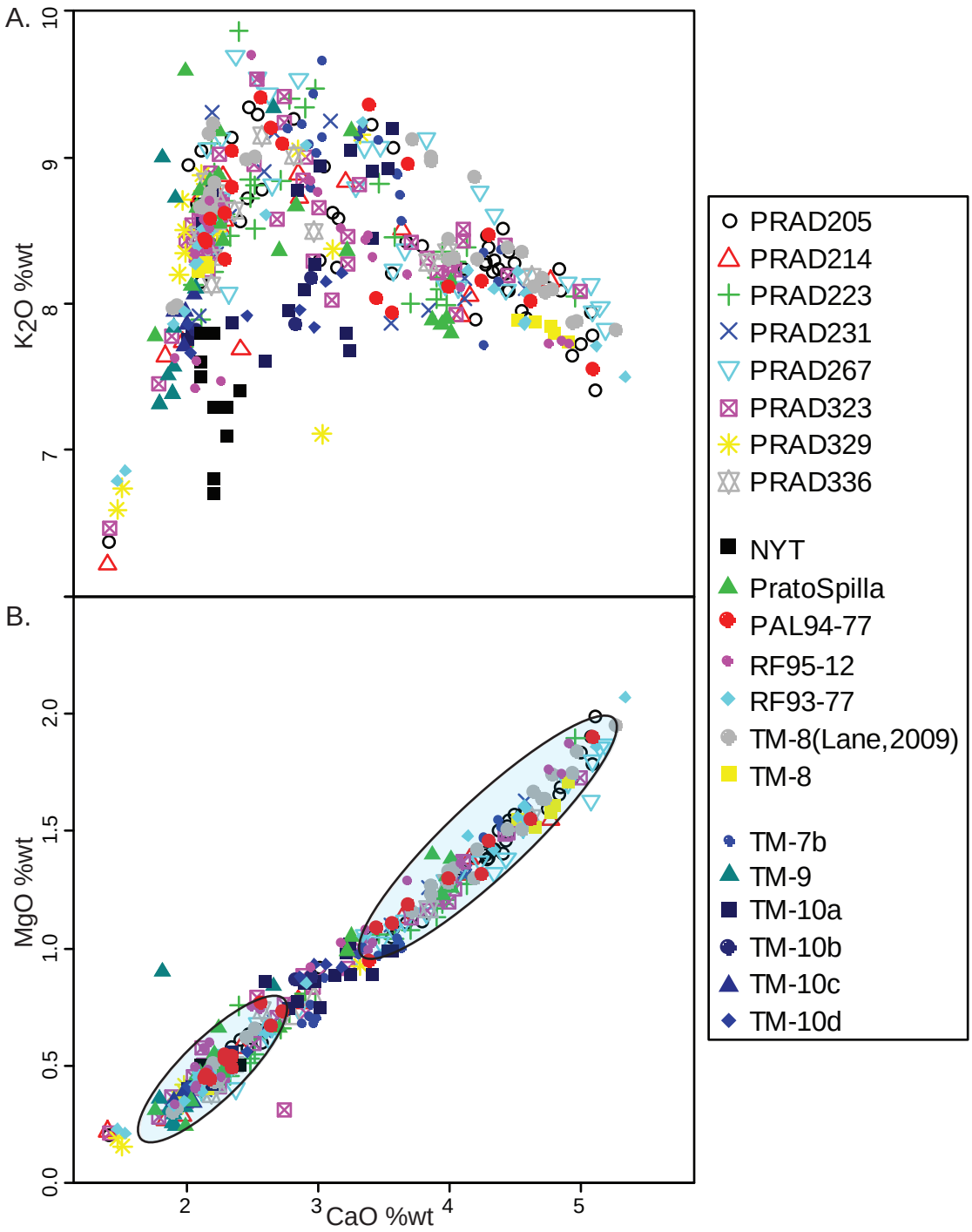

Figure 6.31: a) CaO vs K2O plot and b) CaO vs MgO plot for PRAD-205, PRAD-214, PRAD-223, PRAD-231, PRAD-267, PRAD-323, PRAD-329 and PRAD-336. These are compared with Prato Spilla, a layer correlated to the NYT eruption by Davies et al., (2002), data from layers correlated to the NYT in marine sequences PAL94-77, RF95-12, RF93-77 from Lane (2009), Campi Flegrei layers from LGdM - TM-7b (Pomici Principali), TM-8 (NYT), TM-9 (Tufi Biancastri) and TM-10 a,b,c,d (Lago Amendolare) (Wulf et al., 2004), as well as additional data from TM-8 generated by Lane (2009) and data from a proximal NYT outcrop from Turney et al., (2008). In a) an inflection point related to changes in fractionating minerals can be seen for all of the PRAD layers as well as for all distal tephra layers correlated to the NYT eruption. The TM-9 and TM-10 a,b,c,d layers do not show the same step in the data, although do cluster with one part of the PRAD data but not both. In b) there is clear bimodal distribution in the PRAD layers and layers correlated to the NYT (highlighted) with the other TM layers sitting in between these clusters. Envelopes are drawn around the groups of NYT data simply to aid with their visualisation.

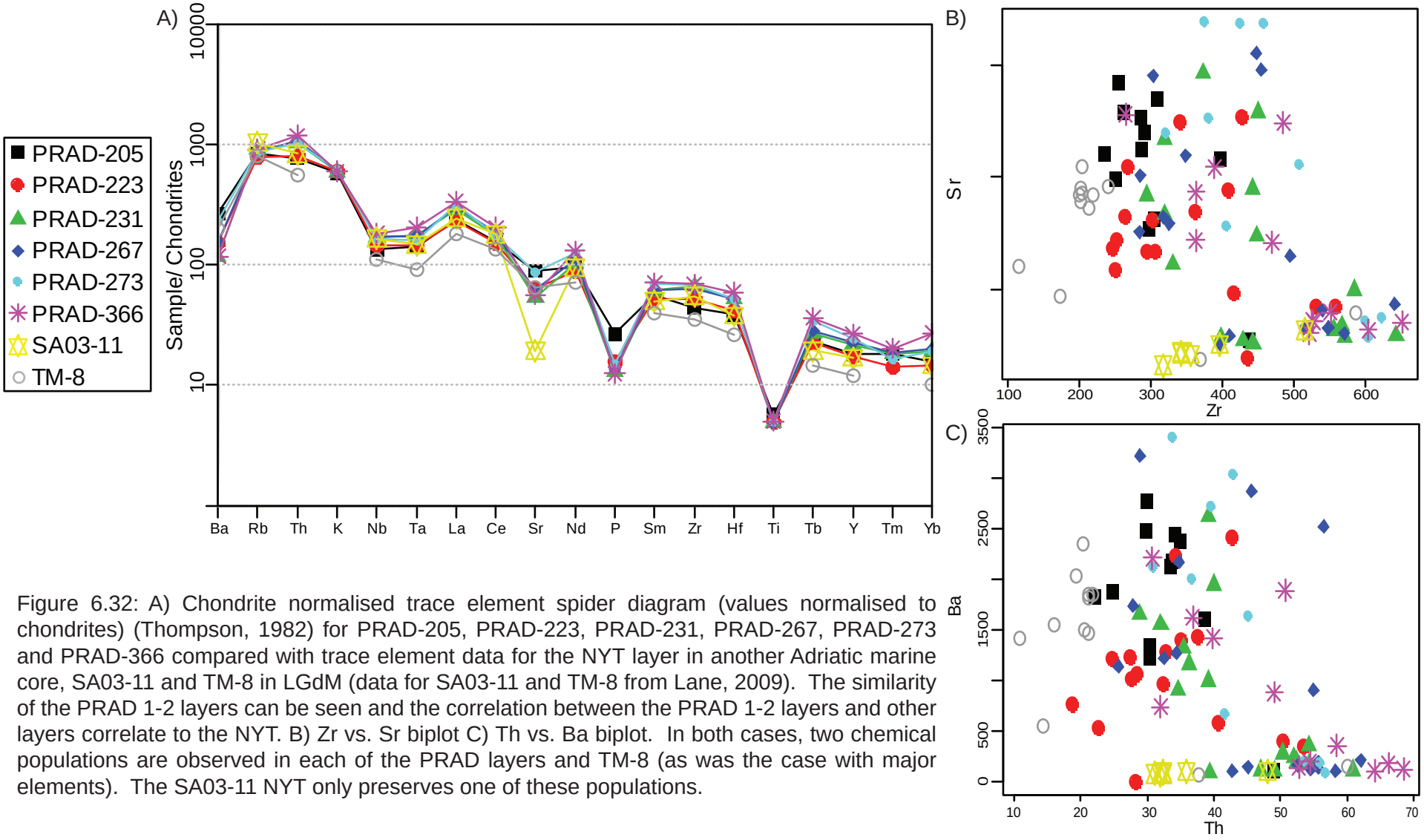

Figure 6.32: A) Chondrite normalised trace element spider diagram (values normalised to chondrites) (Thompson, 1982) for PRAD-205, PRAD-223, PRAD-231, PRAD-267, PRAD-273 and PRAD-366 compared with trace element data for the NYT layer in another Adriatic marine core, SA03-11 and TM-8 in LGdM (data for SA03-11 and TM-8 from Lane, 2009). The similarity of the PRAD 1-2 layers can be seen and the correlation between the PRAD 1-2 layers and other layers correlate to the NYT. B) Zr vs. Sr biplot C) Th vs. Ba biplot. In both cases, two chemical populations are observed in each of the PRAD layers and TM-8 (as was the case with major elements). The SA03-11 NYT only preserves one of these populations.

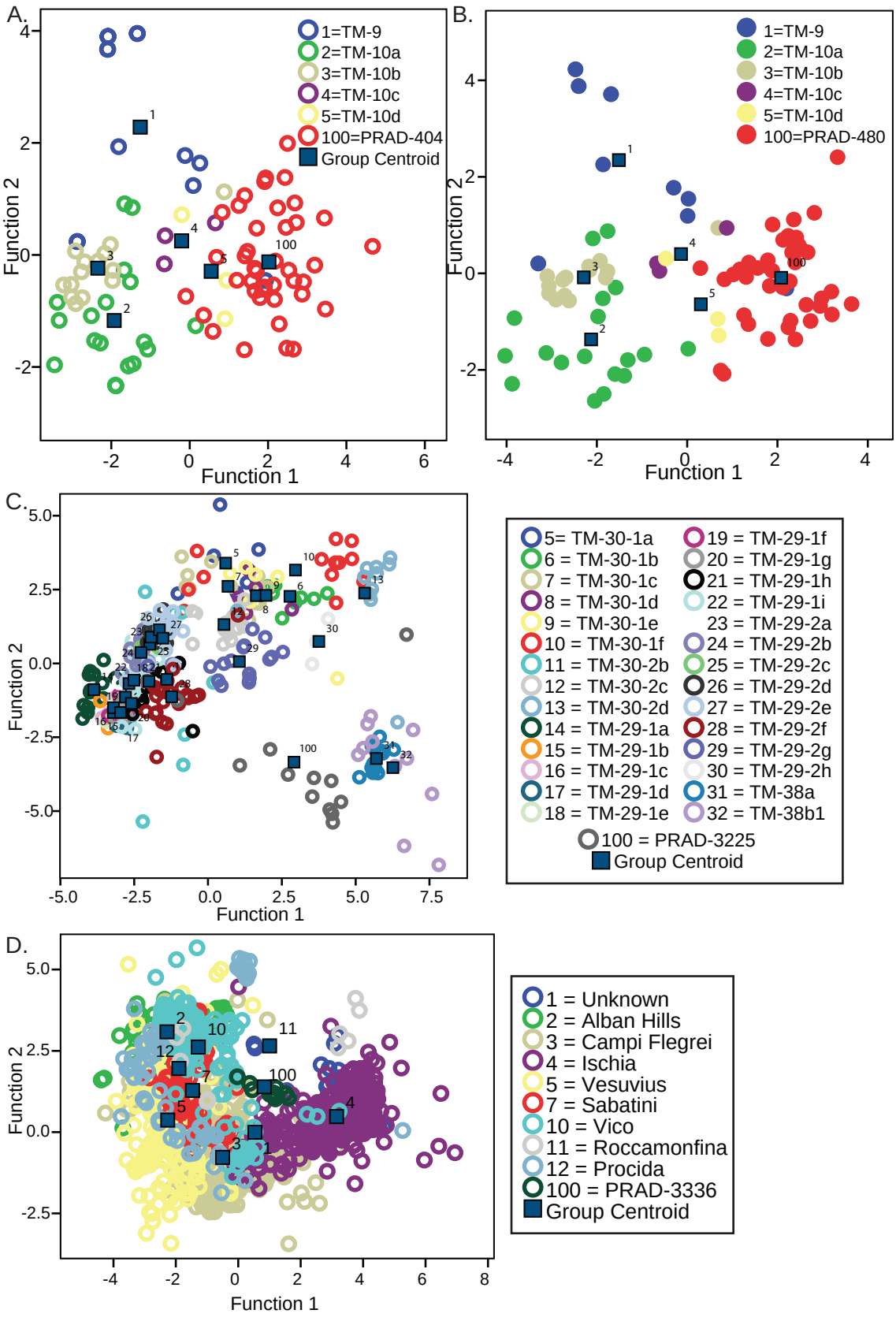

Figure 6.33: Plots of the 1st and 2nd canonical discriminant function axes. A) PRAD-404 and minor cluster B3i (constrained by correlations of other PRAD 1-2 layers), showing no grouping of PRAD-404. B) PRAD-480 and minor cluster B3i (constrained by correlations of other PRAD 1-2 layers), showing no grouping of PRAD-480. C) PRAD-2325 and minor cluster B3ii layers older than TM-27, showing grouping with TM-28a and TM-38b1. D) PRAD-3336 and subset B - showing no grouping to a major cluster.

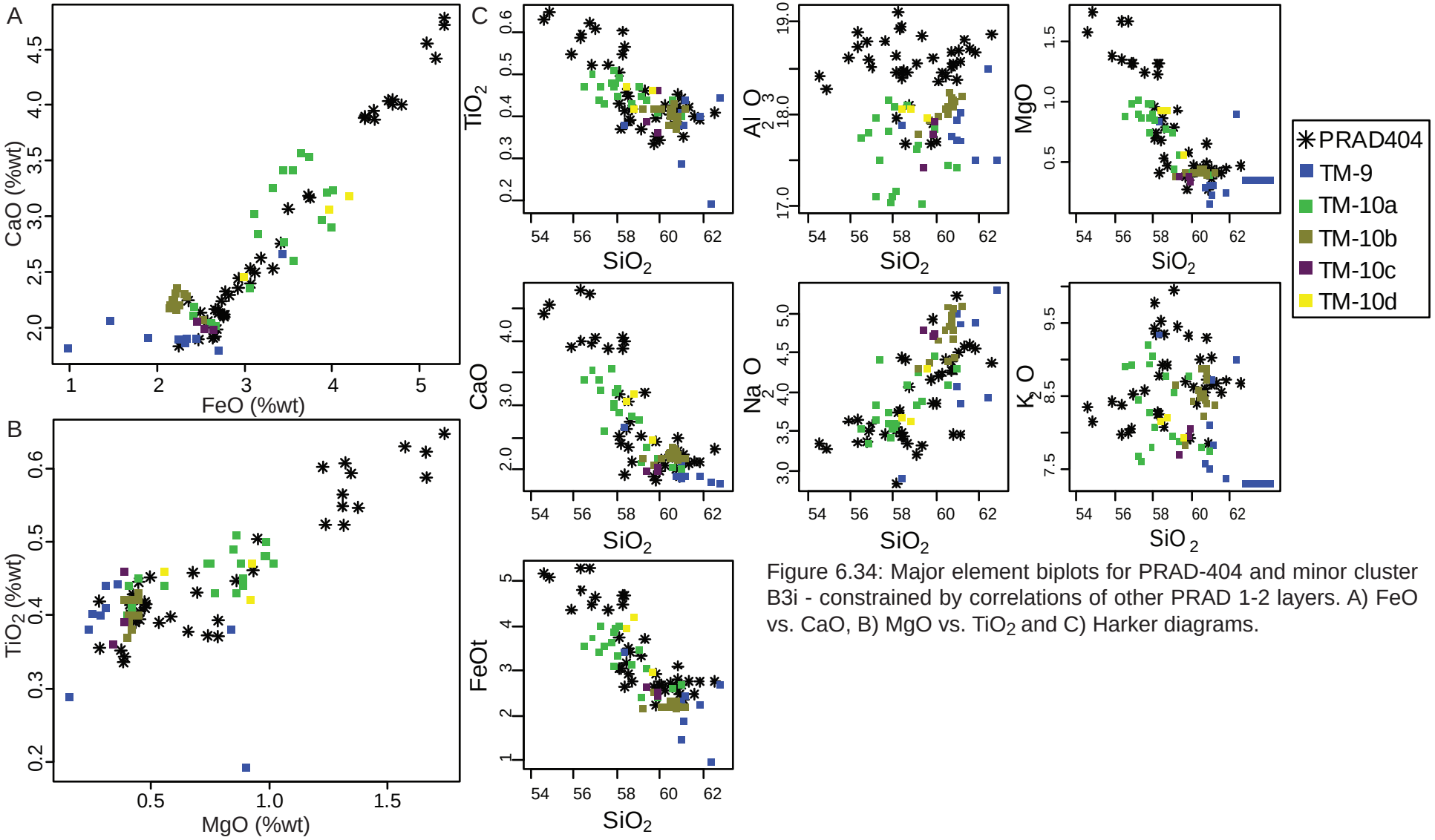

Figure 6.34: Major element biplots for PRAD-404 and minor cluster B3i - constrained by correlations of other PRAD 1-2 layers. A) FeO vs. CaO, B) MgO vs. TiO_2 and C) Harker diagrams.

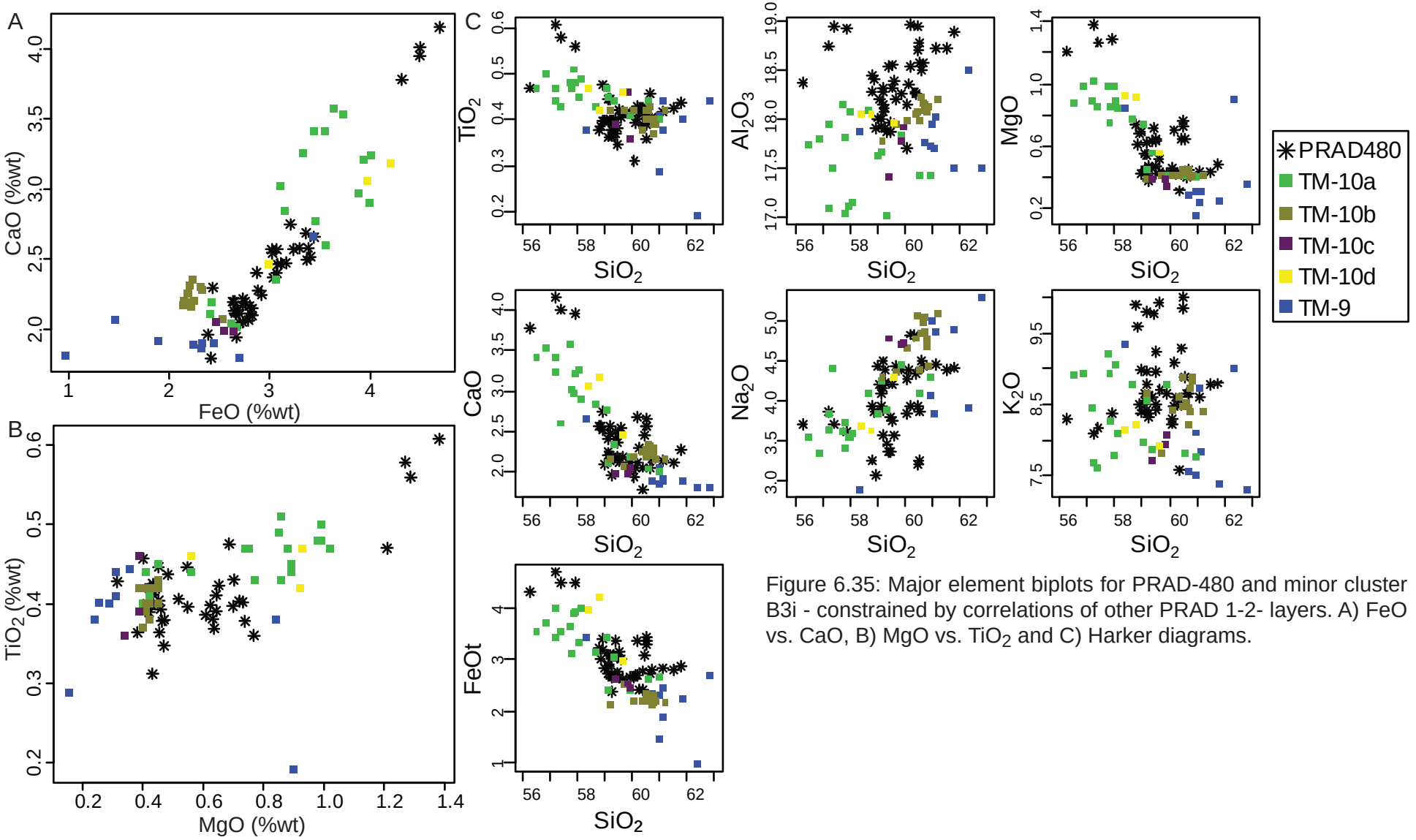

Figure 6.35: Major element biplots for PRAD-480 and minor cluster B3i - constrained by correlations of other PRAD 1-2- layers. A) FeO vs. CaO, B) MgO vs. TiO_2 and C) Harker diagrams.

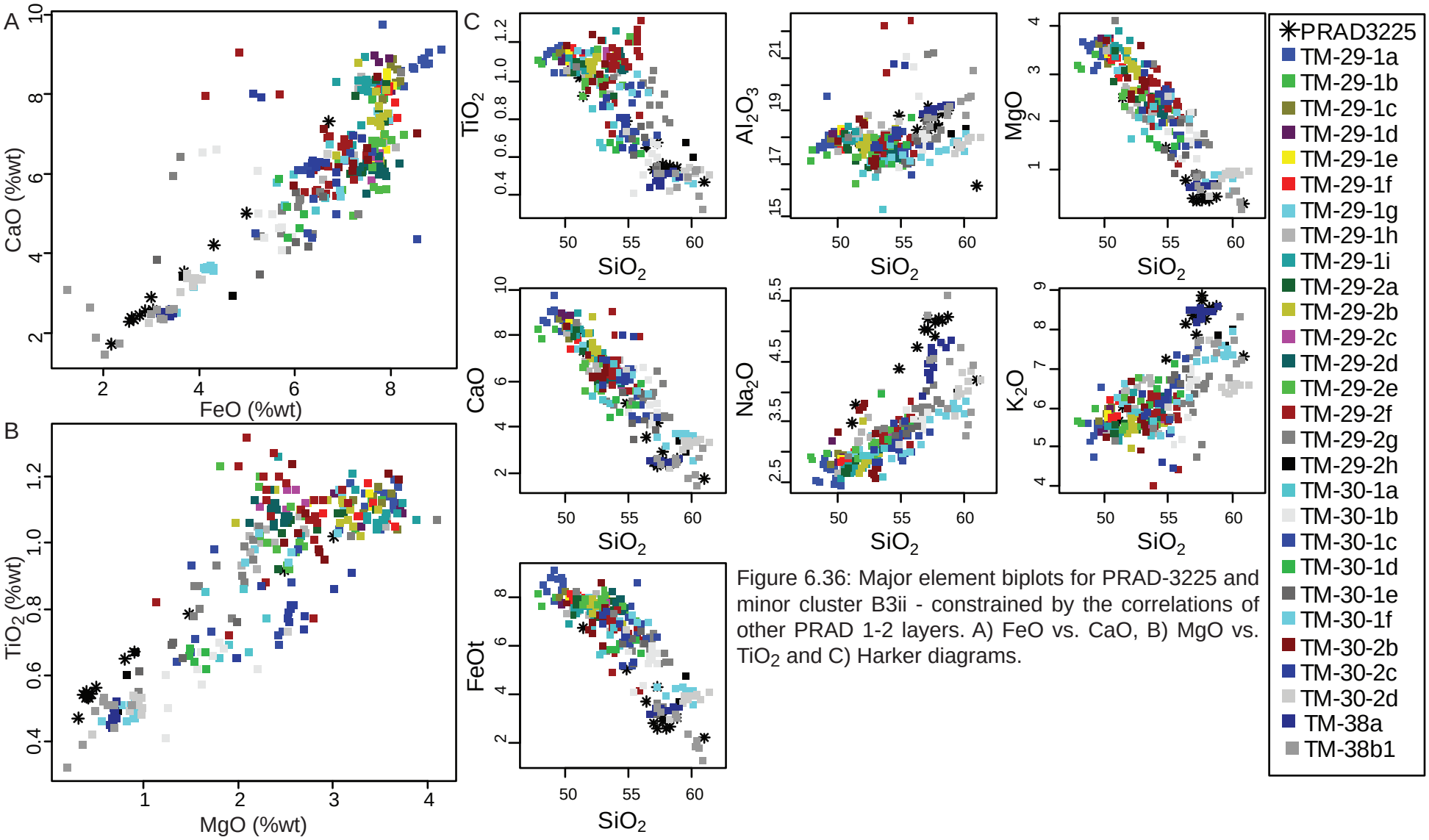

Figure 6.36: Major element biplots for PRAD-3225 and minor cluster B3ii - constrained by the correlations of other PRAD 1-2 layers. A) FeO vs. CaO, B) MgO vs. TiO_2 and C) Harker diagrams.

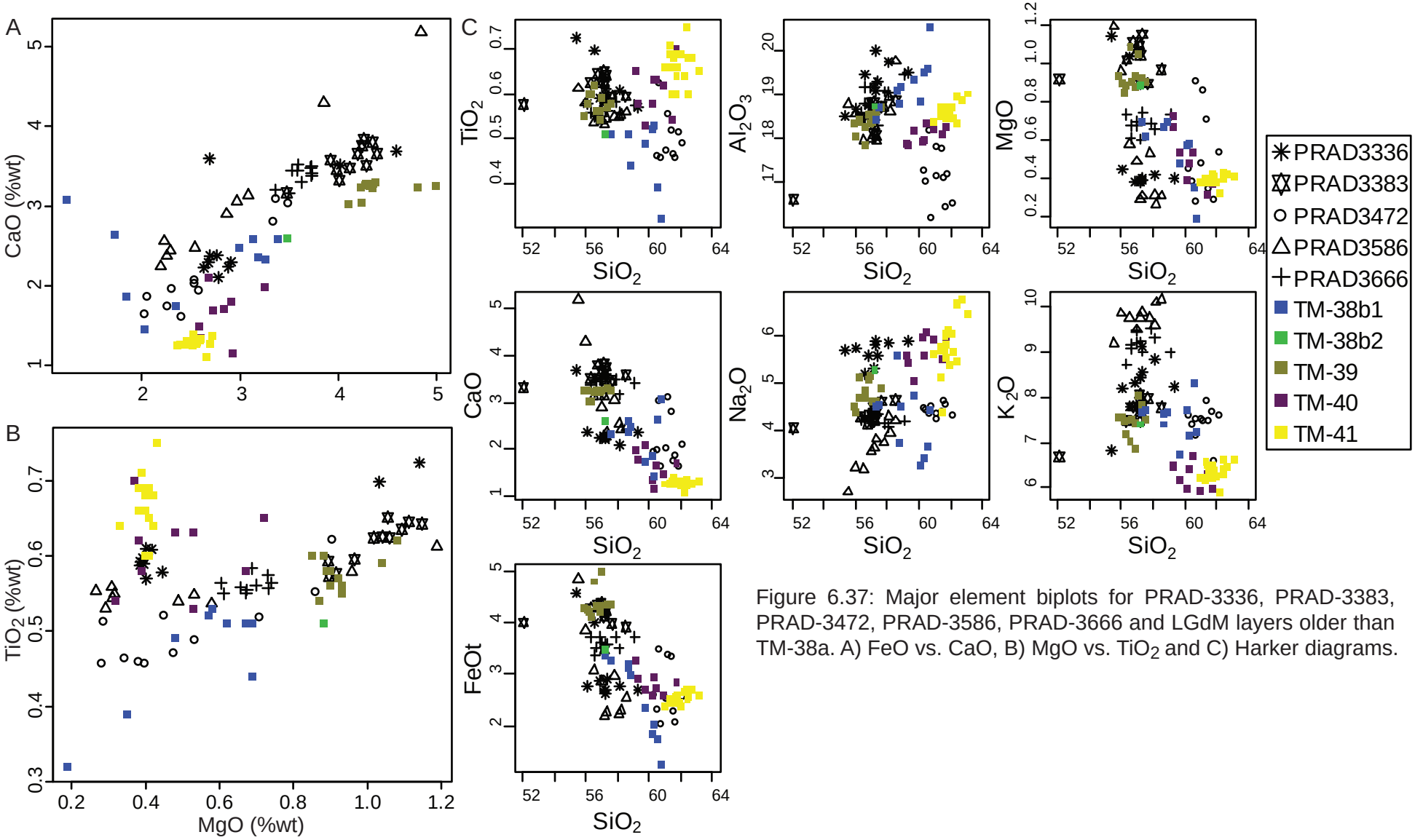

Figure 6.37: Major element biplots for PRAD-3336, PRAD-3383, PRAD-3472, PRAD-3586, PRAD-3666 and LGdM layers older than TM-38a. A) FeO vs. CaO, B) MgO vs. TiO_2 and C) Harker diagrams.

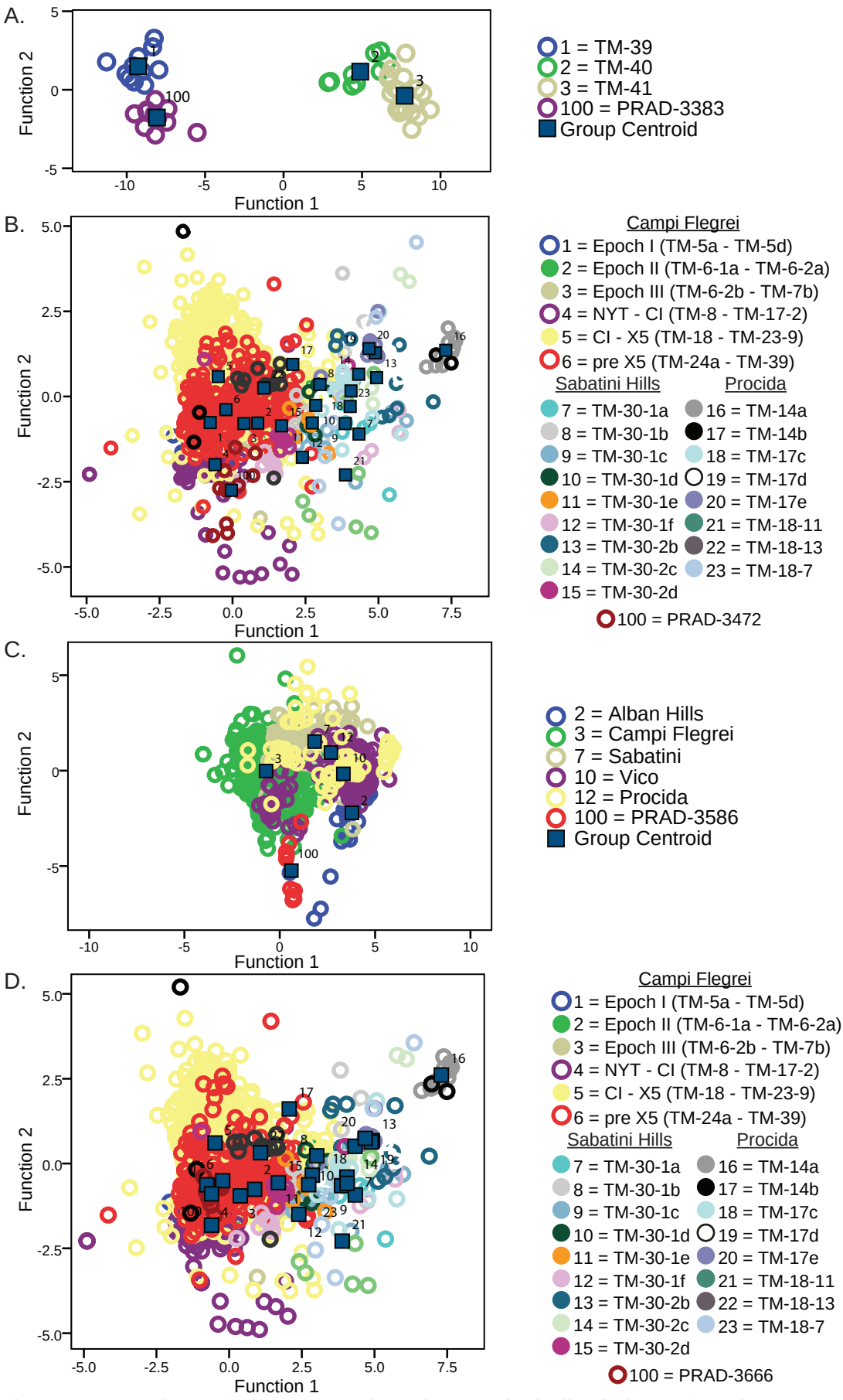

Figure 6.38: Plots of the 1st and 2nd canonical discriminant function axes. A) PRAD-3383 and layers older than TM-38a, showing grouping with TM-39. B) PRAD-3472 and minor cluster B3i. C) PRAD-3586 and major cluster B3 showing no grouping with a minor cluster. D) PRAD-3666 and minor cluster B3i.

Table 6.4: Summary of eruptives geochemically matched between PRAD 1-2 and the Lago Grande di Monticchio data of Wulf *et al.* (2004, 2008). References for the raw ^{14}C dates are provided in the text. Radiocarbon dates were calibrated using OXCAL Version 4.1 (Bronk Ramsey, 2009) and the INTCAL 09 calibration curve for radiocarbon dates (Reimer *et al.,* 2009).

PRAD 1-2 tephra	Monticchio tephra layer	Origin	Volcanic event	Calibrated 2σ age (cal yr)	Dating method	Dated material
PRAD-055	TM-5	Campi Flegrei	Agnano Monte Spina	4690 – 4300 BP	^{14}C	Charcoal (proximal tephra)
PRAD-120	N/A	Campi Flegrei	N/A	N/A	N/A	N/A
PRAD-205	TM-8 (reworked)	Campi Flegrei	Neapolitan Yellow Tuff (reworked)	14,320 – 13,900 BP	^{14}C	Underlying paleosols (proximal tephra)
PRAD-223	TM-8	Campi Flegrei	Neapolitan Yellow Tuff	14,320 – 13,900 BP	^{14}C	Underlying paleosols (proximal tephra)
PRAD-231	N/A	Campi Flegrei	N/A	N/A	N/A	N/A
PRAD-267	N/A	Campi Flegrei	N/A	N/A	N/A	N/A
PRAD-323	N/A	Campi Flegrei	N/A	N/A	N/A	N/A
PRAD-329	N/A	Campi Flegrei	N/A	N/A	N/A	N/A
PRAD-404	N/A	Campi Flegrei	N/A	N/A	N/A	N/A
PRAD-480	N/A	Campi Flegrei	N/A	N/A	N/A	N/A
PRAD-784	TM-12	Vesuvius	Greenish/Verdoline	19,480 – 19,050 BP	^{14}C	Charcoal (proximal tephra)
PRAD-845	TM-13 (reworked)	Vesuvius	Pomici di Base (reworked)	22,240 – 21,150 BP	^{14}C	Underlying paleosols (proximal tephra)
PRAD-875	TM-13	Vesuvius	Pomici di Base	22,240 – 21,150 BP	^{14}C	Underlying paleosols (proximal tephra)
PRAD-1103	TM-14-1	Ischia	Faro di Punta Imperatore	22,420 – 20,280 BP	varves	LGdM sediment chronology
PRAD-1130	Unknown	Unknown	N/A	N/A	N/A	N/A
PRAD-1332	TM-15	Campi Flegrei	Y-3	30,500 – 30,100 BP	$^{40}Ar/^{39}Ar$	Sanidine (proximal tephra)
PRAD-1474	Unknown	Unknown	N/A	N/A	N/A	N/A
PRAD-1494	TM-16b	Vesuvius	Codola (base)	29,921 - 28,896 BP	^{14}C	Underlying paleosols (proximal tephra)
PRAD-1653	TM-18	Campi Flegrei	Campanian Ignimbrite	39,390 – 39,170 BP	$^{40}Ar/^{39}Ar$	Sanidine (proximal tephra)
PRAD-1752	TM-18-1	Ischia	SMP1-a	38,680 – 35,000 BP	varves	N/A
PRAD-1870	TM 19	Ischia	Monte Epomeo Green Tuff	56,400 – 55,600 BP	$^{40}Ar/^{39}Ar$	Sanidine (distal tephra)
PRAD-2040	TM-20-7	Ischia	Pignatiello Formation	79,120 – 71,580 BP	varves	LGdM sediment chronology
PRAD-2375	TM-22	Pantelleria	Ignimbrite z unit	83,500 – 75,100 BP	Unknown	Unknown
PRAD-2525	TM-24	Campi Flegrei	X-5	107,000 – 103,000 BP	$^{40}Ar/^{39}Ar$	Sanidine (distal tephra)

PRAD-2605	Unknown	Unknown	N/A	N/A	N/A	N/A
PRAD-2812	TM-27	Ischia	X-6	109,000 – 105,000 BP	Unknown	Unknown
PRAD-3225	TM-38a	Vico	Ignimbrite D	126,000 – 114,000 BP	$^{40}Ar/^{39}Ar$	Sanidine (proximal tephra)
PRAD-3336	Unknown	Unknown	N/A	N/A	N/A	N/A
PRAD-3383	TM-39	Campi Flegrei	Unknown	130,627 BP	varves	LGdM sediment chronology
PRAD-3472	Unknown	Unknown	Unknown	N/A	N/A	N/A
PRAD-3586	Unknown	Unknown	Unknown	N/A	N/A	N/A
PRAD-3666	Unknown	Unknown	Unknown	N/A	N/A	N/A

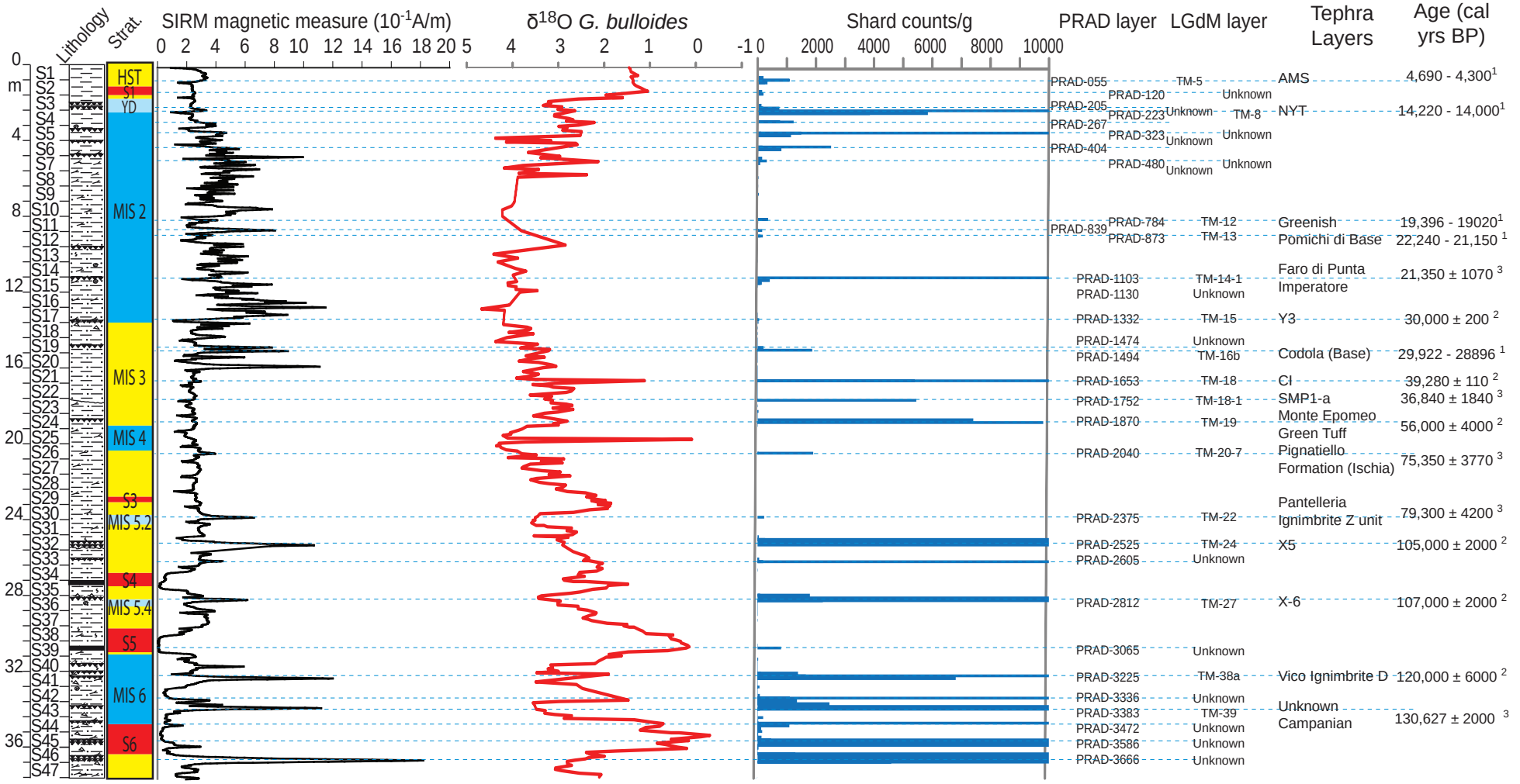

Figure 6.39: Summary diagram for the tephra record obtained from PRAD 1-2 with correlations to LGdM layers, the volcanic event those layers represent and the ages of those layers. Additional stratigraphic information provided by ISMAR, Bologna and published in Piva *et al.*, (2008). Current best age estimates are shown [1] = Calibrated radiocarbon date (shown as an age range), [2] = $^{40}Ar/^{39}Ar$ date and [3] = LGdM varve chronology (both shown as mean age ± error).

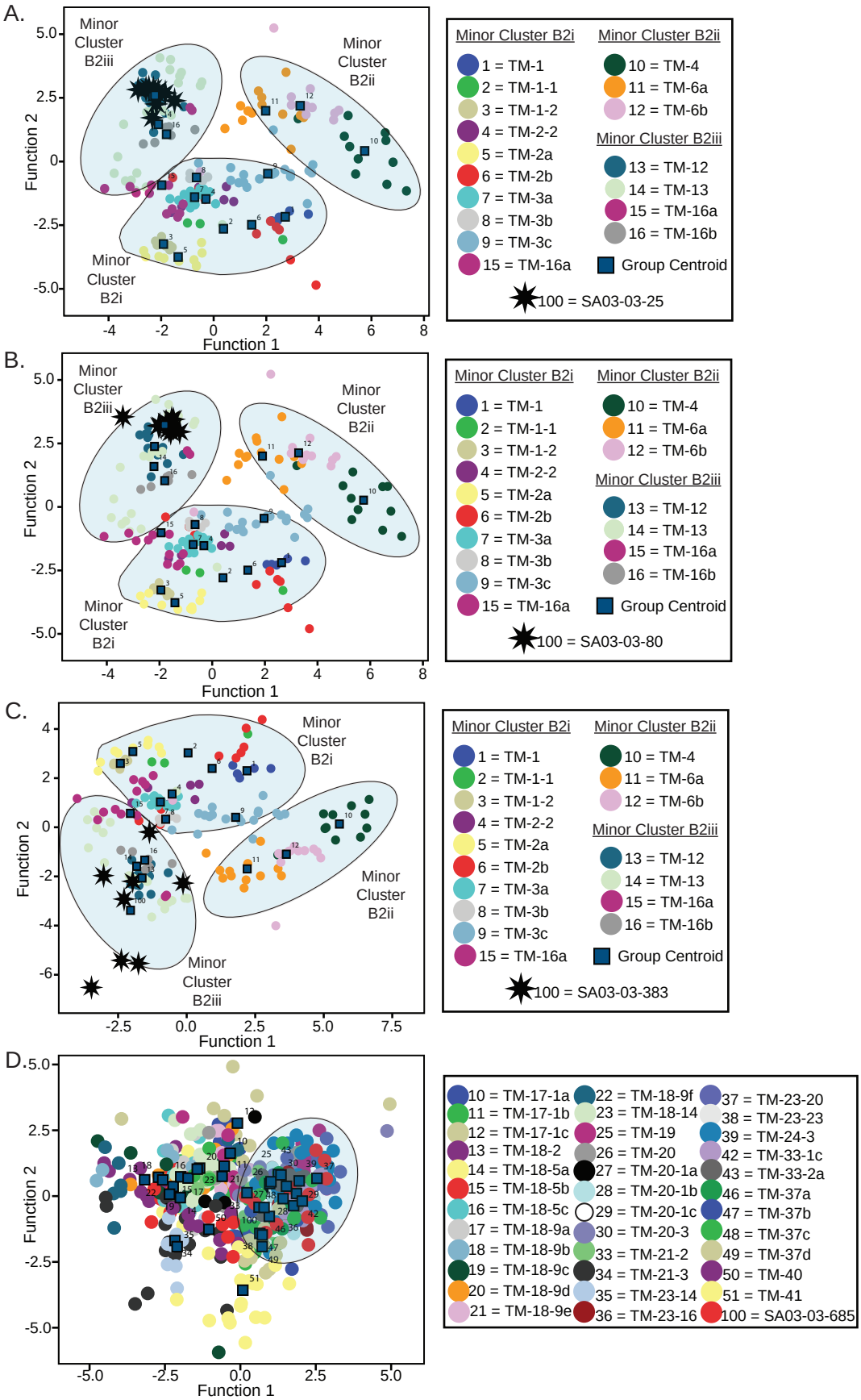

Figure 6.40: Plots of the 1st and 2nd canonical discriminant function axes. A) SA03-03-25 and major cluster B2, showing grouping with minor cluster B2iii. B) SA03-03-80 and major cluster B2, showing grouping with minor cluster B2iii. C) SA03-03-383 and major cluster B2, showing grouping with minor cluster B2iii. D) SA03-03-685 & minor cluster B1i, showing the grouping with TM-19, TM-20 & TM-20-1 (shaded section). Envelopes are drawn around the clusters simply to aid with their visualisation.

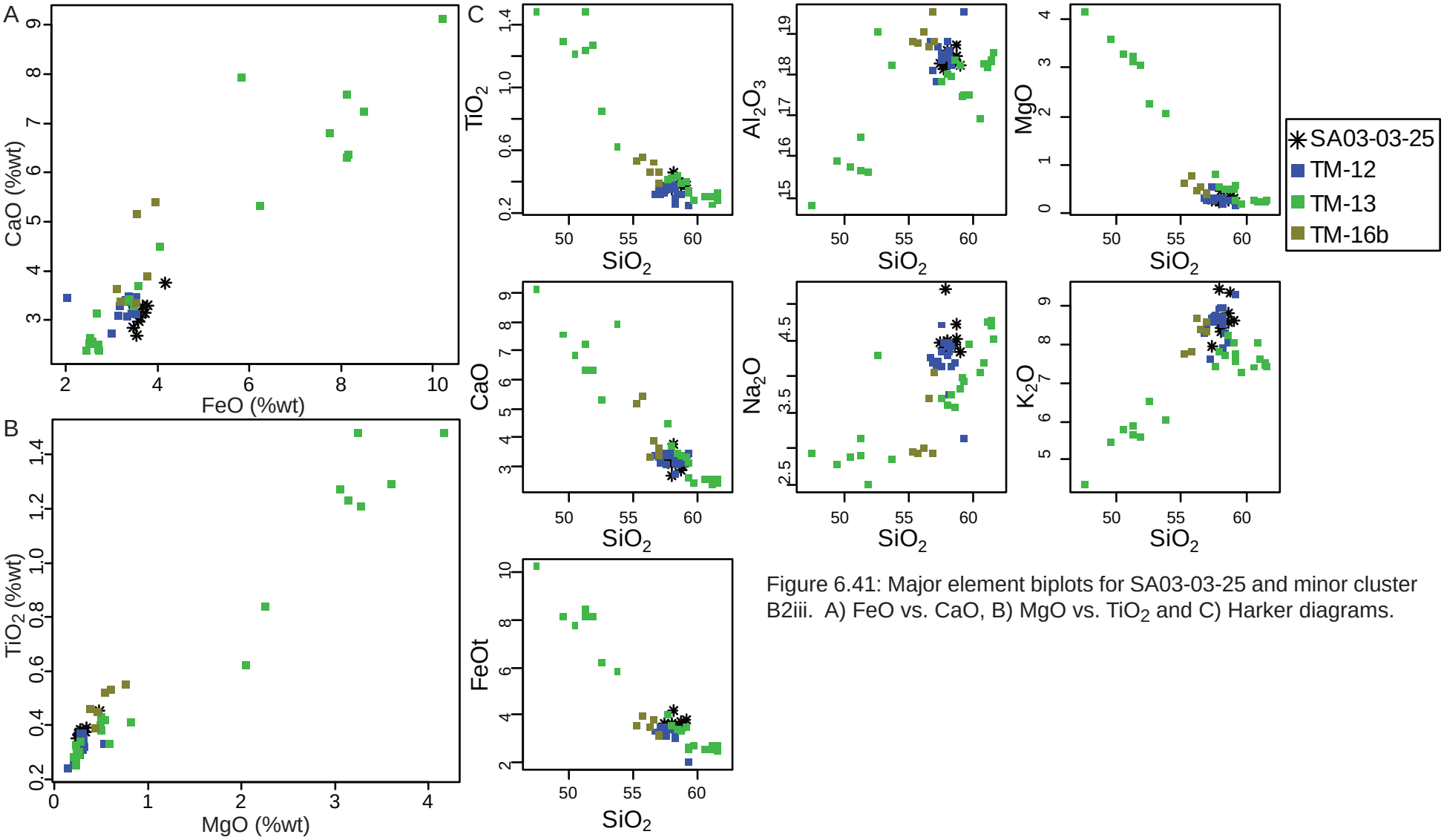

Figure 6.41: Major element biplots for SA03-03-25 and minor cluster B2iii. A) FeO vs. CaO, B) MgO vs. TiO_2 and C) Harker diagrams.

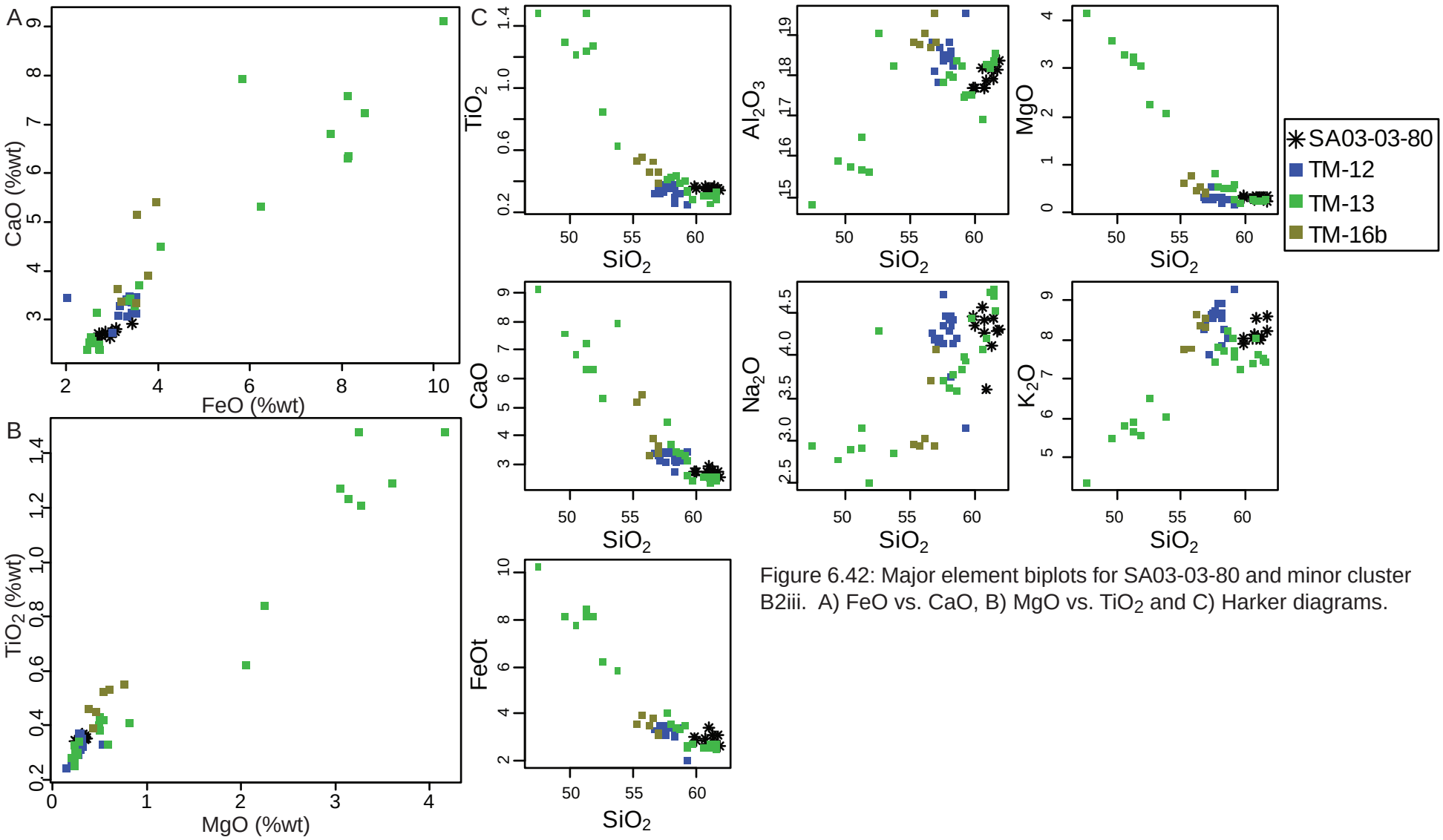

Figure 6.42: Major element biplots for SA03-03-80 and minor cluster B2iii. A) FeO vs. CaO, B) MgO vs. TiO_2 and C) Harker diagrams.

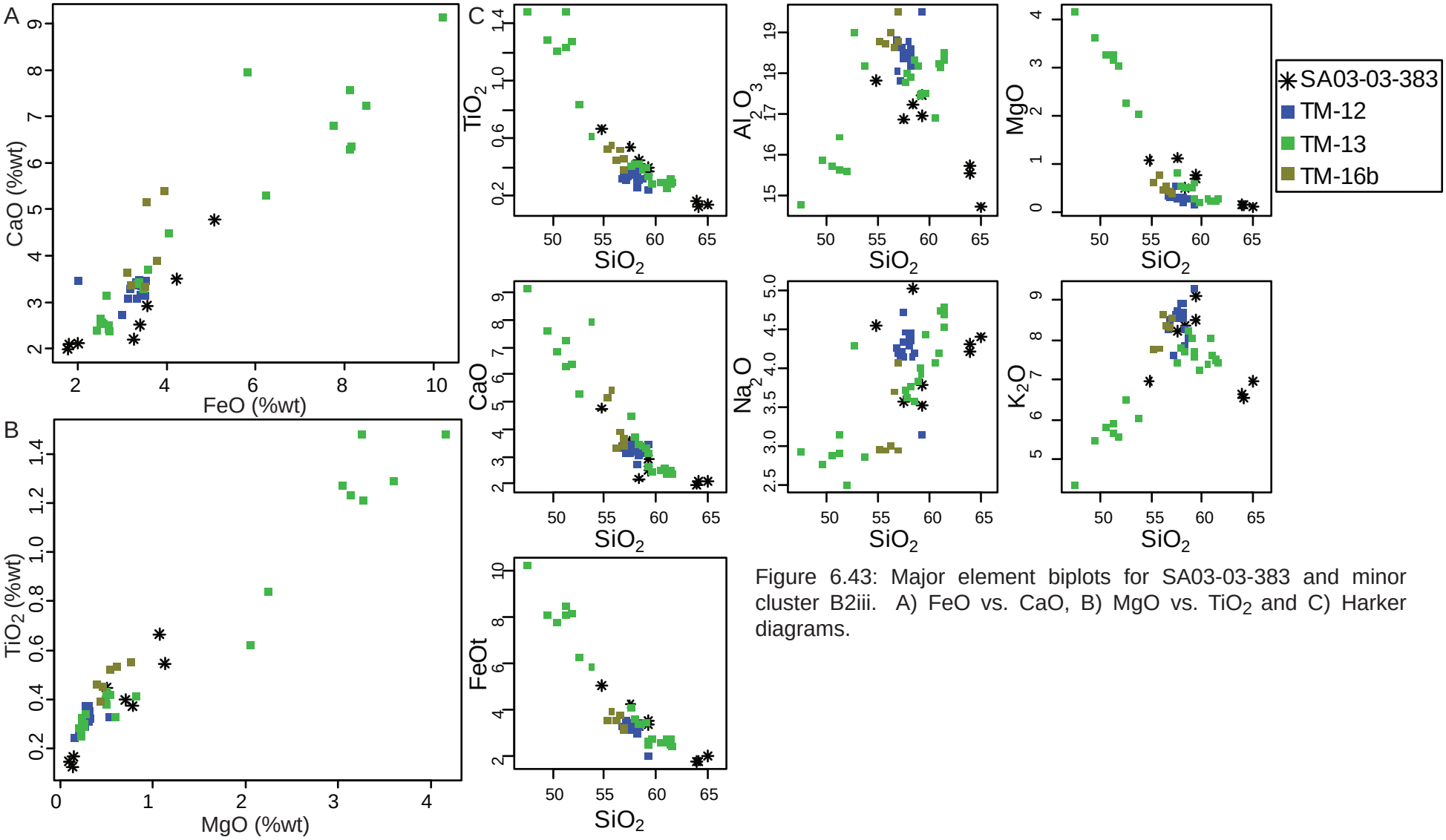

Figure 6.43: Major element biplots for SA03-03-383 and minor cluster B2iii. A) FeO vs. CaO, B) MgO vs. TiO_2 and C) Harker diagrams.

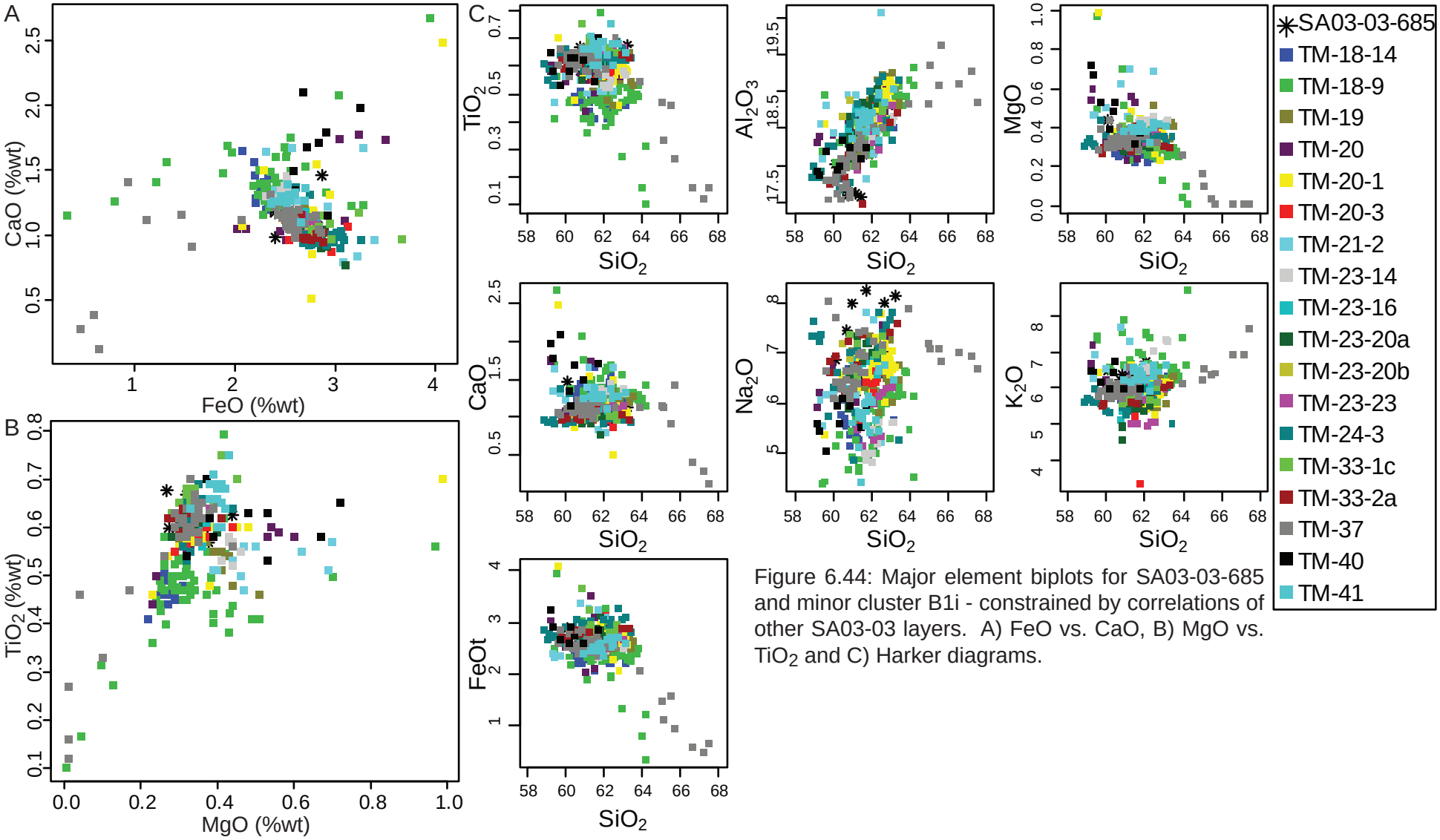

Figure 6.44: Major element biplots for SA03-03-685 and minor cluster B1i - constrained by correlations of other SA03-03 layers. A) FeO vs. CaO, B) MgO vs. TiO_2 and C) Harker diagrams.

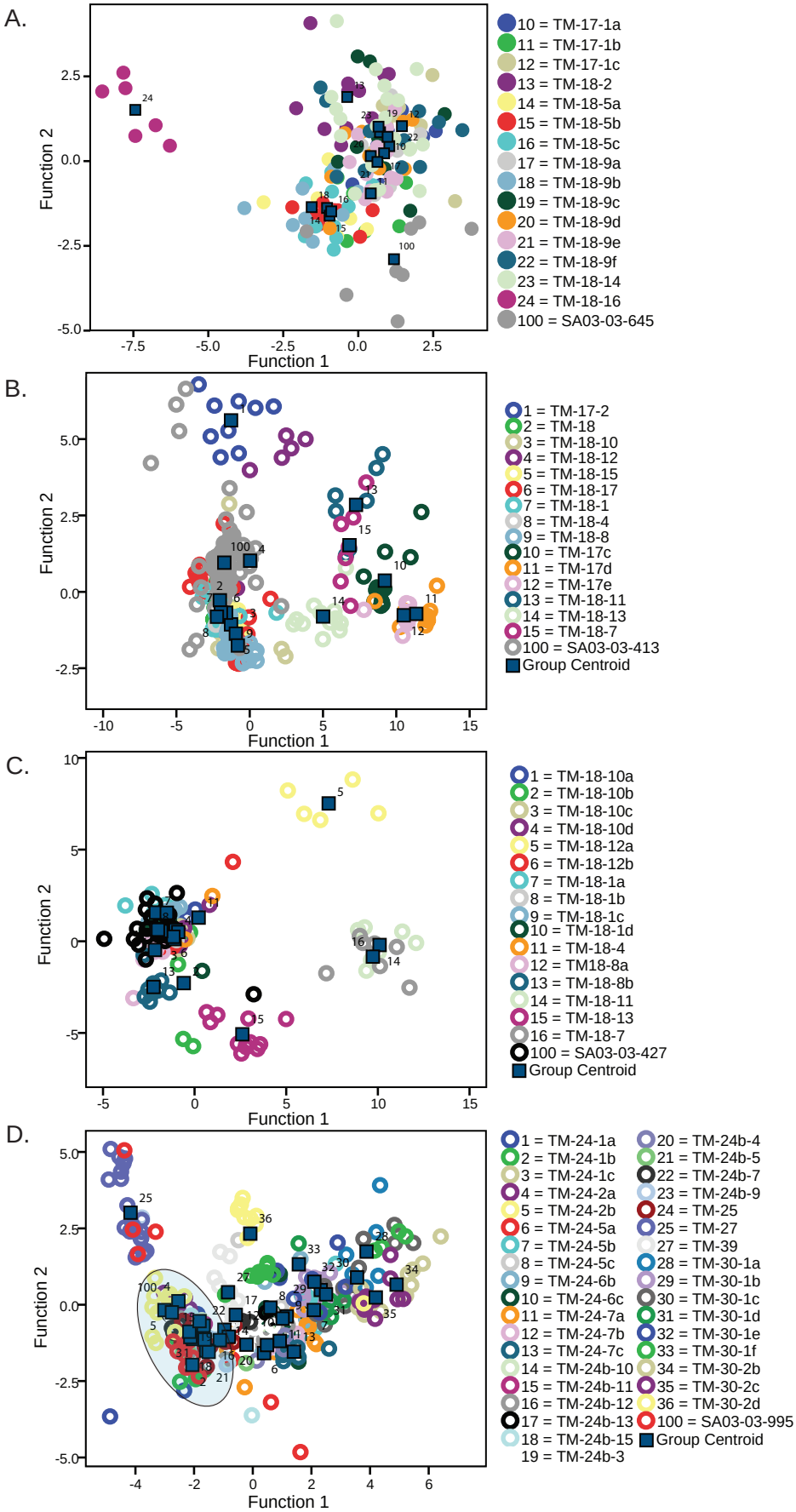

Figure 6.45: Plots of the 1st and 2nd canonical discriminant function axes. A) SA03-03-645 and minor cluster B1i. B) SA03-03-413 and minor cluster B3i. C) SA03-03-427 and minor cluster B3i. D) SA03-03-995 and minor cluster B3i. In all cases the minor clusters have been constrained by correlations to other SA03-03 layers. Envelopes are drawn around the clusters simply to aid with their visualisation.

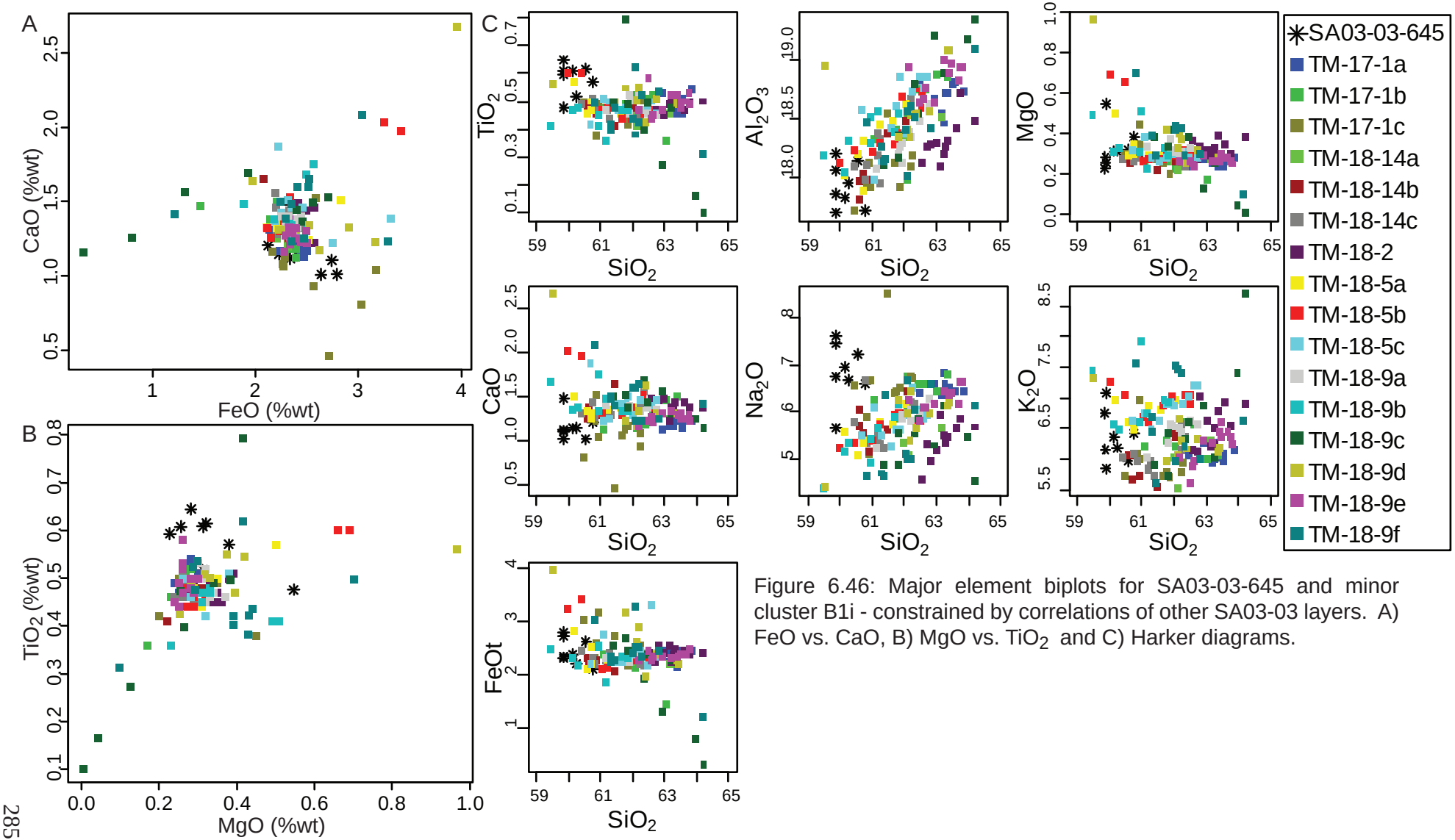

Figure 6.46: Major element biplots for SA03-03-645 and minor cluster B1i - constrained by correlations of other SA03-03 layers. A) FeO vs. CaO, B) MgO vs. TiO_2 and C) Harker diagrams.

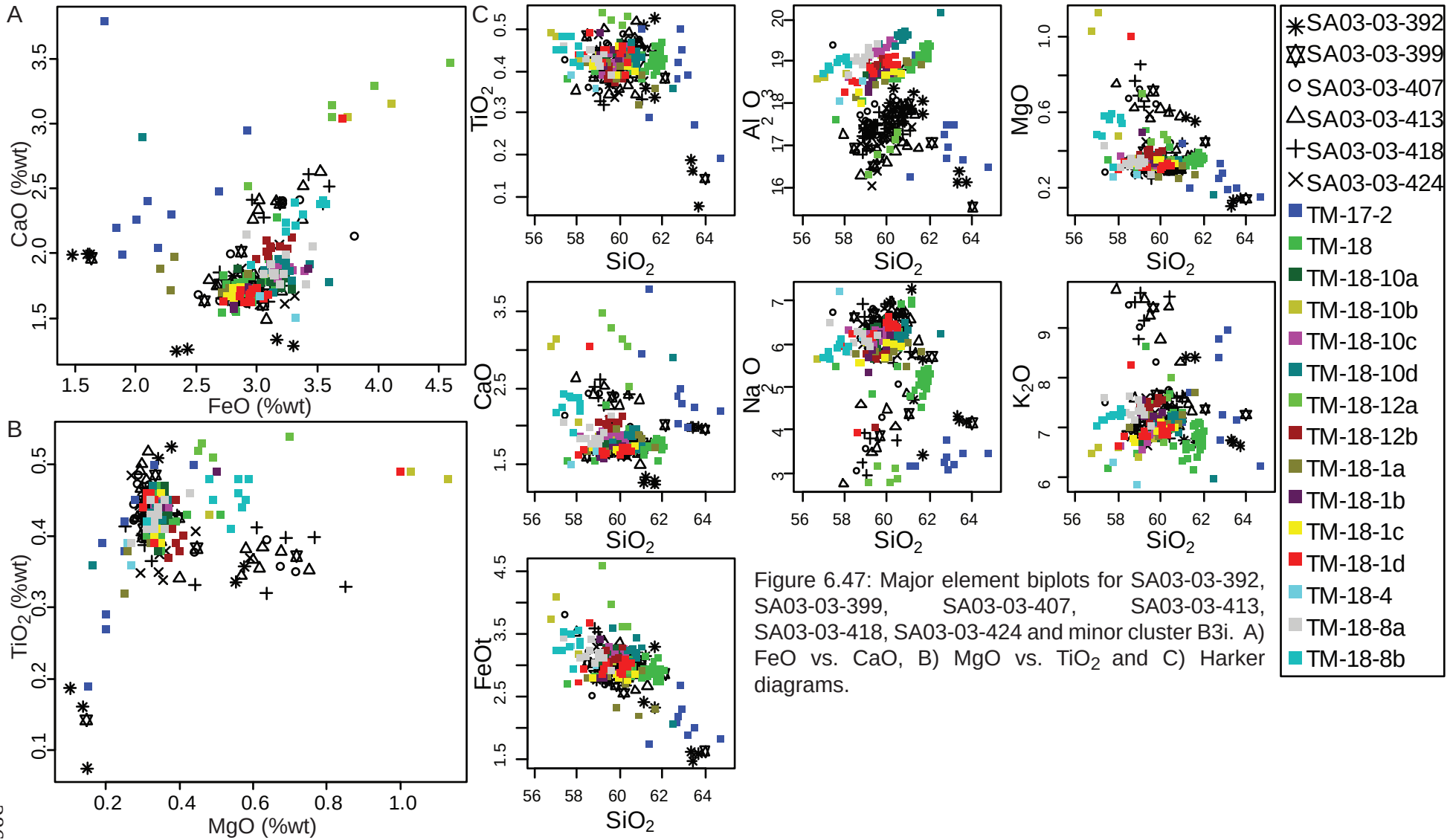

Figure 6.47: Major element biplots for SA03-03-392, SA03-03-399, SA03-03-407, SA03-03-413, SA03-03-418, SA03-03-424 and minor cluster B3i. A) FeO vs. CaO, B) MgO vs. TiO_2 and C) Harker diagrams.

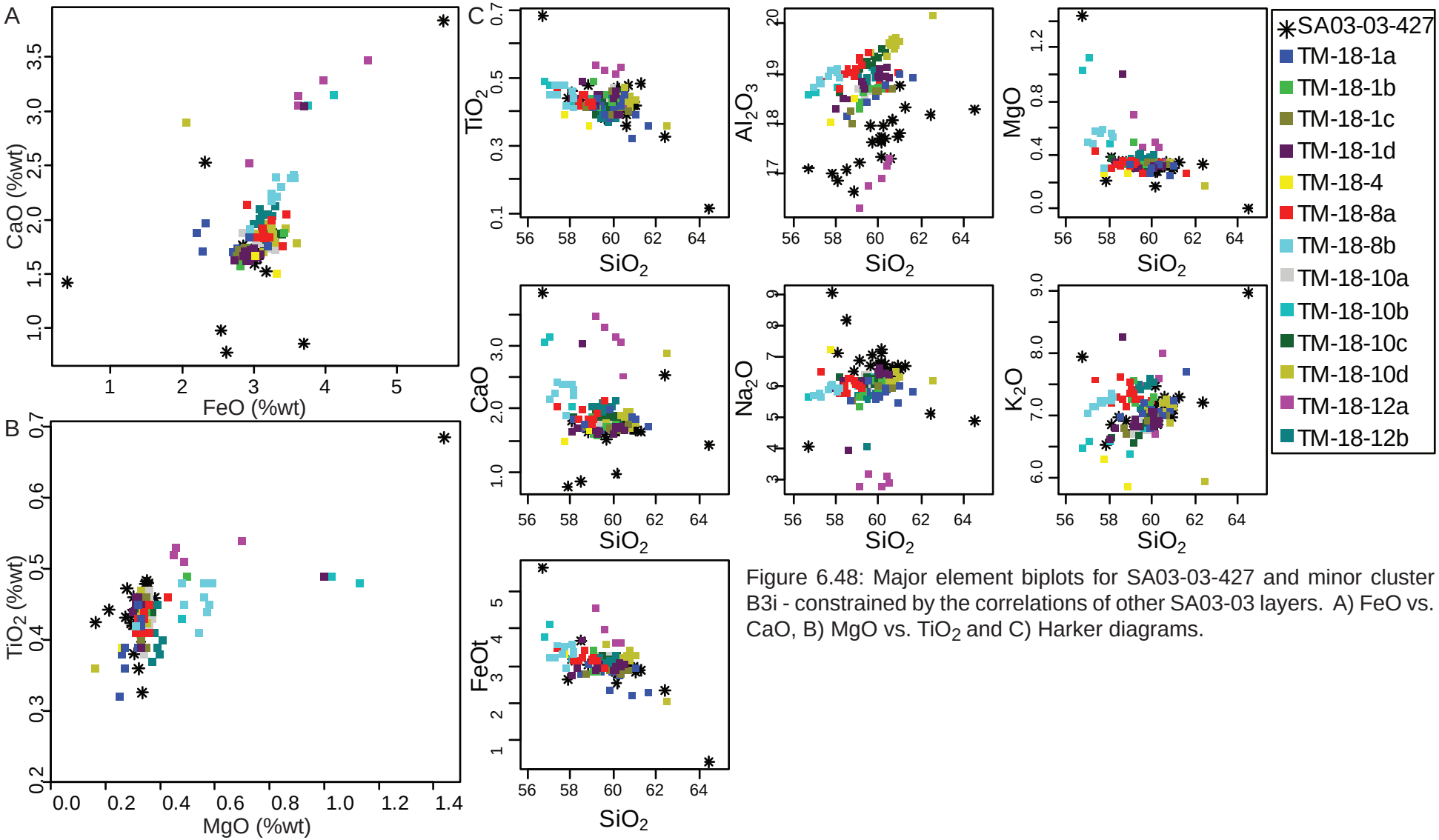

Figure 6.48: Major element biplots for SA03-03-427 and minor cluster B3i - constrained by the correlations of other SA03-03 layers. A) FeO vs. CaO, B) MgO vs. TiO_2 and C) Harker diagrams.

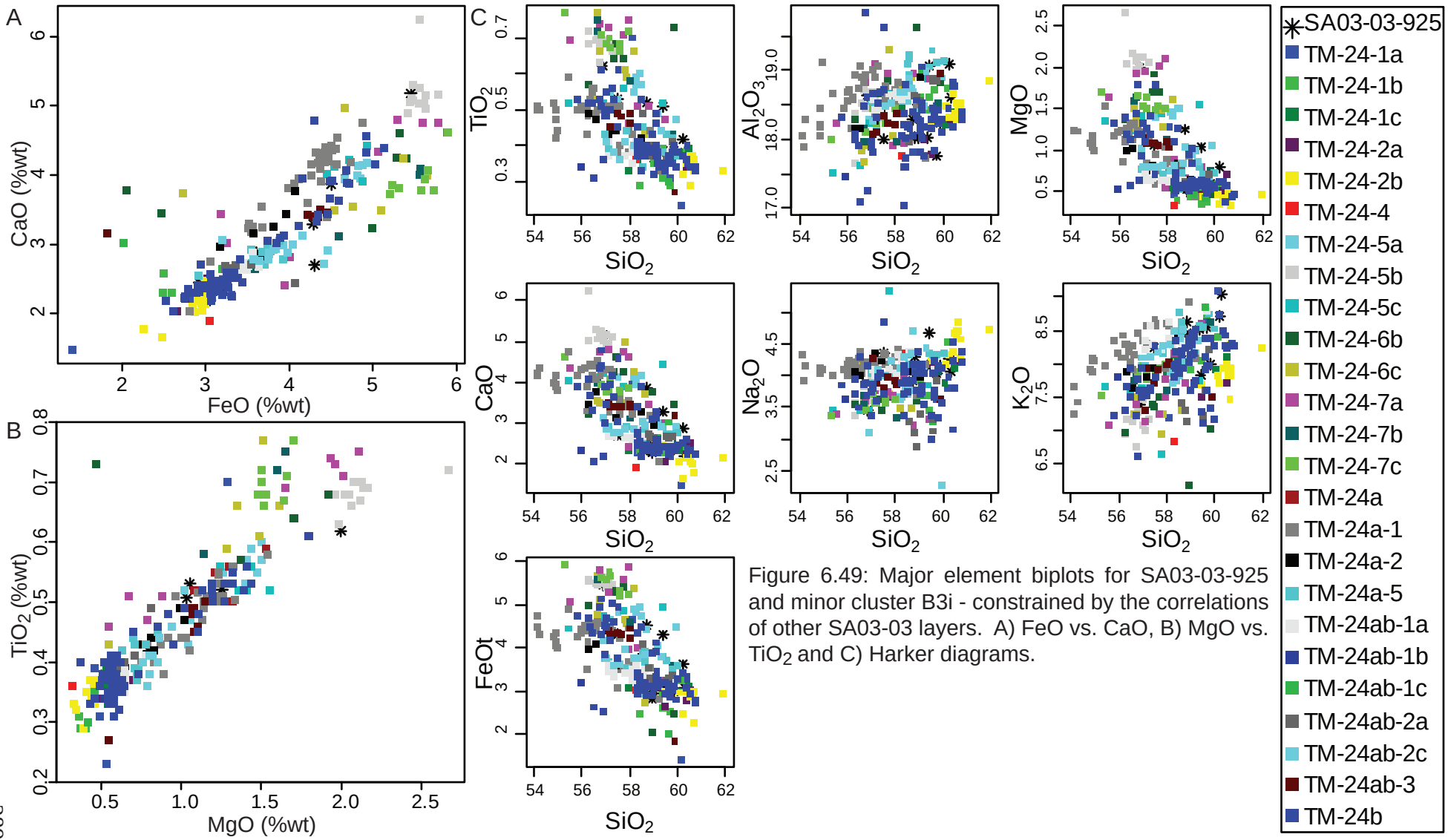

Figure 6.49: Major element biplots for SA03-03-925 and minor cluster B3i - constrained by the correlations of other SA03-03 layers. A) FeO vs. CaO, B) MgO vs. TiO_2 and C) Harker diagrams.

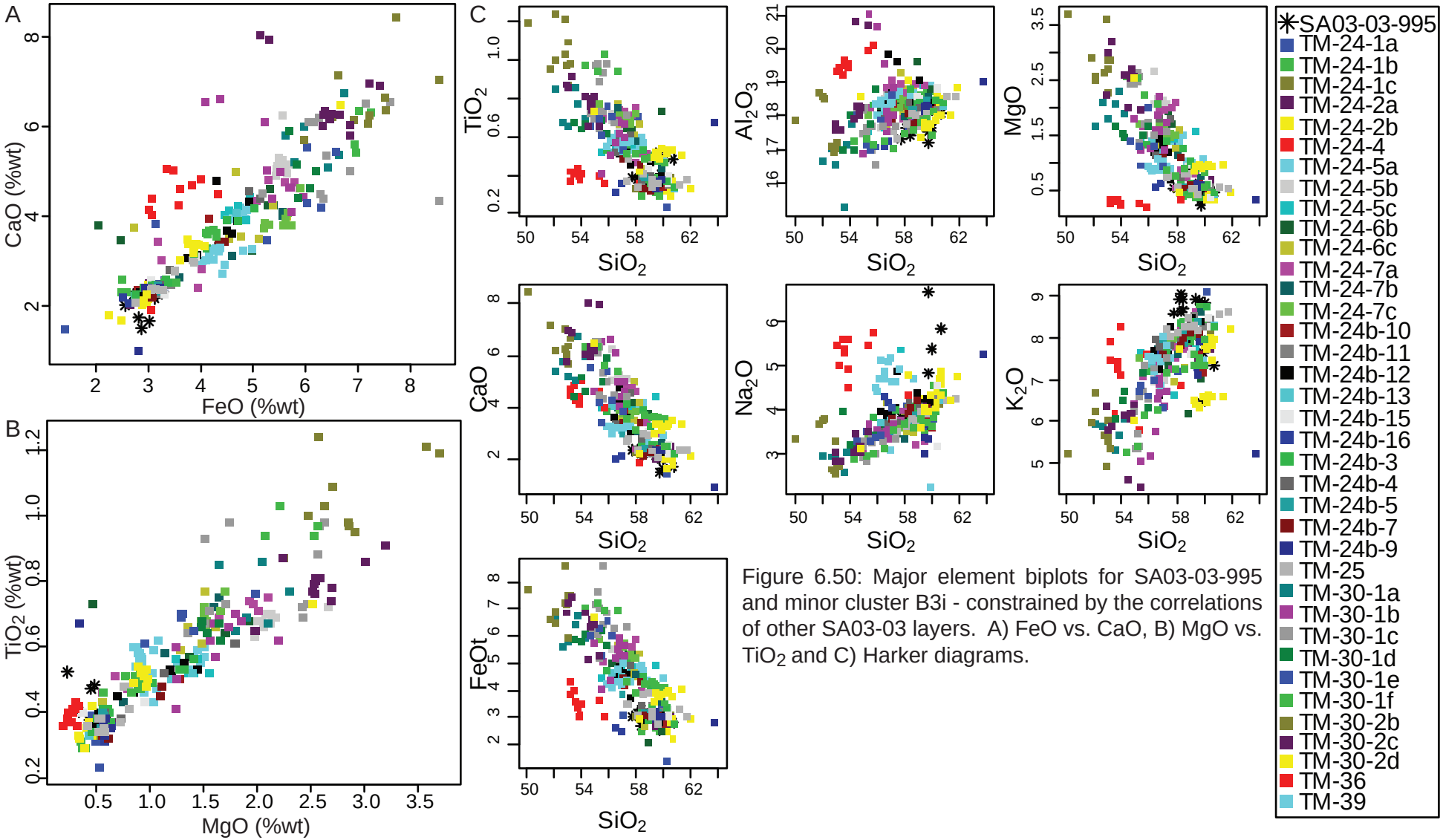

Figure 6.50: Major element biplots for SA03-03-995 and minor cluster B3i - constrained by the correlations of other SA03-03 layers. A) FeO vs. CaO, B) MgO vs. TiO_2 and C) Harker diagrams.

Table 6.6: Summary of eruptives geochemically matched between SA03-03 and the Lago Grande di Monticchio data of Wulf *et al*. (2004, 2008). References for the raw ^{14}C dates are provided in the text. Radiocarbon dates were calibrated using OXCAL Version 4.1 (Bronk Ramsey, 2009) and the INTCAL 09 calibration curve for radiocarbon (Reimer *et al.,* 2009)

SA03-03 tephra	Monticchio tephra layer	Origin	Volcanic event	Calibrated 2σ age (cal yr)	Dating method	Dated material
SA03-03-25	TM-12	Vesuvius	Greenish/Verdoline	19,480 – 19,050 BP	^{14}C	Charcoal (proximal tephra)
SA03-03-80	TM-13	Vesuvius	Pomici di Base	22,240 – 21,150 BP	^{14}C	Underlying paleosols (proximal tephra)
SA03-03-383	TM-16b	Vesuvius	Codola (base)	29,921 - 28,896 BP	^{14}C	Underlying paleosols (proximal tephra)
SA03-03-413	TM-18	Campi Flegrei	Campanian Ignimbrite	39,390 – 39,170 BP	$^{40}Ar/^{39}Ar$	Sanidine (proximal tephra)
SA03-03-427	TM-18-1	Campi Flegrei	SMP1-a	38,680 – 35,000 BP	varves	LGdM sediment chronology
SA03-03-645	TM-18-5, TM-18-9, TM-18-14	Ischia	Citara Series	N/A	N/A	N/A
SA03-03-685	TM-19	Ischia	Monte Epomeo Green Tuff	56,400 – 55,600 BP	$^{40}Ar/^{39}Ar$	Sanidine (distal tephra)
SA03-03-925	TM-24	Campi Flegrei	X-5	107,000 – 103,000 BP	$^{40}Ar/^{39}Ar$	Sanidine (distal tephra)
SA03-03-995	TM-24-2	Campi Flegrei	Unknown	103,556	varves	LGdM sediment chronology

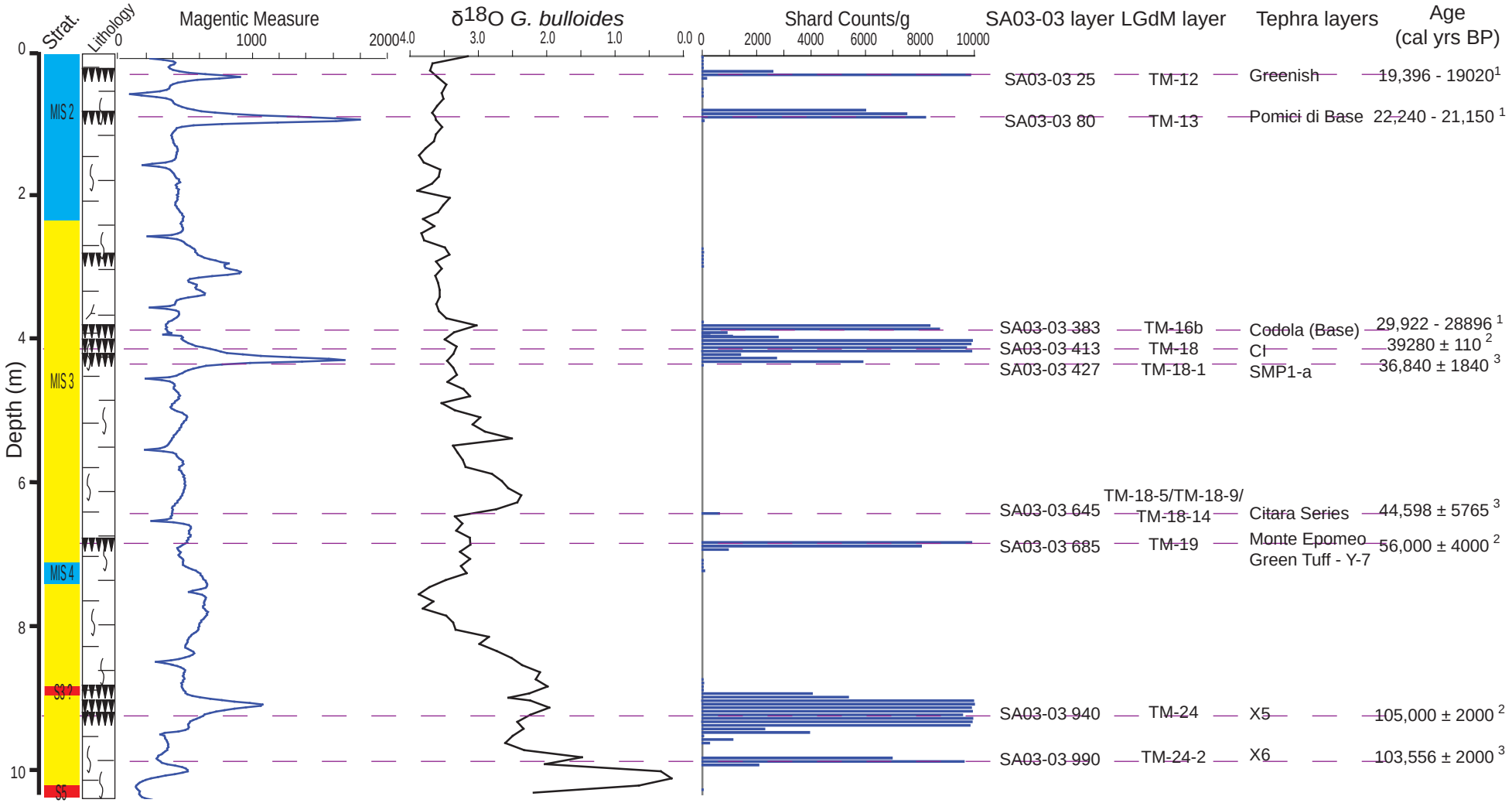

Figure 6.51: Summary diagram for the tephra record obtained from SA03-03 with correlations to LGdM layers, the volcanic event those layers represent and the ages of those layers. Additional stratigraphic information provided by ISMAR, Bologna. Current best age estimates are shown [1] = Calibrated radiocarbon date (shown as an age range), [2] = $^{40}Ar/^{39}Ar$ date and [3] = LGdM varve chronology (both shown as mean age ± error).

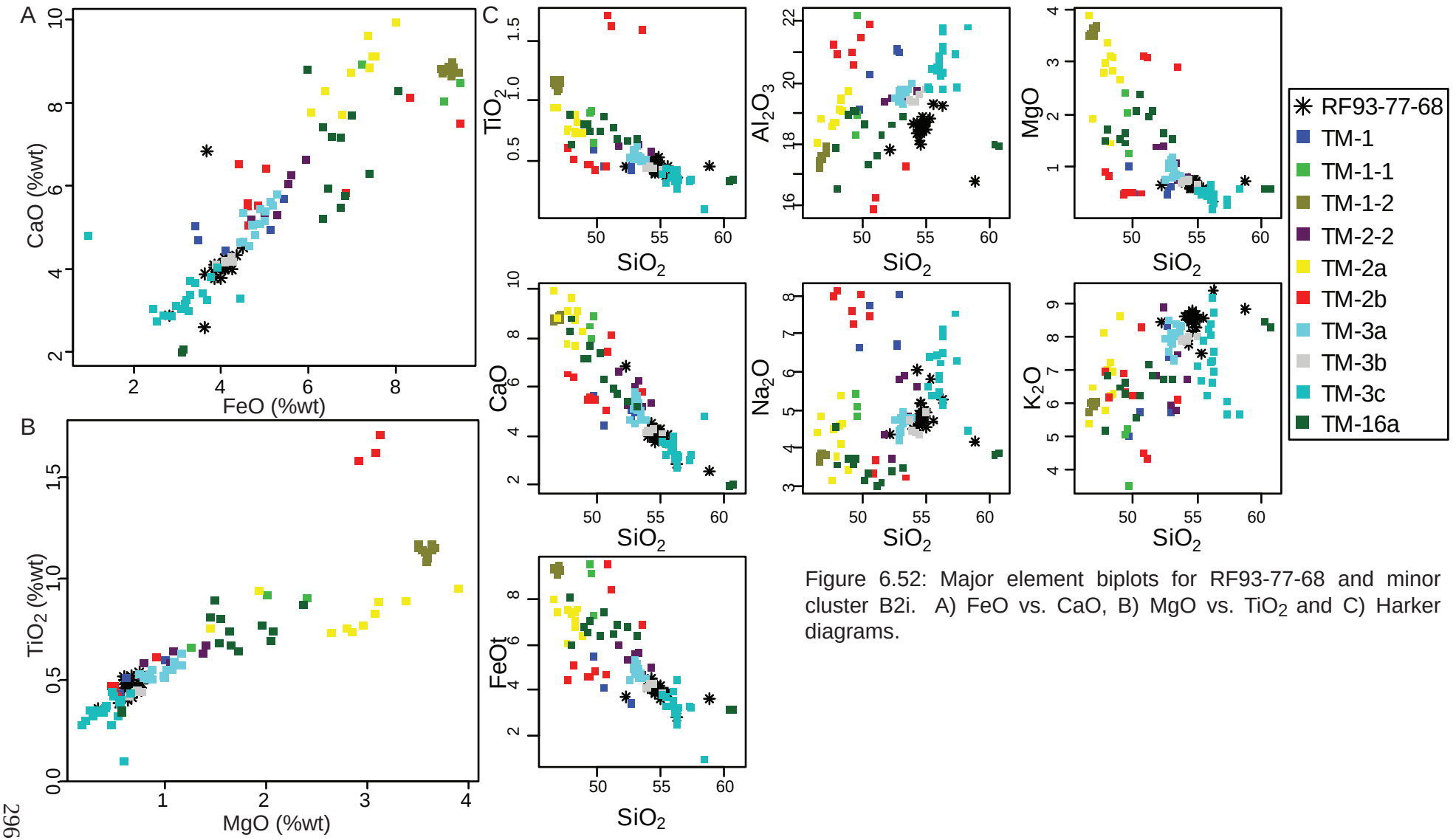

Figure 6.52: Major element biplots for RF93-77-68 and minor cluster B2i. A) FeO vs. CaO, B) MgO vs. TiO_2 and C) Harker diagrams.

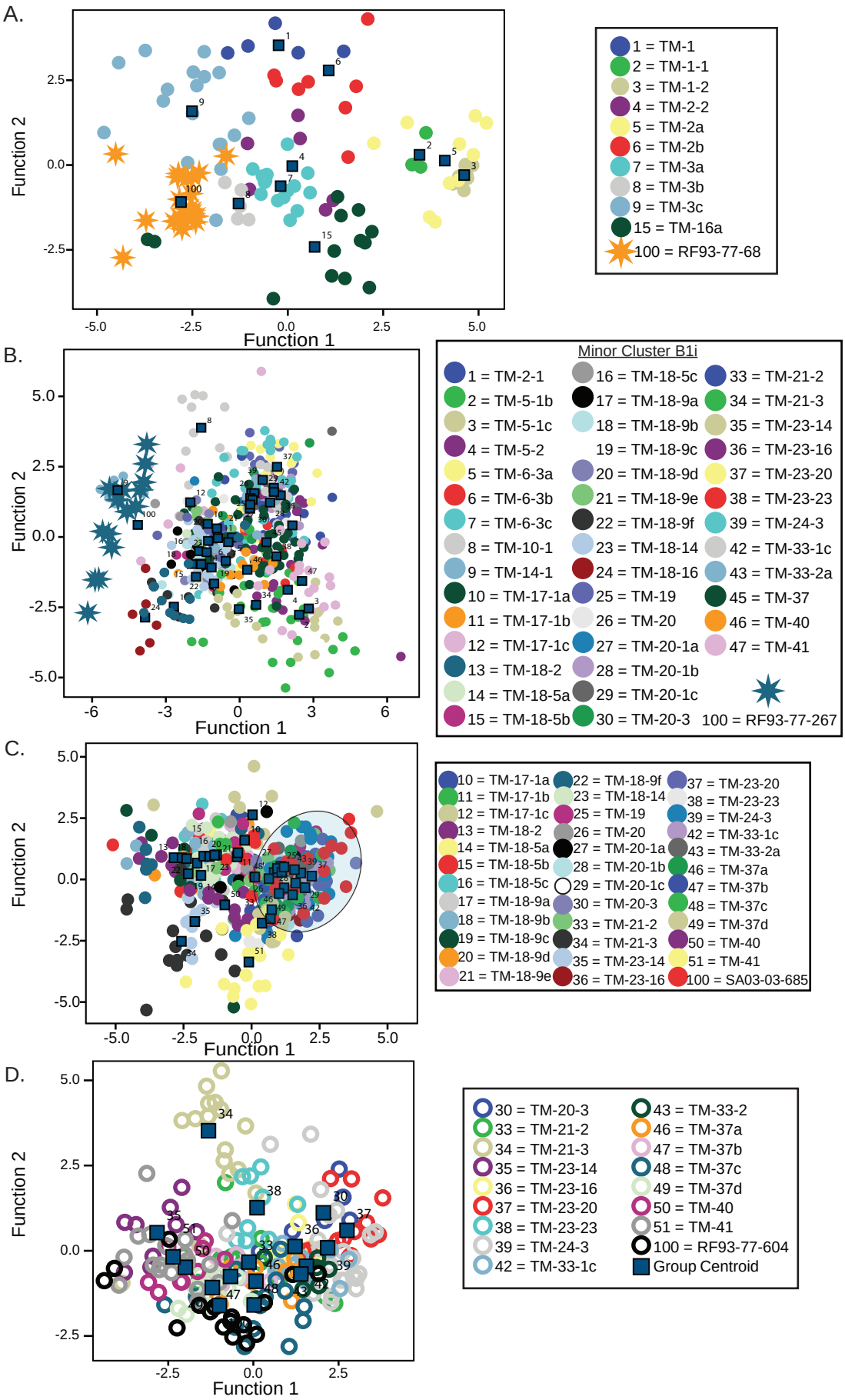

Figure 6.53: Plots of the 1st and 2nd canonical discriminant function axes. A) RF93-77-63 and minor cluster B2i. B) RF93-77-267 and minor cluster B1i. C) RF93-77-450 and minor cluster B1i. D) RF93-77-604 and minor cluster B1i. Envelopes are drawn around the groups of data simply to aid with their visualisation.

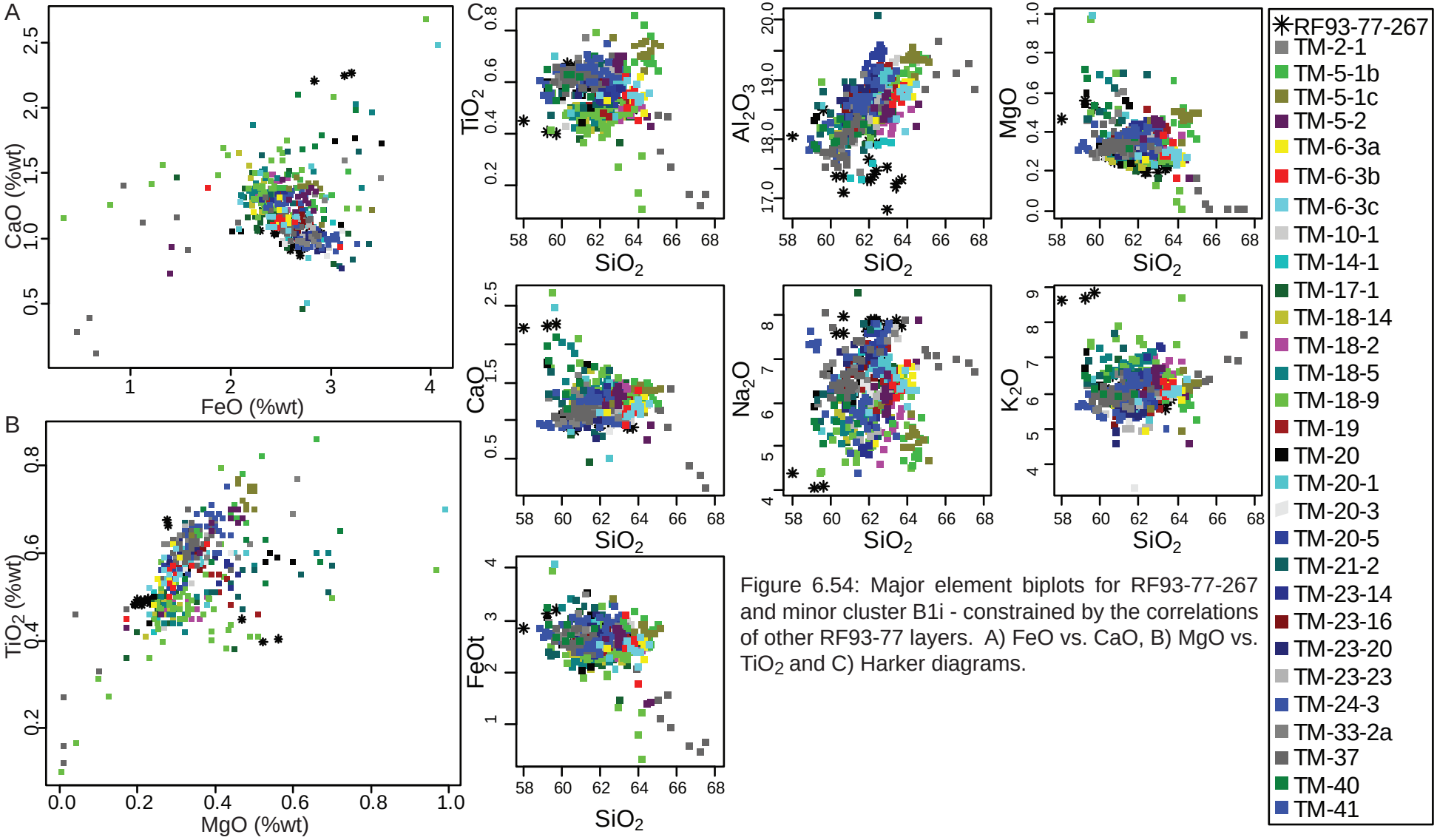

Figure 6.54: Major element biplots for RF93-77-267 and minor cluster B1i - constrained by the correlations of other RF93-77 layers. A) FeO vs. CaO, B) MgO vs. TiO_2 and C) Harker diagrams.

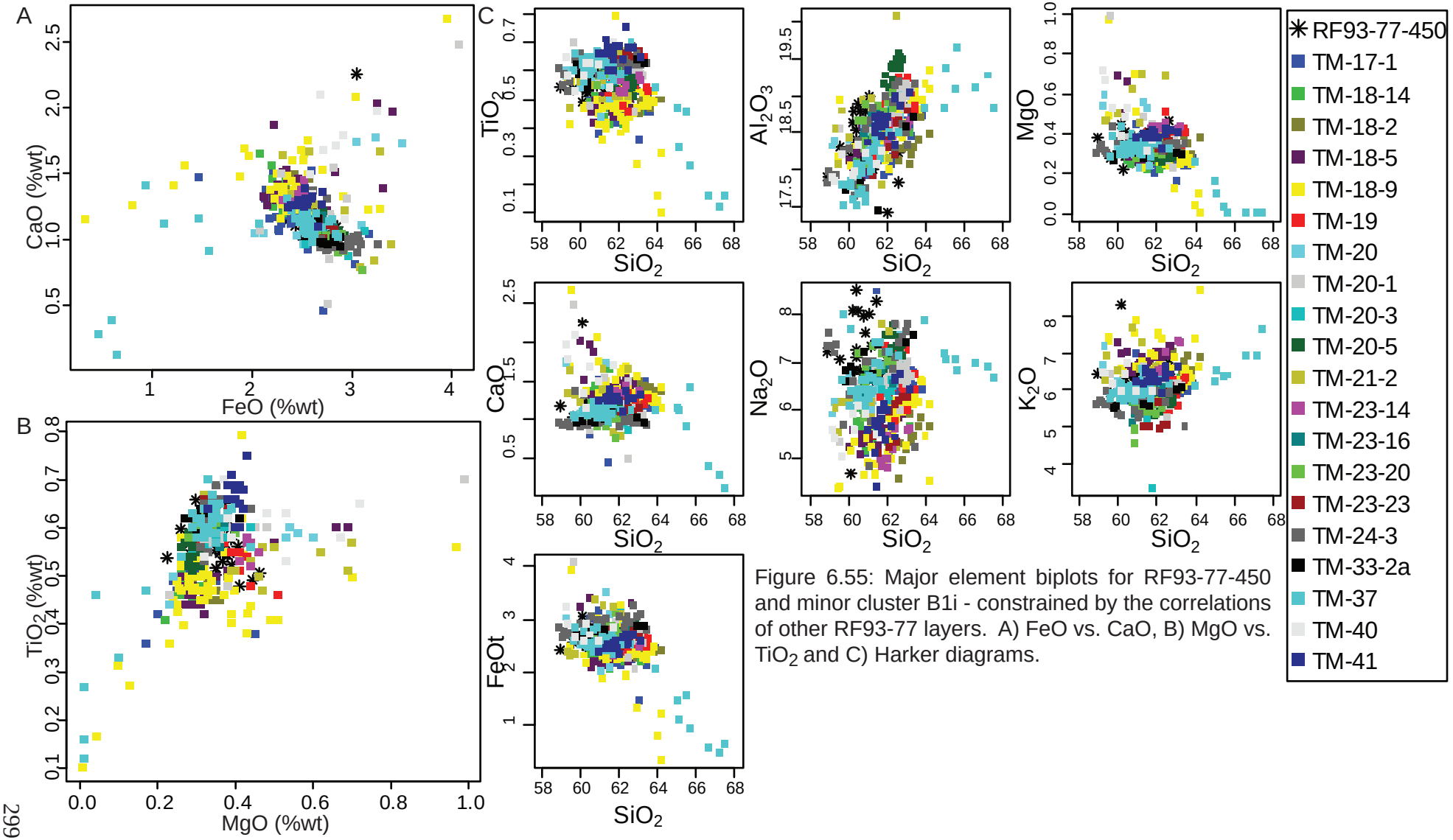

Figure 6.55: Major element biplots for RF93-77-450 and minor cluster B1i - constrained by the correlations of other RF93-77 layers. A) FeO vs. CaO, B) MgO vs. TiO_2 and C) Harker diagrams.

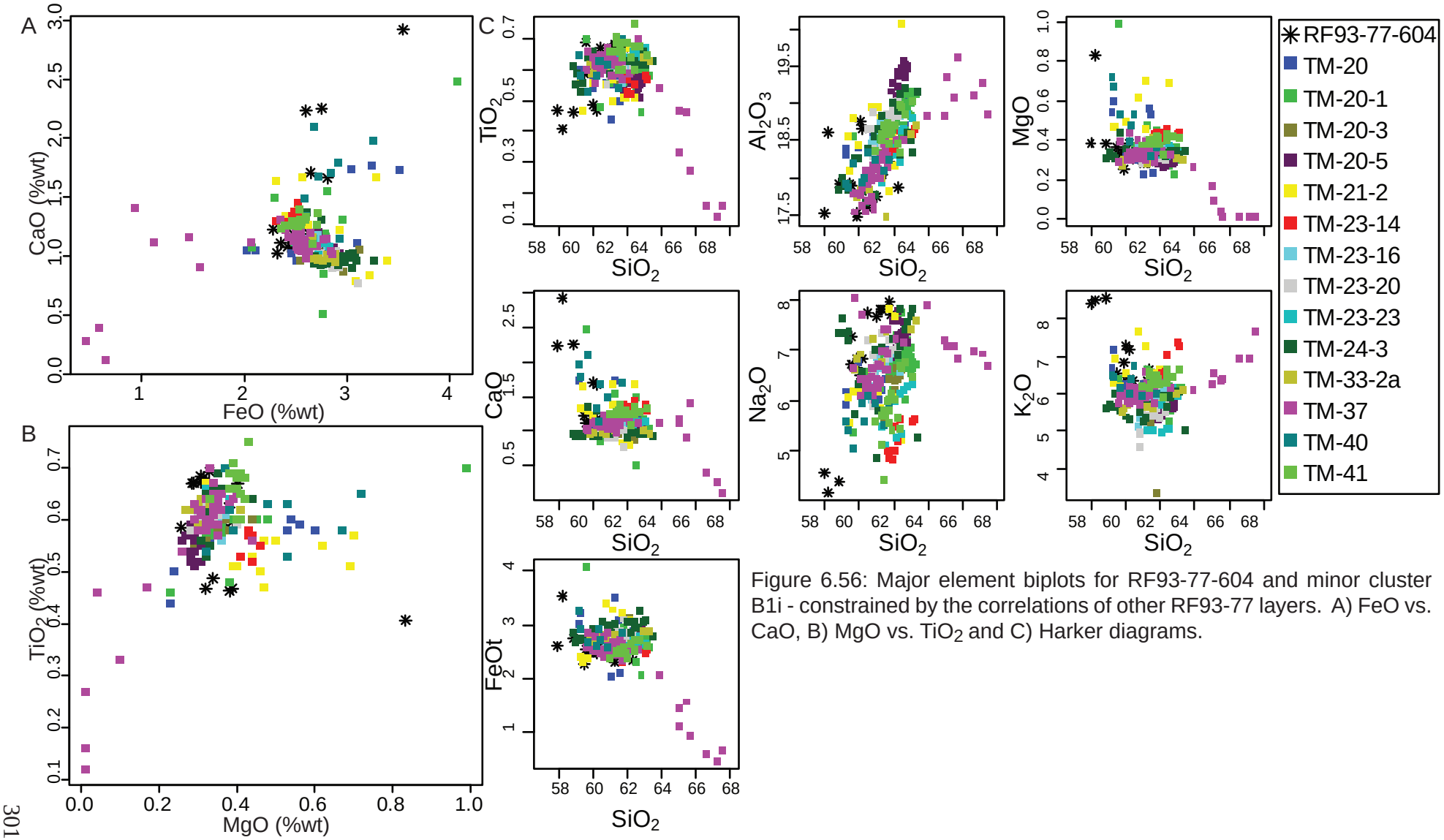

Figure 6.56: Major element biplots for RF93-77-604 and minor cluster B1i - constrained by the correlations of other RF93-77 layers. A) FeO vs. CaO, B) MgO vs. TiO_2 and C) Harker diagrams.

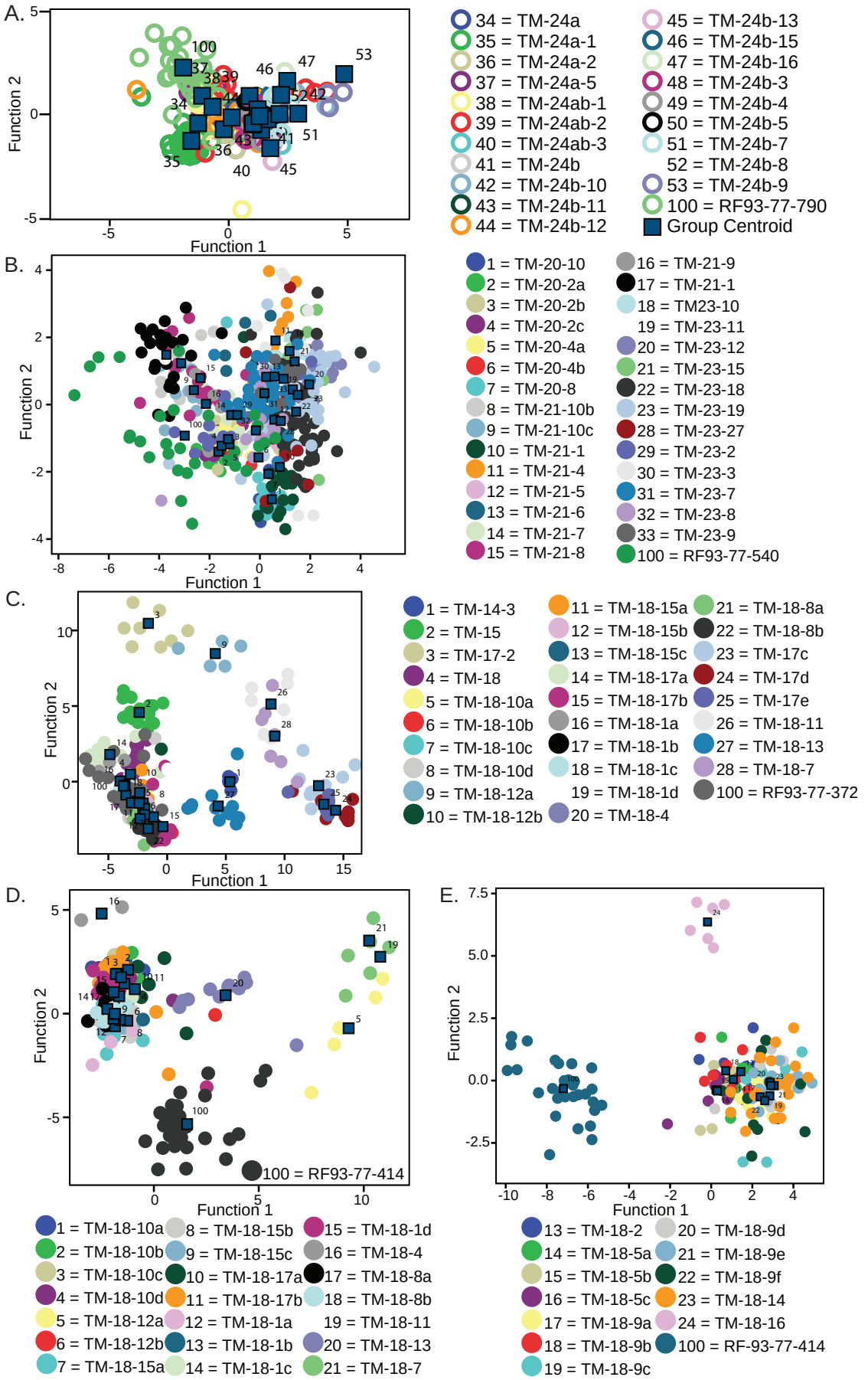

Figure 6.57: A) RF93-77-790 and LGdM layers correlated to the X-5. B) RF93-77-540 and minor cluster B3i. C) RF93-77-372 and minor cluster B3i. D) RF93-77-414 and minor cluster B3i showing no grouping. E) RF93-77-414 and minor cluster B1i showing no grouping.

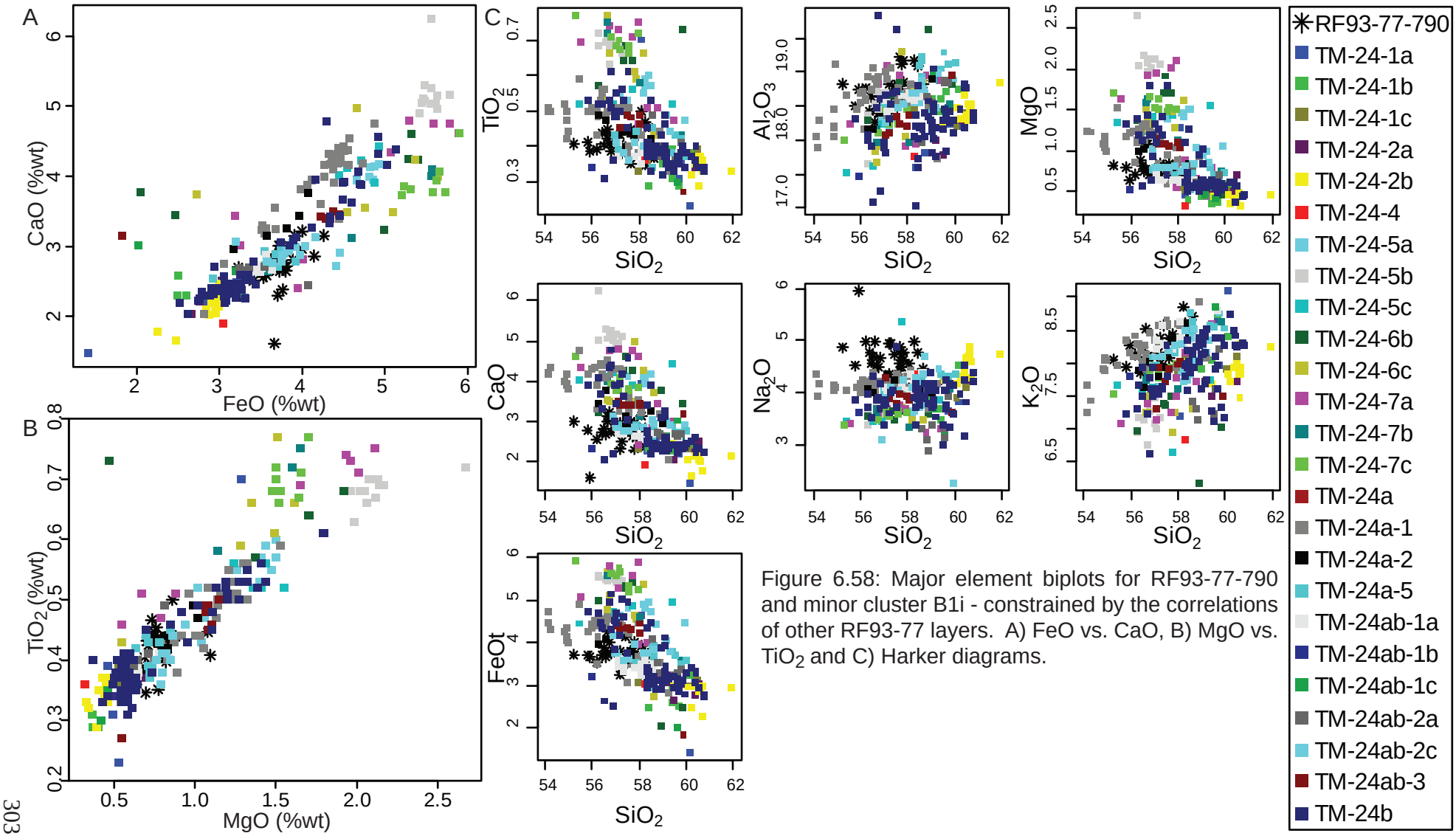

Figure 6.58: Major element biplots for RF93-77-790 and minor cluster B1i - constrained by the correlations of other RF93-77 layers. A) FeO vs. CaO, B) MgO vs. TiO_2 and C) Harker diagrams.

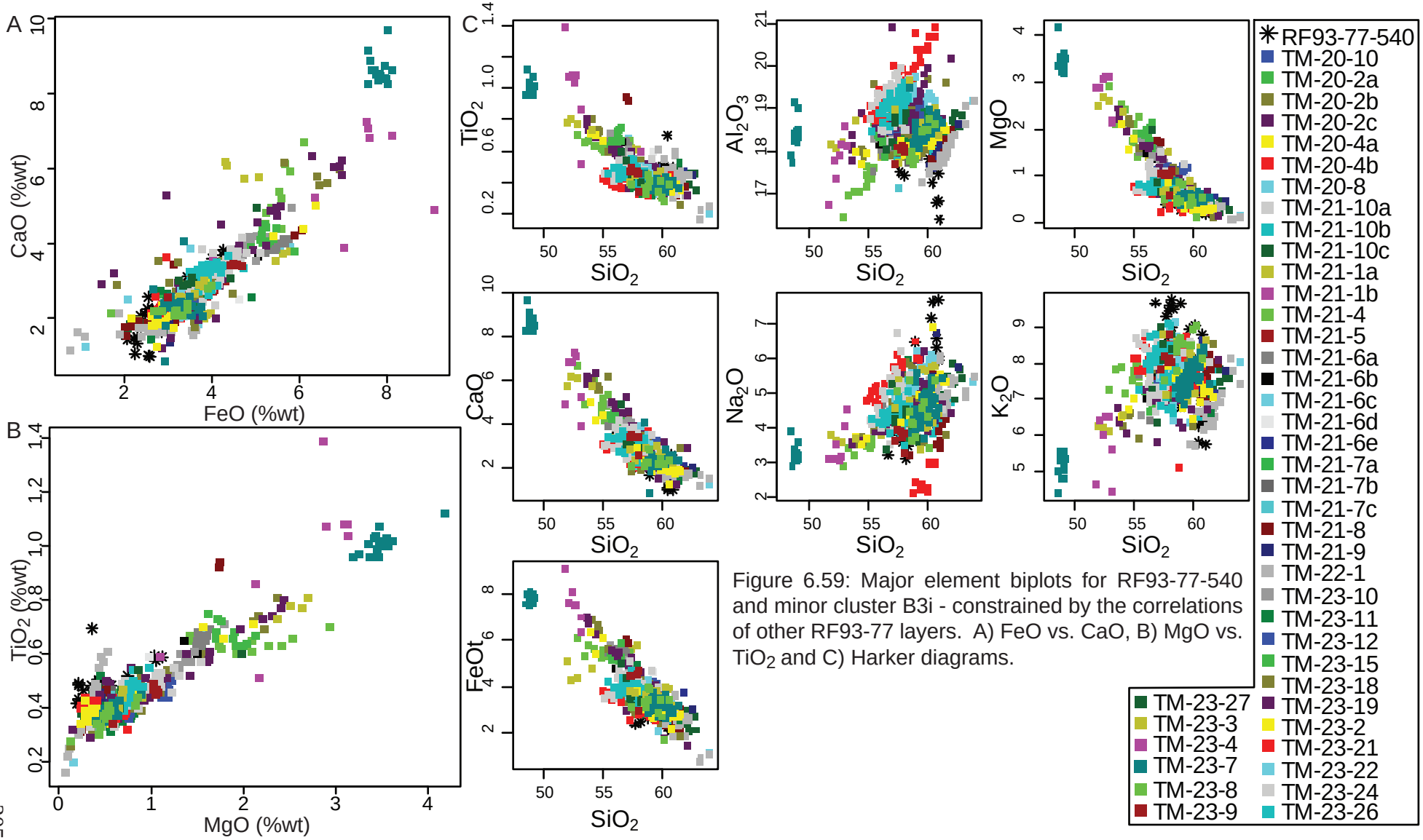

Figure 6.59: Major element biplots for RF93-77-540 and minor cluster B3i - constrained by the correlations of other RF93-77 layers. A) FeO vs. CaO, B) MgO vs. TiO_2 and C) Harker diagrams.

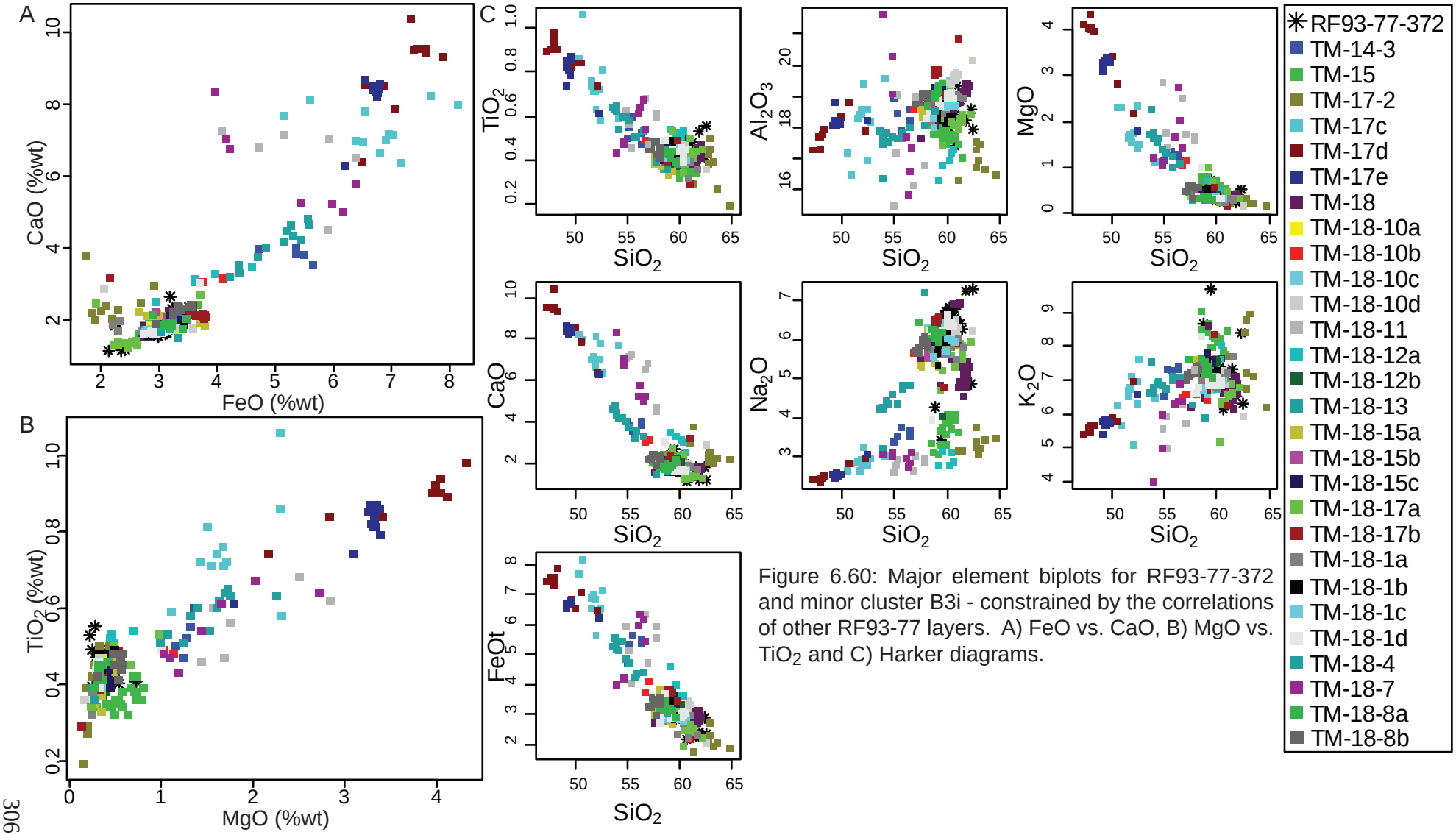

Figure 6.60: Major element biplots for RF93-77-372 and minor cluster B3i - constrained by the correlations of other RF93-77 layers. A) FeO vs. CaO, B) MgO vs. TiO_2 and C) Harker diagrams.

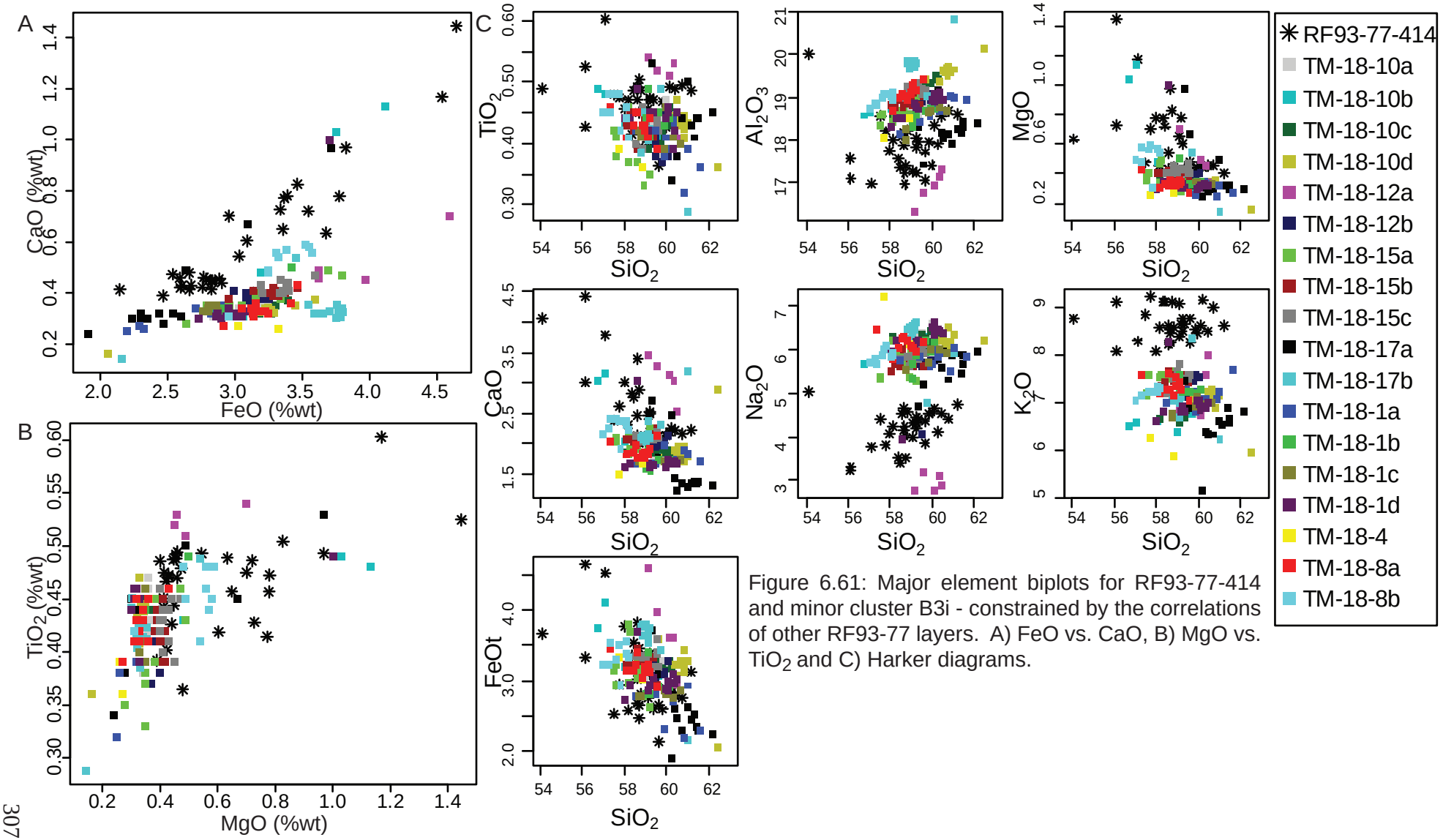

Figure 6.61: Major element biplots for RF93-77-414 and minor cluster B3i - constrained by the correlations of other RF93-77 layers. A) FeO vs. CaO, B) MgO vs. TiO_2 and C) Harker diagrams.

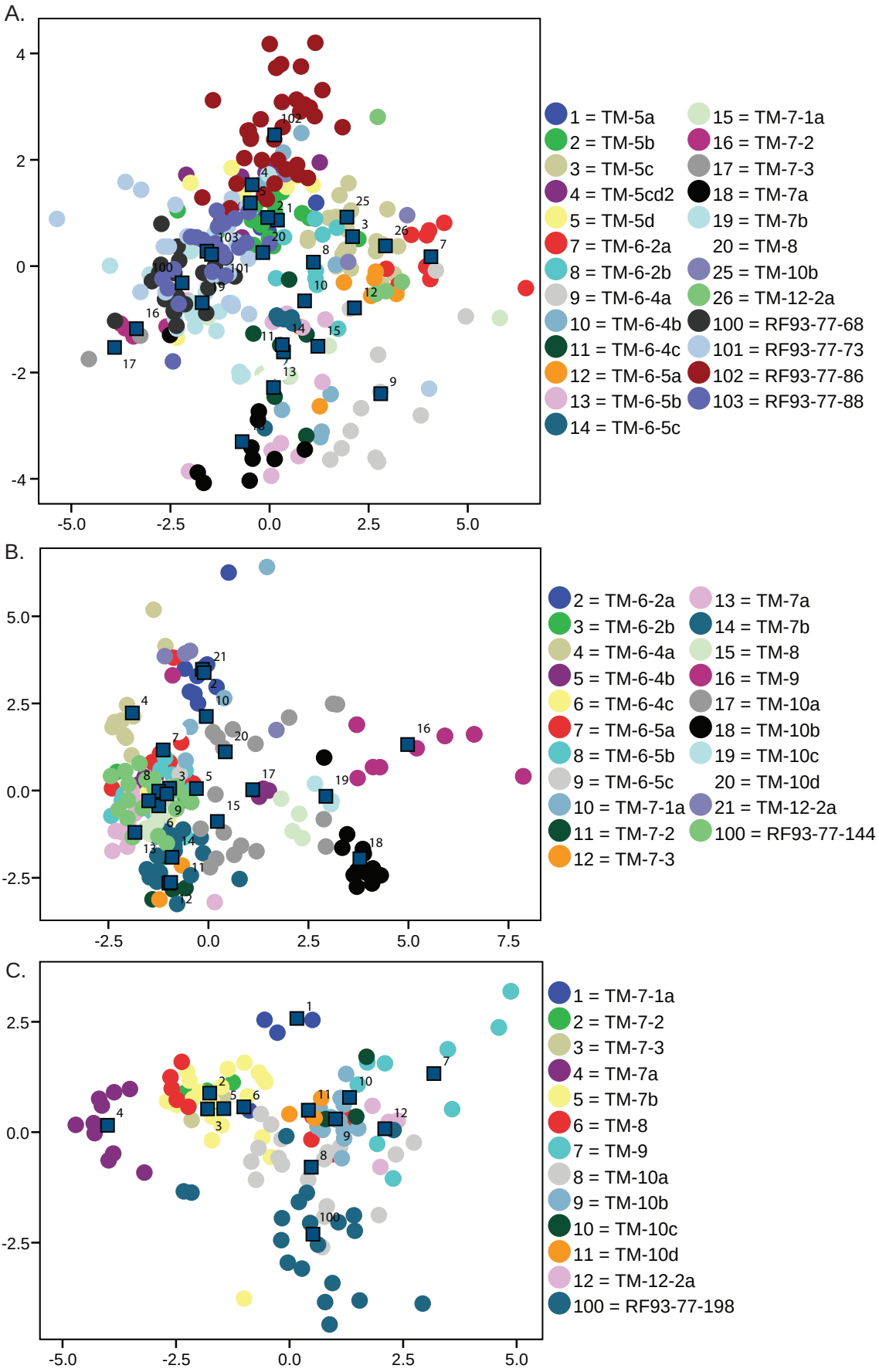

Figure 6.62: A) RF93-77-68, RF93-77-73, RF93-77-86, RF93-77-88 and minor cluster B3i. B) RF93-77-144 and minor cluster B3i. C) RF93-77-198 and minor cluster B3i. In all cases, the minor clusters have been constrained by correlations of other RF93-77 layers.

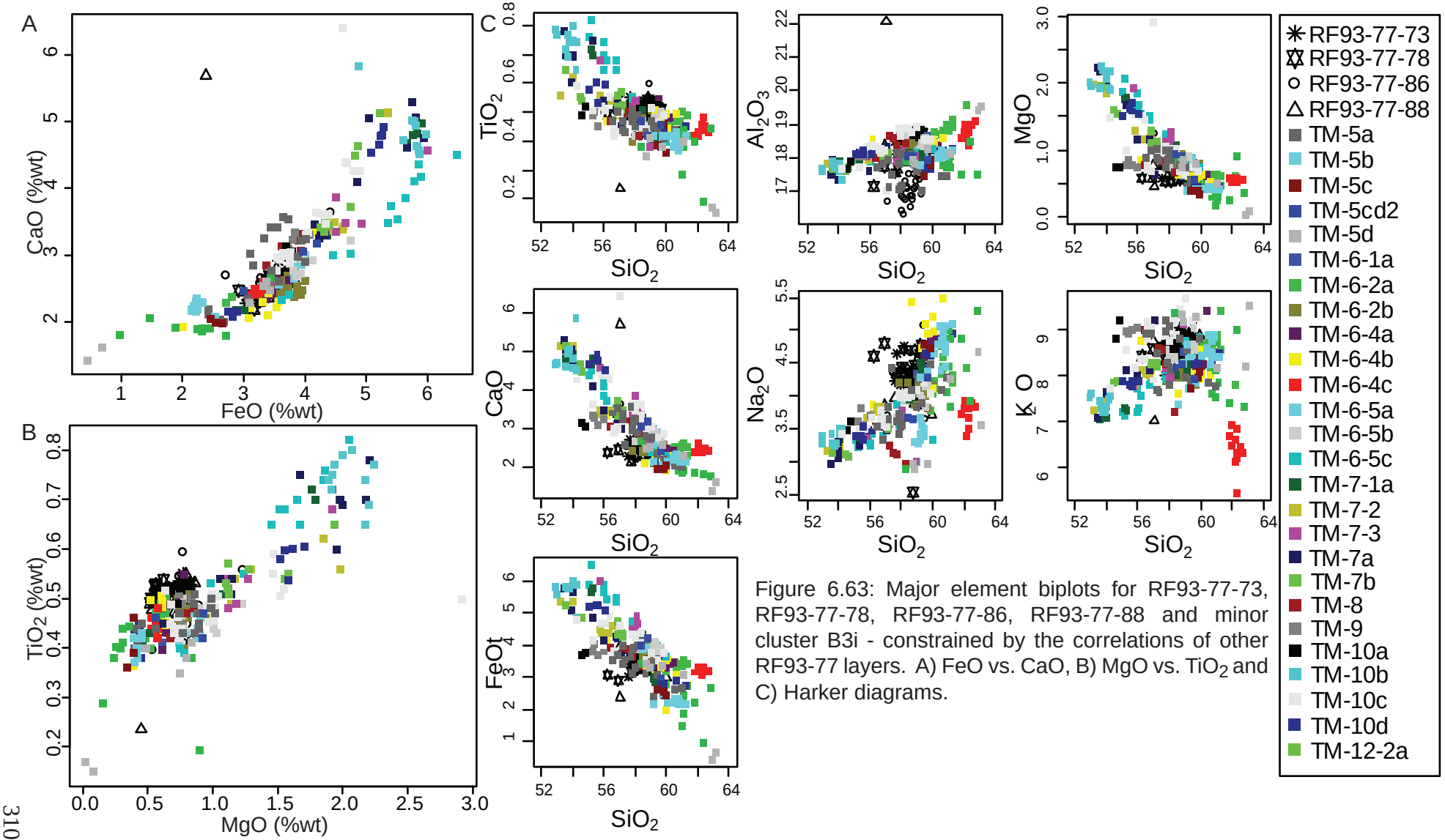

Figure 6.63: Major element biplots for RF93-77-73, RF93-77-78, RF93-77-86, RF93-77-88 and minor cluster B3i - constrained by the correlations of other RF93-77 layers. A) FeO vs. CaO, B) MgO vs. TiO_2 and C) Harker diagrams.

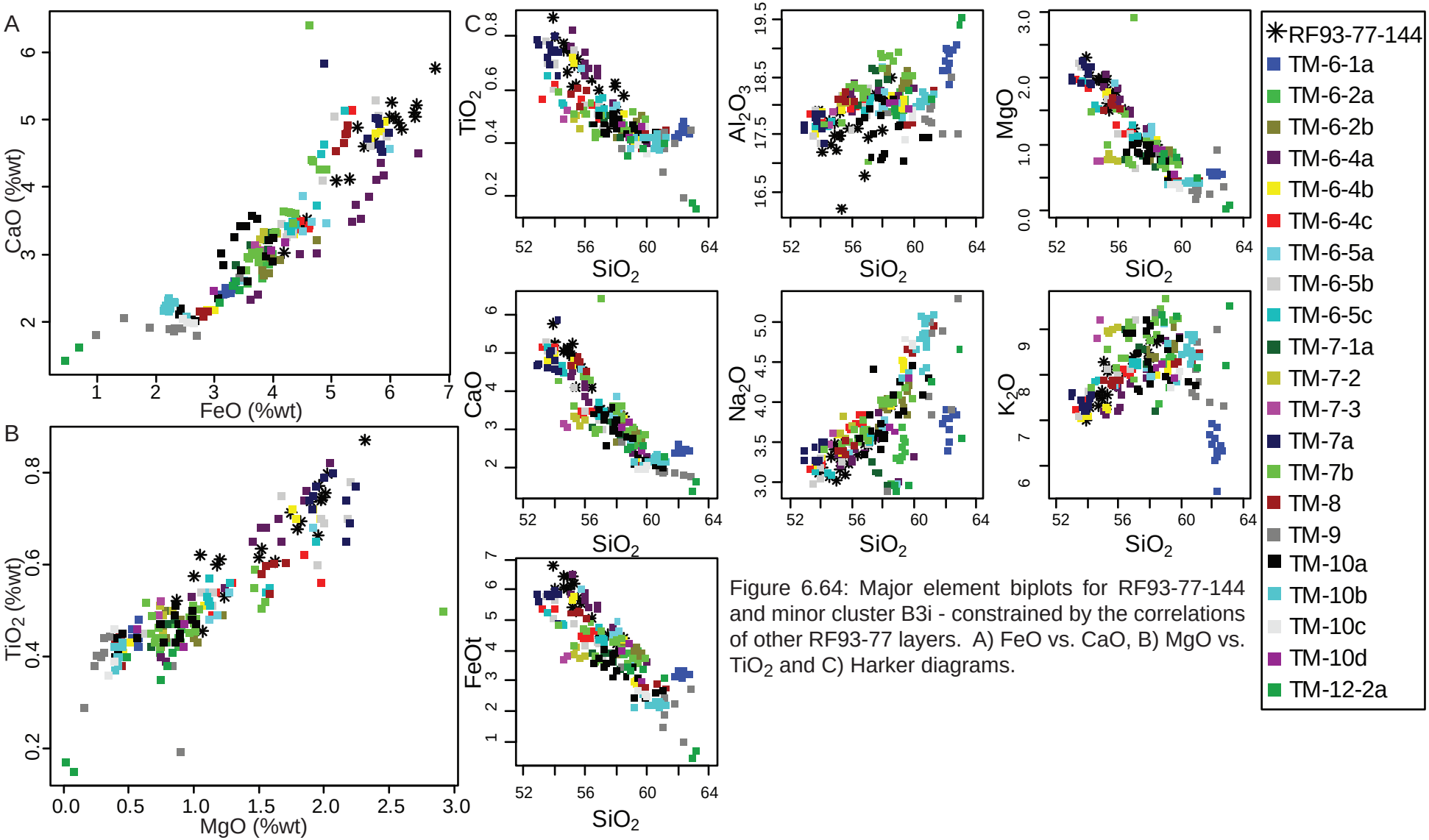

Figure 6.64: Major element biplots for RF93-77-144 and minor cluster B3i - constrained by the correlations of other RF93-77 layers. A) FeO vs. CaO, B) MgO vs. TiO_2 and C) Harker diagrams.

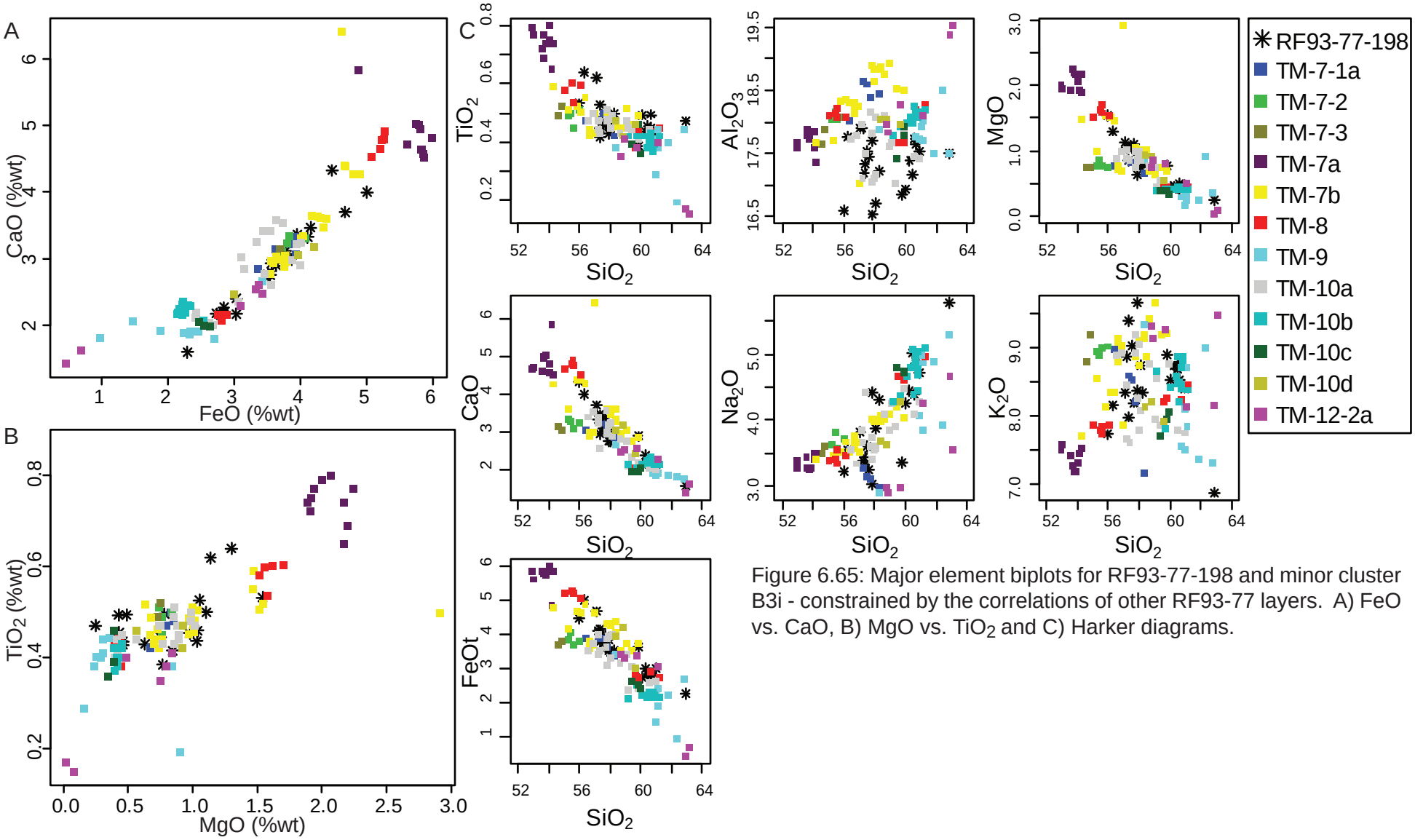

Figure 6.65: Major element biplots for RF93-77-198 and minor cluster B3i - constrained by the correlations of other RF93-77 layers. A) FeO vs. CaO, B) MgO vs. TiO_2 and C) Harker diagrams.

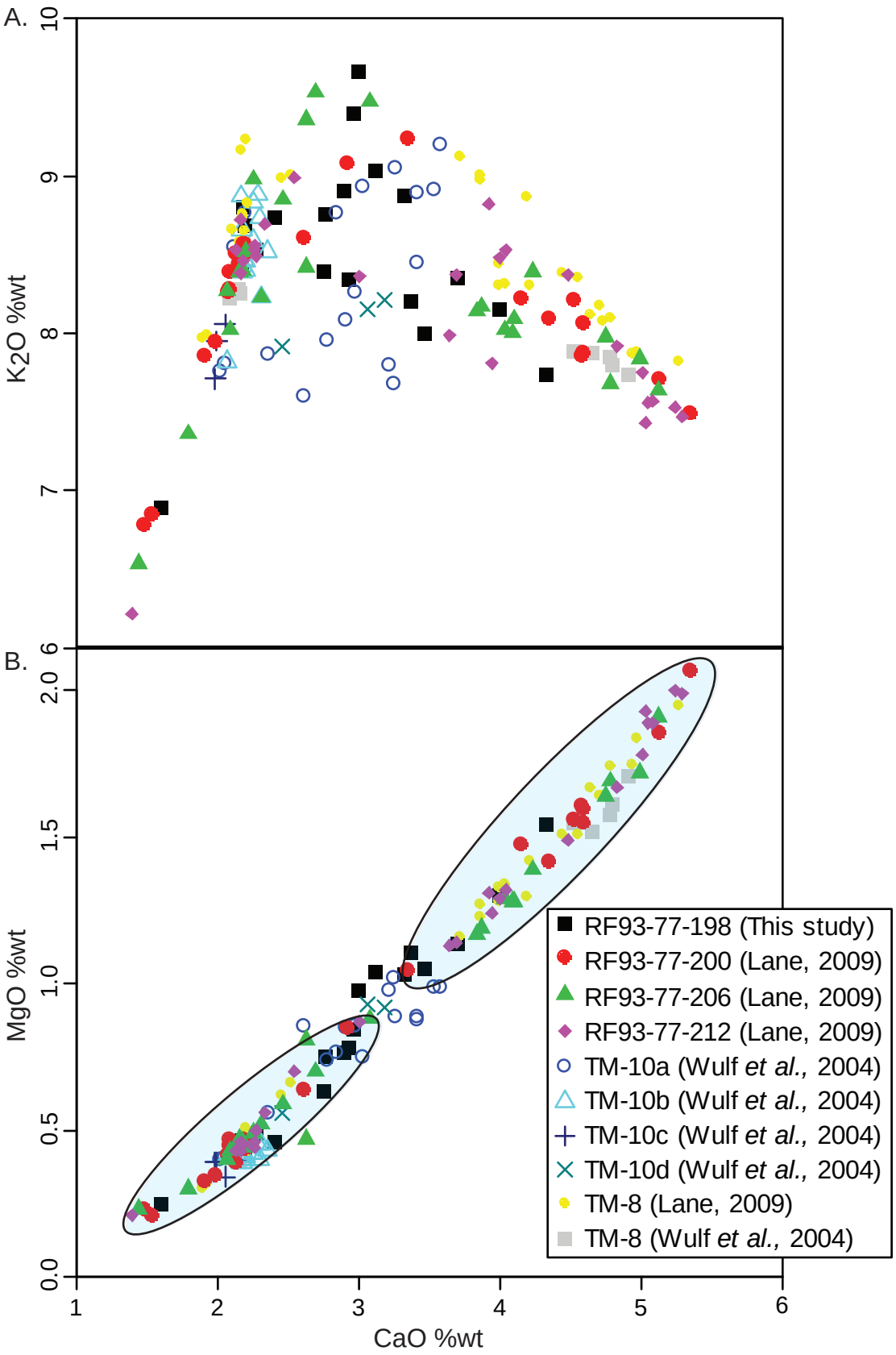

Figure 6.66: a) CaO vs K_2O plot and b) CaO vs MgO plot for RF93-77-198 from this study. This is compared to data from RF93-77 on the layer that Lane (2009) correlated to TM-8 (NYT). The upper, middle and lower levels of the tephra layer were analysed by Lane (2009). Also compared are data from LGdM for TM-8 (NYT) from Wulf *et al.,* 2004 and additional data from Lane 2009 and finally TM-10 a,b,c,d (Lago Amendolare) (Wulf *et al.,* 2004). Envelopes are drawn around the two groups of NYT data simply to aid with their visualisation. See text for full details.

Table 6.8: Summary of eruptives geochemically matched between RF93-77 and the Lago Grande di Monticchio data of Wulf *et al.* (2004, 2008). References for the raw ^{14}C dates are provided in the text. Radiocarbon dates were calibrated using OXCAL Version 4.1 (Bronk Ramsey, 2009) and the INTCAL 09 calibration curve for radiocarbon (Reimer *et al.,* 2009)

RF93-77 tephra	Monticchio tephra layer	Origin	Volcanic event	Calibrated 2σ age (cal yr)	Dating method	Dated material
RF93-77-68	TM-3b	Vesuvius	AP3	2946 - 2744 BP	^{14}C	Charcoal (proximal tephra)
RF93-77-86	TM-5	Campi Flegrei	Agnano Monte Spina	4690 – 4300 BP	^{14}C	Charcoal (proximal tephra)
RF93-77-144	TM-6-5	Campi Flegrei	N/A	12,073	varves	LGdM sediment chronology
RF93-77-198	TM-8	Campi Flegrei	Neapolitan Yellow Tuff	14,320 – 13,900 BP	^{14}C	Underlying palaeosols (proximal tephra)
RF93-77-267	TM-14-1	Ischia	Faro di Punta Imperatore	22,420 – 20,280 BP	varves	LGdM sediment chronology
RF93-77-372	TM-18	Campi Flegrei	Campanian Ignimbrite	39,390 – 39,170 BP	$^{40}Ar/^{39}Ar$	Sanidine (proximal tephra)
RF93-77-414	Unknown	Ischia	N/A	N/A	N/A	N/A
RF93-77-450	TM 19	Ischia	Monte Epomeo Green Tuff	56,400 – 55,600 BP	$^{40}Ar/^{39}Ar$	Sanidine (distal tephra)
RF93-77-540	Unknown	Campi Flegrei	N/A	N/A	N/A	N/A
RF93-77-604	Unknown	Ischia	N/A	N/A	N/A	N/A
RF93-77-790	TM-24	Campi Flegrei	X-5	107,000 – 103,000 BP	$^{40}Ar/^{39}Ar$	Sanidine (distal tephra)

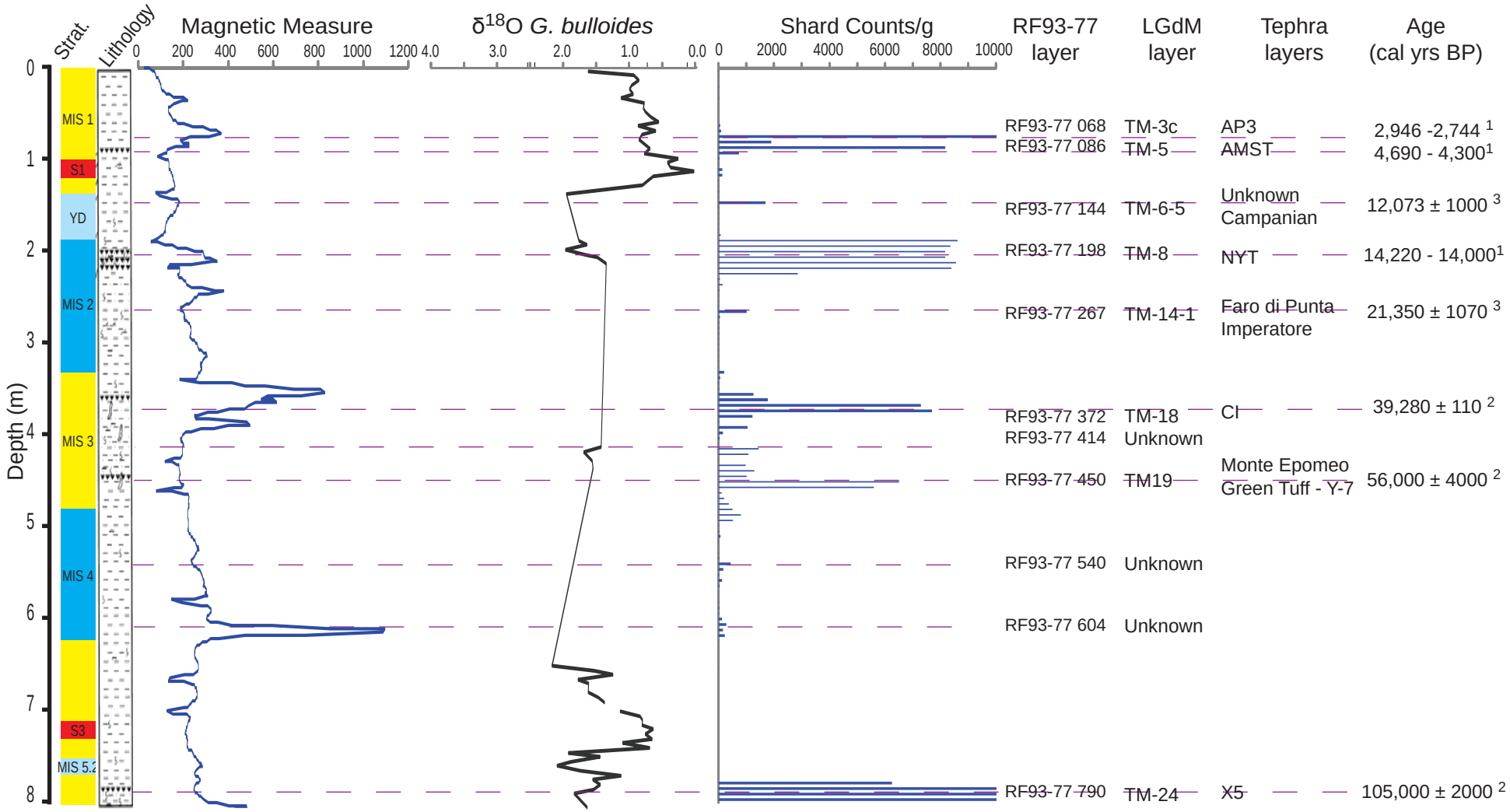

Figure 6.67: Summary diagram for the tephra record obtained from RF93-77 with correlations to LGdM layers, the volcanic event those layers represent and the ages of those layers. Additional stratigraphic information provided by ISMAR, Bologna. Current best age estimates are shown [1] = Calibrated radiocarbon date (shown as an age range), [2] = $^{40}Ar/^{39}Ar$ date and [3] = LGdM varve chronology (both shown as mean age ± error).

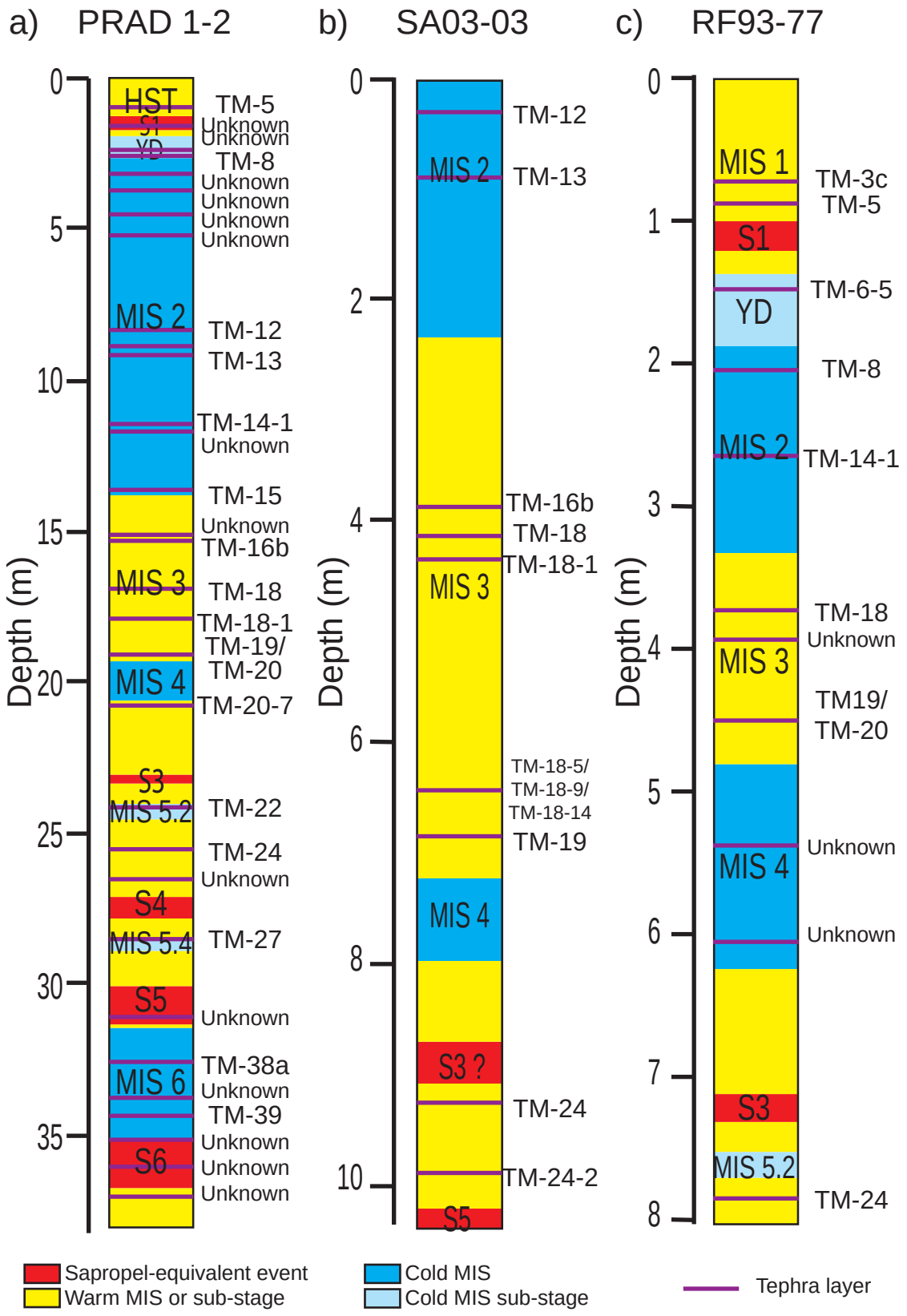

Figure 7.1: Stratigraphic scheme of the three cores with the positions of the tephra layers identified in the sequences marked as purple lines. The equivalent LGdM tephra layer is shown next to the stratigraphic scheme. The stratigraphic scheme is based on a multiproxy approach, including isotope stratigraphy, foraminifera and nannoplankton bioevents, foraminifera warm/cold cyclicity, magnetostratigraphy, ^{14}C AMS radiometric ages and the recognition of sapropel equivalent layers. a) PRAD 1-2, b) SA03-03 and c) RF93-77. Stratigraphic schemes produced by the team at ISMAR Bologna and for PRAD 1-2 by Piva *et al.* (2008a).

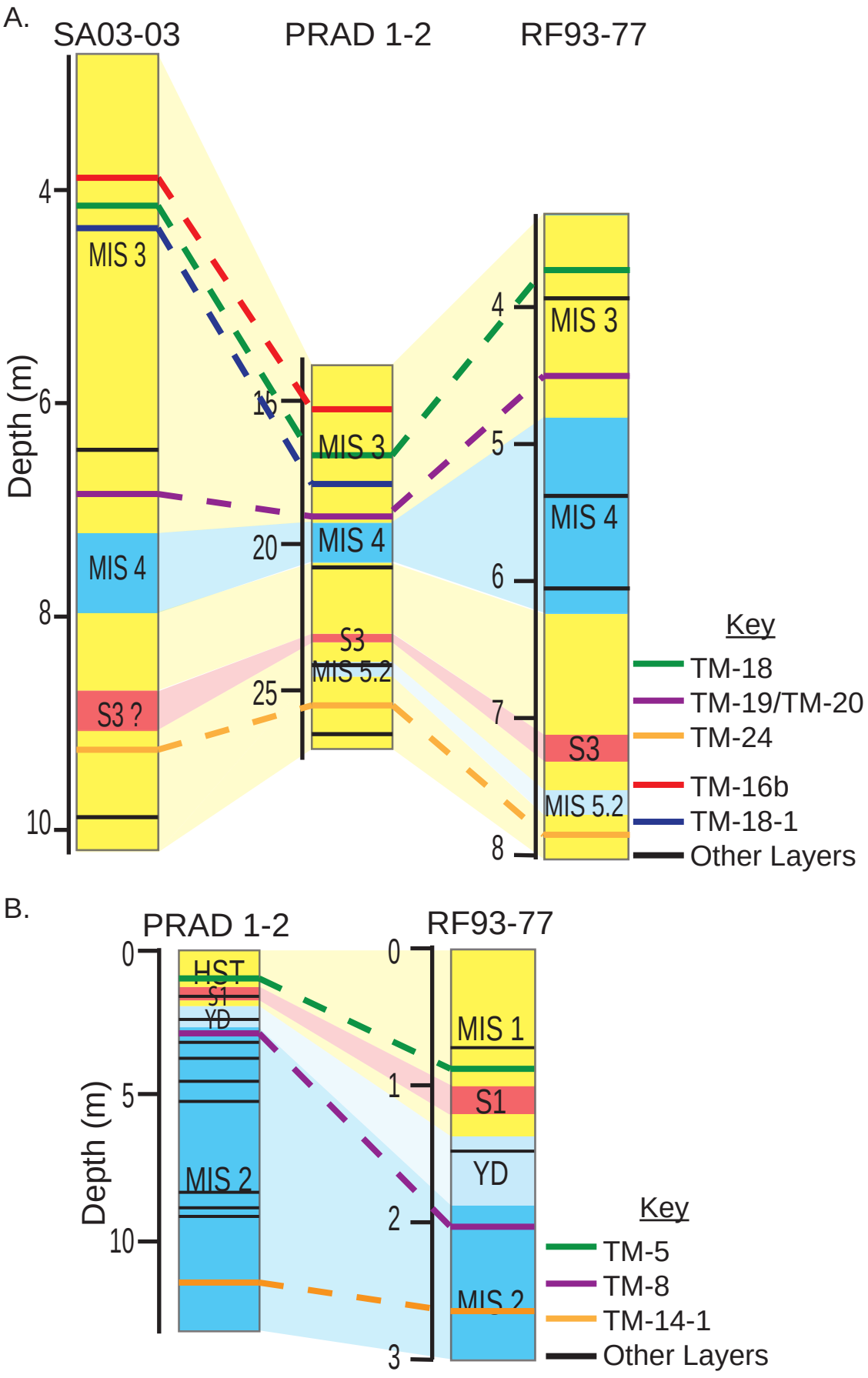

Figure 7.2: Correlation of the stratigraphic schemes of PRAD 1-2, SA03-03 and RF93-77 using the positions of tephra layers common to each sequence. a) MIS5 to MIS3 and b) MIS2 to present day.

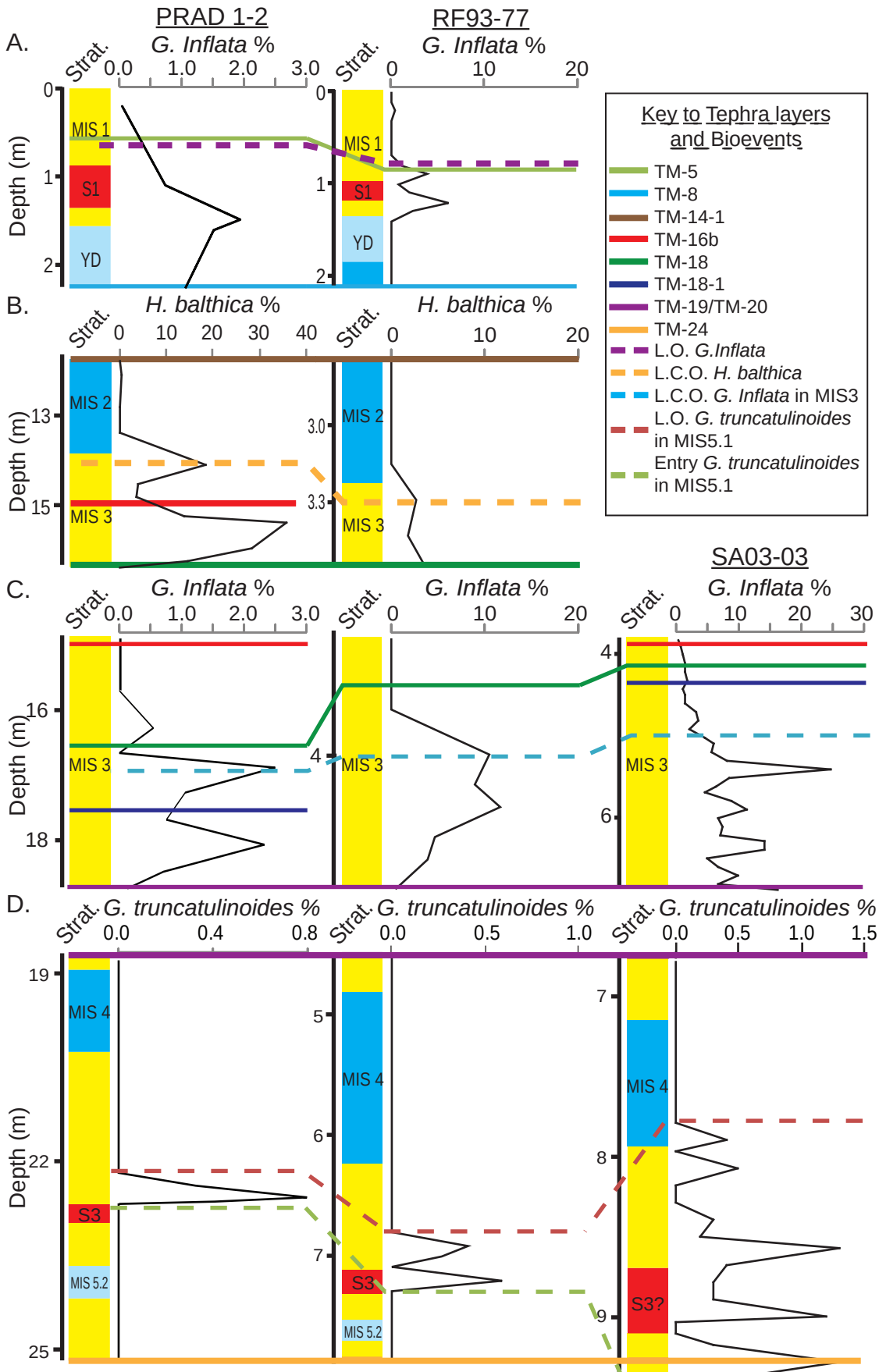

Figure 7.3: Positions of regional bioevents bounded by the stratigraphic positions of tephra layers common to the sequences. A) L.O. *G. inflata* and TM-5, B) L.O.C. *H. balthica* with TM-14-1 and TM-18, C) L.C.O. *G. inflata* in MIS3 with tephra layers TM-18 and TM-18-1 and D) Entry and L.O. of *G. truncatulinoides* in MIS 5.1 TM-19 and TM-24.

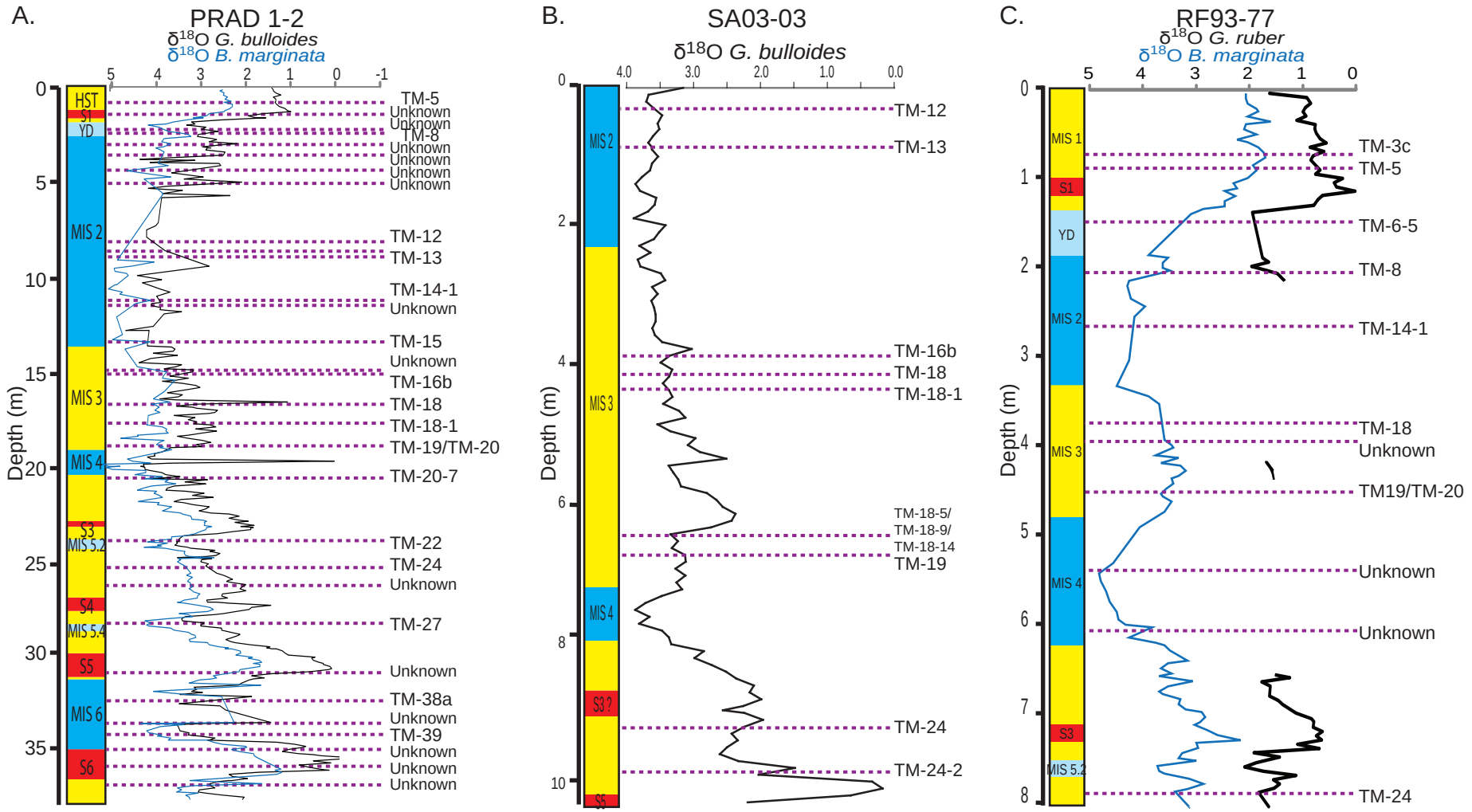

Figure 7.4: Oxygen isotope curves of the three studied marine sequences, with the positions of the tephra layers identified in the sequences marked as purple lines. The LGdM tephra layer each layer is correlated to is shown next to the $\delta^{18}O$ curve. $\delta^{18}O$ records produced by Piva *et al.* (2008a) for PRAD 1-2, Piva and Asioli (unpublished) for SA03-03 and Ariztegui, *et al.* (1996) for RF93-77.

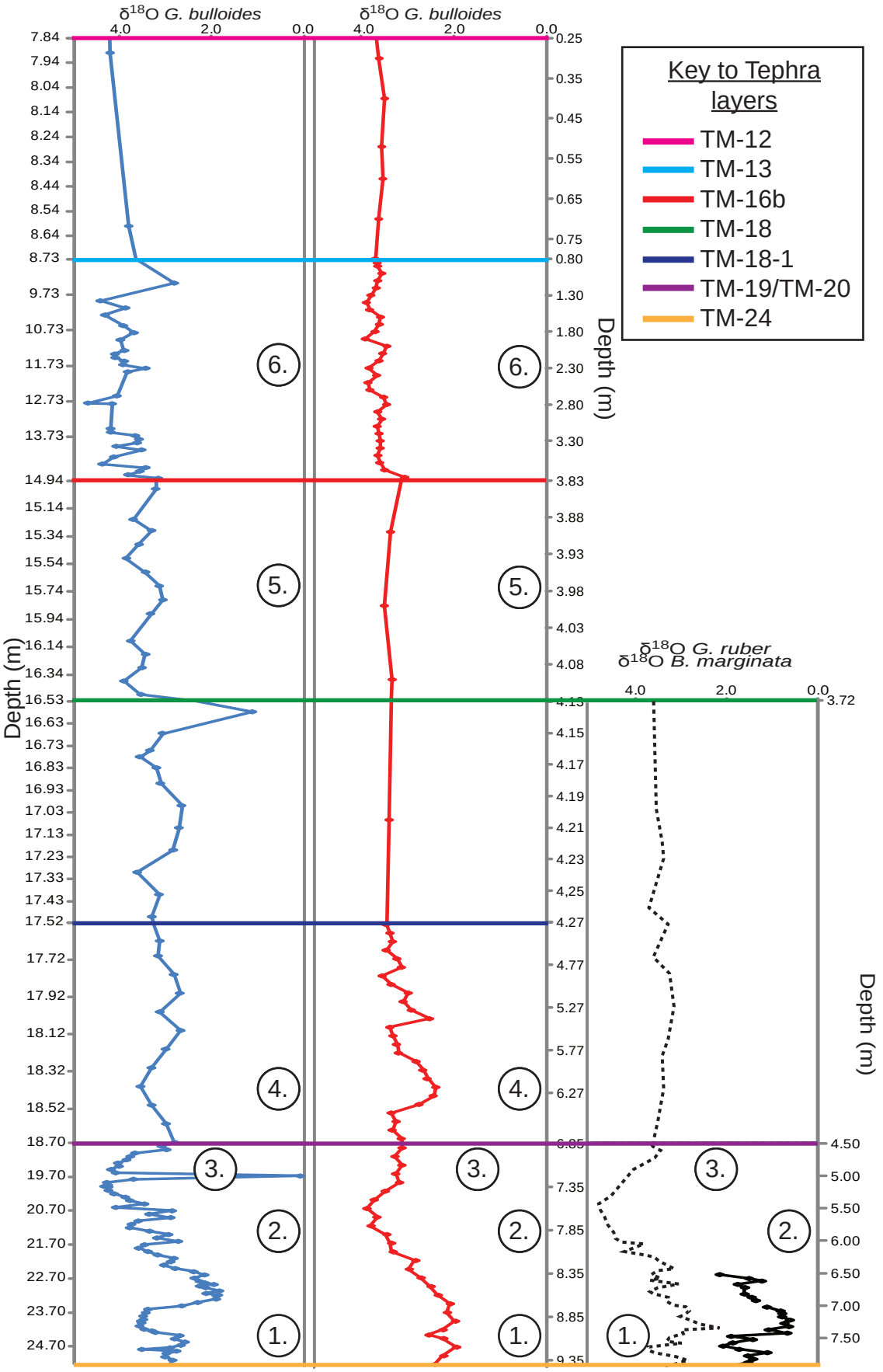

Figure 7.5: $\delta^{18}O$ curves for PRAD1-2 (blue curve), SA03-03 (red curve) and RF93-77 (black curve, dashed curve = benthic record). The curves have been tied to one another based upon the position of tephra layers common to different sequences. The tephra layers are shown as coloured lines correlating the curves at their stratigraphic position in each core.

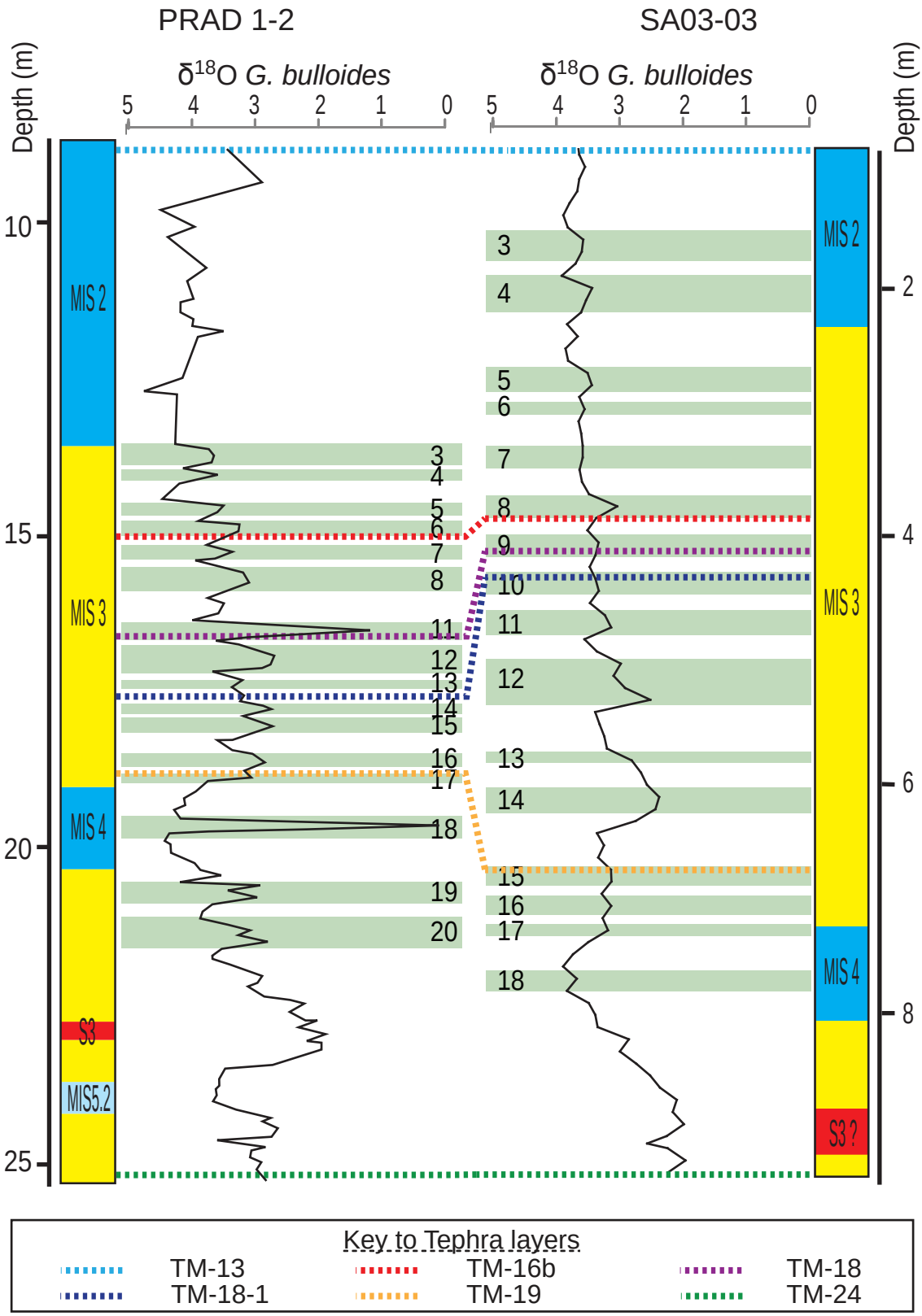

Figure 7.6: Comparison of the Dansgaard-Oeschger cycles identified in PRAD 1-2 (Piva *et al.,* 2008a) and the Dansgaard-Oeschger cycles identified in SA03-03 (Piva *et al.,* 2008d). The D-O interstadial number for each oscillation is marked. The two records are correlated using the stratigraphic position of tephra layers common to each sequence which are shown as dashed lines. The relationship between the tephra layers and D-O interstadials can be used to establish if the events are synchronous or not.

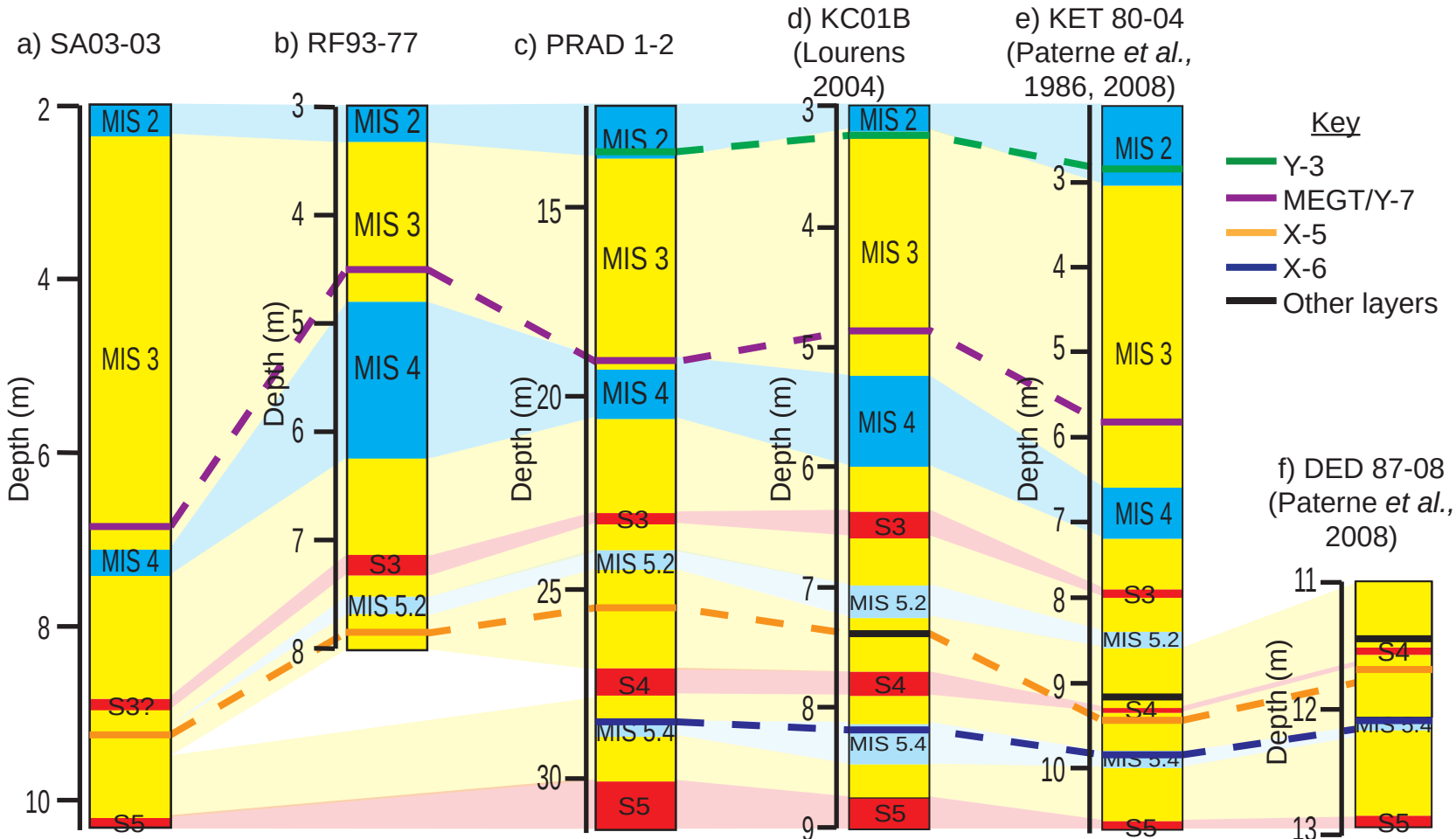

Figure 7.7: Comparison of the stratigraphic positions of tephra layers in SA03-03, RF93-77 and PRAD 1-2 with equivalent tephra layers in published marine records. Tephra layers are classified by the event they correlate to from the scheme outlined by Keller *et al.* (1978). The "other layers" highlighted in d, e and f are layers which have potentially been mis-correlated - see text for full details. Stratigraphic divisions and position of sapropel layers are taken from Cita *et al.* (2005) and Lourens (2004) for KC01B, from Kallell *et al.* (2000) and Paterne *et al.* (1986 and 2008) for KET 80-04 and Paterne *et al.* (2008) for DED 87-08.

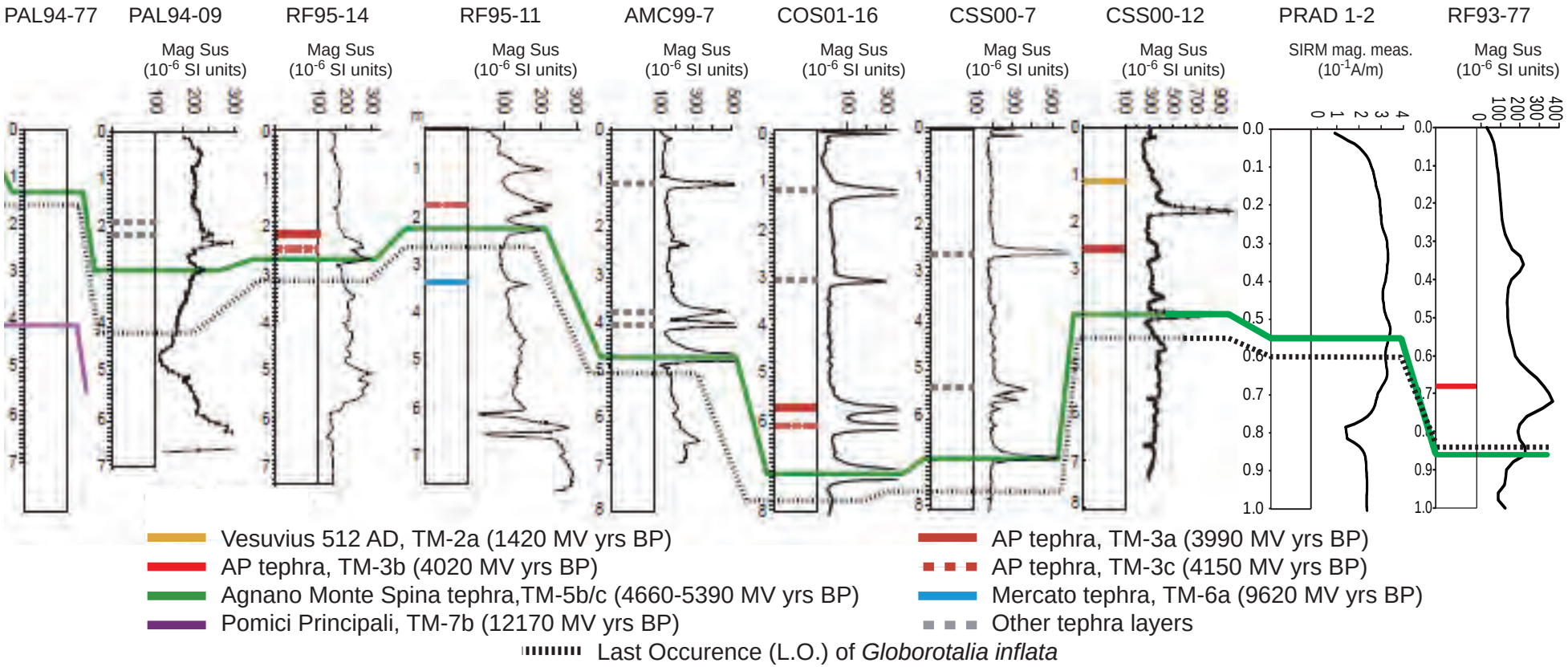

Figure 7.8: Comparison of the position of the Last Occurrence of G. inflata and the Agnano Monte Spina (AMS) tephra (TM-5) in Adriatic marine sequences described in Lowe *et al.* (2007b) and in PRAD 1-2 and RF93-77. In all of the Lowe *et al.* (2007b) cores and in PRAD 1-2 the Last Occurrence of G. inflata precedes the deposition of the AMS tephra. However, in RF93-77 the peak in glass of the AMS tephra precedes the L.O. G. inflata. Diagram is adapted from Figure 8 in Lowe *et al.* (2007b).

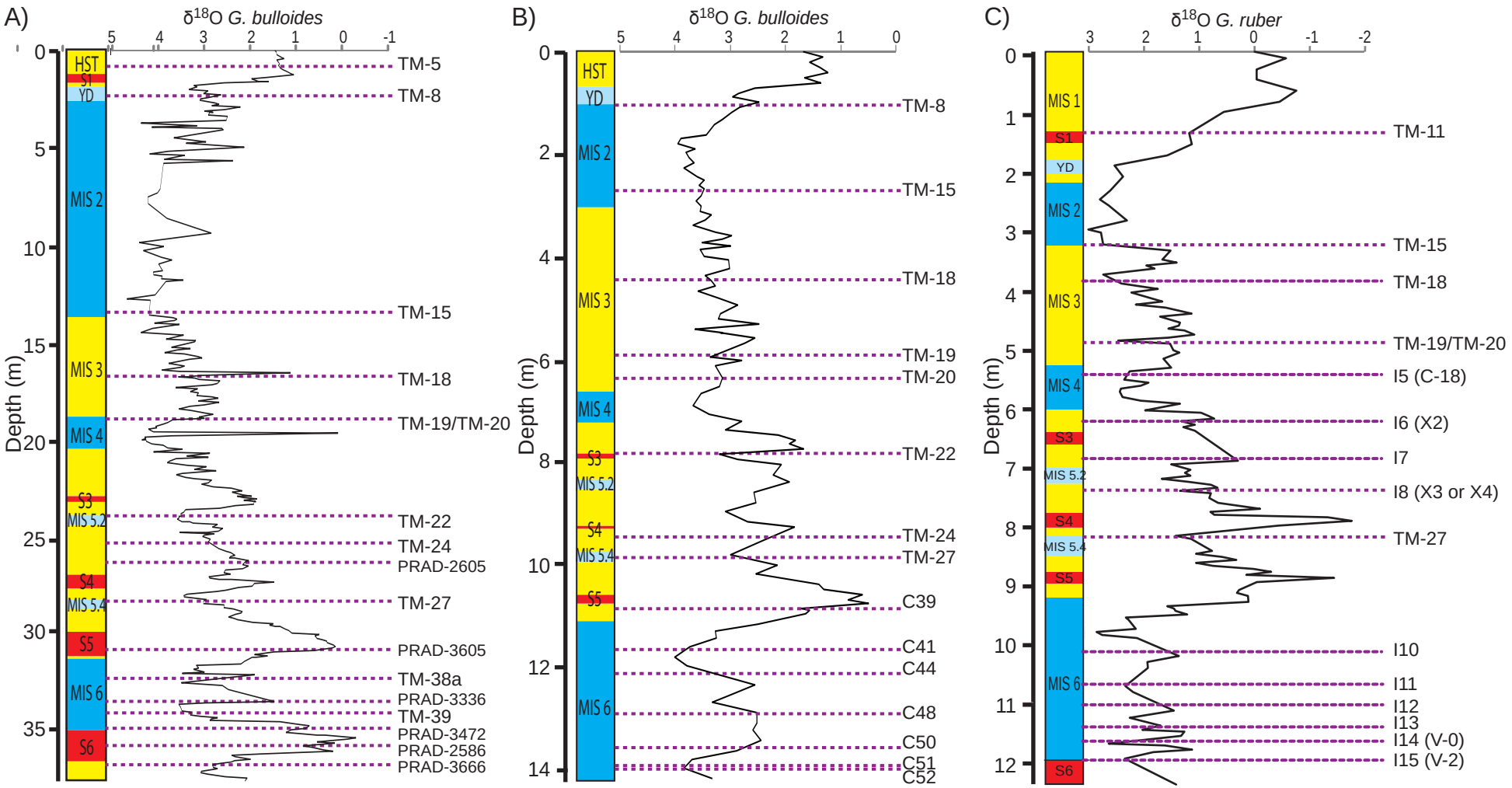

Figure 7.9: $\delta^{18}O$ curves of A) PRAD 1-2 (Piva *et al.,* 2008a), B) KET 80-04 (Paterne *et al.,* 1986) and C) KC01B (Lourens, 2004) with the positions of tephra layers marked as purple lines. Where the tephra layers have been correlated to an eruption that is also found in LGdM, the TM code for the layer is shown for comparison. If the layer is not correlated to an eruption found in LGdM, then the site code for the layer is shown.

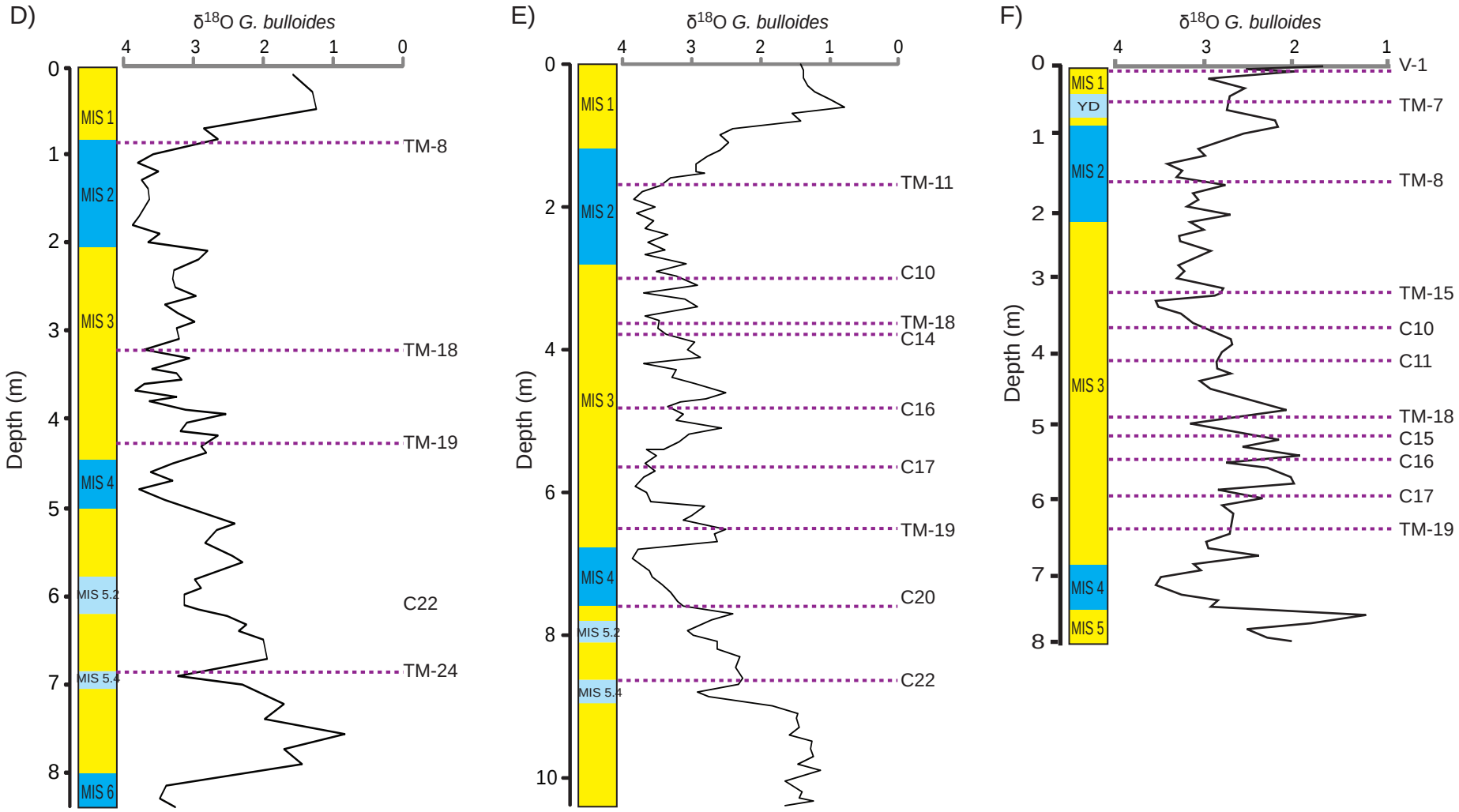

Figure 7.9 *continued*: $\delta^{18}O$ curves of D) KET 80-22 (Paterne *et al.,* 1986), B) KET 80-03 (Paterne *et al.,* 1986) and C) KET 82-18 (Paterne *et al.,* 1986) with the positions of tephra layers marked as purple lines.

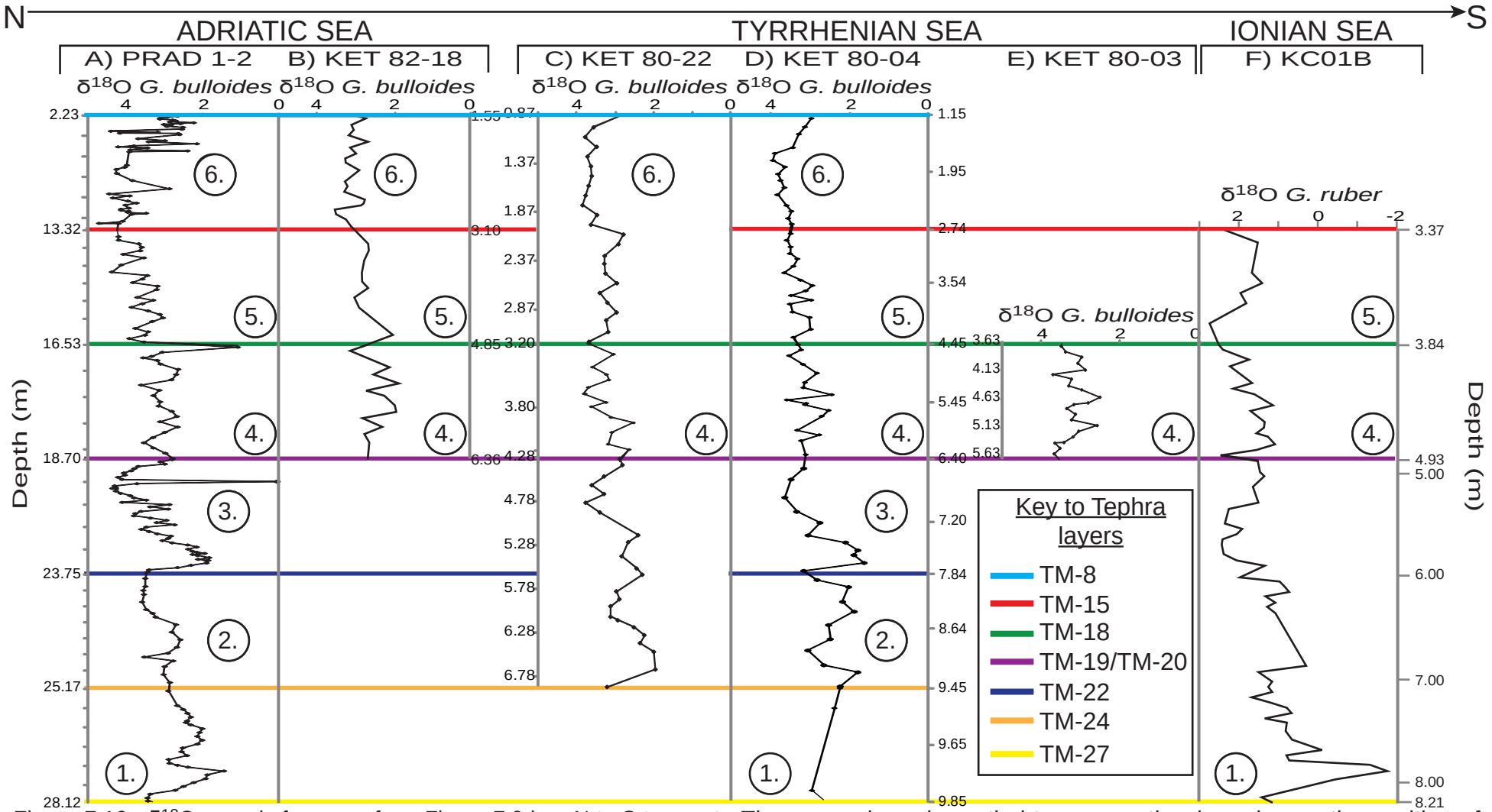

Figure 7.10: $\delta^{18}O$ records for cores from Figure 7.9 in a N to S transect. The curves have been tied to one another based upon the position of tephras common to the sequences. The tephra layers are shown as coloured lines and the numbers refer to key isotopic changes discussed in the text.

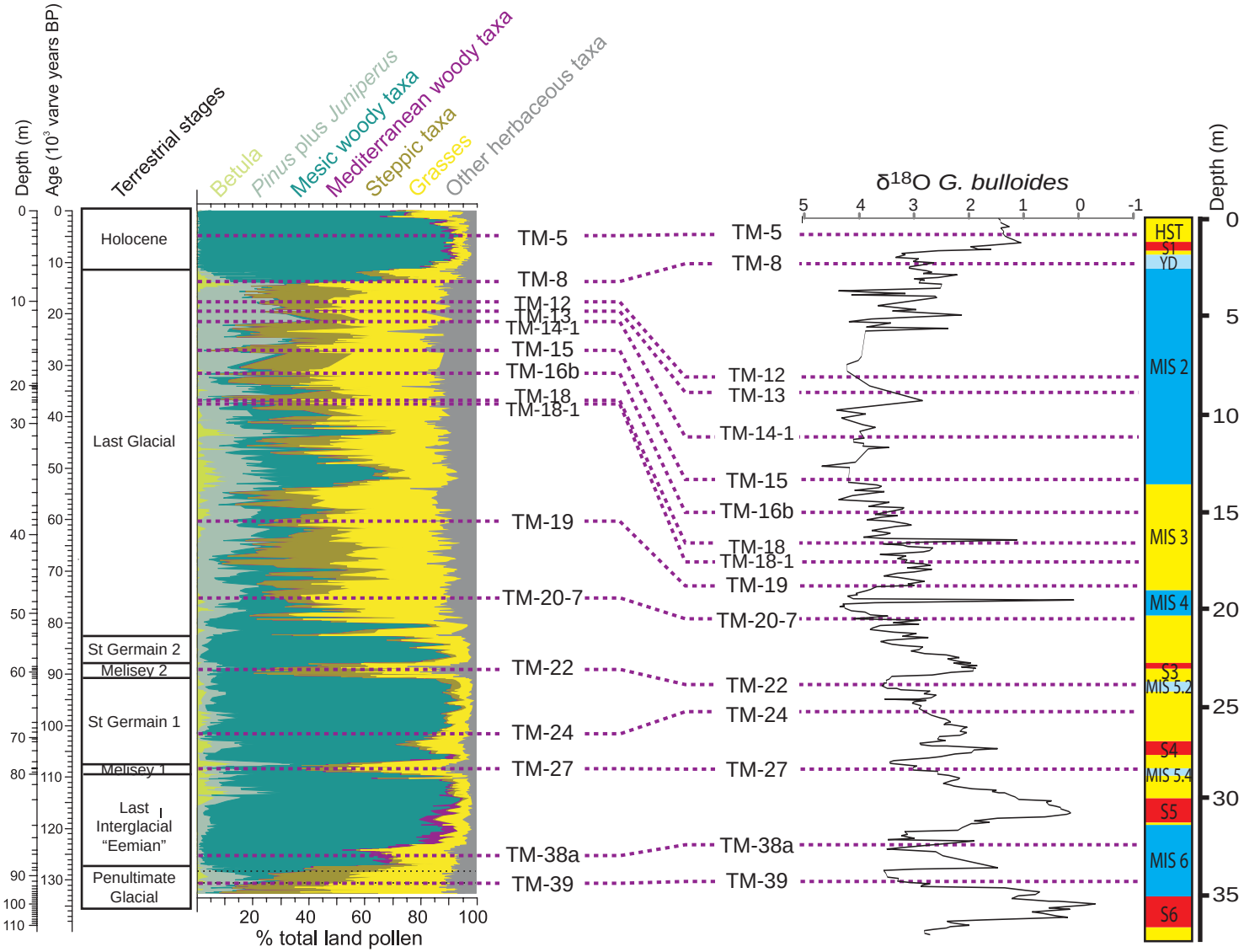

Figure 7.11: Correlation and comparison of the Lago Grande di Monticchio pollen record and the PRAD 1-2 oxygen isotope record. The records have been correlated using the positions of 16 tephra layers which are common to both records. The LGdM record is adapted from Brauer *et al.* (2007) and extends from MIS 6 to the present. The PRAD 1-2 oxygen isotope data is adapted from Piva *et al.* (2008a) and the analysed section of the record also extends from MIS 6 to the present. The positions of the tephra layers on the pollen diagram/oxygen isotope record will be used to establish if the marine and terrestrial paleoenvironmental records are synchronous or not.

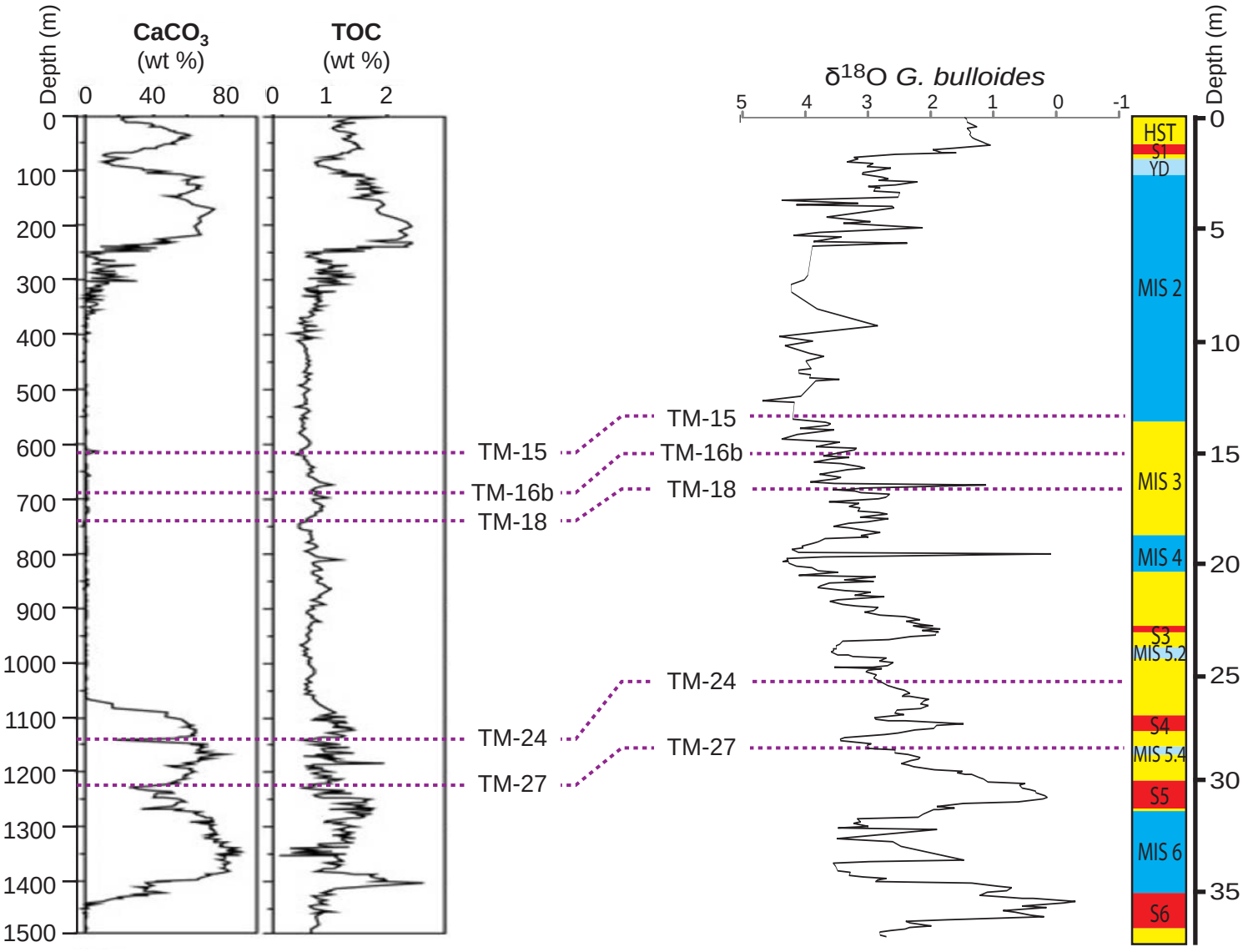

Figure 7.12: Correlation and comparison of the Lake Ohrid Calcium Carbonate and Total Organic Carbon records and the PRAD 1-2 oxygen isotope record. The records have been correlated using the positions of 5 tephra layers which are common to both records. The Lake Ohrid record is adapted from Vogel *et al.* (2010 a and b) and extends from the penultimate glacial period to the present. The PRAD 1-2 oxygen isotope data is adapted from Piva *et al.* (2008a) and the analysed section of the record extends from MIS 6 to the present. The positions of the tephra layers on the $CaCO_3$/TOC diagram and oxygen isotope record will be used to establish if the marine and terrestrial paleoenvironmental records are synchronous or not.

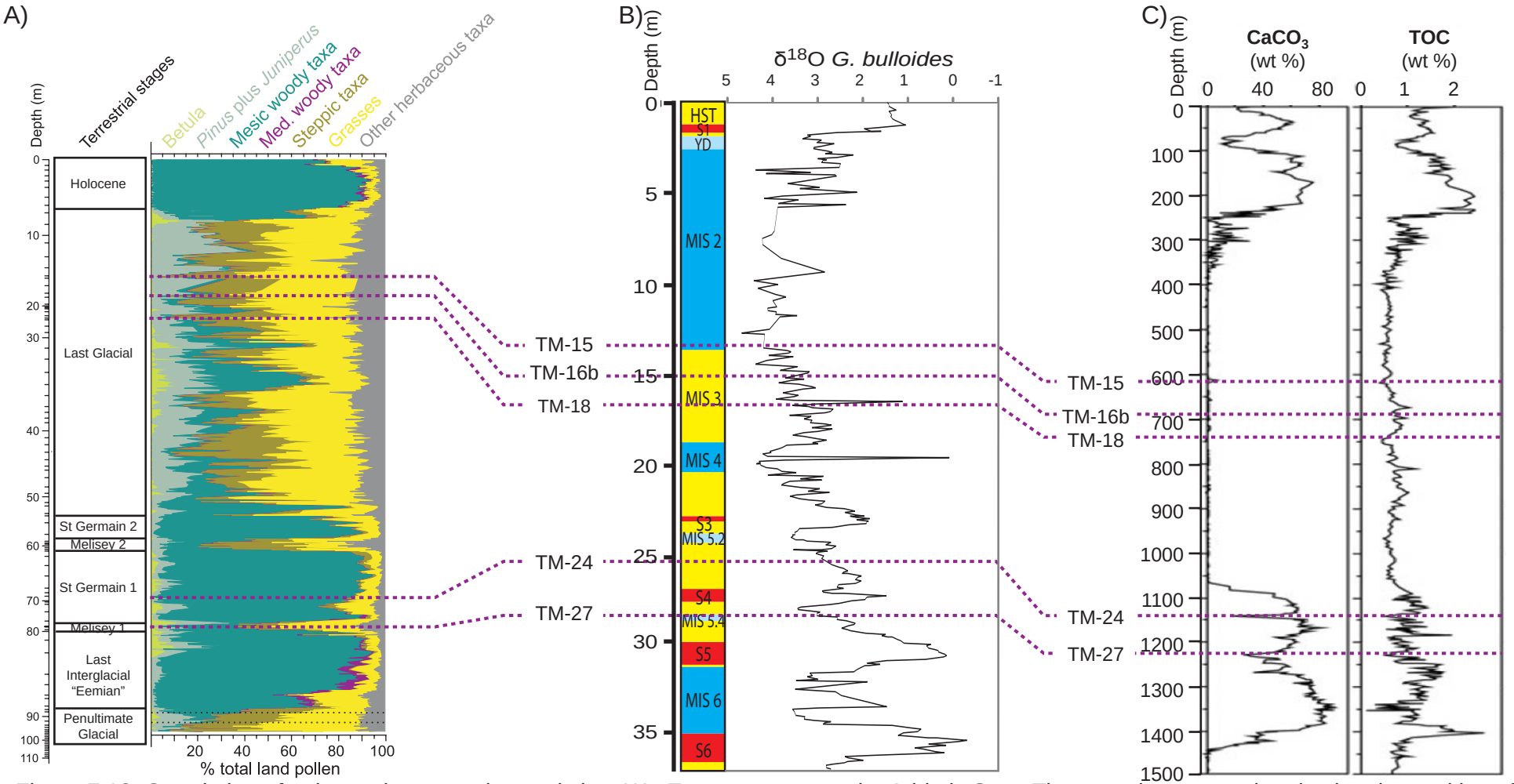

Figure 7.13: Correlation of paleoenvironmental records in a W - E transect across the Adriatic Sea. The records are correlated using the position of tephra layers which are common to each sequence. The tephra layers will be used to establish if the environment is responding synchronously across the transect. A) LGdM pollen record (adapted from Brauer *et al.,* 2007), B) PRAD 1-2 $\delta^{18}O$ record (Piva *et al*., 2008a) and C) Lake Ohrid $CaCO_3$ and TOC records (adapted from Vogel *et al*., 2010b).

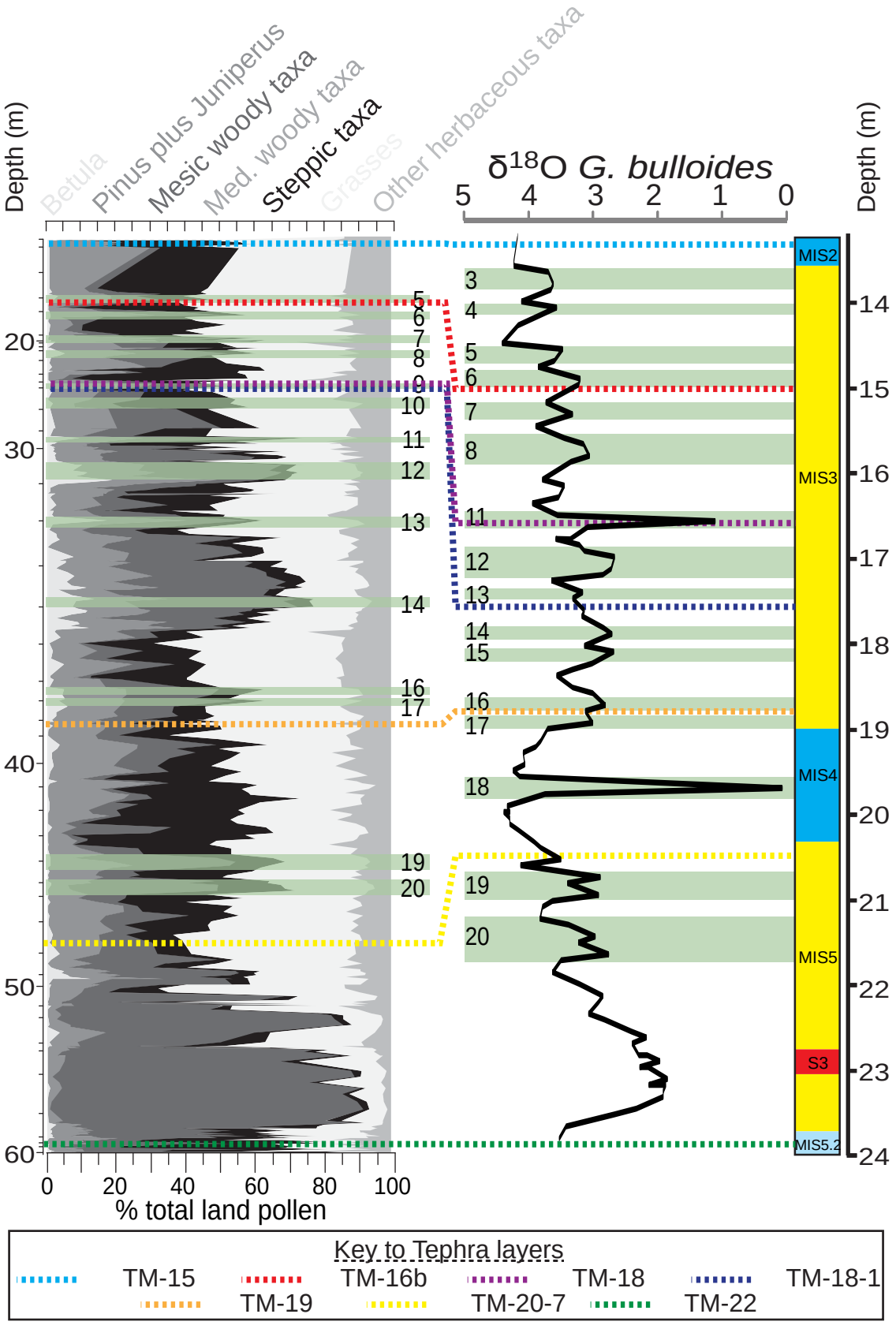

Figure 7.14: Comparison of the Dansgaard-Oeschger cycles identified in Lago Grande di Monticchio (Fletcher *et al.,* 2010, Allen *et al.,* 1999) and the Dansgaard-Oeschger cycles identified in PRAD 1-2 (Piva *et al.,* 2008a). The D-O interstadial number for each oscillation is marked. The two records are correlated using the stratigraphic position of tephra layers common to each sequence which are shown as dashed lines. The relationship between the tephra layers and D-O interstadials can be used to establish if the events are synchronous or not.

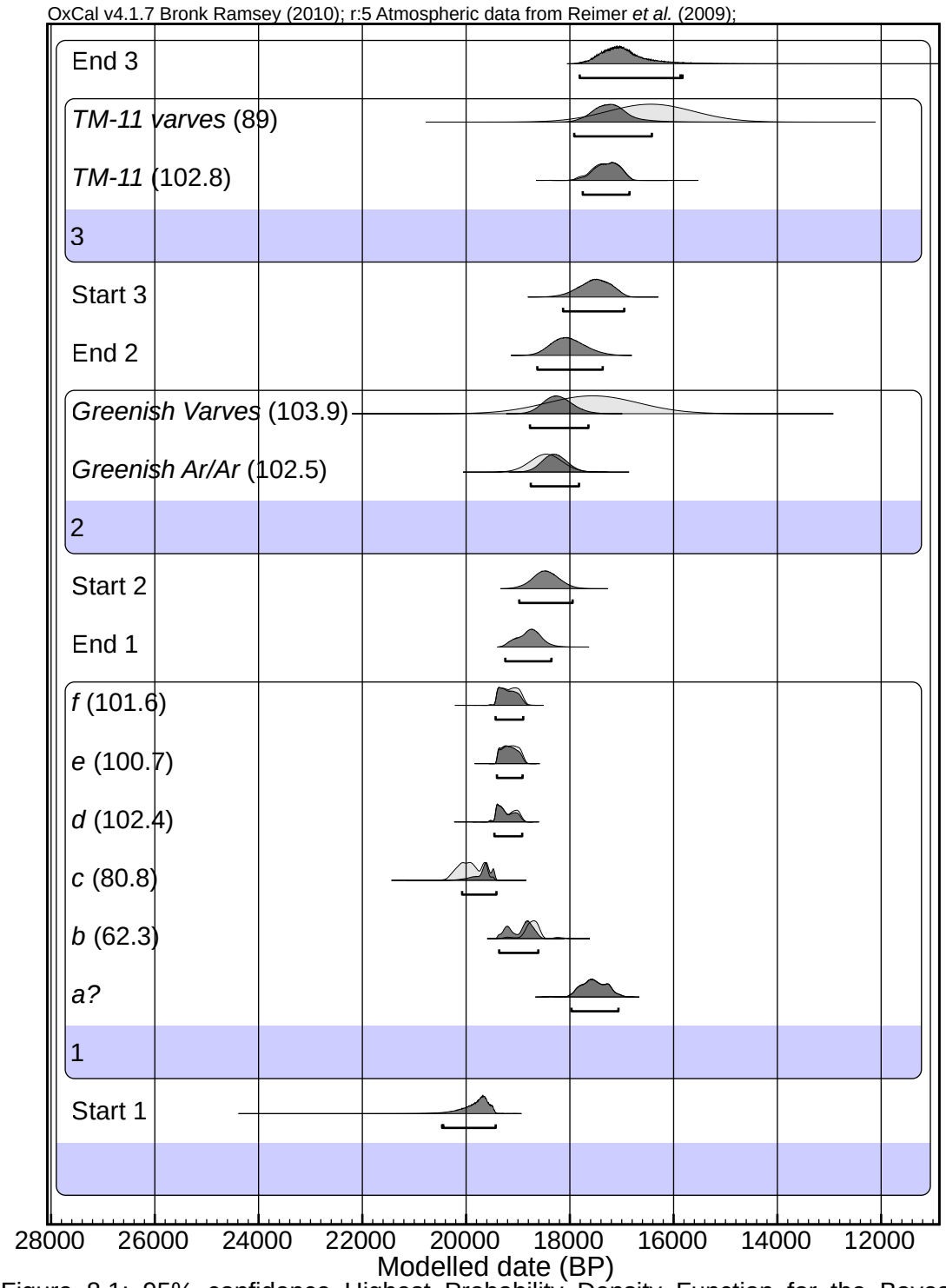

Figure 8.1: 95% confidence Highest Probability Density Function for the Bayesian Sequence age model derived to constrain the ages for the Greenish eruption. Results are modelled in stratigraphical order and separated into different depositional phases, with reference to their stratigraphical relationship to the Greenish tephra. The ages on material stratigraphically above and below the tephra can be used to constrain the age distribution for the Greenish. Phase 1 radiocarbon dates are from: a,b = Delibras *et al.* (1979), c,d = Andronico *et al.* (1995), e,f = Siani *et al.* (2001). Phase 2 dates are from: 40Ar/39Ar = Lanphere *et al.* (2008) and Varve = Wulf *et al.* (2004). Phase 3 dates from TM-11 = Delibras *et al.* (1986) and TM-11 varves = Wulf *et al.* (2004). The percentages, in brackets next to the date name, are agreement indices (AI) which are calculations of the area of the initial calibrated density function taken up by the age after the application of the Bayesian model. Date a is incompatible with the remainder of the data and the overall model and so has been marked as an outlier and removed from the model. For definitions of the main age modelling terms used, see Section 4.8.2, Table 4.3.

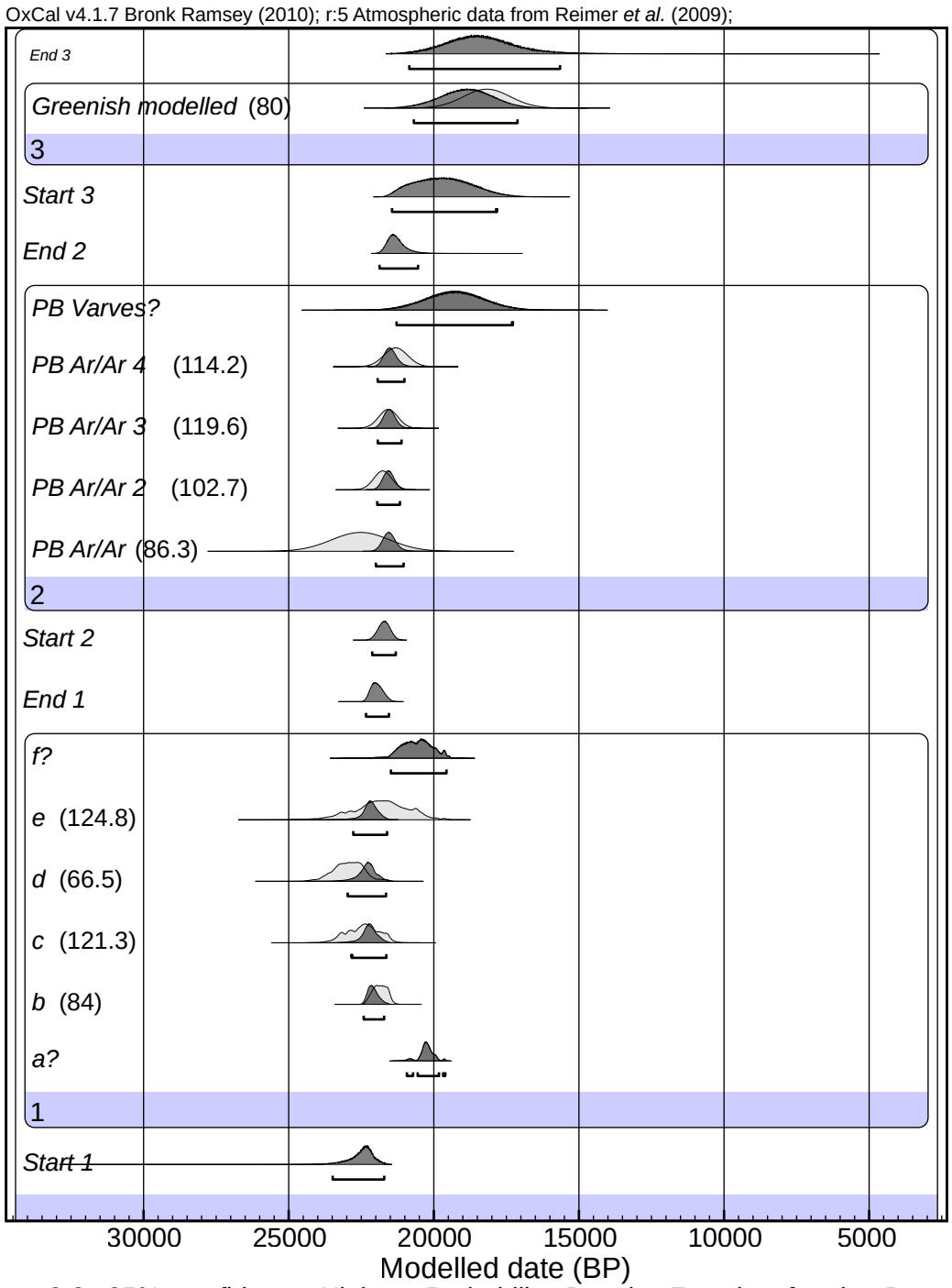

Figure 8.2: 95% confidence Highest Probability Density Function for the Bayesian Sequence age model derived to constrain the age of the Pomici di Base eruption. Results are modelled in stratigraphical order and separated into different depositional phases, with reference to their stratigraphical relationship to the Pomici di Base tephra. The ages on material stratigraphically above and below the tephra can be used to constrain the age distribution for the Pomici di Base. Phase 1 radiocarbon dates are from: a = Delibras *et al.* (1979), b = Andronico *et al.* (1995), c,d = Dertagnini *et al.* (1998) e = Siani *et al.* (2004) and f = Aleisso *et al.* (1974) Phase 2 dates are from: Ar/Ar = Capaldi *et al.* (1985), Ar/Ar 2 and 3 = Delibrias *et al.* (1979), Ar/Ar 4 = Lanphere *et al.* (2008) and Varves = Wulf *et al.* (2004). Phase 3 date is the modelled age range for the Greenish eruption (Section 8.1.1). The percentages, in brackets next to the date name, are agreement indices (AI), which are calculations of the area of the initial calibrated density function taken up by the age after the application of the Bayesian model. Dates a, f and PB varves are incompatible with the remainder of the data and the overall model and have been marked as outliers and removed from the model. For definitions of the main age modelling terms used, see Section 4.8.2, Table 4.3.

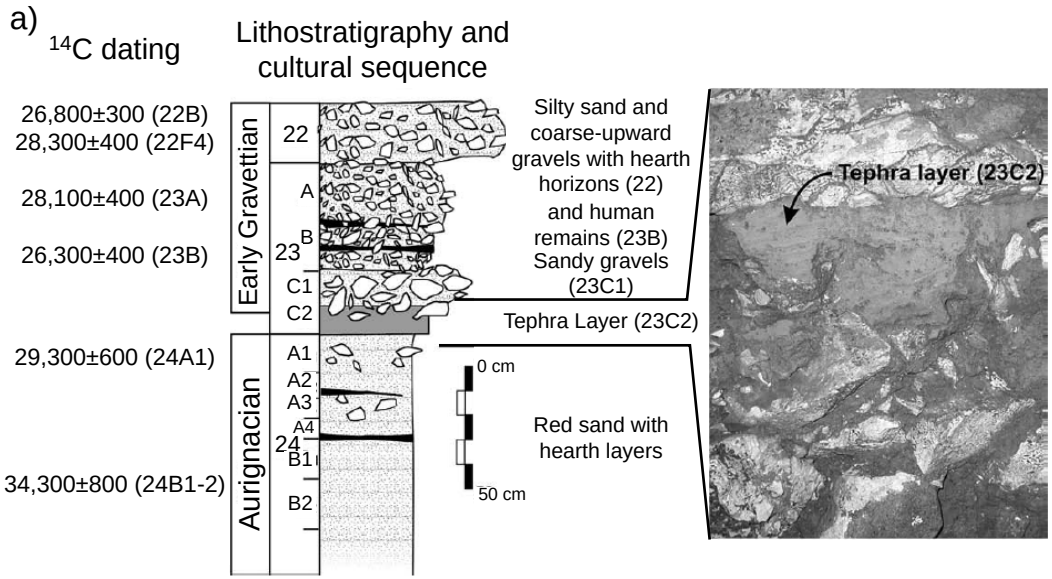

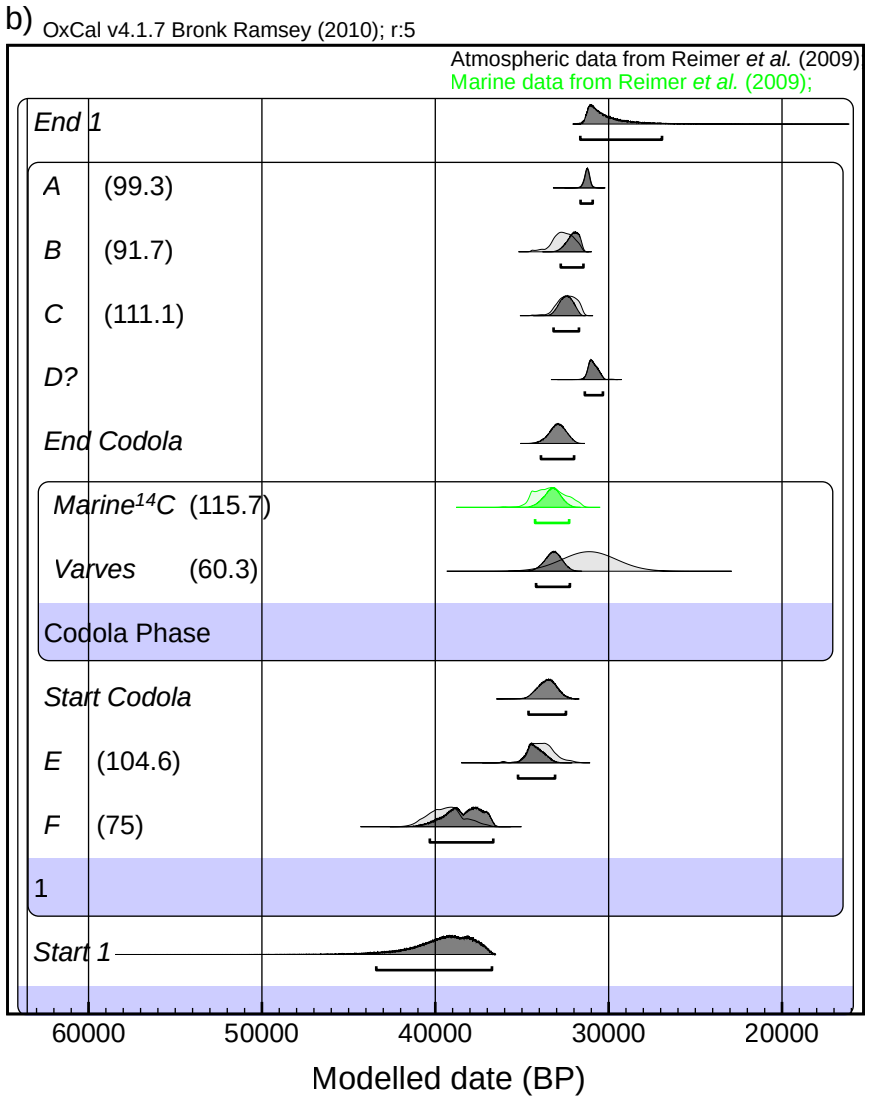

Figure 8.3: a) Stratigraphic section of the lowermost part of the Palaeolithic sequence at Paglicci Cave, Italy, showing the position of the Codola tephra layer and the stratigraphic order of the radiocarbon dates obtained from the site. Figure redrawn from Giaccio *et al.* (2008).

b) 95% confidence Highest Probability Density Function, for the Bayesian Sequence age model used to constrain the age of the Codola eruption. Radiocarbon dates A - F are from Giaccio *et al.* (2008), the Marine ^{14}C date within the Codola phase is from Paterne *et al.* (1999) and the Varves date within the Codola Phase is from Wulf *et al.* (2004). The percentages, in brackets next to the date name, are agreement indices (AI), which are calculations of the area of the initial calibrated density function taken up by the age after the application of the Bayesian model. Date D is incompatible with the remainder of the data and the overall model and so was marked as an outlier and removed from the model. For definitions of the main age modelling terms used, see Section 4.8.2, Table 4.3.

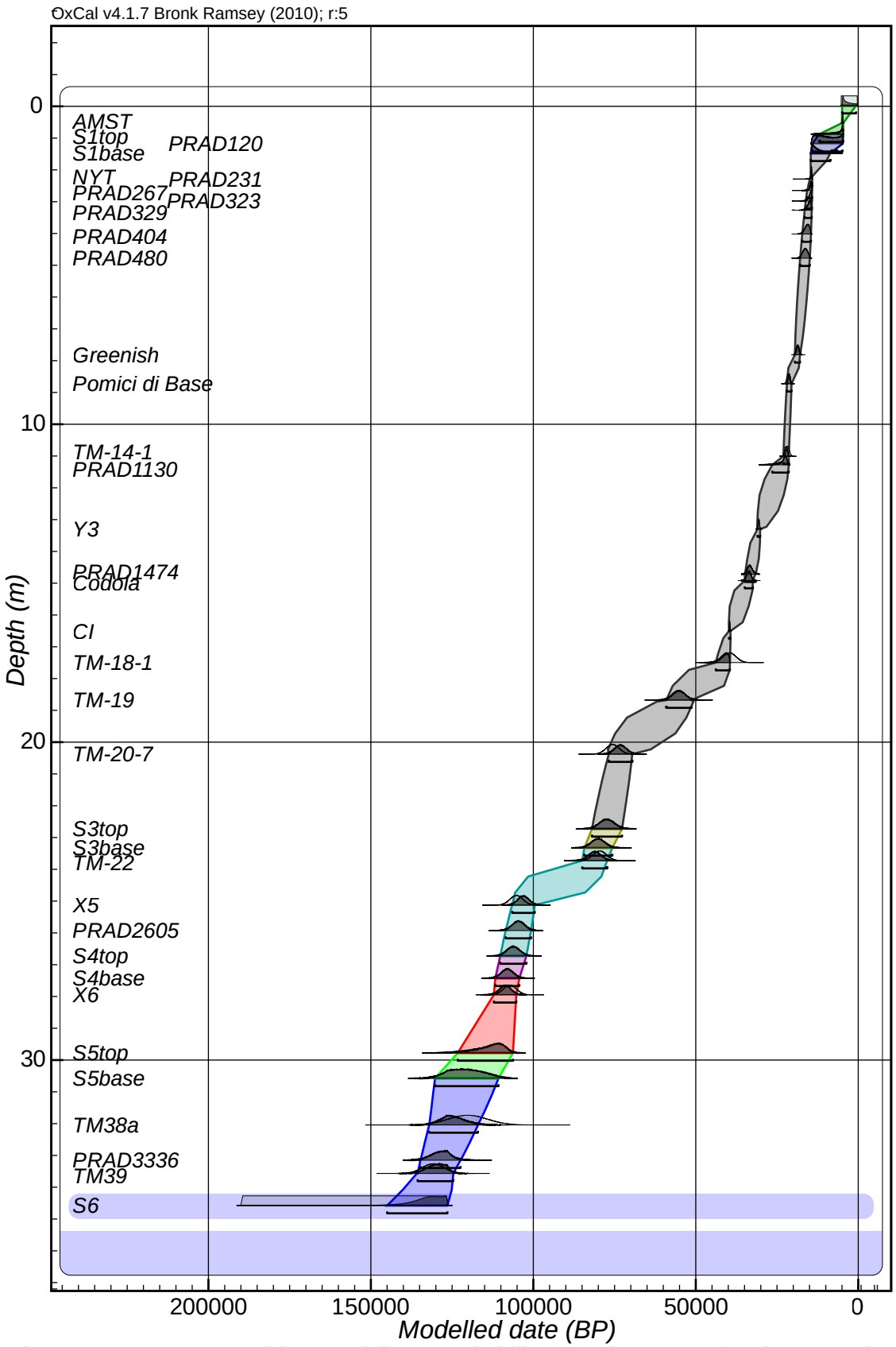

Figure 8.4: 95.4% confidence Highest Probability Density output for the Bayesian age/depth model for the PRAD 1-2 sequence (run using a Poisson model). The model was constructed using the best constrained age estimates for the tephra layers identified in the sequence. Boundaries were inserted at the top and base of the sequence, as well as at the top and base of sapropel layers on the assumption that deposition of these units would cause a change in sedimentation rate. For definitions of the main age modelling terms used, see Section 4.8.2, Table 4.3.

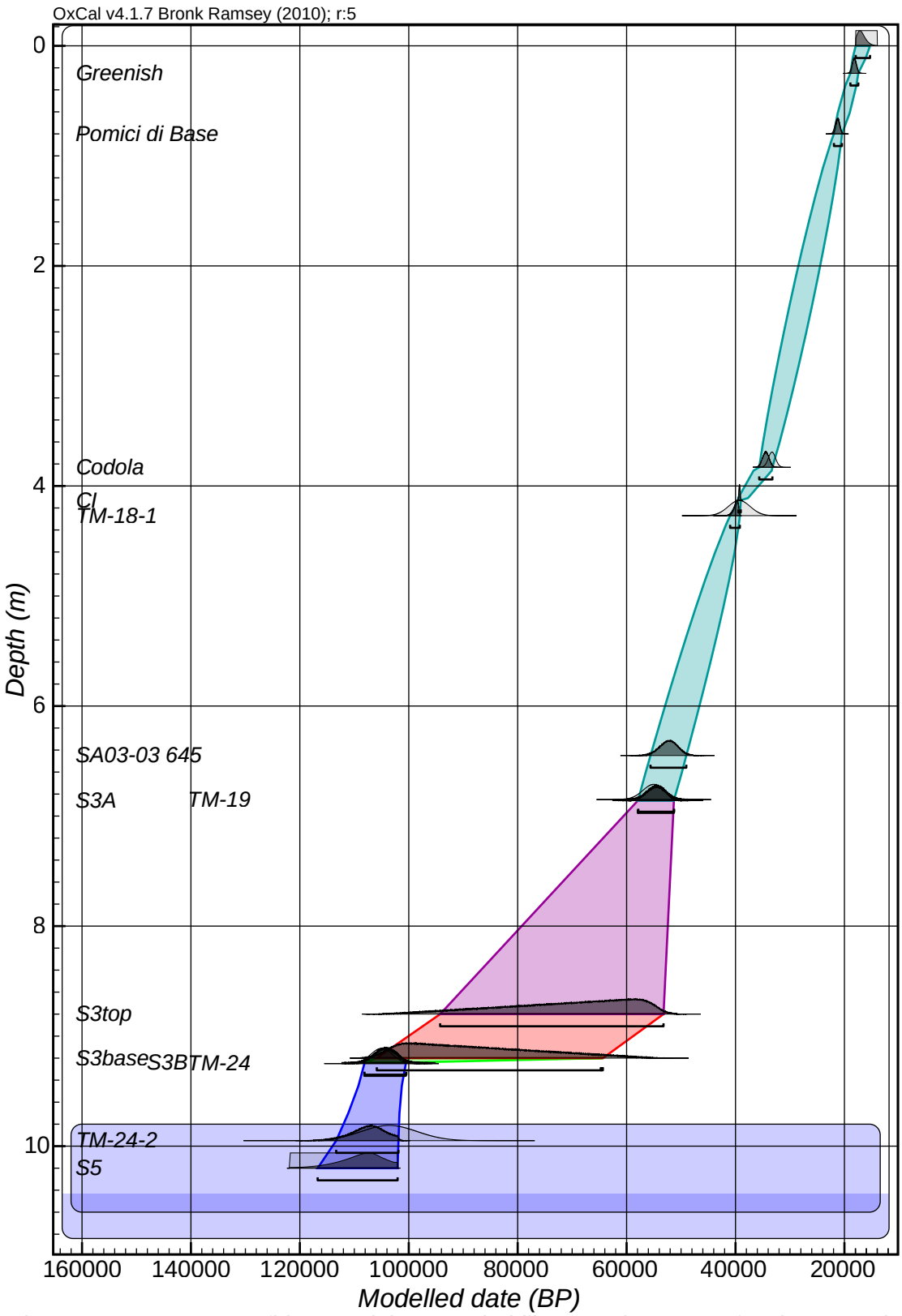

Figure 8.5: 95.4% confidence Highest Probability Density output for the Bayesian age/depth model for the SA03-03 sequence (run using a Poisson model). The model was constructed using the best constrained age estimates for the tephra layers identified in the sequence. Boundaries were inserted at the top and base of the sequence, as well as at the top and base of sapropel layers on the assumption that deposition of these units would cause a change in sedimentation rate. Additional boundaries are inserted immediately post TM-24 deposition and immediately prior to TM-19 deposition for reasons provided in the text. For definitions of the main age modelling terms used, see Section 4.8.2, Table 4.3.

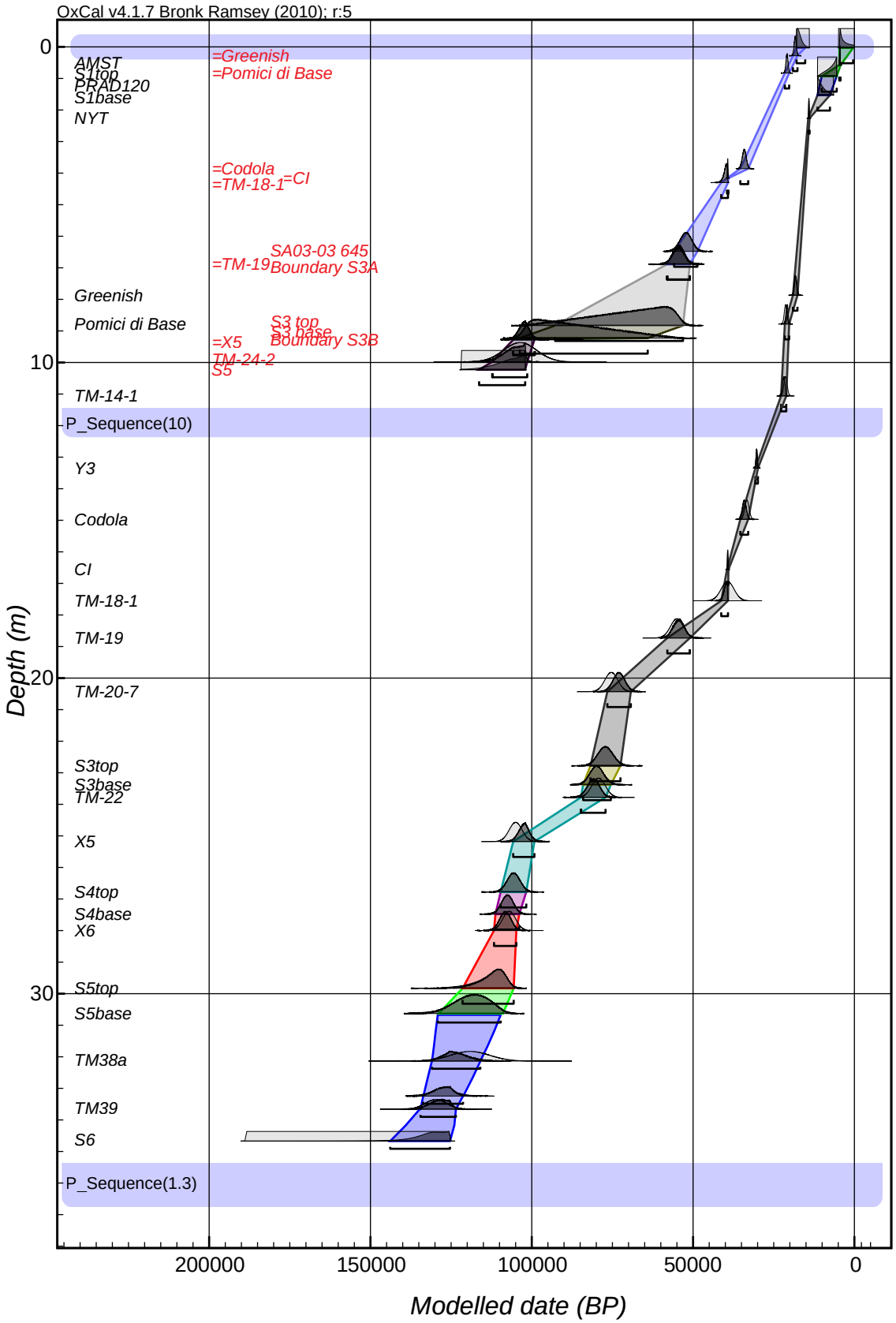

Figure 8.6: 95.4% confidence Highest Probability Density combined output for the Bayesian age/depth models for the PRAD 1-2 and SA03-03 sequences (run using a Poisson model). The top model and date titles in red represent the SA03-03 sequence. The tephra layers common to both sequences have been forced to adopt the same age by the model in an attempt to improve the age range estimates for SA03-03.

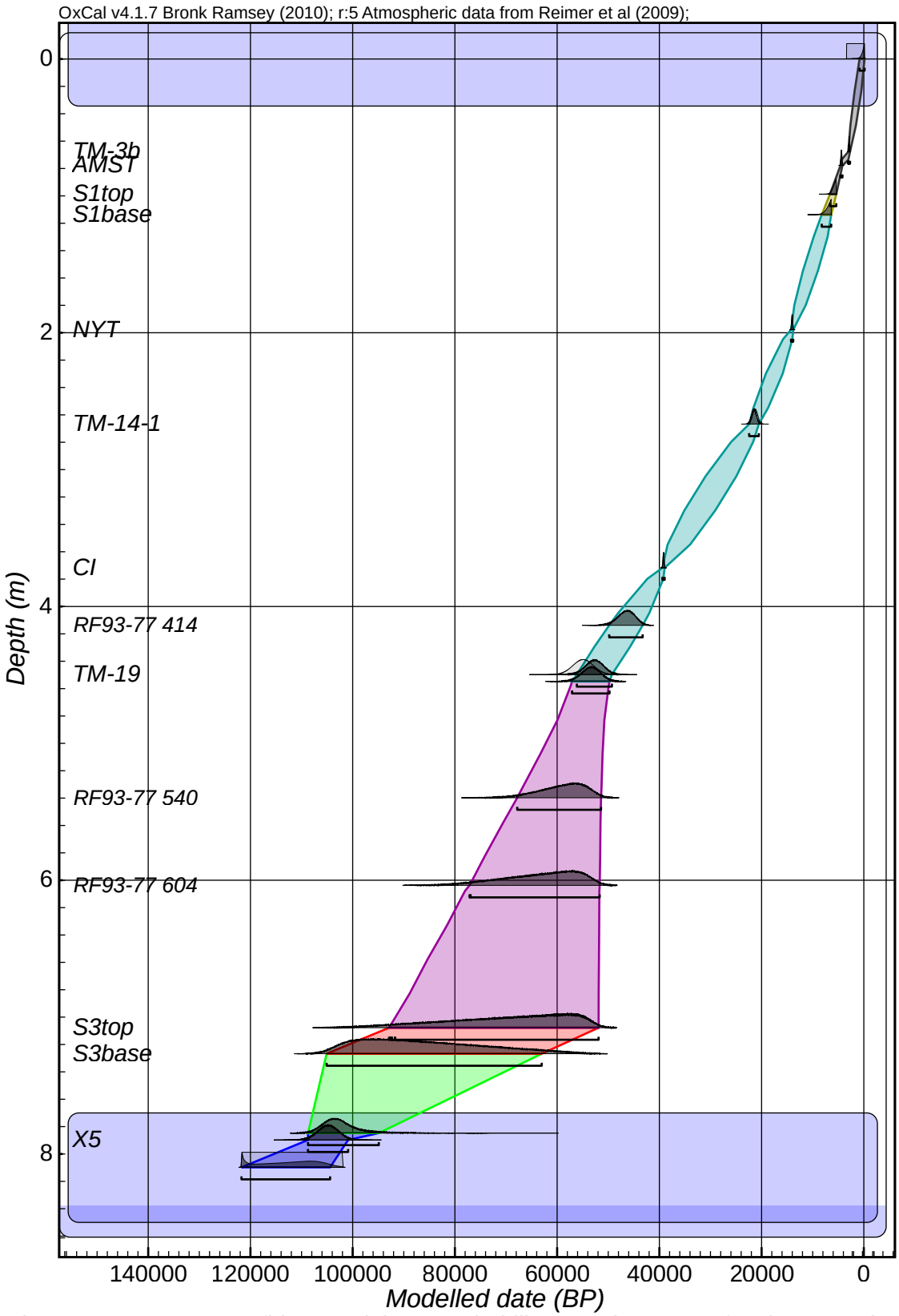

Figure 8.7: 95.4% confidence Highest Probability Density output for the Bayesian age/depth model for the RF93-77 sequence (run using a Poisson model). The model was constructed using the best constrained age estimates for the tephra layers identified in the sequence. Boundaries were inserted at the top and base of the sequence, as well as at the top and base of sapropel layers on the assumption that deposition of these units would cause a change in sedimentation rate. Additional boundaries are inserted immediately post TM-24 deposition and immediately prior to TM-19 deposition, for reasons provided in the text. For definitions of the main age modelling terms used, see Section 4.8.2, Table 4.3.

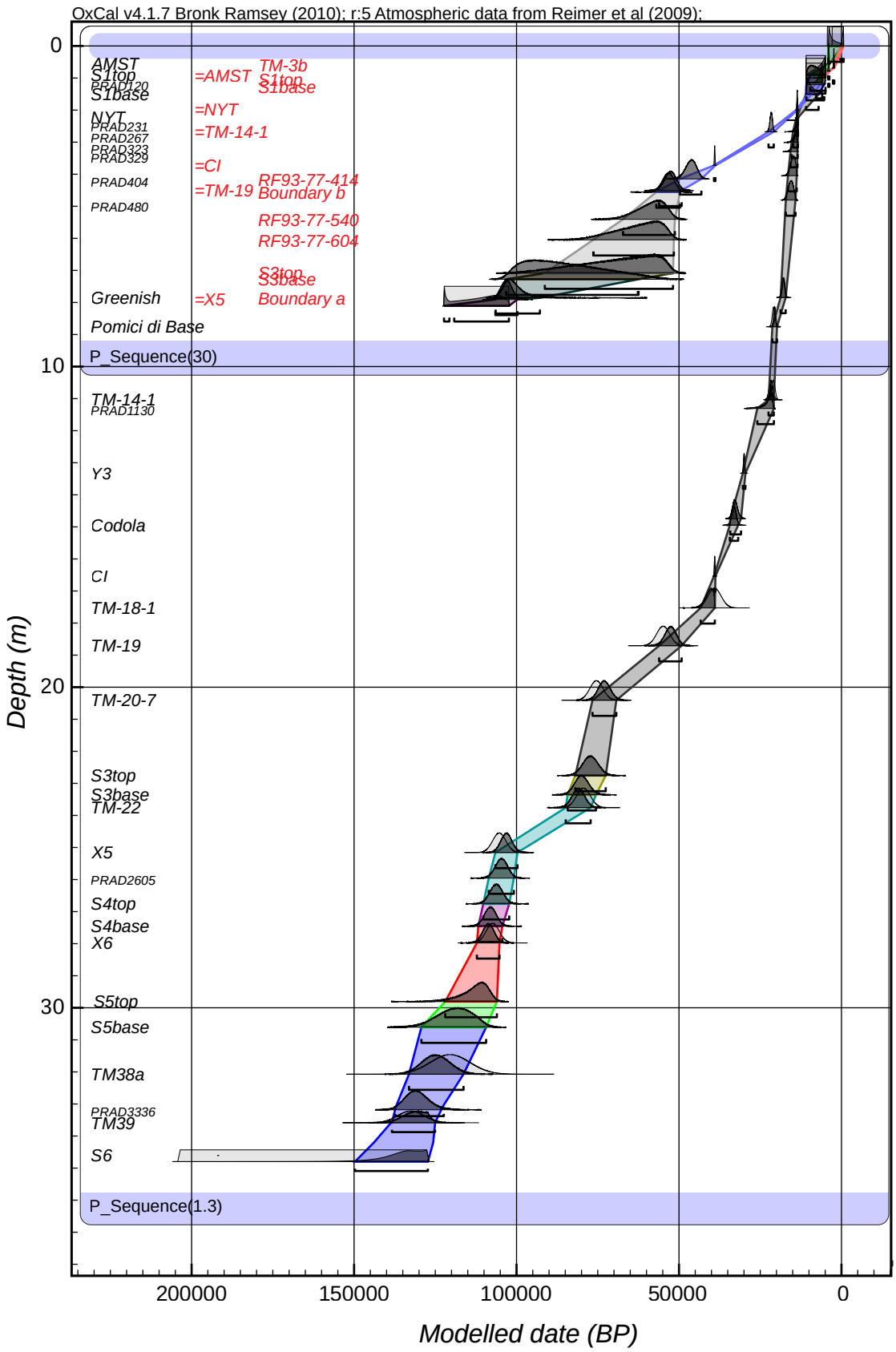

Figure 8.8: 95.4% confidence Highest Probability Density combined output for the Bayesian age/depth models for the PRAD 1-2 and RF93-77 sequences (run using a Poisson model). The top model and date titles in red represent the RF93-77 sequence. The tephra layers common to both sequences have been forced to adopt the same age by the model in an attempt to improve the age range estimates for RF93-77.

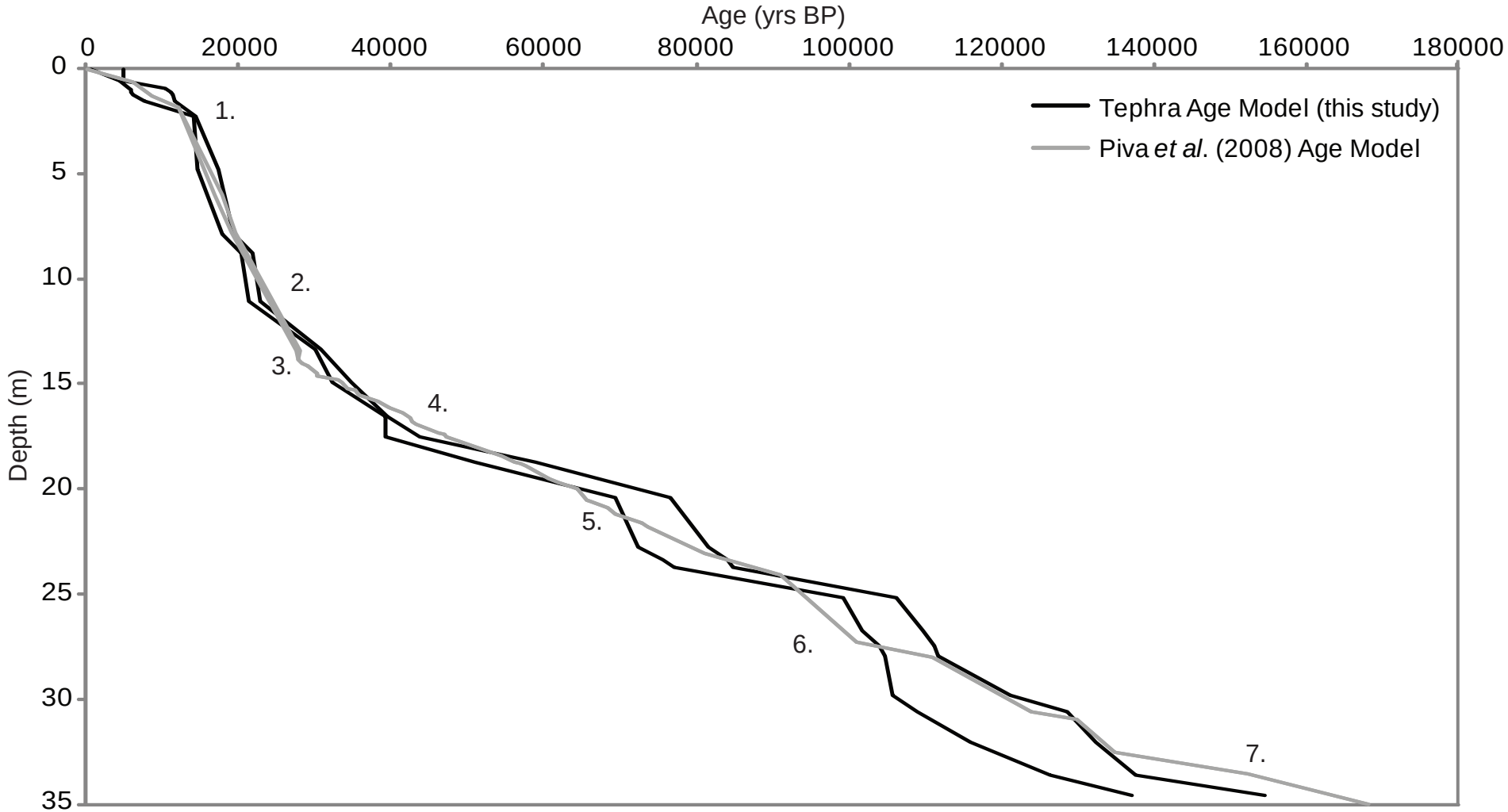

Figure 8.9: Comparison of the PRAD 1-2 independent tephra-derived age model and the PRAD 1-2 age model produced by Piva *et al.* (2008). The two darker lines represent the 2σ errors limits of the age estimates derived by Bayesian modelling in this research. Only mean ages are provided for the Piva *et al.* (2008) age model (lighter line), as no errors were supplied. Numbers 1 to 7 mark seven key junctures where the models disagree (see text).

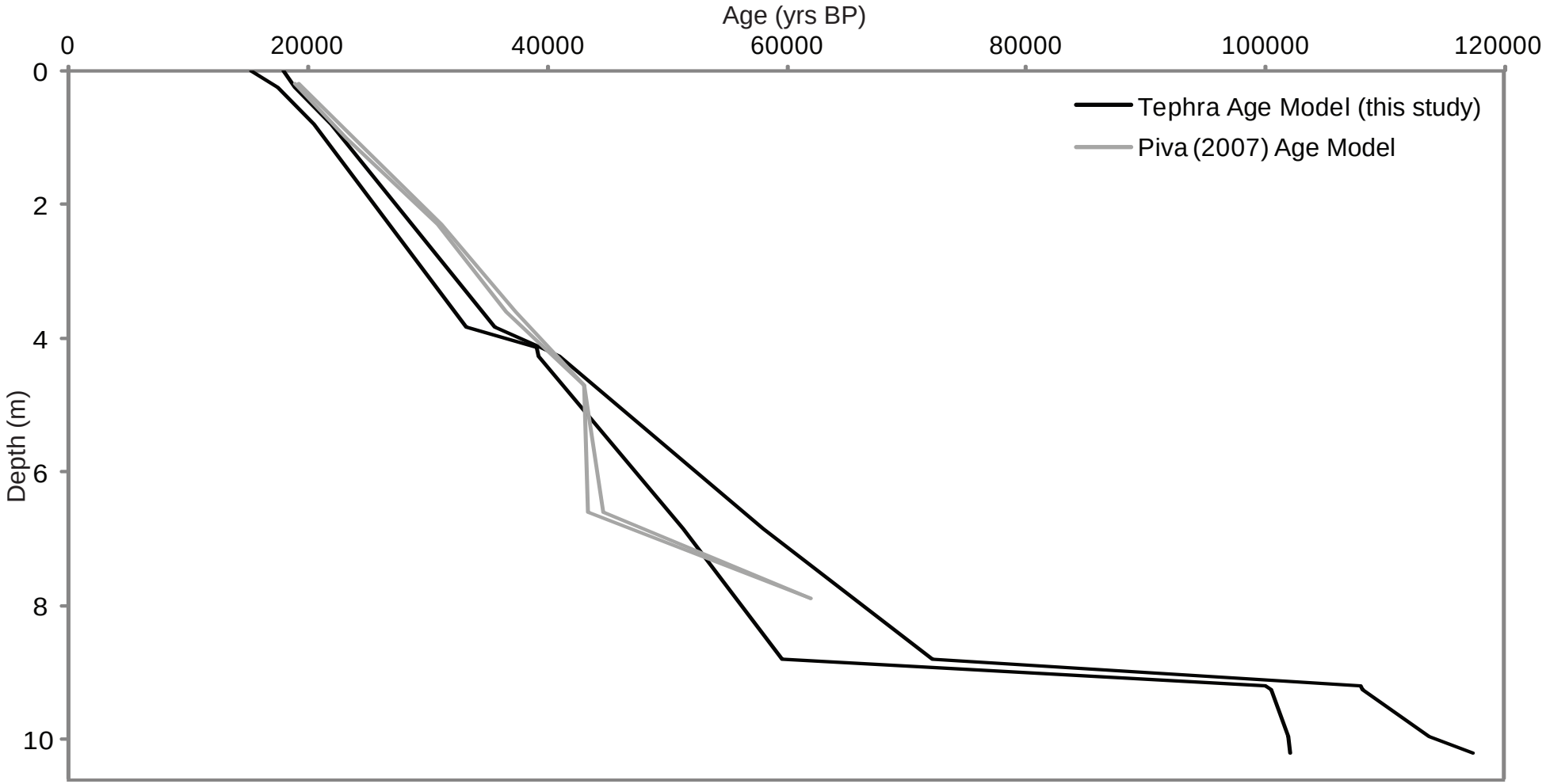

Figure 8.10: Comparison of the SA03-03 independent tephra-derived age model and the SA03-03 age model produced by Piva (2007). The two darker lines represent the 2σ errors limits of the age estimates derived by Bayesian modelling in this research. The two lighter lines represent the 1σ errors limits of the age estimates derived by Piva (2007). The Piva (2007) model is based on radiocarbon dates and therefore does not extend to the base of the sequence.

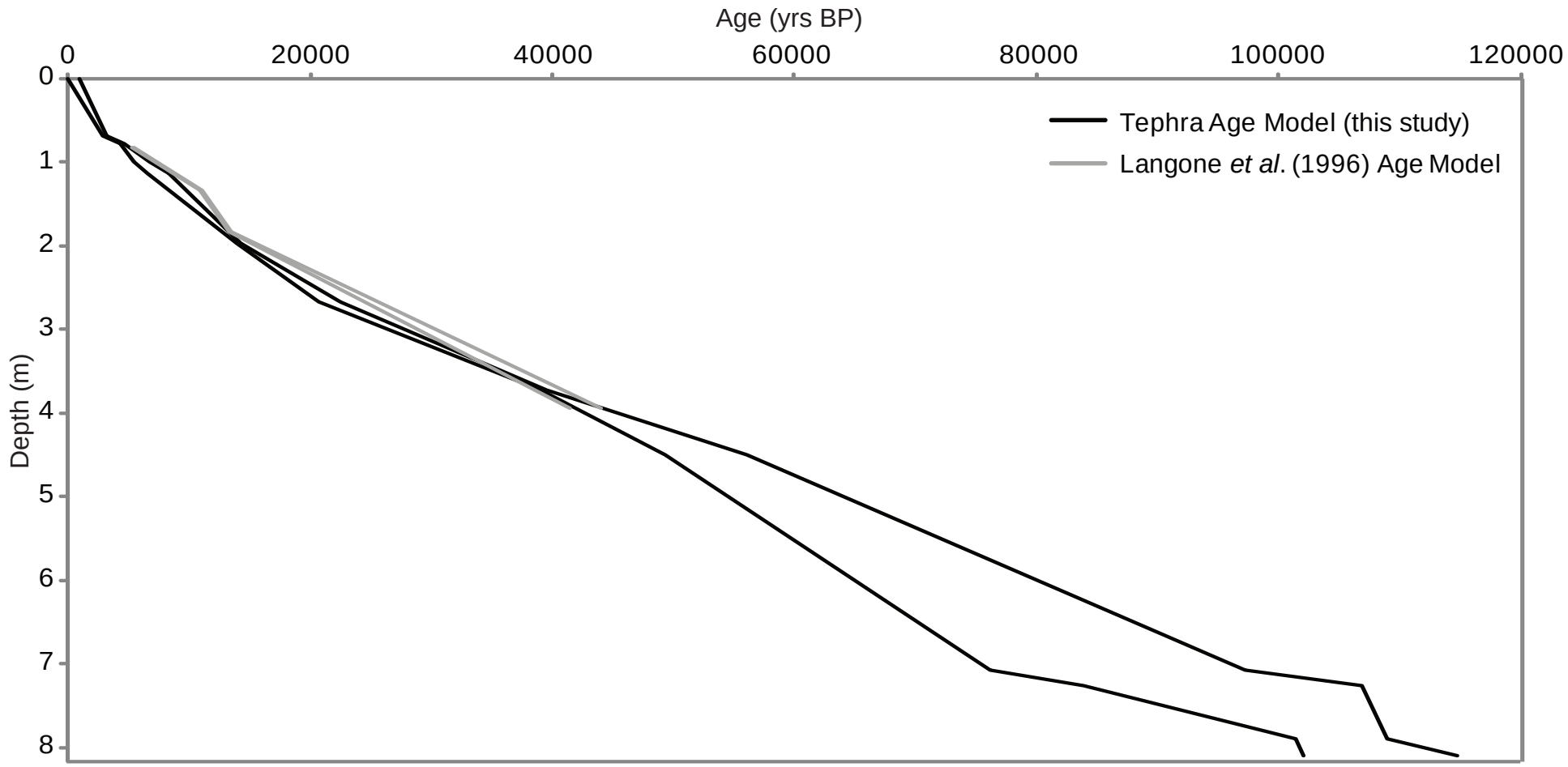

Figure 8.11: Comparison of the RF93-77 independent tephra-derived age model and the RF93-77 age model produced by Langone *et al.* (1996). The two darker lines represent the 2σ errors limits of the age estimates derived by Bayesian modelling in this research. The two lighter lines represent the 1σ errors limits of the age estimates derived by Langone *et al.* (1996). The Langone *et al.* (1996) model is based solely on radiocarbon dates which do not extend beyond ca. 45 ka BP.

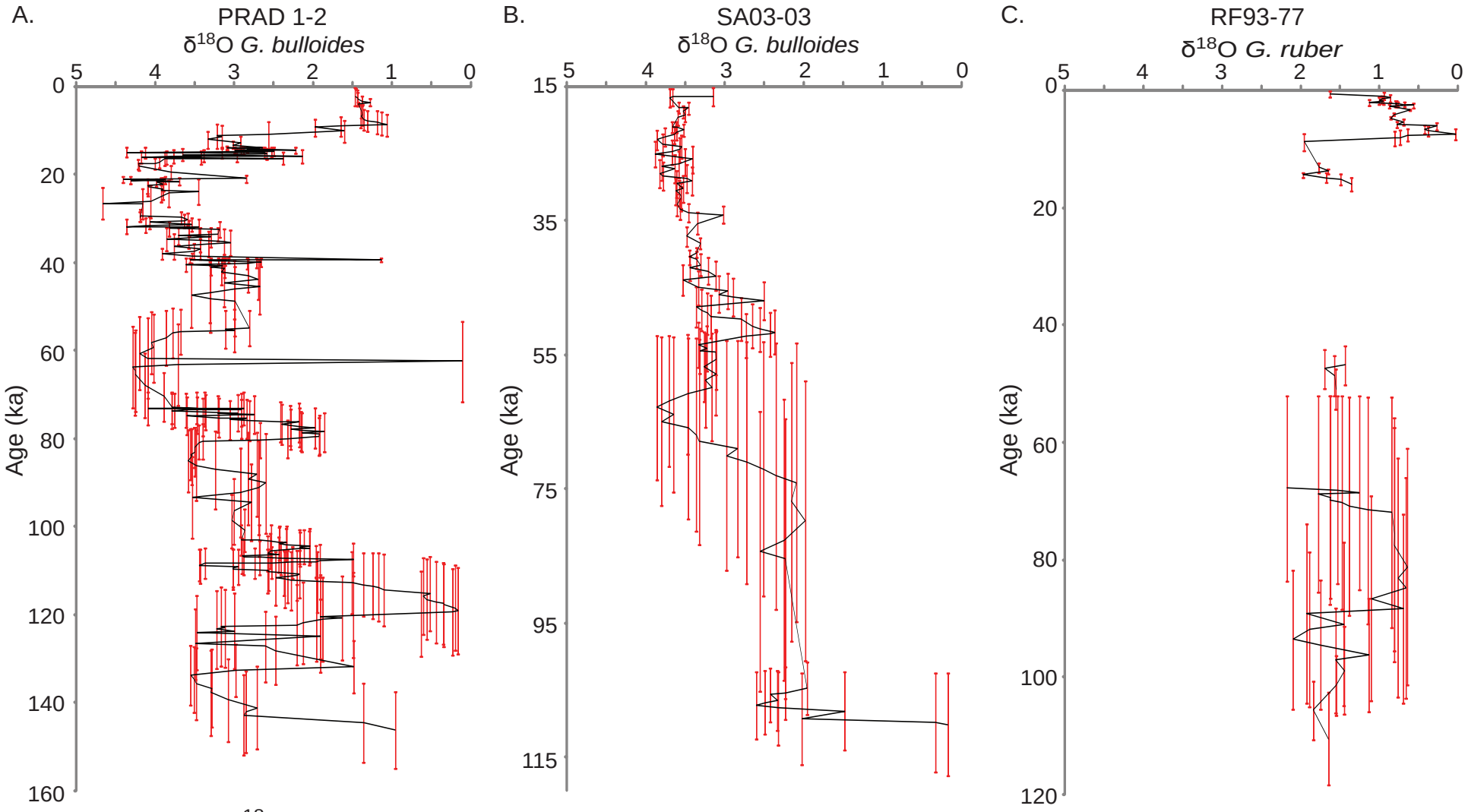

Figure 8.12: Timing of $\delta^{18}O$ isotope changes in A) PRAD 1-2, B) SA03-03 and C) RF93-77. The red lines represent the 2σ errors associated with each age estimate.

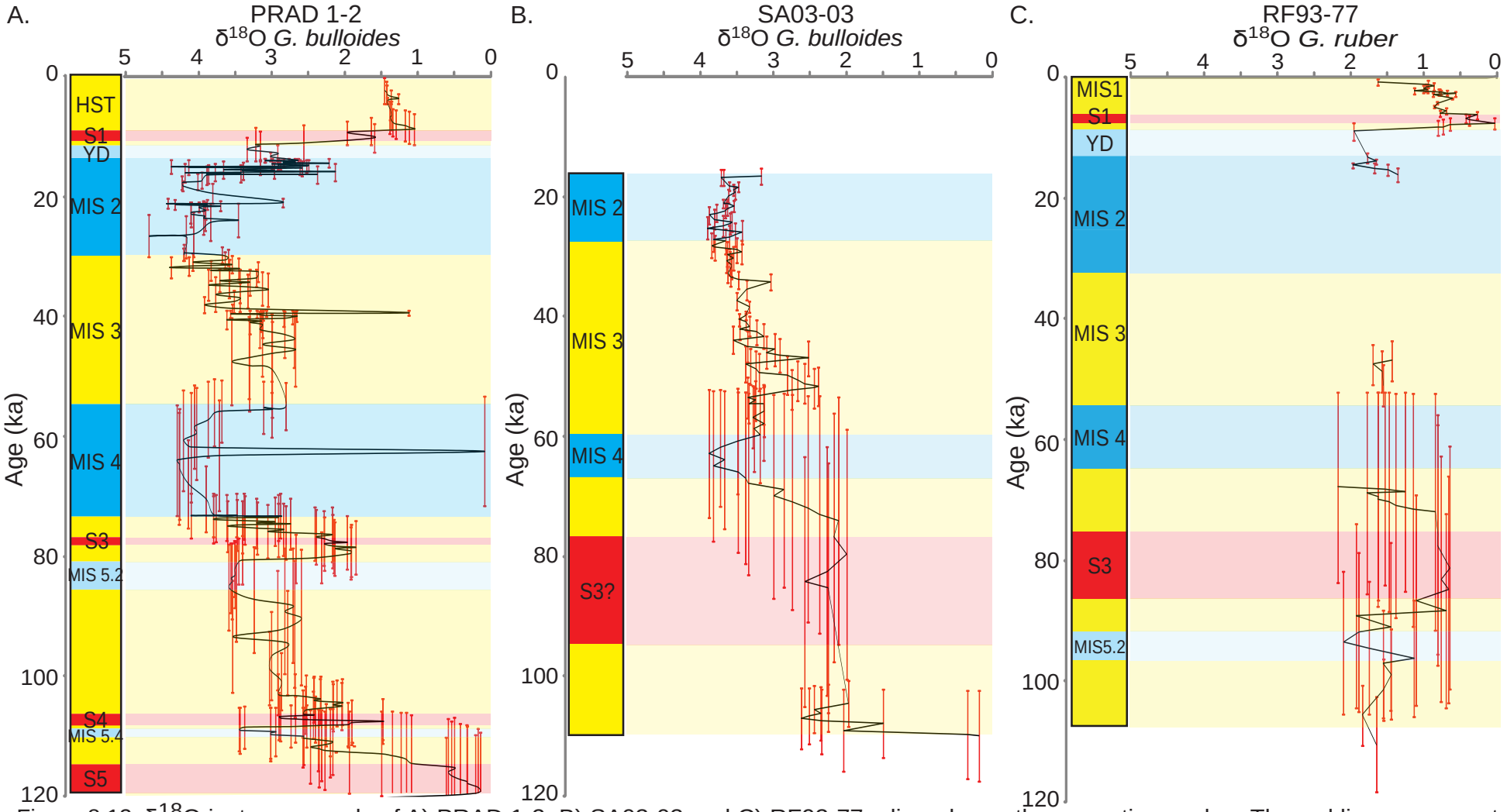

Figure 8.13: $\delta^{18}O$ isotope records of A) PRAD 1-2, B) SA03-03 and C) RF93-77, aligned over the same timescale. The red lines represent the 2σ errors associated with each age estimate. The stratigraphic scheme for each core is also shown, with the stratigraphic boundaries plotted against age using the tephra-based age model (see text).

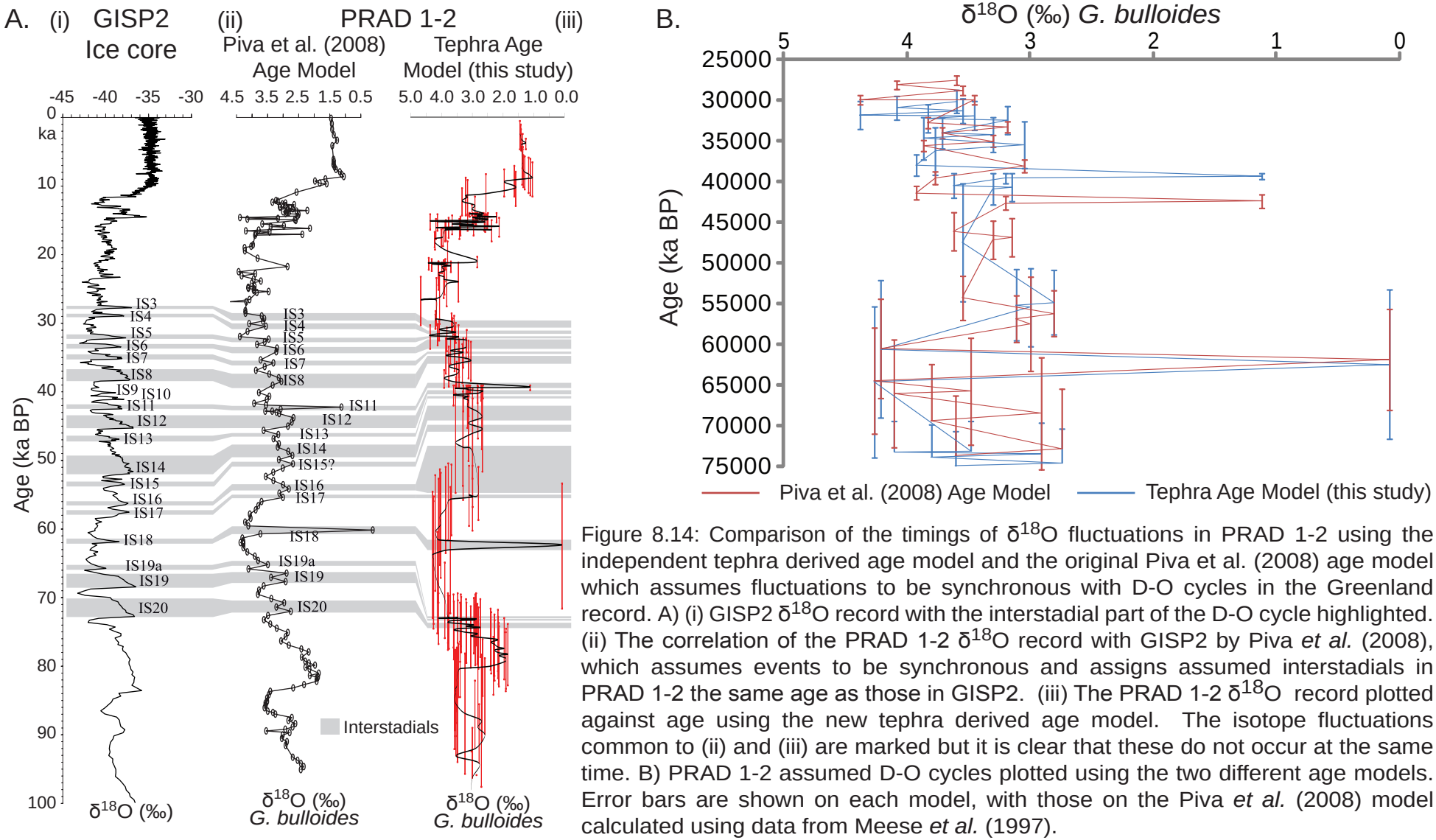

Figure 8.14: Comparison of the timings of $\delta^{18}O$ fluctuations in PRAD 1-2 using the independent tephra derived age model and the original Piva et al. (2008) age model which assumes fluctuations to be synchronous with D-O cycles in the Greenland record. A) (i) GISP2 $\delta^{18}O$ record with the interstadial part of the D-O cycle highlighted. (ii) The correlation of the PRAD 1-2 $\delta^{18}O$ record with GISP2 by Piva *et al.* (2008), which assumes events to be synchronous and assigns assumed interstadials in PRAD 1-2 the same age as those in GISP2. (iii) The PRAD 1-2 $\delta^{18}O$ record plotted against age using the new tephra derived age model. The isotope fluctuations common to (ii) and (iii) are marked but it is clear that these do not occur at the same time. B) PRAD 1-2 assumed D-O cycles plotted using the two different age models. Error bars are shown on each model, with those on the Piva *et al.* (2008) model calculated using data from Meese *et al.* (1997).

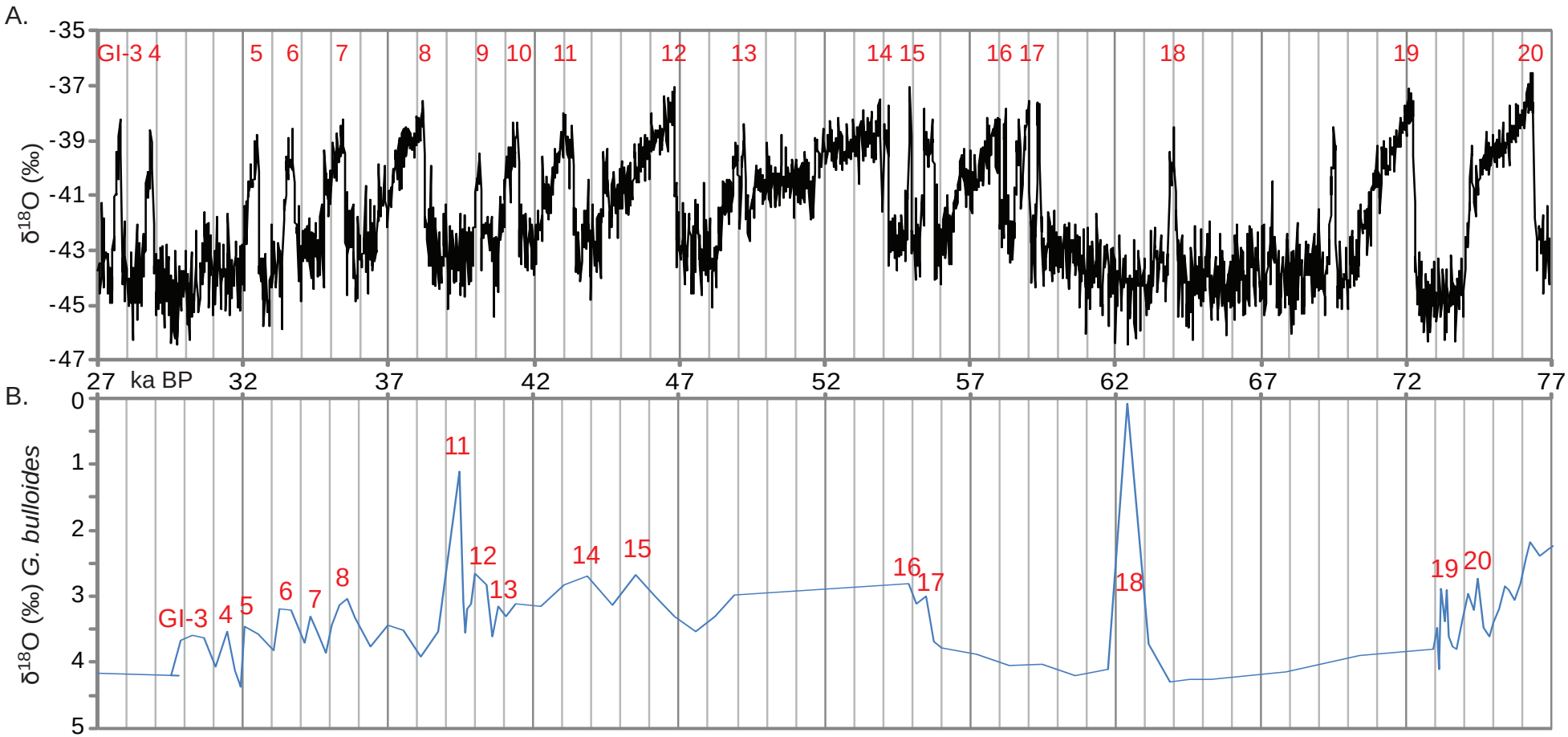

Figure 8.15: Comparison of the NGRIP $\delta^{18}O$ record plotted on the GICC05 modelext timescale and the PRAD 1-2 $\delta^{18}O$ record plotted on the tephra-derived timescale. The NGRIP dates have been adjusted to ka BP to allow for direct comparison with the PRAD 1-2 record. The Greenland Interstadials (GI) are marked on the NGRIP record. The interstadials that Piva *et al.* (2008a) correlated to PRAD 1-2 $\delta^{18}O$ fluctuations are marked on the PRAD 1-2 record.

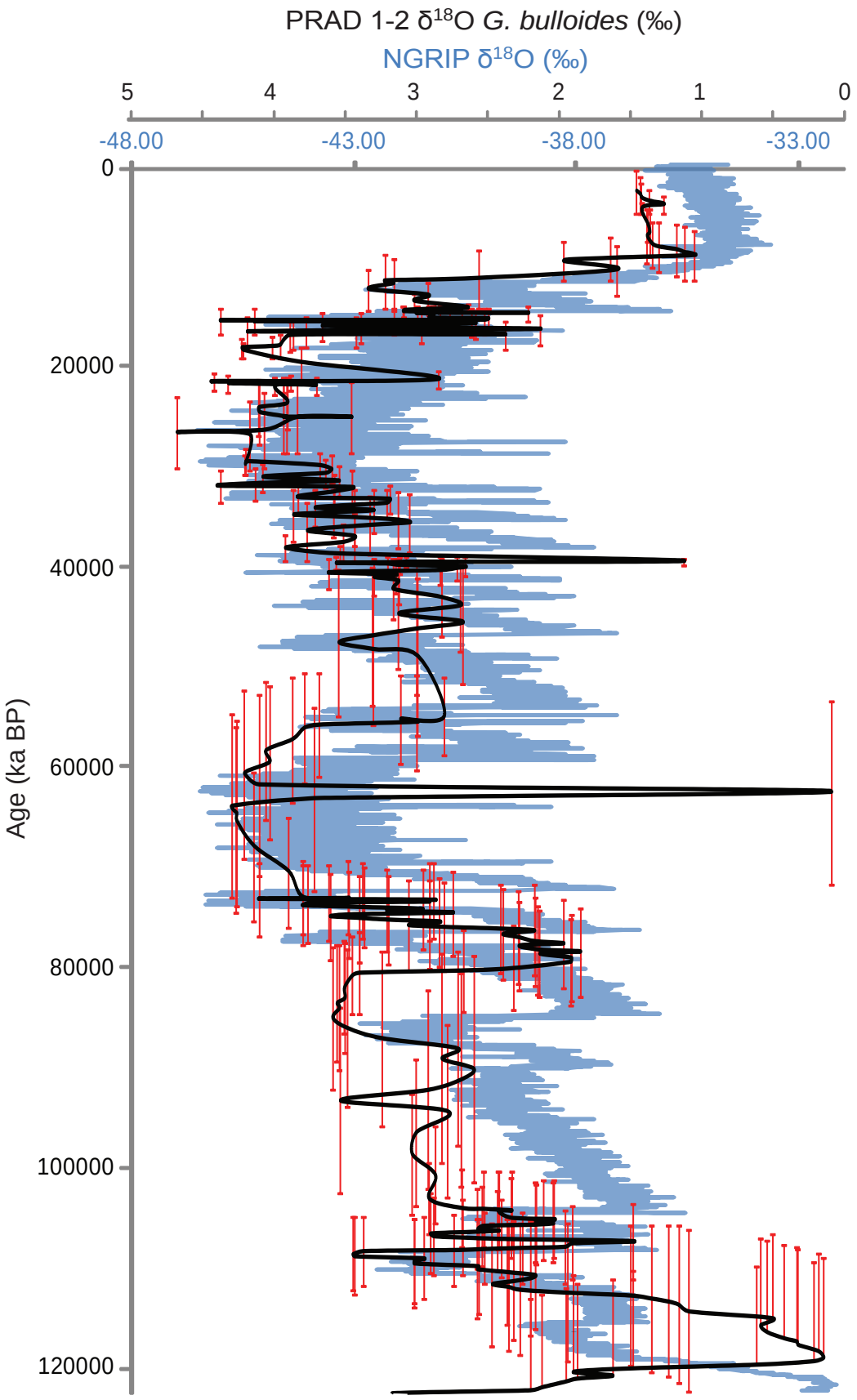

Figure 8.16: Comparison of isotopic trends in the NGRIP (blue) and PRAD 1-2 (black) $\delta^{18}O$ records. The NGRIP record is plotted on the GICC05 modelext timescale (Svensson *et al.,* 2008) and, due to the way the timescale was extended dates older than 60.2 ka b2k should be treated with caution. NGRIP ages have been converted to ka BP for comparison. The PRAD 1-2 record is plotted on the independent tephra-derived timescale.

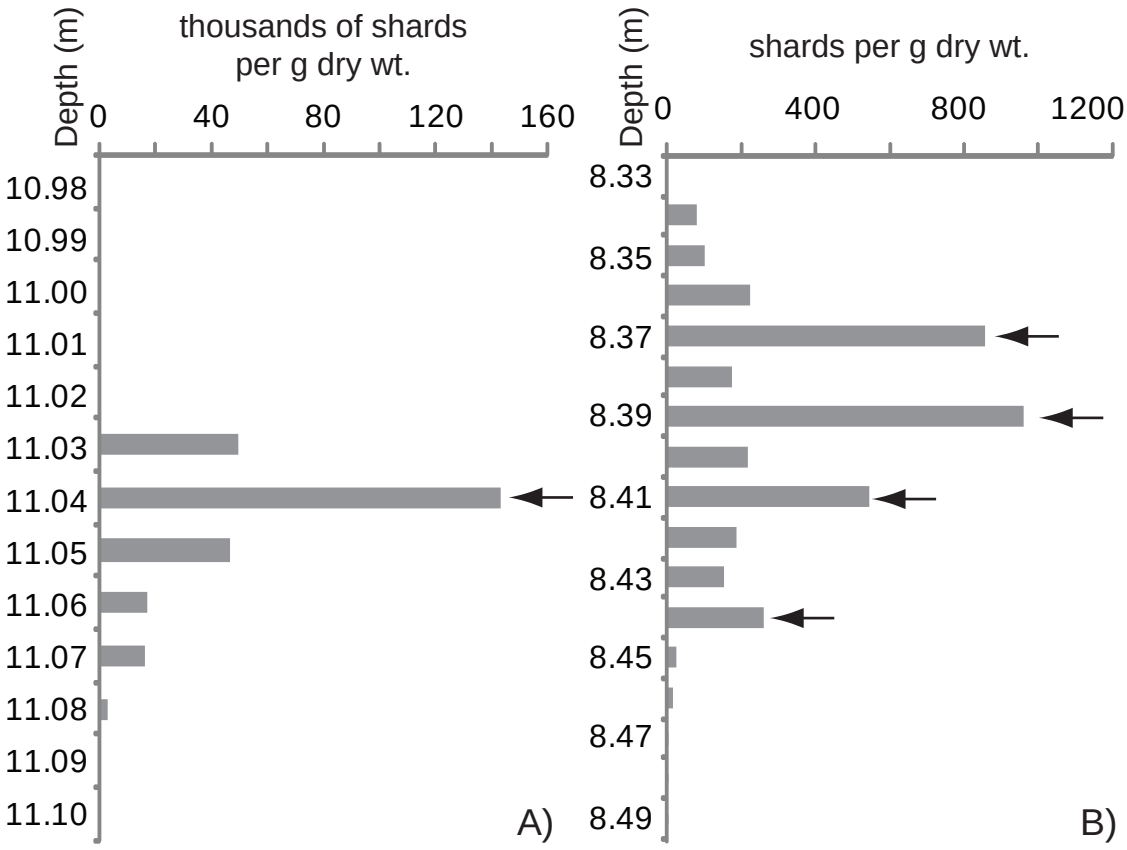

Figure 9.1: Examples of how shard distributions affect the position of the tephra isochron. A) PRAD-1104 shard counts. Shards are only spread over 6 cm, with a defined peak in glass concentration. B) PRAD-839 shard counts. 839 cm is taken as the isochron but the vertical distribution of glass shards is over 13 cm and there are four peaks in glass within the tephra distribution. Therefore the uncertainty in the position of the isochron is greater in B, than A, making it less robust.

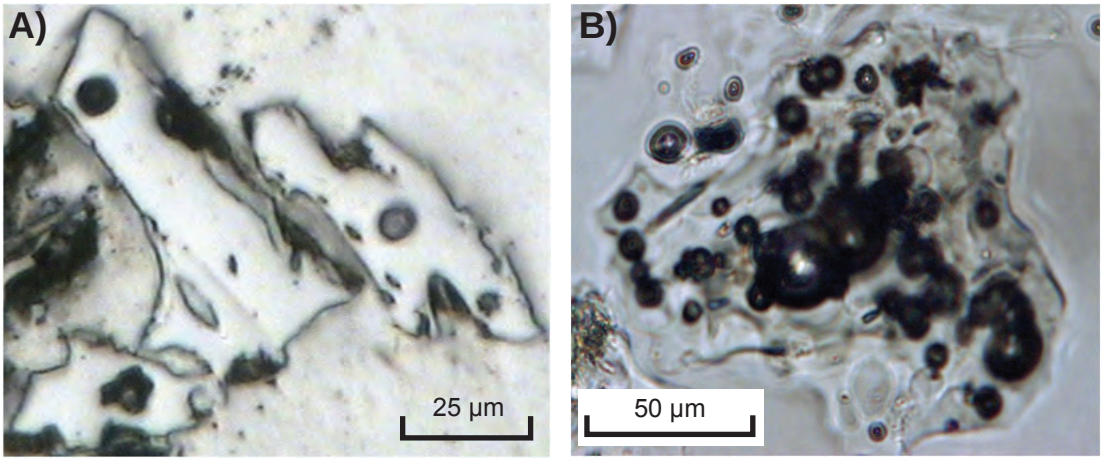

Figure 9.2: Examples of the effect of shard size on WDS-EPMA acquisitions. A) SEM image of PRAD 1-2 tephra shards. Shards are only ca. 25 µm wide. The black circles on each of the three shards show the location of the 10 µm electron beam and indicate why EPMA measurements may be difficult. B) Photomicrograph of a highly vesicular tephra shard from SA03-03. This indicates that whilst the shard is > 100 µm in diameter the glass surface area free from vesicles is very small.

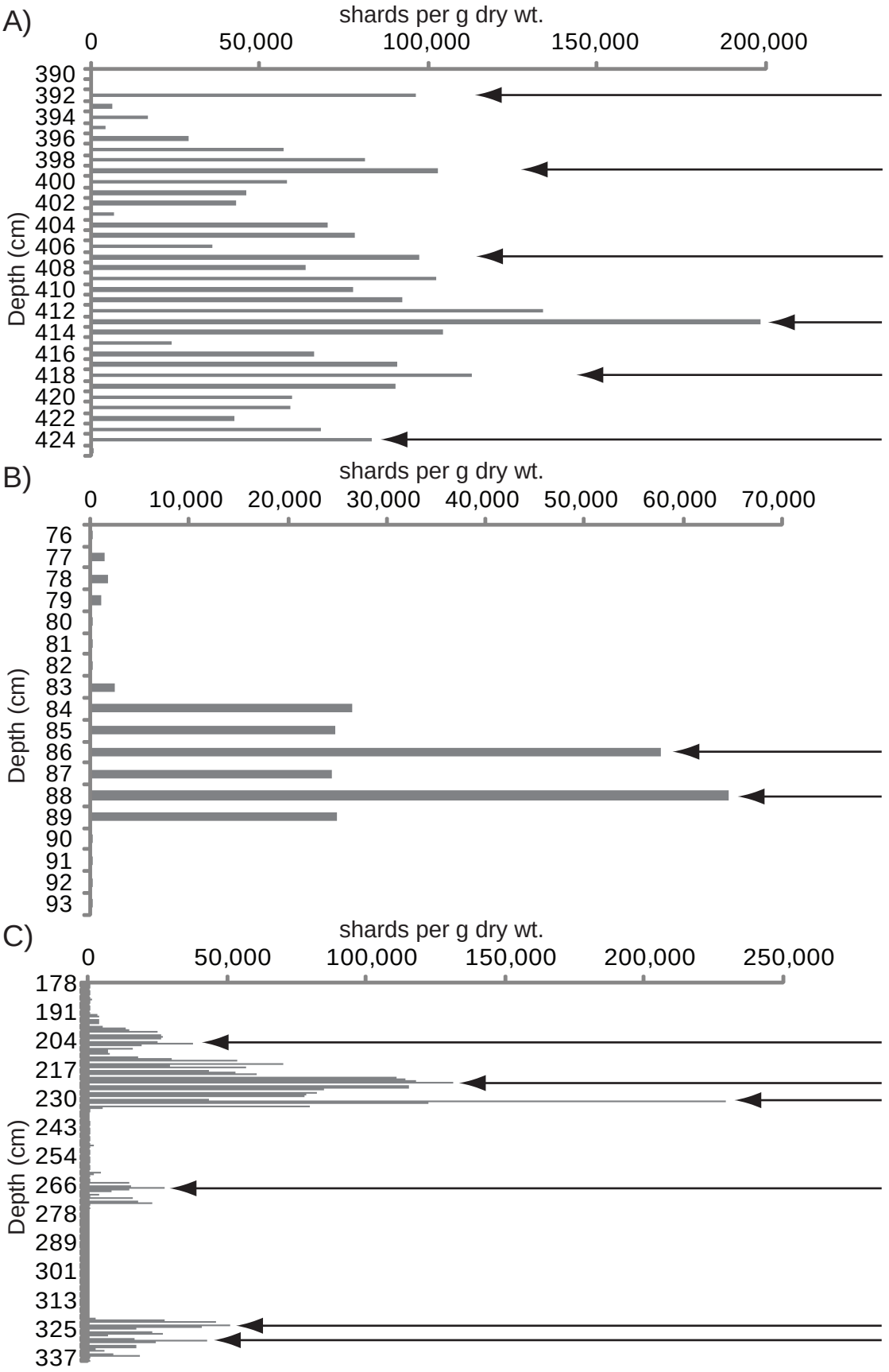

Figure 9.3: Shard distributions of layers with indistinguishable major element geochemistry. In all cases black arrows represent the positions sampled for geochemical analysis. A) SA03-03 390 - 424 cm, B) RF93-77 76 - 93 cm and C) PRAD 1-2 178 - 337 cm. In A) and B) the shard distribution appears to be one event, with multiple peaks in glass probably due to the Lycopodium counting method. However in C) there are clearly 3 or 4 separate tephra layers, suggesting multiple layers with indistinguishable geochemical signatures.

PRAD 1-2 1 cm resolution trace element data for samples PRAD-205, PRAD-223, PRAD-231, PRAD-267, PRAD-273 and PRAD-336. All elemental data is presented at p.p.m.

Sample	Crater (µm)	Rb	Sr	Y	Zr	Nb	Cs	Ba	La	Ce	Pr	Nd	Sm	Eu	Gd	Tb	Dy	Ho	Er	Tm	Yb	Lu	Hf	Ta	Pb	Th	U
PRAD-205	20	299.93	1421	32.58	255.50	43.97	14.53	2775.25	76.38	133.03	14.58	59.77	12.47	3.09	8.69	1.05	5.86	1.39	3.61	0.69	3.13	0.45	6.94	2.73	45.64	30.05	6.93
PRAD-205	20	331.26	768	32.29	297.54	50.64	16.25	1334.46	65.52	114.10	12.96	48.76	9.96	2.23	8.85	0.94	7.33	1.25	3.26	0.56	3.44	0.51	7.55	3.07	49.22	30.42	8.98
PRAD-205	20	266.42	992	34.13	251.76	39.41	12.79	1866.24	64.92	113.51	12.90	54.45	10.92	2.71	8.16	1.17	6.55	1.15	3.40	0.48	3.67	0.47	7.37	2.50	39.49	24.89	6.26
PRAD-205	10	290.52	1968	65.70	607.96	58.12	18.62	3488.74	133.52	170.94	23.74	100.28	17.13	2.93	20.13	1.88	12.50	1.79	5.96	0.65	5.89	0.87	14.03	3.66	57.03	51.52	8.21
PRAD-205	20	307.59	816	33.61	304.67	46.08	16.00	1228.48	64.57	113.68	13.54	48.52	9.67	2.76	8.02	1.30	5.89	1.29	3.83	0.60	3.87	0.40	8.25	2.75	45.89	30.49	8.04
PRAD-205	20	274.17	1265	35.55	285.75	43.55	14.45	2176.85	80.26	135.31	16.67	60.50	13.35	2.83	9.19	1.43	8.01	1.29	4.06	0.70	3.40	0.54	7.87	2.98	44.25	33.79	7.66
PRAD-205	20	280.14	1123	37.15	287.63	44.57	14.63	2369.15	79.20	148.90	16.17	62.01	12.62	3.05	9.75	1.02	6.95	1.33	4.10	0.74	3.01	0.54	7.93	2.86	43.13	34.91	8.53
PRAD-205	20	275.34	1287	33.42	262.46	44.49	13.99	2465.62	77.31	139.67	15.78	58.63	10.14	3.05	9.00	1.17	7.23	1.18	2.90	0.48	2.90	0.50	6.64	2.27	40.72	29.69	7.45
PRAD-205	20	263.34	1103	32.36	235.05	37.80	12.62	1813.67	62.81	108.07	13.20	52.18	10.37	2.50	9.88	1.09	5.83	1.50	2.78	0.53	2.77	0.54	5.35	2.32	36.41	22.05	5.39
PRAD-205	20	294.64	1345	37.77	307.98	45.29	16.13	2435.41	86.34	144.55	16.35	69.97	11.35	3.03	9.69	1.31	7.98	1.43	4.26	0.62	3.80	0.53	7.87	2.79	50.78	34.09	8.01
PRAD-205	20	376.05	271	45.30	437.23	71.86	23.07	95.23	112.65	185.27	20.78	78.84	13.50	2.80	11.60	1.30	9.94	1.78	4.69	0.91	4.75	0.74	10.88	4.32	60.60	48.93	12.74
PRAD-205	20	278.19	1199	35.15	292.08	43.75	15.26	2126.11	78.88	138.66	16.45	62.88	11.39	3.24	10.41	1.24	7.11	1.55	3.49	0.40	3.30	0.52	7.16	2.80	45.35	33.45	7.98
PRAD-223	10	337.33	342	74.42	856.16	82.83	20.06	124.75	153.60	217.12	27.83	103.82	15.84	3.22	19.97	2.70	12.81	2.23	5.09	0.81	7.35	0.69	18.44	5.19	73.45	73.21	14.54
PRAD-223	10	278.74	859	49.07	596.08	58.62	13.19	1138.91	105.32	151.00	19.76	66.82	11.10	3.47	15.13	1.51	9.77	1.68	4.83	0.91	5.91	0.43	12.18	3.83	56.31	47.16	8.69
PRAD-223	10	272.86	1711	50.42	495.55	55.96	13.77	3011.05	106.19	163.40	22.31	78.91	12.62	3.76	13.63	1.56	8.45	1.63	4.92	0.69	4.02	0.74	8.83	3.42	51.64	47.09	7.64
PRAD-223	20	278.59	1044	29.38	266.54	44.39	14.59	-0.99	69.11	128.44	14.31	52.67	9.67	2.52	11.63	1.05	5.58	1.02	2.79	0.43	2.66	0.41	6.26	2.38	43.63	28.18	7.76
PRAD-223	20	276.78	723	26.05	251.52	41.44	14.84	1214.71	54.65	99.96	10.98	40.80	7.58	1.91	9.06	0.85	5.13	0.90	2.64	0.36	2.48	0.40	5.89	2.33	40.49	24.76	7.53
PRAD-223	20	254.85	589	26.40	248.99	41.85	12.26	534.31	58.48	102.15	11.38	40.37	7.52	1.85	9.51	0.88	5.16	0.99	2.58	0.42	2.47	0.39	6.28	2.23	36.72	22.75	5.99
PRAD-223	20	288.20	485	40.91	415.55	59.99	17.75	582.63	91.29	151.49	16.96	64.51	11.80	2.60	14.31	1.32	7.37	1.46	4.04	0.51	3.70	0.67	9.32	3.32	43.69	40.58	9.27
PRAD-223	10	280.35	1109	55.67	587.55	56.05	12.67	1335.78	111.00	159.38	20.21	73.87	16.97	3.39	14.18	2.15	12.62	1.62	4.35	0.54	6.60	0.71	13.98	3.98	60.13	43.64	8.00
PRAD-223	10	282.16	1369	36.85	423.43	46.31	14.22	1903.26	87.74	129.77	16.53	61.21	12.56	2.48	14.43	0.67	6.66	1.21	4.25	0.40	1.86	0.46	8.86	2.59	53.61	34.67	6.40
PRAD-223	10	344.20	314	54.37	571.22	79.41	21.75	123.64	117.87	216.07	22.40	77.76	13.74	2.73	12.58	1.67	10.33	1.79	5.10	0.73	5.16	0.73	12.48	4.15	68.98	56.54	13.09
PRAD-223	20	265.61	666	28.64	293.60	45.40	13.90	1012.09	58.14	104.61	11.63	46.75	8.23	1.83	10.25	0.98	5.26	1.03	3.18	0.54	3.03	0.44	6.84	2.60	34.42	27.63	7.34
PRAD-223	20	301.80	810	31.44	301.02	50.55	17.89	1278.90	76.87	137.42	15.29	57.44	10.36	2.56	13.79	1.11	6.07	1.14	3.42	0.44	3.18	0.50	7.16	2.90	48.66	32.88	9.10
PRAD-223	10	279.07	1507	57.43	598.75	59.81	14.71	2240.71	117.48	169.54	22.26	81.56	16.01	3.98	14.93	1.48	9.48	1.75	6.00	0.80	3.70	0.70	12.25	3.54	68.10	48.02	9.32
PRAD-223	10	298.49	1074	41.91	391.15	55.42	16.21	1787.41	87.74	144.87	16.98	69.00	12.14	2.39	11.31	1.49	7.50	1.55	4.11	0.56	3.56	0.55	8.98	2.77	58.66	38.54	9.03
PRAD-223	20	310.66	670	28.50	305.03	47.83	16.06	1068.93	60.45	104.17	12.37	43.54	8.78	1.90	10.84	0.98	5.38	1.03	3.14	0.46	2.87	0.45	7.32	2.52	45.18	28.44	8.65

PRAD-223	20	276.54	825	27.58	262.83	41.45	14.72	1228.75	64.12	110.40	12.56	46.77	8.18	2.40	10.31	0.91	4.80	0.95	2.59	0.38	2.69	0.39	5.94	2.23	39.05	27.51	6.78
PRAD-231	20	333.73	284	40.95	398.70	57.97	19.48	81.90	83.11	141.91	15.91	59.93	12.62	2.84	10.39	1.23	8.30	1.66	4.06	0.71	4.33	0.71	10.30	3.98	64.46	39.48	10.66
PRAD-231	10	275.25	838	55.25	482.38	60.66	11.20	843.89	106.92	158.95	19.32	72.88	11.87	2.87	14.18	1.75	7.53	1.43	6.06	0.53	6.74	0.86	12.41	3.80	50.09	38.45	8.70
PRAD-231	10	293.75	1220	59.94	517.88	57.40	14.47	1861.38	112.55	178.02	22.39	79.90	15.80	2.78	15.74	2.33	10.83	2.49	5.65	0.74	5.05	0.67	11.99	3.68	52.15	44.37	9.03
PRAD-231	20	358.13	260	42.62	443.63	64.54	22.49	96.50	98.42	170.70	18.85	71.75	12.74	2.32	11.26	1.48	9.09	1.58	4.82	0.60	4.18	0.56	10.22	3.92	63.32	49.12	11.79
PRAD-231	20	304.28	835	34.81	319.83	48.86	16.93	1318.05	79.30	139.20	15.55	59.88	11.24	2.89	10.81	1.21	7.20	1.20	3.51	0.69	3.58	0.53	8.50	2.88	57.02	35.52	9.18
PRAD-231	10	330.71	354	75.48	694.57	78.40	19.63	150.62	140.11	208.59	24.69	103.09	19.11	2.69	17.97	2.78	13.43	2.84	6.68	1.02	7.18	0.86	14.81	5.86	71.77	63.43	12.06
PRAD-231	10	326.44	420	68.44	699.15	84.24	18.82	220.02	141.86	201.71	26.39	94.52	17.92	2.85	17.76	1.89	12.72	1.89	10.00	1.37	9.83	1.13	16.18	4.15	67.81	65.44	14.33
PRAD-231	10	309.98	1452	73.30	645.04	70.75	16.84	2168.55	148.00	215.64	28.73	109.76	19.18	4.69	19.90	3.17	13.76	1.80	6.99	0.66	5.40	0.78	15.26	3.54	64.53	60.97	10.58
PRAD-231	20	355.63	268	42.71	429.77	69.79	22.71	107.30	97.08	189.35	18.67	65.34	11.83	2.44	10.22	1.33	8.71	1.52	4.41	0.66	4.31	0.63	10.05	3.76	61.86	47.03	12.29
PRAD-231	10	334.34	461	76.66	733.97	86.30	19.30	203.47	149.62	243.44	28.08	103.21	16.43	3.85	16.21	2.04	12.56	3.23	7.52	0.63	9.05	0.84	16.32	4.28	69.43	79.66	12.95
PRAD-231	20	308.41	919	32.93	294.30	48.70	16.93	1551.13	72.27	126.95	14.15	57.97	10.46	2.13	9.20	1.19	6.33	1.32	3.56	0.50	2.97	0.47	7.23	2.51	52.60	32.06	8.48
PRAD-231	10	276.25	1089	53.45	483.03	58.49	14.63	1628.85	108.63	162.68	19.26	77.26	17.41	3.66	12.20	1.86	12.62	2.52	4.95	0.89	5.14	0.97	10.32	4.08	53.12	47.95	20.49
PRAD-231	10	369.74	411	93.74	867.09	86.54	19.45	133.16	173.56	238.93	31.01	135.68	17.37	3.60	22.61	3.19	14.51	3.48	7.99	0.92	12.09	1.49	23.91	6.14	78.88	82.37	14.26
PRAD-231	10	265.74	1494	44.15	352.41	49.67	14.34	2540.39	91.73	155.60	18.96	72.65	12.40	3.59	12.52	1.53	8.63	1.50	4.73	0.55	4.28	0.59	7.68	2.91	50.86	37.00	7.71
PRAD-231	10	312.64	415	71.58	701.55	82.71	19.51	404.17	148.52	234.82	29.35	110.77	16.90	3.44	17.35	2.54	15.54	2.33	7.55	0.81	6.67	0.92	15.85	5.85	68.41	70.31	14.54
PRAD-231	10	325.61	373	79.44	803.73	89.25	19.12	113.51	161.24	237.05	29.96	119.46	22.86	3.39	19.23	3.08	14.75	2.39	6.42	0.63	8.43	1.33	18.25	5.85	75.95	77.19	14.83
PRAD-231	20	264.71	611	31.98	331.03	49.56	14.99	902.99	73.16	125.85	13.86	50.89	10.20	2.15	8.39	1.18	7.05	1.51	3.71	0.43	2.56	0.51	8.41	3.20	45.54	34.62	8.55
PRAD-267	20	329.39	252	39.42	397.97	68.14	19.90	97.29	94.18	159.52	17.63	68.50	11.97	2.17	12.18	1.34	7.22	1.49	3.79	0.59	4.01	0.64	9.72	3.81	57.14	42.77	10.83
PRAD-267	10	275.40	1814	57.69	595.92	54.12	12.11	2899.20	133.12	167.85	23.76	97.80	16.00	3.78	20.20	2.60	12.31	2.06	3.80	0.59	3.87	0.38	16.42	3.17	69.33	67.94	8.37
PRAD-267	10	309.94	756	59.75	658.35	76.21	20.41	1032.63	133.00	202.79	22.22	85.87	14.91	2.89	14.99	2.03	13.20	2.13	6.27	0.64	6.09	1.08	15.28	4.86	63.24	66.11	14.60
PRAD-267	20	320.23	647	46.93	495.33	66.98	21.32	896.12	109.54	177.71	18.52	72.16	12.84	2.58	12.18	1.62	11.13	1.80	5.42	0.58	5.08	0.92	12.30	4.40	56.71	54.99	13.71
PRAD-267	20	255.64	1454	34.28	303.04	40.38	13.13	3215.45	77.33	127.41	14.06	60.47	8.66	3.35	8.97	1.27	6.60	1.15	3.59	0.51	3.69	0.53	7.35	2.22	35.50	28.87	5.86
PRAD-267	20	270.29	823	36.72	318.04	51.42	15.34	1268.51	80.85	137.61	15.58	57.32	10.57	2.51	10.86	1.23	6.60	1.37	3.55	0.51	3.65	0.54	7.94	2.72	46.76	34.40	9.39
PRAD-267	10	247.42	1698	43.64	402.77	45.95	12.57	3705.24	93.89	145.39	16.87	71.96	10.06	3.75	11.04	1.60	7.83	1.36	4.15	0.57	4.42	0.62	9.13	2.45	39.59	34.70	6.24
PRAD-267	10	261.60	962	46.74	422.71	58.51	14.68	1461.73	98.16	157.03	18.69	68.22	12.27	2.81	13.36	1.54	7.82	1.61	4.10	0.56	4.38	0.63	9.86	3.00	52.14	41.35	10.00
PRAD-267	10	288.32	924	40.29	432.14	52.01	14.21	1399.93	79.40	129.22	16.41	60.66	12.15	2.04	12.23	1.39	7.87	1.29	3.78	0.57	4.38	0.49	9.12	3.67	61.24	39.08	8.82
PRAD-267	10	262.42	1282	48.54	463.96	52.27	13.45	2500.26	102.85	153.20	19.42	75.31	13.88	3.06	14.56	1.56	8.36	1.75	3.97	0.67	4.85	0.70	10.38	2.96	60.46	41.80	8.69
PRAD-267	10	343.29	371	59.53	740.83	81.25	20.40	265.98	127.47	191.69	24.42	78.70	15.78	2.28	17.07	1.67	11.22	2.61	6.71	0.45	5.13	1.08	15.18	4.29	70.17	62.56	11.91
PRAD-267	20	259.74	757	33.86	283.88	41.97	14.14	1135.12	57.99	103.56	12.16	49.60	9.88	2.35	10.63	1.13	6.90	1.24	3.31	0.46	3.16	0.42	7.31	2.45	38.18	25.75	6.95
PRAD-267	20	341.01	292	42.49	410.07	65.48	21.18	142.85	103.11	171.21	19.10	72.03	12.54	2.68	13.32	1.41	7.98	1.49	3.91	0.71	4.43	0.69	9.22	3.58	58.94	45.09	11.15
PRAD-267	10	256.20	714	40.71	439.97	56.40	14.35	1040.54	88.82	143.62	16.62	60.57	11.85	2.41	10.32	1.47	8.36	1.78	4.29	0.48	3.07	0.60	10.45	3.53	50.78	41.62	9.10
PRAD-267	10	318.80	294	50.18	528.95	77.54	19.05	112.11	114.35	182.04	21.15	81.52	13.90	2.43	14.99	1.68	8.56	1.75	4.39	0.65	4.81	0.75	12.08	4.21	63.72	51.42	11.54
PRAD-267	10	320.23	506	94.05	853.60	85.14	20.39	237.12	165.57	234.48	30.69	100.88	19.71	2.71	20.31	2.09	14.54	4.54	6.58	0.84	7.18	1.33	19.40	3.56	66.34	74.65	13.77
PRAD-267	20	294.01	325	52.33	514.58	80.48	22.48	129.76	121.09	193.29	22.29	83.34	14.21	2.63	15.04	1.60	9.95	1.85	5.19	0.72	5.19	0.79	12.73	4.69	59.39	55.74	13.07
PRAD-273	10	258.58	1472	57.49	506.34	53.82	11.80	2440.72	110.56	161.17	21.95	85.12	13.67	2.90	10.50	2.19	9.50	1.09	5.86	0.47	4.17	1.18	10.10	2.04	43.81	37.11	7.05

PRAD-273	10	312.59	334	75.25	804.66	84.62	17.53	89.22	155.38	207.56	25.63	117.46	21.86	3.67	19.55	3.07	13.53	3.17	4.99	0.82	6.70	1.48	16.97	3.99	70.43	68.17	13.16
PRAD-273	10	318.93	1395	48.42	427.83	52.55	15.08	2296.67	103.44	163.25	19.93	77.25	13.72	3.02	14.17	1.55	9.76	1.79	5.13	0.50	3.95	0.59	10.26	3.04	53.25	44.22	8.36
PRAD-273	10	305.02	910	52.61	540.40	60.47	15.71	759.92	112.32	154.50	19.71	77.50	13.91	3.51	12.33	1.39	8.80	1.77	3.58	0.58	5.00	0.73	10.81	3.01	66.31	50.16	9.13
PRAD-273	10	306.76	827	64.12	625.22	71.74	15.20	1011.71	132.90	193.29	23.34	98.82	13.11	4.02	20.08	2.19	10.73	2.24	4.38	0.40	6.22	0.55	13.41	4.34	66.25	59.03	11.19
PRAD-273	10	331.48	414	68.24	798.20	80.63	20.38	233.09	143.66	195.17	25.20	90.15	16.26	3.05	13.94	2.57	13.18	1.55	6.64	0.82	5.52	0.83	15.68	4.96	70.15	64.42	11.40
PRAD-273	10	282.99	1235	66.17	676.78	64.87	15.48	1882.37	132.96	189.66	26.62	115.23	13.59	4.55	14.36	2.44	11.01	2.87	5.05	-0.39	4.60	0.56	12.43	3.59	50.96	54.38	8.96
PRAD-273	10	259.24	1975	49.24	498.00	52.74	12.22	3909.24	107.68	155.61	21.58	81.72	14.45	3.54	15.92	1.92	10.49	1.60	3.97	0.93	4.17	0.47	9.77	3.09	55.46	40.72	7.63
PRAD-273	20	329.52	1194	38.04	321.89	46.18	15.75	1993.08	85.19	143.06	16.61	64.91	11.81	2.70	11.52	1.23	8.23	1.51	4.44	0.45	3.30	0.50	8.26	2.75	47.76	36.78	7.85
PRAD-273	10	342.27	438	69.15	829.08	84.87	21.02	212.51	143.37	198.04	26.48	98.68	24.59	2.71	20.03	3.40	9.40	2.02	8.74	1.01	6.31	1.12	15.76	5.44	80.18	67.26	11.80
PRAD-336	10	332.80	379	68.21	728.70	80.86	37.34	180.43	139.32	203.55	26.49	105.65	16.89	3.28	17.99	2.49	11.85	2.23	5.06	0.92	7.97	0.56	15.95	4.68	74.63	63.24	12.23
PRAD-336	10	316.02	475	66.90	718.89	81.25	19.90	215.66	147.69	215.42	26.37	96.86	17.89	3.15	19.54	1.93	12.02	2.38	7.48	1.01	6.00	1.07	15.57	4.72	74.89	66.96	14.15
PRAD-336	20	274.56	1278	34.69	265.15	43.65	14.98	2204.58	75.55	136.35	15.81	61.05	10.68	3.21	10.18	1.22	7.28	1.27	4.09	0.49	3.57	0.50	6.19	2.63	45.61	30.77	7.24
PRAD-336	10	284.56	380	66.61	683.93	91.58	21.52	149.52	147.02	220.57	26.74	99.18	16.50	2.94	18.51	2.00	11.80	2.18	6.00	0.79	6.22	0.93	15.81	5.17	66.22	67.02	13.92
PRAD-336	10	268.60	1967	63.62	565.49	59.71	13.50	3120.30	121.36	165.24	23.95	91.51	14.37	3.62	15.71	2.19	10.18	1.92	5.72	0.80	4.47	0.84	15.05	2.69	61.45	47.60	8.46
PRAD-336	10	336.53	384	64.17	730.08	87.42	18.83	128.85	142.58	227.51	27.58	92.88	17.63	2.87	19.54	1.90	12.40	2.67	5.77	0.67	5.55	0.85	14.00	4.95	64.82	65.56	13.97
PRAD-336	10	323.65	356	69.14	760.06	84.50	20.42	117.84	143.88	214.70	26.34	94.48	16.23	3.14	21.49	2.17	11.80	2.32	5.19	0.87	6.16	1.08	15.39	4.29	81.31	70.07	13.14
PRAD-336	10	251.39	884	43.11	377.32	47.76	13.54	1308.02	70.41	118.17	14.59	59.02	11.47	2.63	13.07	1.41	8.18	1.47	3.83	0.51	3.79	0.49	9.08	2.70	42.57	30.96	7.40
PRAD-336	10	330.04	341	54.08	545.03	74.50	20.27	164.61	125.19	195.37	22.91	85.73	14.56	3.00	16.39	1.76	9.46	1.76	4.52	0.79	5.31	0.81	11.45	3.95	65.72	54.22	11.88
PRAD-336	10	242.71	1179	39.66	379.38	47.02	11.93	2000.01	87.16	150.76	17.81	69.03	9.97	3.04	13.48	1.61	6.36	1.60	3.76	0.54	4.24	0.56	9.01	2.58	53.37	33.52	9.11
PRAD-336	10	274.74	1726	65.98	604.23	70.39	14.27	3299.28	117.90	170.96	21.29	71.35	13.66	3.29	16.49	1.74	9.53	1.48	3.81	0.76	4.85	0.79	13.52	4.39	66.38	54.95	11.12
PRAD-336	20	285.42	932	41.99	363.42	51.40	15.28	1413.54	89.47	142.56	16.05	64.91	15.00	3.27	9.92	1.49	10.64	2.13	4.28	0.80	4.29	0.83	8.31	3.70	47.64	39.88	19.24